Préface

Le thème traité dans cette thèse est la résistance à l'effort tranchant des dalles en béton armé sans armature d'effort tranchant appuyées linéairement et chargées par de forces concentrées. Les applications les plus importantes sont les dalles de roulement de pont (ponts en béton armé et ponts mixtes) avec appuis de la dalle représentés par les âmes et charges intenses reparties sur des petites surfaces dues à l'action des poids-lourds. Du fait que les actions prépondérantes sont celles du trafic, la résistance à la fatigue de ces dalles peut être déterminante.

Ce thème est devenu important depuis une douzaine d'années car précédemment, avec les anciennes règles de dimensionnement à l'effort tranchant, c'était la flexion qui était déterminante. De ce fait, un grand nombre de dalles de roulement de ponts existants n'a pas été vérifié à l'effort tranchant lors du dimensionnement. C'est avec l'introduction des normes de nouvelle génération que l'effort tranchant est devenu déterminant de sorte qu'un bon nombre de ponts existants ne satisfont plus les exigences normatives. Malgré l'importance pratique, les recherches dans ce domaine sont encore rares et certains problèmes, comme par exemple la redistribution des efforts due à la fissuration, la transmission par appuis direct des charges en proximité des âmes, l'influence de la présence des câbles de précontrainte dans la dalle de roulement des ponts construits en encorbellement ainsi que la résistance à la fatigue sont encore peu étudiés et mal compris.

Le travail de thèse de Francisco Natário représente une contribution importante dans ces domaines et a permis de développer des méthodes de vérification simples et utilisables par les ingénieurs. Nos remerciements vont à l'Office Fédéral des Routes qui a soutenu de façon déterminante cette recherche (projet AGB 2009/008) ainsi qu'aux membres de la commission accompagnante (Jean-Christophe Putallaz, Dr. Manuel Alvarez , Stéphane Cuennet et Dr. Hans Rudolf Ganz) pour le suivi et les remarques constructives.

Lausanne, juillet 2015

Prof. Dr. Aurelio Muttoni

Funding

The author would like to gratefully acknowledge the funding and support of the Swiss Federal Road Authority and VSL (Suisse) SA for providing the ducts used in the experimental work described in this thesis.

Para a Miana,
Orlanda e Isabel

Alcança quem não cansa - ex libris de Aquilino Ribeiro

Ao Sul, à procura do meu Norte
Subo as àguas desse rio
Onde a barca dos sentidos nunca partiu
Lá longe inventei o dia azul
E o desejo de partir
Pelo prazer de chegar ao Sul
Cada um tem a sina que tem
Os caminhos são sempre de alguém ao Sul
Ao Sul, entre dois braços abertos
Bate um coração maltês
Que se rende, que se dá, de vez
Por amor corto os frutos que criei
Corto os ramos que estendi
Pela raiz que abracei ao Sul
Cada um tem a sina que tem
Os caminhos são sempre de alguém ao Sul

João Monge

Acknowledgements

This thesis was developed over the last four and a half years at the Structural Concrete Laboratory (IBETON) of the École Polytechnique Fédérale de Lausanne under the supervision of Prof. Aurelio Muttoni. To him I would like to express my gratitude for the opportunity and for his wise guidance.

This work was done in close collaboration with Dr. Miguel Fernández Ruiz, who has greatly helped me through our numerous discussions, both on theoretical and practical levels. His enthusiasm, amiableness and remarkable capacity for motivating were deeply appreciated.

I would like to acknowledge the members of the jury, namely Prof. Ian Smith (president), Prof. Alain Nussbaumer, Prof. Günter Rombach and Prof. Carlos Zanuy. Their comments and suggestions were extremely pertinent and allowed me to improve this thesis.

I would also like to gratefully acknowledge the funding and support of the Swiss Federal Road Authority and VSL (Suisse) SA for providing the ducts used in the experimental work described in this thesis.

One part of this thesis was performed in collaboration with Dr. Juan Manuel Gallego, Prof. Carlos Zanuy and Prof. Luis Albajar. To them I express my gratitude. Special thanks to Dr. Juan Manuel Gallego for kindly sharing his database on shear-fatigue, for providing numerous papers, for his friendly attitude and for his help in the laboratory.

Special thanks to Filip Niketić for reading this thesis. Thanks to Maléna, Bastian, Marie-Rose, Francesco, Raffaele, Angelica and Juan Manuel for the abstract translations. Thanks to Karin Reissen for her comments.

I have sporadically collaborated with Dr. Olivier Burdet on my French publications and in planning laboratory related activities. I would like to acknowledge his comments and suggestions, some of them included in this thesis.

Special thanks to Yvonne, who helped me in many ways. It was also extremely interesting and personally rewarding our joint organization of the successful laboratory trip to Oporto in October 2012.

For more that two and a half years I have performed twenty-seven tests at the Structural Laboratory. This task was made easier by the friendly technical group: Frédérique, Gilles, Gérald, Patrice and Sylvain. Special thanks to Gilles for teaching me everything on how to perform the experiments and to Gérald for his resourcefulness. I would also like to acknowledge the competent assistance provided by Mr. Robert Čermák, the Head of Software Development of Inova Testing Systems, who remotely taught us how to pilot such a complex fatigue test setup. This was a perfect example on how complicated it may be to transpose a theoretical idea from planning into real life. I shall never forget the constant search of more than five months that

Sylvain and I did on how to pilot the test setup, and the stress that it has caused.

The friendly and collaborative environment of IBETON provided by my colleagues Darko, Fabio, Filip, Francesco, Franco, Galina, Ioannis, João, Jürgen, Luca, Maria, Marie-Rose, Michael, Raffaele, Stefan, Stefano, Thibault and guest colleagues Binbin, Jakob, Juan Manuel, Jaime and Mathieu is gratefully acknowledged. They provided me an excellent research environment and fruitful discussions. Our coffee, lunch and ice cream (summer!) breaks, as well as our side activities, made my PhD life in Lausanne much more interesting. Special thanks to Stefano, who has warmly welcomed me from day 0. Very special thanks to my office mate Marie-Rose for the excellent work environment, our helpful discussions about research and everyday life questions, and for sharing her experience at EPFL, which allowed me to have a better understanding of EPFL's teaching system and standards.

I would also like to thank the friends and colleagues from other research units. We have done many interesting things inside and outside EPFL. I have also learned from their experiments in the laboratory. Thanks to Albano, Alessandro, Ben, Carlos, Cláudio, Farshid, Gary, Georgia, Hadi, Maléna, Mark, Marina, Pia, Raluca, Raphaël, Sarah and Shenghan.

Many students helped me in the laboratory. To all them I express my gratitude. Special thanks to Agustí and Antoine for their hard work.

I first heard of EPFL when I was a student at my *alma mater* Instituto Superior Técnico, in Lisbon, from Prof. José Câmara. My application to EPFL was then supported by Prof. João Teixeira de Freitas, Prof. Luís Castro and Prof. Nuno Silvestre. To these excellent lecturers who influenced my research attitude and to my *alma mater* I would like to express my gratitude.

Before coming to EPFL I have worked for two years at the design office of Teixeira Duarte Engenharia e Construções, where I learned many things. This experience allowed me to always keep in mind that research becomes more useful if it can be used in practice. To Eng. Baldomiro Xavier and all his team I express my gratitude.

The PhD degree marks the end of more than twenty-one years in schools, made possible by my family, the Portuguese public education system and EPFL. To them I express my gratitude.

My basic science background was deeply influenced by my mother, my father, my sister and my brothers, and my high-school teachers Dra. Maria José Balsa and Dra. Rita Pissarra. At the experimental level I shall never forget the excellent three-year course in Physics Laboratory Experiments. Special thanks to my mother for her perseverance on closely following and supporting at home my development at school.

Huge thanks to all my friends for their support and warm welcoming whenever and wherever we are together.

Special thanks to all my family (and specially my nephews!) for their love and full support.

Last but not least, huge thanks to my wife Miana for her unconditional love and support. I shall never forget her courage in accepting to live far away from each other for almost two years, then in joining me in Lausanne, and all the sacrifices she has endured since we fist met. You make me proud, feel loved, blessed and lucky.

Francisco

Abstract

Reinforced concrete slabs without shear reinforcement under concentrated loads near linear supports are typical cases of bridge deck slabs, transfer slabs or pile caps. Such members are often designed or assessed in shear/punching shear with code provisions calibrated on the basis of tests on beams or one-way slabs loaded over the full width, as well as tests on isolated flat slab elements supported on columns in axis-symmetric conditions. However, these tests are not representative of the actual behavior of slabs under concentrated loads near linear supports, due to the non-parallel direction of shear forces and potential shear redistributions (associated with shear failures), and the non-axis-symmetric punching conditions (associated with punching shear failures).

In addition, the presence of prestressing ducts in the deck slab of balanced cantilever concrete bridges, or slab inserts in flat slabs of buildings approximately perpendicular to the shear flow, may influence the shear strength.

Moreover, concentrated loads of heavy vehicles have a repetitive nature, causing loss of stiffness and potential strength reductions due to fatigue phenomena. With respect to shear-fatigue behavior of reinforced concrete members without shear reinforcement, it has been observed to be potentially governing for structural members subjected to large live loads of repetitive nature (as traffic, wind or wave actions). Although extensive experimental programmes on beams have been performed in the past, and a rational approach to the problem can be performed on the basis of Fracture Mechanics (FM), most design codes still ground shear-fatigue design/assessment on empirical equations fitted on the basis of existing data.

In this thesis, two experimental campaigns are presented. The first one consists of twelve static tests on six full-scale cantilever slabs subjected to a concentrated load with a central line support, that allows tracing the linear reaction evolution. Parameters such as the location of the concentrated load, and the presence, material and injection of ducts were varied. All slabs failed in shear and significant redistributions of the linear reactions were observed prior to failure.

The second campaign has a similar test setup and consists of four static tests on two full-scale cantilever slabs (reference tests) and other eleven fatigue tests on eight identical slabs. The results show that cantilever slabs are significantly less sensitive to shear-fatigue failures than beams without shear reinforcement. The static reference tests presented shear failures. Some of the fatigue tested slabs failed due to rebar fractures. They presented significant remaining life after the first rebar failure occurred and eventually failed due to shear.

The shear failures exhibited by the static tests on cantilever slabs from this thesis and others from the literature can be reasonably predicted with the Critical Shear Crack Theory (CSCT), provided that the influence of direct load strutting and redistribution of internal forces is accounted

for, and that no contribution due to the inclination of tapered members to shear transferring is considered. The calculation of internal forces is proposed to be performed with Linear Elastic Finite Elements, using shell elements with shear deformation. The adoption of a zero Poisson's ratio and one eight of the concrete shear modulus is in good agreement with the measured line reactions at failure.

Simply supported slabs under concentrated loads near linear supports may exhibit shear or punching shear failures. Factors like the ratio between the dimension of the load parallel to the support and the slab width, or the type of loading (monolithic or not) seem to be crucial to determinate the failure mode. However, for very large slab widths with concentrated loads not acting close to the free edge, test results from the literature suggest that punching shear is the governing failure mode. In this thesis it is proposed to use the CSCT for both shear and non-axis-symmetric punching shear, combined with certain proposals on how to determine the internal forces and the shear and punching shear perimeter lengths, to assess tests from the literature. The proposed approaches are not fully capable of predicting the correct failure mode, but allow a safe design. A reasonable accuracy is obtained, either knowing or not *a priori* the correct failure mode.

A consistent design approach for shear-fatigue failures of reinforced concrete members without shear reinforcement is also presented, based on FM applied to *quasi*-brittle materials in combination with the CSCT. This leads to simple, yet sound and rational design equation incorporating the different influences of fatigue actions (minimum and maximum load levels) and shear strength (size and strain effects, material and geometrical properties). The accuracy of the design expression is checked against available test data in terms of Wöhler ($S - N$) and Goodman diagrams, showing consistent agreement to experimental evidence. In addition, the estimate of the number of cycles until failure is shown to be significantly more accurate and with lower scatter than current empirical shear-fatigue formulations of codes of practice.

Keywords: reinforced concrete; deck slab; flat slab; concentrated load; linear support; shear strength; punching shear strength; prestressing ducts; fatigue behavior; shear-fatigue; Critical Shear Crack Theory (CSCT).

Résumé

Les dalles en béton armé sans armature d'effort tranchant soumises à des charges concentrées au voisinage d'un appui linéaire sont des configurations typiques de dalles de roulement de ponts, dalles de transition ou semelles sur pieux. Ces éléments sont souvent dimensionnés ou vérifiés à l'effort tranchant et au poinçonnement avec des règles normatives. Celles-ci sont calibrées avec des essais sur poutres ou bandes de dalles chargées sur toute leur largeur ou bien des essais sur des éléments de dalles isolés appuyés sur une colonne en conditions axisymétriques. Ces essais ne sont pas représentatifs du comportement de dalles soumises à des charges concentrées à proximité d'un appui linéaire. Ce type de configuration soumet les dalles à des flux de cisaillement ni parfaitement parallèles ni parfaitement radiaux et permet une potentielle redistribution de l'effort tranchant avant la rupture. Elle donne aussi lieu à des configurations de poinçonnement non-axisymétrique.

En outre, la présence de gaines de précontrainte à l'intérieur des dalles de roulement de ponts construits par encorbellement ou de conduites à l'intérieur des plancher-dalles de bâtiments, approximativement perpendiculaires au flux de cisaillement, peut influencer la résistance à l'effort tranchant.

Enfin, les charges concentrées de poids lourds ont une nature répétitive qui peut engendrer des pertes de rigidité et de résistance liées à des phénomènes de fatigue. En ce qui concerne la fatigue à l'effort tranchant d'éléments en béton armé sans armature d'effort tranchant, elle est potentiellement déterminante pour des éléments structuraux soumis à des grandes charges utiles de nature répétitive (comme le trafic, le vent ou les ondes maritimes). Même si de nombreux programmes expérimentaux ont été réalisés dans le passé et qu'une approche rationnelle du problème peut être réalisée sur la base de la Mécanique de la Rupture (MR), la plupart des normes basent leurs règles de fatigue à l'effort tranchant sur des équations empiriques calibrées sur les essais existants dans la littérature.

Dans cette thèse, deux campagnes expérimentales sont présentées. La première contient douze essais statiques sur six dalles à pleine échelle soumises à une charge concentrée avec un appui linéaire au centre qui permet le suivi de la réaction linéaire. Des paramètres comme la position de la charge, la présence de gaines, leur matériau et l'injection de celles-ci ont été variés. Toutes les dalles ont subi des ruptures à l'effort tranchant et des redistributions importantes des réactions linéaires ont été observées avant la rupture.

Pour la deuxième campagne expérimentale avec un bâti de charge similaire, quatre essais statiques sur deux dalles à pleine échelle (essais de référence) sont réalisés ainsi qu'onze essais de fatigue sur huit dalles identiques. Les résultats montrent que les dalles en porte-à-faux soumises à des charges concentrées sont significativement moins sensibles aux phénomènes de fatigue à l'effort tranchant que les poutres sans étriers. Les essais statiques de référence ont présenté des

ruptures à l'effort tranchant. Certaines dalles testées en fatigue ont présenté des ruptures de barres d'armature, avec une importante vie résiduelle après la première rupture de barre. La rupture finale a été à l'effort tranchant.

Les ruptures à l'effort tranchant lors d'essais statiques sur dalles en porte-à-faux présentées dans cette thèse ainsi que d'autres de la littérature peuvent être raisonnablement prévues avec la Théorie de la Fissure Critique (CSCT, l'acronyme en anglais), si l'influence de l'appui direct et de la redistribution d'efforts sont prises en compte et qu'aucune contribution de l'effet Résal n'est considérée. Il est proposé de déterminer les efforts dans la dalle à l'aide d'éléments finis élastiques linéaires, en utilisant des éléments coques avec déformation de cisaillement. L'adoption d'un coefficient de Poisson nul et d'un huitième du module de cisaillement du béton est en bon accord avec les réactions linéaires mesurées lors des ruptures.

Les dalles simplement appuyées soumises à des charges concentrées au voisinage d'un appui linéaire peuvent avoir des ruptures d'effort tranchant ou de poinçonnement. Des facteurs comme le rapport entre la dimension de la charge parallèle au support et la largeur de la dalle, ou le type de chargement (monolithique ou pas) sont apparemment cruciaux afin de déterminer le bon mode de rupture. Cependant, pour des dalles très larges avec des charges concentrées agissant loin d'un bord libre, les essais de la littérature semblent indiquer que le poinçonnement est le mode de rupture déterminant. Dans cette thèse, afin de reproduire les résultats d'essais de la littérature, il est proposé d'utiliser la CSCT pour l'effort tranchant et le poinçonnement non-symétrique, combinée avec certaines propositions pour déterminer les efforts internes et les longueurs des périmètres de contrôle d'effort tranchant et de poinçonnement. Les approches proposées ne sont pas capables de prédire avec une certitude absolue le bon mode de rupture, mais permettent un dimensionnement sûr. Une fiabilité satisfaisante est obtenue, même si l'on connait ou pas le bon mode de rupture.

Une approche consistante pour la vérification des ruptures de fatigue à l'effort tranchant d'éléments en béton armé sans étriers est aussi présentée, basée sur la MR appliquée aux matériaux *quasi*-fragiles en combinaison avec la CSCT. Ceci mène à une équation de dimensionnement simple et rationnelle, qui incorpore les différentes paramètres influents des efforts de fatigue (niveaux maximaux et minimaux du chargement) et de la résistance à l'effort tranchant (effet taille, effet de la déformation, propriétés géométriques et du matériau). L'équation de dimensionnement est en bon accord avec les résultats d'essais existants dans la littérature. En outre, l'estimation du nombre de cycles jusqu'à la rupture est significativement plus précise et présente moins de dispersion que les formulations actuelles des normes.

Mots-clefs: béton armé; dalle de roulement; plancher-dalle; charge concentrée; appui linéaire; résistance à l'effort tranchant; résistance au poinçonnement; gaines de précontrainte; comportement à la fatigue; fatigue à l'effort tranchant; Théorie de la Fissure Critique (CSCT).

Zusammenfassung

Stahlbetonplatten ohne Schubbewährung unter konzentrierten Punktlasten in der Nähe von Linienauflagern kommen typischerweise in Brückendeckplatten, punktgelagerten Platten belastet mit tragenden Wänden oder Pfahlköpfen vor. Die Bemessung des Querkraft-/ Durchstanzwiderstands solcher Bauteile erfolgt mit Normvorgaben welche auf der Basis von Testergebnissen einachsiger Platten, belastet über die gesamte Breite, sowie isolierter Platten, gelagert auf Stützen, unter axialsymmetrischen Randbedingungen kalibriert wurden. Solche Versuche spiegeln allerdings nicht das tatsächliche Verhalten von Platten unter konzentrierten Punktlasten nahe linienförmiger Auflager wider. Unter dieser Art der Belastung sind die Richtungen des Schubflusses weder parallel noch radial (strahlenförmig) und eine mögliche Umverteilung der Schubkräfte kann dem Schubbruch vorausgehen. Ferner kann ein nichtsymmetrisches Durchstanzversagen auftreten. Desweitern können die in Deckenplatten von Kragarmbrücken vorhandenen Vorspannrohre, sowie Einlegeteile in Geschossplatten von Gebäuden welche ungefähr orthogonal zum Schubfluss verlaufen, die Schubfestigkeit beeinflussen.

Hinzu kommt, dass konzentrierte Lasten von schweren Fahrzeugen zyklischer Natur sind, was in einem Verlust von Steifigkeit und Querkraftwiderstand aufgrund von Ermüdungserscheinungen resultieren kann. Das Schubermüdungsverhalten von Stahlbetonteilen ohne Schubbewährung kann massgebend sein für Bauteile die grossen repetitiven Lebendlasten (Verkehr, Wind, Wellen) ausgesetzt sind. Obwohl in der Vergangenheit umfangreiche Versuchsreihen durchgeführt wurden und das Problem mit einer rationalen Herangehensweise, basierend auf der Bruchmechanik, behandelt werden kann, gründen die meisten Bemessungsnormen die Schubermüdungsbemessung und -Bewertung noch immer auf empirischen Gleichungen welche auf existierende Versuchsdaten angepasst sind.

In der vorliegenden Arbeit werden zwei Versuchsreihen vorgestellt. Die erste umfasst zwölf statische Tests an sechs Kragarmplatten üblicher Grösse auf einem zentralen Linienauflager, belastet mit einer Punktlast. Diese Konfiguration erlaubt es die Entwicklung der linearen Auflagerreaktion nachzuvollziehen. Parameter, wie die Position der Punktlast, sowie das Vorhandensein, das Material und die Position von (Vorspannungs-) Schächten wurden variiert. Alle Platten zeigten Schubversagen und signifikante Umlagerungen der Linienauflagerreaktionen vor Versagen.

Die zweite Reihe von Versuchen hat einen ähnlichen Aufbau und setzt sich aus vier statischen Tests an zwei Kragarmplatten üblicher Grösse, sowie elf weiteren Ermüdungsversuchen an acht identischen Platten zusammen. Die Resultate zeigen, dass Platten die als Kragarm wirken signifikant weniger anfällig sind durch Schubermüdung zu versagen als Balken ohne Schubbewährung. Die statisch durchgeführten Referenztests wiesen ein Schubversagen auf. In einigen der auf Ermüdung getesteten Platten stellte sich zuerst ein Bruch der Bewährung ein. Im weiteren Verlauf der Versuche konnte, trotz bereits bestehender Bewährungsbrüche, eine beträchtliche

Restlebensdauer der Versuchskörper festgestellt werden. Alle Platten versagten schlussendlich auf Schub.

Schubversagen, die in den statisch durchgeführten Versuchen auf Kragarmplatten, jene dieser Arbeit und der Literatur, auftraten, können einigermassen gut mit der Critical Shear Crack Theory (CSCT - *Kritischer-Schubriss-Theorie*) vorhergesagt werden. Dies gilt unter der Voraussetzung, dass der Einfluss von direkten Lastabtragungen und die Umverteilung innerer Kräfte berücksichtigt werden und der Beitrag von geneigten Druckgurten am Schubtransfer vernachlässigt wird. Es wird vorgeschlagen, die Berechnung der inneren Kräfte mittels linear-elastischen finiten Elementen unter der Anwendung von Schalenelementen mit Schubdeformation durchzuführen. Setzt man die Querdehnzahl zu null und wendet man ein Achtel des Bentonschubmoduls an, führt das zu guter Übereinstimmung mit den gemessenen Linienauflagerreaktionen bei Versagen.

Einfach gelagerte Platten unter Punktlasten nahe Linienauflagern weisen Schub- oder Durchstanzversagen auf. Faktoren wie das Verhältnis zwischen der Grösse der Last parallel zum Auflager und der Plattenbreite, sowie die Belastungsart (monolithisch oder nicht), scheinen bestimmend für den Versagensmodus zu sein. Bei Platten grosser Breite, mit Punktlasten fern des freien Randes, findet sich in der Literatur jedoch meistens Durchstanzen als massgebende Versagensart. Deshalb wird in der vorliegenden Arbeit vorgeschlagen die CSCT für beide Versagensmodi; Schub und nichtsymmetrisches Durchstanzen, in Kombination mit einigen Vorschriften zur Bestimmung der inneren Kräfte sowie der Schub- und Durchstanzumkreise anzuwenden, um Versuchsergebnisse aus der Literatur zu bewerten. Die vorgeschlagenen Vorgehensweisen sind nicht durchgängig in der Lage die richtige Versagensart vorauszusagen, erlauben aber eine sichere Bemessung. Des Weiteren kann eine ausreichende Genauigkeit erzielt werden, ob nun der Versagensmodus *a priori* bekannt ist oder nicht.

Ein einheitlicher Bemessungsansatz für Schubermüdungsversagen von Stahlbetonteilen ohne Schubbewährung, basierend auf Bruchmechanik in Anwendung auf quasi-spröde Materialien, in Kombination mit der CSCT, wird ebenfalls vorgestellt. Dies führt zu einfachen und doch sicheren sowie rationalen Bemessungsgleichungen unter Berücksichtigung verschiedener Einflüsse von Ermüdung (Minimal- und Maximallastniveaus) und Schubfestigkeit (Grössen- und Verformungseffekte, Material- und geometrische Eigenschaften). Die Genauigkeit der Bemessungsausdrücke wird mit zugänglichen Testdaten validiert. Die Wöhler- ($S-N$) und Goodmandiagramme zeigen eine konsistente Übereinstimmung mit den Versuchen. Hinzu kommt, dass die Anzahl der Lastzyklen bei Versagensauftritt signifikant genauer und mit geringerer Streuung abgeschätzt werden kann, als mit den derzeitigen empirischen Schubermüdungsgleichungen in den Bemessungsnormen für die Praxis.

Schlüsselwörter: Stahlbeton; Deckplatte; Platte; Punktlast; konzetrierte Last; Linienauflager; Schubfestigkeit; Durchstanzschubfestigkeit; Vorspannrohre; Ermüdungsverhalten; Schubermüdung; Critical Shear Crack Theory (CSCT).

Riassunto

Piastre in calcestruzzo armato senza armatura a taglio soggette a carichi concentrati vicino ad appoggi lineari sono soluzioni strutturali tipiche di impalcati da ponte, piastre di ripartizione e plinti di fondazione su pali. Questi elementi sono spesso progettati o verificati per le azioni di taglio e punzonamento in accordo con prescrizioni normative calibrate su risultati sperimentali su travi o piastre monodirezionali, o su solai semplicemente appoggiati su colonne in condizioni di assialsimmetria. Tuttavia questi test non sono rappresentativi del comportamento di piastre soggette a carichi concentrati vicino ad appoggi lineari. Tale configurazione determina lo sviluppo di campi di taglio né perfettamente paralleli né radiali e potenziali ridistribuzioni delle azioni di taglio prima della rottura. Essa può anche dar luogo a punzonamento non simmetrico.

Inoltre, la presenza di guaine di precompressione nelle mensole degli impalcati da ponte in calcestruzzo armato o di solette di ripartizione approssimativamente perpendicolari al campo di taglio può influenzare la resistenza a taglio.

Per di più, i carichi concentrati dovuti a mezzi pesanti hanno una natura ripetiva e ciclica, che può determinare perdite di rigidezza e di resistenza dovute a fenomeni di fatica. Per tale motivo, i carichi accidentali di natura ciclica (come traffico, vento, onde marine) sono stati indentificati come potenzialmente significativi sulla resistenza a fatica a taglio di elementi in calcestruzzo armato senza armatura a taglio. Nonostante numerose campagne sperimentali siano state eseguite in passato, e il problema possa essere studiato applicando la meccanica della frattura, le prescrizioni di fatica a taglio della maggior parte delle norme sono basate su equazioni empiriche calibrate su test esistenti in letteratura.

In questa tesi sono presentate due campagne sperimentali. La prima consiste in dodici test statici su sei piastre a mensola a grandezza naturale soggette a carico concentrato appoggiate simmetricamente su un supporto lineare che permette di seguire l'andamento delle reazioni. Parametri come la posizione del carico, la presenza di guaine, il loro materiale e l'iniezione delle guaine sono state variate nei differenti test. Tutte le piastre hanno raggiunto una rottura a taglio e significative ridistribuzioni delle reazioni lineari sono state osservate prima della rottura.

La seconda campagna sperimentale ha un test setup simile, e consiste in quattro test statici su due piastre a grandezza naturale (test di riferimento) e undici test a fatica su otto piastre identiche. I risultati mostrano che le piastre a mensola soggette a carichi concentrati sono significativamente meno sensibili ai fenomeni di fatica a taglio rispetto a travi senza armatura trasversale. I test statici di riferimento hanno mostrato una rottura a taglio. Alcune piastre testate a fatica hanno evidenziato rottura di barre longitudinali con un'importante vita residua dopo la rottura della prima barra; la rottura finale si è verificata per taglio.

Le rotture a taglio nei test statici su piastre a mensola presentati in questa tesi e in letteratura possono essere stimati con la teoria della fessura critica (acronimo inglese CSCT) se sono presi in considerazione l'influenza dell'appoggio diretto e la ridistribuzione degli sforzi interni, e se è trascurato il contributo resistente dovuto all'inclinazione di elementi a sezione rastremata. Viene proposto di calcolare gli sforzi interni mediante una modellazione ad elementi finiti elastico lineari utilizzando elementi shell con deformazione a taglio. L'utilizzo di un coefficiente di Poisson nullo e di un modulo di elasticità tangenziale del calcestruzzo armato pari a un ottavo del modulo elastico iniziale ha mostrato una buona corrispondenza con le misure sperimentali delle reazioni a rottura.

Piastre semplicemente appoggiate soggette a carichi concentrati vicino ad appoggi lineari possono evidenziare rottura a taglio o a punzonamento. Parametri quali il rapporto tra la dimensione del carico parallelo all'appoggio e la larghezza della piastra o la natura del carico (monolitico o meno) sembrano essere cruciali nella determinazione del tipo di rottura. Tuttavia, per piastre di grande larghezza soggette a carichi concentrati agenti lontano dagli appoggi, i risultati dei test presenti in letteratura suggeriscono che il punzonamento sia il tipo di rottura predominante. In questa tesi, al fine di riprodurre i risultati delle campagne sperimentali presenti in letteratura, si propone di utilizzare la teoria della fessura critica sia per il taglio che per il punzonamento non simmetrico combinato ad alcuni approcci proposti per determinare gli sforzi interni e la lunghezza del perimetro di controllo. Gli approcci proposti non sono del tutto in grado di predirre accuratamente il tipo di rottura, ma permettono un dimensionamento a favore di sicurezza. Una soddisfacente accuratezza è ottenuta anche non conoscendo *a priori* il meccanismo di rottura.

E' inoltre proposto un criterio di dimensionamento per elementi in calcestruzzo armato senza armatura trasversale soggetti a fatica a taglio basato sulla meccanica della frattura applicata a materiali quasi-fragili combinata con la teoria della fessura critica. Questo approccio, ha prodotto una semplice ma efficace equazione per il dimensionamento, che tiene in conto sia dell'influenza delle azioni di fatica (massimo e minimo livello di carico) sia della resistenza a taglio (effetto scala e di deformazione, proprietà di materiale e geometriche). L'accuratezza delle equazioni di design è verificata utilizzando i dati dei test disponibili in letteratura attraverso i diagrammi di Wöhler ($S-N$) e Goodman, evidenziando una buona corrispondenza con i risultati sperimentali. Inoltre, la stima del numero di cicli a rottura risulta più accurata e con una dispersione minore rispetto alle formulazioni empiriche correnti utilizzate nelle norme.

Parole-chiave: calcestruzzo armato; impalcati da ponte; piaste; carico concentrato; appoggi lineari; resistenza a taglio; resistenza a punzonamento; precompressione; comportamento a fatica; fatica a taglio; teoria della fessura critica (CSCT).

Resumen

Las losas de tableros de puentes, losas de transición o encepados sin armadura transversal son elementos estructurales cuya situación de proyecto determinante corresponde a la aplicación de cargas concentradas próximas a apoyos lineales. Generalmente, el dimensionamiento o la verificación de estos elementos frente a esfuerzos de cortante y punzonamiento se efectúa mediante fórmulas de diseño calibradas experimentalmente a partir de ensayos. Dichos ensayos suelen corresponder a elementos unidireccionales cargados a lo largo de todo su ancho, así como ensayos simétricos en losas aisladas sometidas a cargas concentradas. Sin embargo, estos ensayos no son representativos del comportamiento real de este tipo de losas sometidas a cargas concentradas próximas a apoyos lineales debido a la dirección no paralela de la dirección principal de las tensiones tangenciales, a la redistribución potencial de esfuerzos cortantes (roturas por cortante) y a las condiciones no simétricas de los esfuerzos de punzonamiento (roturas de punzonamiento).

Además, la presencia de vainas de pretensado en las losas superiores de tableros de puentes o en losas de edificación de reducido espesor pueden condicionar la resistencia a cortante de estos elementos.

Por otra parte, las cargas concentradas asociadas al tráfico de vehículos pesados tienen una naturaleza repetitiva que conlleva la pérdida de rigidez y la reducción de la resistencia de estos elementos como consecuencia de la fatiga. El comportamiento a fatiga por cortante de elementos de hormigón armado sin armadura transversal está gobernado por las cargas repetidas originadas por el tráfico, el viento o el oleaje. A pesar del elevado número de trabajos experimentales existentes en vigas, y de que una aproximación racional al problema pueda obtenerse a partir de la Mecánica de la Fractura, la mayor parte de las normativas existentes todavía proponen criterios de dimensionamiento y comprobación basados en expresiones empíricas obtenidas a partir de ajustes de datos experimentales.

En esta Tesis se presentan dos campañas experimentales. La primera de ellas consta de doce ensayos estáticos llevados a cabo en seis losas de hormigón armado sin armadura transversal a escala real sometidas a dos cargas concentradas simétricas con un apoyo central lineal del que se ha determinado la evolución de la reacción lineal. La posición de la carga concentrada y la presencia de vainas de pretensado han sido estudiados como principales parámetros. Todas las losas ensayadas presentaron roturas por cortante con una significativa redistribución de la reacción lineal medida en el apoyo central antes de producirse la rotura.

La segunda campaña de ensayos presenta una configuración similar a la anterior, estando compuesta de cuatro ensayos estáticos realizados en dos losas de hormigón armado sin armadura transversal a escala real (ensayos de referencia) y once ensayos de fatiga en ocho losas de similares características. Los resultados obtenidos indican que este tipo de elementos son menos sensibles al fallo por fatiga a cortante que las vigas sin armadura transversal. Los ensayos

estáticos de referencia presentaron roturas por cortante. Varias de las losas ensayadas a fatiga colapsaron debido a la rotura por fatiga de barras de la armadura longitudinal en tracción. Estos elementos presentaron una importante resistencia adicional tras producirse la rotura por fatiga de la primera barra de la armadura longitudinal desarrollando finalmente un fallo por cortante.

Las roturas por cortante observadas en los ensayos estáticos en losas de hormigón armado sin armadura transversal llevados a cabo en esta Tesis, así como en otros trabajos existentes en la literatura, pueden ser estimadas con suficiente precisión mediante la teoría de la fisura crítica del cortante (CSCT, acrónimo en inglés) siempre que se tenga en cuenta la influencia de la esbeltez de cortante en la transmisión de parte de la carga aplicada directamente al apoyo, la redistribución de esfuerzos y que no se considere el efecto del canto variable en la transmisión del esfuerzo cortante. La determinación de los esfuerzos se ha llevado a cabo mediante un modelo de elementos finitos elástico y lineal en el que se han empleado elementos de tipo lámina y se ha tenido en cuenta la deformación por cortante. En este modelo el coeficiente de Poisson se ha considerado nulo y el módulo de elasticidad transversal se ha tomado igual a un octavo del valor del módulo de elasticidad transversal del hormigón de acuerdo con las medidas registradas en el apoyo lineal en el instante de rotura.

Las losas de hormigón armado simplemente apoyadas y sometidas a cargas concentradas próximas a apoyos lineales presentan roturas por cortante o punzonamiento. Parámetros como la relación entre la dimensión de la carga paralela al apoyo y el ancho de la losa o el tipo de carga aplicada (monolítica o no) son determinantes para definir el modo de rotura de estos elementos. Sin embargo, en losas de gran anchura sometidas a cargas concentradas próximas a apoyos lineales, los resultados experimentales observados en los trabajos existentes indican que el tipo de fallo por punzonamiento es el mecanismo de rotura que gobierna este tipo de elementos. En la presente Tesis, con el objetivo de reproducir los resultados experimentales existentes, se ha propuesto el uso de la CSCT para ambos modos de rotura empleando criterios adicionales para determinar la distribución de esfuerzos en la losa y las longitudes efectivas que condicionan las roturas de cortante y punzonamiento. A pesar de que la metodología propuesta no es capaz de predecir el modo de rotura en todos los casos analizados, aporta un criterio seguro de diseño. Independientemente de que se conozca o no el modo rotura, se obtiene además una precisión correcta de la resistencia a través de la metodología propuesta.

Una metodología para la evaluación de la resistencia a fatiga por cortante de elementos de hormigón armado sin armadura transversal se presenta en esta Tesis basada en conceptos de Mecánica de la Fractura aplicada a materiales cuasi-frágiles en combinación con la CSCT. A partir de esta metodología se ha propuesto una expresión de dimensionamiento simple y racional en la que intervienen las principales variables asociadas a las acciones de fatiga (niveles de carga máxima y mínima) y a la resistencia a cortante (efecto tamaño, influencia de la deformación de la armadura longitudinal, propiedades geométricas y de los materiales empleados). La precisión de la expresión de diseño propuesta ha sido contrastada mediante curvas de Wöhler ($S - N$) y diagramas de Goodman. Los resultados que se obtienen haciendo uso de la expresión propuesta en esta Tesis para la estimación del número de ciclos resistentes hasta producirse la rotura por fatiga a cortante presentan mayor precisión y menor dispersión que los obtenidos empleando las expresiones empíricas existentes en los principales códigos de diseño actuales.

Palabras Clave: hormigón armado; losas de tableros de puentes; losas planas; cargas concentradas; apoyos lineales; resistencia a cortante; resistencia a punzonamiento; vainas de pretensado; comportamiento a fatiga; fatiga por cortante; teoría de la fisura critica de cortante (CSCT).

Sumário

As lajes em betão armado sem estribos solicitadas por cargas concentradas na vizinhança de um apoio linear são casos típicos de lajes de tabuleiros de pontes, lajes de transição ou maciços de encabeçamento de estacas. Estas estruturas são habitualmente dimensionadas ao esforço transverso e punçoamento com regras normativas que foram calibradas através de ensaios de vigas sem estribos, bandas de lajes solicitadas em toda a sua largura, ou ainda lajes isoladas apoiadas sobre uma coluna, em condições axissimétricas. No entanto, estes ensaios não são representativos do comportamento de lajes solicitadas por cargas concentradas na vizinhança de um apoio linear. Esta configuração de carregamento cria nas lajes um fluxo de esforço transverso que não é nem perfeitamente paralelo, nem perfeitamente radial, e que permite redistribuições de esforço transverso antes da rotura. No que diz respeito ao punçoamento, esta configuração está associada a condições não-axissimétricas.

No caso específico de pontes construídas por avanços sucessivos, a presença de bainhas para cabos longitudinais de pré-esforço no interior da laje de tabuleiro pode também influenciar a resistência ao esforço transverso, assim como as condutas no interior de lajes fungiformes de edifícios.

Por outro lado, as cargas concentradas que solicitam as lajes de tabuleiros de pontes (provenientes da acção do tráfego de pesados) são de natureza repetitiva, actuando um determinado número de vezes durante a vida útil da obra e podendo deste modo originar problemas de fadiga. No que diz respeito à rotura ao esforço transverso por fadiga de elementos em betão armado sem estribos, ela pode ser potencialmente determinante em elementos estruturais solicitados por elevadas sobrecargas de natureza repetitiva (como o tráfego, o vento ou as ondas marítimas). Muito embora várias campanhas experimentais tenham sido levadas a cabo no passado, e que uma abordagem do problema possa ser efectuada com base na Mecânica da Fractura (MF), a maior parte dos códigos de dimensionamento possui regras de dimensionamento empíricas, calibradas com base nos ensaios existentes na literatura.

Nesta tese são apresentadas duas campanhas experimentais. A primeira é composta por 12 ensaios estáticos de grande escala de 6 lajes em consola, solicitadas por uma carga concentrada na proximidade de um apoio linear, apoio este que permite registar a evolução da reacção linear. Redistribuições importantes das reacções lineares de apoio foram observadas antes da rotura. A influência de parâmetros como a posição da carga concentrada e a presença de bainhas de pré-esforço no interior das lajes foi investigada.

A segunda campanha experimental é semelhante, e contém 4 ensaios estáticos de grande escala de duas lajes (ensaios de referência) e 11 ensaios de fadiga de 8 outras lajes idênticas. Os resultados experimentais mostram que as lajes são menos susceptíveis a uma rotura de esforço transverso por fadiga do que as vigas sem estribos. Algumas das lajes testadas apresentaram roturas de

barras de armadura, exibindo uma vida residual bastante significativa após a rotura da primeira barra. As roturas finais foram ao esforço transverso.

As roturas ao esforço transverso de lajes em consola podem ser satisfatoriamente estudadas com a Teoria da Fissura Crítica de Esforço Transverso (CSCT, no acrónimo inglês), desde que a influência do apoio directo e da redistribuição de esforços seja tomada em conta, e que nenhuma contribuição para a transferência de esforço transverso devida à inclinação da corda comprimida em flexão seja considerada. Para a determinação dos esforços nas lajes são propostas análises com elementos finitos elásticos lineares, utilizando elementos casca com deformação por corte. A adopção de um coeficiente de Poisson nulo e de um oitavo do módulo de distorção do betão origina uma boa correspondência entre os modelos e as reacções lineares medidas aquando das roturas.

As lajes simplesmente apoiadas e solicitadas por cargas concentradas na vizinhança de um apoio linear podem apresentar roturas de esforço transverso ou de punçoamento. Factores como o rácio entre a dimensão da carga paralela ao apoio e a largura da laje, ou o tipo de carregamento (monolítico ou não) são aparentemente cruciais para determinar o modo de rotura correcto. No entanto, para lajes muito largas solicitadas por cargas concentradas suficientemente afastadas de um bordo livre, os ensaios existentes na literatura sugerem que o punçoamento é o modo de rotura determinante. Nesta tese é proposta a utilização da CSCT para eforço transverso e punçoamento não-simétrico para análise dos fenómenos. Estas teorias são combinadas com determinadas propostas de como determinar os esforços actuantes e os comprimentos dos perímetros de controlo de punçoamento e de esforço transverso a adoptar, de modo a reproduzir os resultados de ensaios experimentais da literatura. As metodologias propostas não são capazes de prever com certeza absoluta o modo de rotura correcto, mas permitem um dimensionamento seguro. Uma fiabilidade satisfatória é obtida, conhecendo ou não à partida qual o modo de rotura.

Uma metodologia consistente e racional para a verificação de roturas ao eforço transverso em fadiga de elementos em betão armado sem estribos é também apresentada, baseada na MF dos materiais *quasi*-frágeis combinada com a CSCT. Esta metodologia origina uma fórmula de dimensionamento simples e ao mesmo tempo racional, que incorpora as diferentes influências das solicitações de fadiga (níveis máximos e mínimos do carregamento) e da resistência ao eforço transverso (efeito escala, efeito da deformação, propriedades geométricas e materiais). A precisão da expressão de dimensionamento é controlada através de diagramas de Wöhler ($S - N$) e de Goodman de ensaios existentes na literatura, obtendo-se uma boa correspondência entre os ensaios e o modelo. Adicionalmente, a estimativa do número de ciclos até à rotura é significativamente mais precisa e com menos dispersão do que as formulações das normas actuais.

Palavras-chave: betão armado; laje de tabuleiro; laje fungiforme; carga concentrada; apoio linear; resistência ao esforço transverso; resistência ao punçoamento; bainhas de pré-esforço; comportamento em fadiga; resistência ao esforço transverso em fadiga; Teoria da Fissura Crítica de Esforço Transverso (CSCT).

Contents

Notation

A variable not present in this list is defined in the manuscript. The following notation is used in this thesis:

Latin characters

lower case

a	crack length
a	shear span (distance between the center of the loading plate and the center of the support)
a'	effective crack length
a^*	reference crack length
a_0	initial crack length
a_c	critical crack length
a_{ef}	effective shear span
a_f	crack length leading to failure
a_l	ligament length
$a_l{}^*$	transitional ligament length
a_N	crack length after N cycles
a_P	shear span
a_v	free shear span (distance between the edge of the loading plate and the edge of the support)
b	beam or strip width
b_0	control perimeter
$b_{0,el}$	elastic control perimeter
b_s	support strip width
b_x	control perimeter in x direction
b_w	effective shear width
b_w	beam width
b_y	control perimeter in y direction

c	compression zone depth
c	loading plate dimension
c	concrete cover
c_N	factor independent of size characterizing the structure shape and type of loading
c_1	depth of flexural crack tip
c_x	loading plate x-dimension
c_y	loading plate y-dimension
d	effective flexural depth
d	characteristic dimension
d	plate width
d_0	insertion dimension
d_0	transitional characteristic dimension
d_a	maximum aggregate size
d_g	maximum aggregate size
d_s	effective flexural depth
$d_{\max}$	maximum effective flexural depth
d_v	effective shear depth
d_{xb}	effective flexural depth of bottom reinforcement in x direction
d_{xt}	effective flexural depth of top reinforcement in x direction
d_{yb}	effective flexural depth of bottom reinforcement in y direction
d_{yt}	effective flexural depth of top reinforcement in y direction
f_c	compressive strength of concrete measured in cylinders
$f_{c,cube}$	compressive strength of concrete measured in cubes
$f_{c,N}$	compressive strength of concrete after N cycles
$f_{c,Ref}$	compressive strength of concrete measured in cylinders of the static test
f_{cm}	compressive strength of injection mortar
f_q	linear load
f_s	yielding strength of reinforcement steel
f_t	tensile strength
f_t'	tensile strength
f_u	ultimate strength of reinforcement steel
f_y	reinforcement steel stress
f_y	yielding strength of reinforcement steel
g_f	local fracture energy
h	height
k_d	SIA262:2013 parameter related to strain and size effect

k_{dg}	*fib*-Model Code 2010 parameter related to maximum aggregate size
k_g	SIA262:2013 parameter related to maximum aggregate size
k_v	*fib*-Model Code 2010 shear parameter
k_ψ	*fib*-Model Code 2010 punching shear parameter
l	length
l	span
l_{ch}	characteristic length
m	Paris-Erdogan's law parameter for shear-fatigue model
m	unitary bending moment
$m_{\max}$	maximum unitary bending moment
m_r	radial moment
m_R	yielding bending moment
m_s	applied bending moment
m_{xx}	unitary bending moment in x direction
m_{xy}	torsional moment
m_{yy}	unitary bending moment in y direction
n	Paris-Erdogan's law parameter
n	number of cycles for Palmgren-Miner's rule
r	radius
r_0	punching cone maximum radius
r_l	first-order plastic zone radius
r_p	second-order plastic zone radius
r_q	load radius
r_s	distance from the center of the load or column to the point of zero radial moment
t	time
q_l	linear load at cantilever tip
u	displacement
u_y	displacement in y direction
v	unitary shear force
v_0	intensity of resultant unitary shear force
$v_{avd,4d}$	averaged perpendicular shear force over a distance $4d$
$v_{avd,4d+c_y}$	averaged perpendicular shear force over a distance $4d + c_y$
$v_{el,perp}$	elastic unitary shear force perpendicular to control perimeter
$v_{el,perp,\max}$	maximum elastic unitary shear force perpendicular to control perimeter
$v_{el,tot}$	total elastic unitary shear force
v_{perp}	unitary shear force perpendicular to control perimeter

$v_{perp,\max}$	maximum unitary shear force perpendicular to control perimeter
$v_{\max}$	maximum unitary shear force
v_R	unitary shear strength
$v_{R,x}$	unitary shear strength in x direction
$v_{R,y}$	unitary shear strength in y direction
v_{tot}	total unitary shear force
v_x	unitary shear force in x direction
v_y	unitary shear force in y direction
x	x-axis or coordinate
x_0	x coordinate of initiation section
$x_{control}$	control section x coordinate
x_N	required depth of compression zone
x_{rot}	depth of compression zone at failure
w	crack width
w_c	thickness of fracture zone
w_{cr}	crack width
$w_{cr,\max}$	maximum crack width
$w_{cr,\min}$	minimum crack width
w_l	limit crack width for stress transfer
y	y-axis or coordinate
z	inner flexural arm

upper case

A	crack area
A_s	reinforcement area
B	thickness
B	Bažant's size effect law parameter
C	compliance
C	compressive force
C	Paris-Erdogan's law parameter
C_N	unloading compliance in cycle N
$\overline{C}$	Paris-Erdogan's law parameter
$CMOD$	crack mouth opening displacement
$CTOD$	crack tip opening displacement
$CTOD_c$	elastic critical crack tip opening displacement
D	discontinuity depth

$D_{\max}$	maximum aggregate size
E	Young's modulus
E_c	Young's modulus of concrete
E_s	Young's modulus of steel
E_s	strain softening modulus
F	applied load
F_c	compressive force
F_{calc}	calculated load
F_{flex}	bending strength
$F_{\max}$	maximum applied load
F_s	steel force
F_u	ultimate load
G	shear modulus
G	energy release rate (crack-extension force)
G_c	measured energy release rate
G_f	global fracture energy
G_F	fracture energy
H	characteristic dimension
K	kinetic energy
K	stress intensity factor
K_c	measured fracture toughness
K_F	fracture toughness
K_I	stress intensity factor in mode I
K_I^S	stress intensity factor in mode I calculated at the tip of the effective crack
$K_{I,Mom}^S$	stress intensity factor in mode I calculated at the crack tip due to bending moment
$K_{I,Steel}^S$	stress intensity factor in mode I calculated at the crack tip due to closure effect of reinforcement
K_{Ic}	fracture toughness in mode I
K_{Ic}^S	critical stress intensity factor in mode I calculated at the tip of the effective crack
K_{If}	fracture toughness of concrete in mode I
K_T	stress concentration factor
L	length
L_0	vertical crack length
LL	load level
M	bending moment

M_E	acting bending moment
M_{Ed0}	design acting bending moment
N	cycle
N	fatigue life
N	normal force
N_{diag}	number of cycles to diagonal cracking
N_R	number of cycles to failure
N_{rot}	number of cycles at failure
P	applied load
P_u	ultimate load
$P_{u,d}$	ultimate load associated to distributed load
$P_{u,p}$	ultimate load associated to point load
R	ratio between minimum and maximum stress levels
R_l	linear reaction force
R_{tests}	ratio between minimum and maximum stress levels of experimental tests
R_{tot}	total measured reaction
S	stress level
T	period
T	tensile force
Q	applied load
Q_u	ultimate load
U_{total}	total energy
U_E	elastic energy
U_P	plastic energy
V	shear force
V_c	concrete contribution to shear strength
$V_{c,1}$	monotonic shear strength
$V_{c,N}$	shear strength after N cycles
V_{cu}	static shear strength
V_{calc}	calculated shear strength
V_{CC}	shear force transferred by the compression chord
V_{CSC}	shear force transferred through the critical shear crack
V_{CSCT}	shear strength calculated according to the CSCT
V_{DA}	shear force transferred by dowel action
V_{Ecd}	design acting shear force transferred due to the inclination of the compression chord
V_E	acting shear force

$V_{E,\max}$	maximum acting shear force
$V_{E,\min}$	minimum acting shear force
V_{Ed}	design acting shear force not transferred due to the inclination of the compression chord
V_{Ed0}	design acting shear force
V_f	punching shear force
V_{flex}	shear force corresponding to bending strength
$V_{\max}$	maximum shear force
$V_{\max}^{tot}$	maximum total applied shear force
$V_{\min}$	minimum shear force
V_{pl}	plastic shear strength
V_R	shear strength
V_{Ref}	reference static shear strength
$V_{R,x}$	shear strength in x direction
$V_{R,y}$	shear strength in y direction
$V_{R,c}$	concrete contribution to shear strength
V_{static}	static shear strength
V_{test}	experimental shear strength
V_{tot}	total applied shear force
W	energy
W	work
W	plate width
Y	geometry factor

Greek characters

lower case

α	compression chord inclination
α	notch depth ratio
β	brittleness number
β	shear force reduction factor due to arching action
β_L	reduction factor of shear strength calculated over the full width
γ	diagonal crack angle
γ	energy required to form unit new material surface
δ	displacement
δ	distance
ε	strain

ε_0	strain corresponding to zero tensile stress after post-peak behavior
ε_c	concrete compressive strain
ε_{ct}	strain corresponding to peak tensile stress
$\varepsilon_{\max}$	maximum strain
$\varepsilon_{\min}$	minimum strain
ε_p	strain corresponding to peak tensile stress
ε_v	SIA262:2013 reference strain for shear
ε_x	*fib*-Model Code 2010 reference strain for shear
η	shear strength increasing factor due to loading rate
θ	angle in polar coordinates
θ_{limit}	angle to limit control perimeter in a given direction
κ	proportionality factor
λ	Bažant's size effect law parameter
λ_0	Bažant's size effect law parameter
ν	Poisson's ratio
ρ	root radius
ρ	reinforcement ratio
ρ_l	longitudinal reinforcement ratio
ρ_{xb}	reinforcement ratio of bottom reinforcement in x direction
ρ_{xt}	reinforcement ratio of top reinforcement in x direction
ρ_{yb}	reinforcement ratio of bottom reinforcement in y direction
ρ_{yt}	reinforcement ratio of top reinforcement in y direction
σ	stress
σ_c	concrete compressive stress
σ_c	critical stress
σ_I	principal stress I
σ_{II}	principal stress II
$\sigma_{\max}$	maximum stress
σ_N	nominal stress
σ_{ys}	yielding stress in y direction
σ_{yy}	stress in y direction
τ	shear stress
τ_c	shear strength stress of concrete
$\tau_{\max}$	maximum shear stress
ϕ	reinforcement diameter
ϕ_0	angle of resultant unitary shear force
ϕ_{duct}	diameter of duct

ϕ_{rebar}	reinforcement diameter
ψ	slab rotation
ψ_f	slab rotation at failure
$\psi_{\max}$	rotation on the direction of maximum rotation
$\psi_{\min}$	rotation on the direction of minimum rotation
ψ_x	slab rotation in x direction
ψ_y	slab rotation in y direction

upper case

Γ	energy spent in increasing crack area
Π	potential energy

Acronyms

CSCT	Critical Shear Crack Theory
FE	Finite Elements
FM	Fracture Mechanics
FPZ	Fracture Process Zone
LEFE	Linear Elastic Finite Elements
LEFM	Linear Elastic Fracture Mechanics
NLFE	Nonlinear Finite Elements
NLFM	Nonlinear Fracture Mechanics
SOM	Strength of Materials

Chapter 1

Introduction

1.1 Problem statement

The static design of reinforced concrete bridge deck slabs without shear reinforcement is generally governed by the action of concentrated loads of heavy vehicles, which may cause shear, punching shear or flexural failures. The concentrated loads resulting from heavy vehicles have a repetitive nature and may cause potential stiffness and strength reductions due to fatigue effects.

Investigations on the static and shear-fatigue behavior of reinforced concrete members without shear reinforcement have mainly focused in the past on tests on beams or one-way slabs loaded over their full width (static and fatigue cases) and two-way axis-symmetric flat slab elements supported on columns (static cases). However, it should be noted that the results from these tests are not directly applicable to slabs under concentrated loads near linear supports, due to the principal direction of the shear force (not perfectly parallel or radial) and the acting shear force and bending moment at the shear critical region, which may potentially vary as the level of load increases, due to redistributions on shear and moment fields after cracking and/or yielding of the flexural reinforcement.

The rational and sound models for shear and punching shear existing nowadays might need to be adapted to study slabs under concentrated loads near linear supports in a simple and practical manner.

With respect to shear-fatigue assessment, rational approaches also exist. However, their use for practical purposes is not straightforward, and simpler, yet sound and rational approaches are desirable.

1.2 Aims

The main objectives of this thesis are:

— To increase the number of available monotonic tests on typical European cantilever bridge deck slabs under concentrated loads near linear supports;

— To study the influence of internal forces redistributions, the location of the concentrated load and the presence of injected or non-injected ducts parallel to the support (classic case of the deck slabs of prestressed balanced cantilever bridges);
— To perform fatigue tests on typical European cantilever deck slabs under concentrated loads;
— To study the influence of fatigue loading on the shear-fatigue strength of cantilever slabs;
— To present simplified rules to account for shear force redistributions due to both shear and flexural cracking;
— To present simple guidelines on how to model with linear elastic finite elements reinforced concrete slabs (which present a highly nonlinear behavior), in order to determine internal forces for shear and punching/shear assessment;
— To develop and validate a simple, yet sound and rational shear-fatigue model, based on the Critical Shear Crack Theory (CSCT).

1.3 Structure

This thesis is organized as follows:

— Chapter 2 provides a phenomenological description of the static and fatigue shear/punching shear behavior of reinforced concrete members without shear reinforcement. Existing static tests on cantilever slabs and simply supported one-way slabs under concentrated loads, as well as fatigue campaigns on beams and simply supported slabs are presented;
— Chapter 3 presents sound and rational models to suitably model shear, punching shear and shear-fatigue failures. The basic principles of linear elastic fracture mechanics (LEFM) and fracture mechanics (FM) applied to quasi-brittle materials are also presented;
— Chapter 4 presents and discusses the main aspects and results of an experimental static campaign on cantilever slabs under concentrated loads near linear supports;
— Chapter 5 describes and discusses the main aspects and results of an experimental fatigue campaign on cantilever slabs under concentrated loads near linear supports;
— Chapter 6 presents several proposals on how to apply the CSCT for both shear and punching shear assessment of slabs under concentrated loads near linear supports, combined with linear elastic finite elements (LEFE);
— Chapter 7 presents a simple and practical, yet sound and rational approach to determine the shear-fatigue strength of reinforced concrete members without shear reinforcement;
— Chapter 8 draws the main findings of this thesis, shows the main contributions and outlines future research lines.

Chapter 2

Phenomenological description and available testing

2.1 Introduction

The present chapter aims to provide a phenomenological description of the static and fatigue shear/punching shear behavior of reinforced concrete members without shear reinforcement. In order to study one-way slabs under concentrated loads near linear supports and beams or one-way slabs loaded over their full width, several static experimental programmes on haunched beams, cantilever slabs and simply supported one-way slabs subjected to concentrated loads are presented. In addition, experimental campaigns on the shear-fatigue behavior of beams and simply supported or inner slabs are also presented.

The chapter is organized as follows:

— Section 2.2 presents the shear-transfer actions in reinforced concrete members without shear reinforcement;

— Some experimental tests on haunched beams are presented in Section 2.3, in order to discuss whether there is a contribution due to the inclination of the compression chord in shear transferring;

— The punching behavior of slabs is introduced in Section 2.4. Comparisons between beams failing in shear and slabs failing in punching are performed;

— Section 2.5 presents the shear fields in reinforced concrete slabs, which is an useful tool to visualize how the shear flux develops in these elements;

— The mechanical behavior of reinforced concrete slabs subjected to concentrated loads near linear supports is presented in Section 2.6. Comparisons between the behavior of clamped and simply supported slabs are also performed in this section;

— Section 2.7 and Section 2.8 present experimental programmes on cantilever and one-way slabs subjected to concentrated loads near linear supports, respectively;

— Section 2.9 presents the shear-fatigue behavior of beams without shear reinforcement and several experimental campaigns from the literature;

— Section 2.10 presents some fatigue tests on simply supported or inner slabs and explains why these tests are not representative of cantilevers slabs subjected to concentrated loads.

2.2 Shear-transfer actions

Reinforced concrete beams without shear reinforcement can only be analyzed using the theory of elasticity at an early loading stage, due to the much weaker tensile strength of concrete when compared with its compressive one. With increasing load levels, flexural cracks appear in several locations of a beam subjected to a point load, leading to the initial cracking pattern of Figure 2.1(e). Shear can still be transferred through the following actions [Mut10] (an extensive list of published works on each action can be found in references [Cam13a, Cam13b]):

— cantilever action (Figure 2.1(a)): the concrete teeth (as named by Kani [Kan64]) between two consecutive flexural cracks are horizontally loaded by the flexural reinforcement, due to the varying acting bending moment in the longitudinal direction (beam axis). These uneven tensile forces acting on the reinforcement are equilibrated by a diagonal strut and tie, allowing shear transfer. This shear-transfer action is known as cantilever action because each tooth is clamped in the compression zone;

— aggregate interlock (Figure 2.1(b)): this shear-transfer action is originated when aggregates on one side of a crack contact the cement paste on the opposite side, creating normal and tangential stresses, allowing shear transfer through a compression strut (Figure 2.1(b)). The aggregate interlock stress intensity depends on the crack opening, relative slip and crack roughness. Larger crack openings or lower roughnesses are associated with lower aggregate interlock shear-transfer potential, as the contact surface area diminishes. One of the most widely spread aggregate interlock models has been developed by Walraven [Wal81];

— dowel action (Figure 2.1(c)): the flexural reinforcement can transfer shear forces from a diagonal strut to a diagonal tie through cracks by acting as a dowel. The ability to transfer the shear force depends on the reinforcement bar stiffness, which on its turn depends on the diameter, the concrete cover and tensile strength, and boundary conditions that might prevent concrete spalling or delamination;

— residual tensile strength (Figure 2.1(d)): up to a certain crack opening, concrete can transfer tensile stresses through cracks, allowing diagonal ties carrying shear forces to develop near the crack tip [Hil83] (the so-called fracture process zone (FPZ), refer to Section 3.7.1).

The so-far presented shear-transfer actions are referred as beam shear-carrying actions, as they allow keeping an almost constant lever arm between the compression and tension chords. The forces in these chords vary according to the acting bending moment at each section. The stress state created in concrete by these actions (Figure 2.1(f)) leads to the propagation of flexural cracks into shear cracks (Figure 2.1(g)), reducing or even

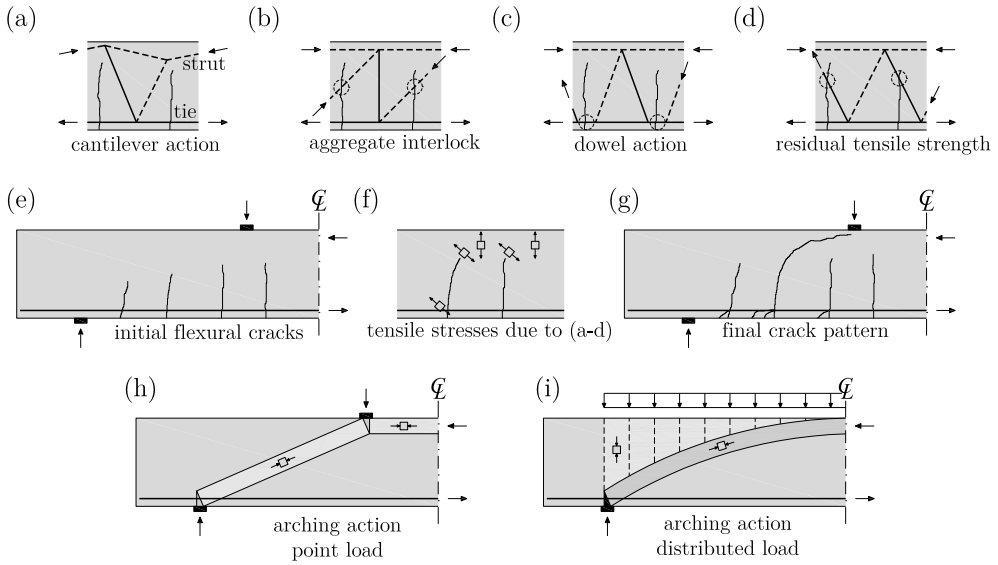

Figure 2.1: Shear transfer actions and development of cracking pattern [Mut10]: **(a)** cantilever action; **(b)** aggregate interlock; **(c)** dowel action; **(d)** residual tensile strength; **(e)** initial flexural cracks; **(f)** tensile stresses due to (a-d); **(g)** final crack pattern; **(h)** arching action for point load; and **(i)** distributed load

disabling their shear-transferring capacity.

Shear forces can also be transferred through arching action assuming a constant force in the flexural reinforcement, leading to the plasticity-based stress field of Figures 2.1(h,i) proposed by Drucker [Dru61]. The plasticity-based arching action is in agreement with test results for short span members ($a/d < 2.5$, refer to Figure 2.2(a)) [Sag10], but not for slender beams with corrugated flexural reinforcement, as for these the full plastic strength can not be attained because flexural cracks might develop across the compressive strut, diminishing its strength [Kan64, Mut08a].

The development of a shear crack might still allow shear to be transferred by arching action [Mut08a] through an elbow-shaped strut (limited by the member tensile strength) and a direct strut developing through the so-called critical shear crack thanks to aggregate interlock and residual tensile strength, as it will be shortly presented (refer to cases B and C in Figure 2.2(b)). However, for large shear spans the propagation of the critical shear crack leads to failure.

The governing shear-transfer actions at failure depend on the member slenderness. This fact is shown in Kani's valley, refer to Figure 2.2.

For very low shear spans (region A of Figure 2.2(a)) the shear strength V_R is the plastic strength V_{pl} corresponding to the stress field of Figure 2.1(h), because flexural cracks do not penetrate the compression strut (Figure 2.2(b)).

Increasing the shear span (region B of Figure 2.2(a)) might allow the penetration of flexural cracks within the compression strut, and consequently reducing the strut strength, as it becomes dependent on the aggregate interlock force transfer across the critical shear crack and on the elbow-shaped compression strut (Figure 2.2(b)) [Mut08a]. This region

of the Kani's valley (the so-called left-hand side or stable crack propagation side) can be properly investigated with stress fields [Cam13b] that account for the influence of cracking in the compression field strength [Vec86]. In this region of Kani's valley the development of inclined cracks through the compression strut is done in a stable way and failure is due to concrete crushing, which presents a reduced strength caused by transverse tensile strains and crack propagation [Cam13b].

Larger shear spans (region C of Figure 2.2(a)) develop simultaneously arching action and beam shear-transfer actions (Figure 2.2(b)), and the latter becomes dominant for even larger shear spans (region D, Figure 2.2(b)), before bending becomes once again the governing failure mode (region E of Figure 2.2(a)). The so-called right-hand size of Kani's valley exhibits an instable crack propagation [Cam13b], as an important and fast localization of deformations occurs in the critical shear crack.

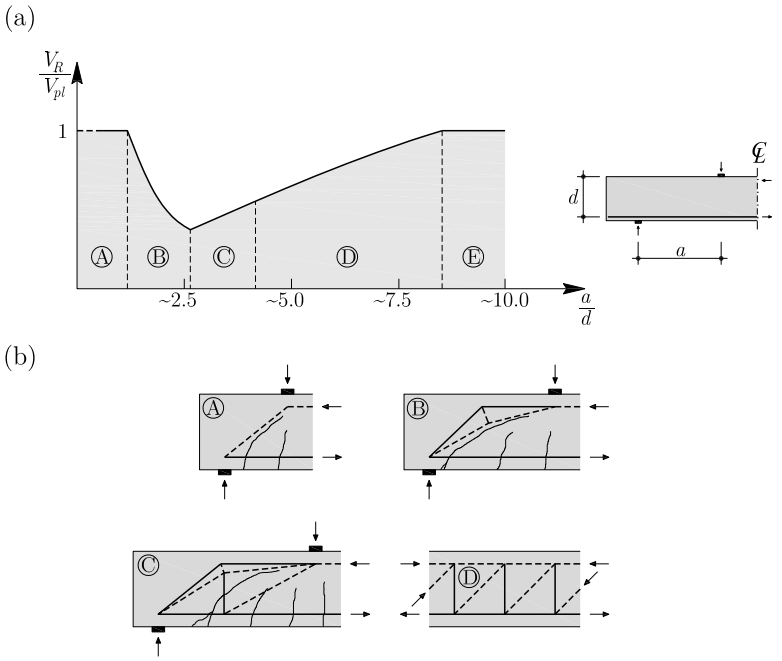

Figure 2.2: Kani's valley: **(a)** subsets of Kani's valley; and **(b)** governing shear transfer actions [Mut10]

The slender members located on the right-side of Kani's valley might present the following shear-transfer actions at failure (Figure 2.3): residual tensile strength of concrete and aggregate interlock (V_{CSC}), compression chord (V_{CC}) and dowel action (V_{DA}) (which may be neglected [Mut08a]). The shear component transferred through the critical shear crack V_{CSC} is highly dependent on the crack opening. This dependency is the basis of the important size-effect observed for slender members [Cam13b]. The behavior of these members can be suitably analysed with the Critical Shear Crack Theory (CSCT) [Mut08a] (Section 3.2), which accounts for size and strain effects. According to the CSCT, the shear strength depends on the critical shear crack width and its roughness. The critical shear crack width is proportional to the strain state in a control

section, which on its turn is proportional to the applied bending moment.

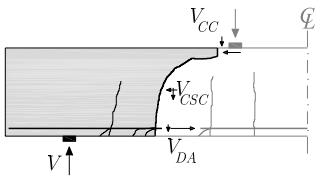

Figure 2.3: Shear-transfer actions at failure for slender members

Shear failures are generally brittle, *i.e.*, no visible signs of an imminent failure can be perceived from a structural visual inspection, reason why engineers shall design their structures in such a way that these kind of failures do not become governing.

2.3 Haunched beams without shear reinforcement

Haunched geometries are usually employed in reinforced concrete structures, such as bridge deck slabs (Figure 2.4), bridge girders, pile caps, framed structures, etc., as they allow material and weight savings.

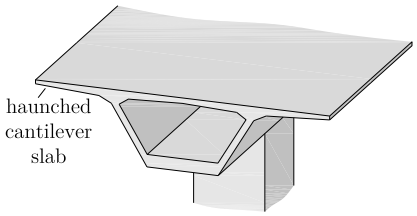

Figure 2.4: Haunched bridge deck slab

Several codes of practice (*fib*-Model Code 2010 [MC2010], Eurocode 2 [EC2-1], Swiss code [SIA262:2013]) consider that shear forces in reinforced concrete members without shear reinforcement may also be carried by the compression and tension chords, refer to Figure 2.5.

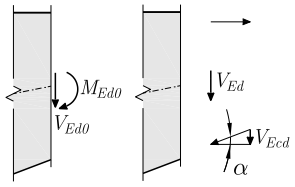

Figure 2.5: Inclined chord contribution to shear transfer

For members without prestressing and with horizontal flexural reinforcement subjected to a shear force V_{Ed0} and a bending moment M_{Ed0}, the shear force not carried by the compression chord V_{Ed} is given by:

$$V_{Ed} = V_{Ed0} - \frac{M_{Ed0}}{z} \tan \alpha \tag{2.1}$$

where z is the inner arm (that can generally be taken as $0.9d$, being d the flexural depth) and α is the compression chord inclination.

The very first tests on haunched beams failing in shear were performed by Mörsch [Mor29], refer to Figure 2.6. A description and interpretation of these tests can be found in reference [Mut90]. Plain rebars were used in this test series. The reinforcement ratio ($\rho = A_s/bd_{\max} = 1.67\%$) and the shear span ($a/d_{\max} = 2.1$) were kept constant. Two haunched beams were tested, with an inclination angle $\alpha = 18.4°$. Beam 1037 differed from beam 1034 because it had stirrups in the non-tapered region. Compared with the reference non-tapered beam 1027, beam 1034 without stirrups presented a lower strength. On the contrary, beam 1037 with stirrups presented an increase of strength. These tests set up a design philosophy for the following years.

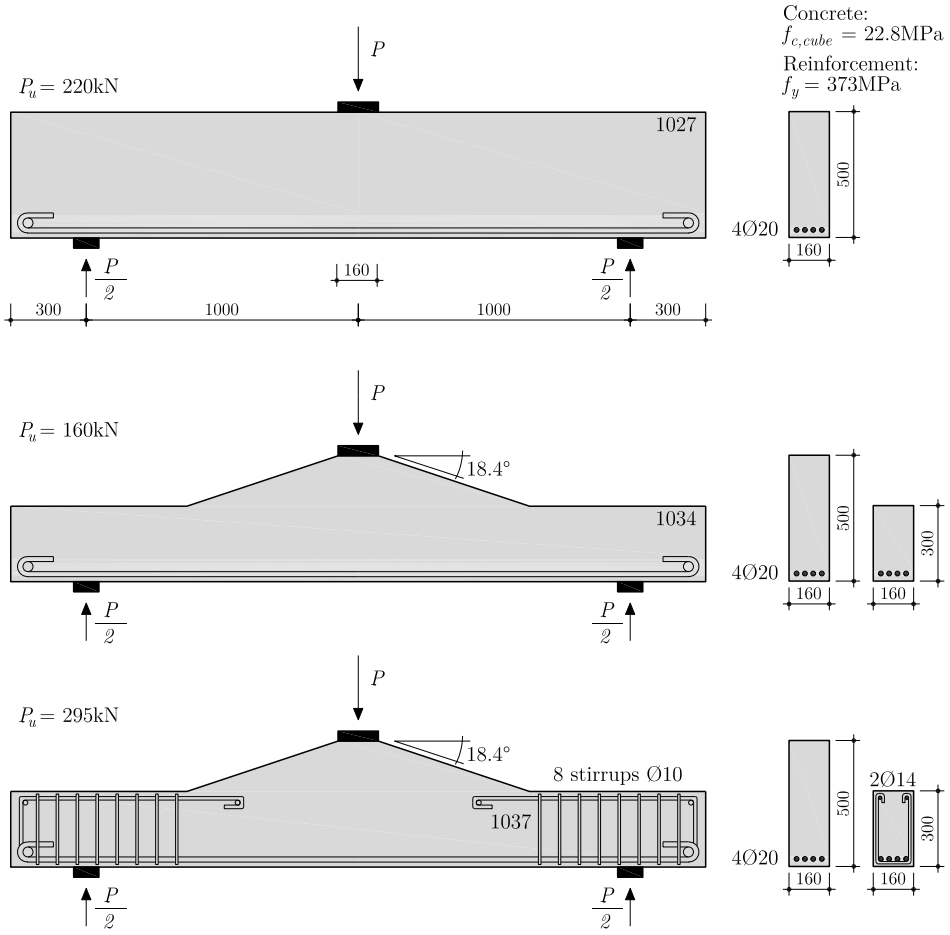

Figure 2.6: Tests on haunched beams performed by Mörsch [Mor29] (dimensions in [mm])

Many years later, in 1982, Debaiky and Elniema [Deb82] published a series of tests on 33 beams with shear reinforcement to study the behavior of haunched members, having proposed the following formula for the concrete contribution to shear strength:

$$\frac{V_c}{bd_s} = 0.66\sqrt{f_c}(1 + 1.7\tan\alpha) \tag{2.2}$$

where b is the beam width, d_s is the effective depth at the support and f_c is the concrete compressive strength. According to these authors the shear contribution of the inclined chord to the overall shear strength can be obtained by the factor $1.7\tan\alpha$.

Some years later (1994) MacLeod and Houmsi [Mac94] presented a series of tests on haunched beams failing in shear, varying the inclination angle from $\alpha = 0.0 - 10.4°$, refer to Figure 2.7. Four beams presented a shear span $a/d_{\max} = 4.8$ and a reinforcement ratio $\rho = A_s/bd_{\max} = 2.25\%$, and one other beam $a/d_{\max} = 3.9$ and $\rho = A_s/bd_{\max} = 1.83\%$. A positive contribution of the inclination angle could be observed in this test series.

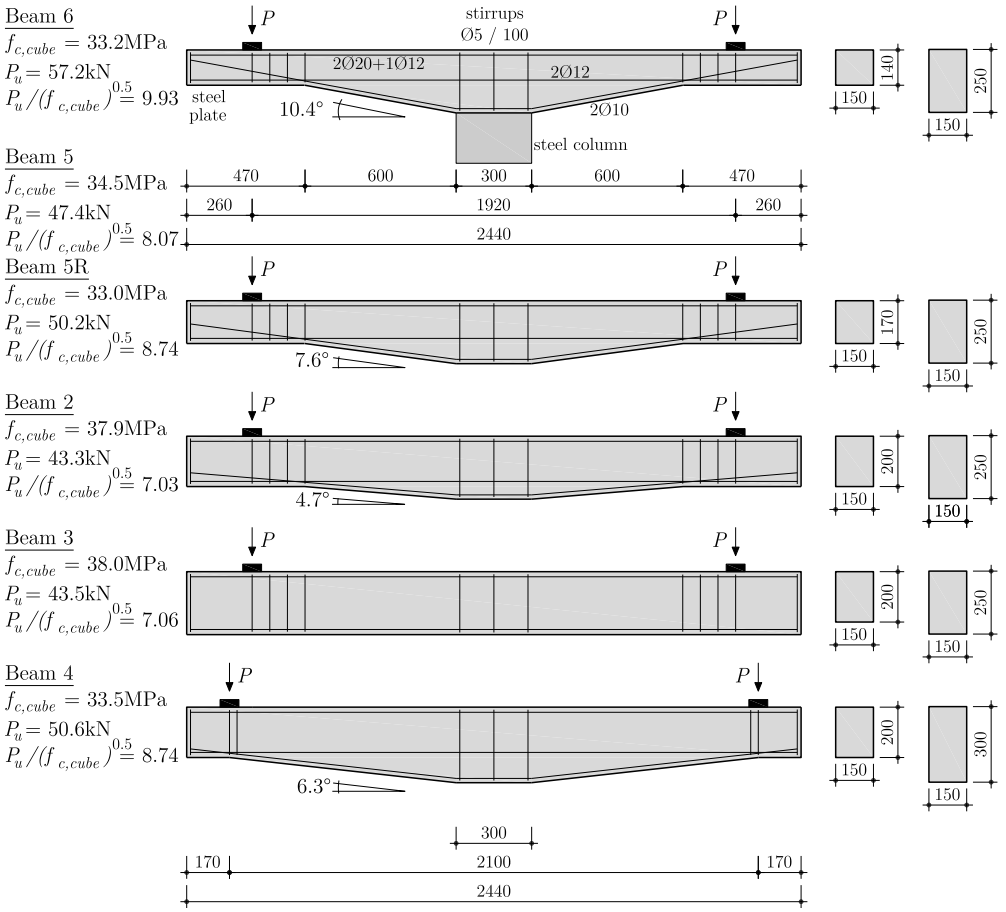

Figure 2.7: Tests on haunched beams performed by MacLeod and Houmsi [Mac94] (dimensions in [mm])

More recently (2011) an experimental campaign on haunched beams was performed by Rombach and Nghiep [Rom11], refer to Figure 2.8. The reinforcement ratio $\rho = A_s/bd_{\max} = 1.56\%$ was the same for all beams. Four beams failing in shear with a shear span $a/d_{\max} = 3.0$ and with an inclination varying from $\alpha = 0.0 - 10.0°$ showed a positive contribution of the inclination compared to a non-tapered beam. However, larger values

of inclination did not always imply larger shear strengths. Three others beams with a larger shear span $a/d_{\max} = 5.0$ and an inclination varying from $\alpha = 0.0 - 5.9°$ also failing in shear presented a negative contribution of the inclination angle.
In 2012, Pérez Caldentey et al. [Per12] presented a series of tests failing in shear on cantilever beams subjected to rectangular and triangular distributed loads, as well as point loads, refer to Figure 2.9. The adopted reinforcement ratio was $\rho = A_s/bd_{\max} = 0.79\%$. Point load tests presented a shear span $a/d_{\max} = 2.9$. Cantilevers subjected to rectangular distributed load presented a ratio between the cantilever length and the maximum effective depth of $l/d_{\max} = 5.7$, while cantilevers with triangular distributed load presented a $l/d_{\max} = 8.6$ ratio. A positive contribution of the inclination could only be clearly observed for the tests on cantilevers under rectangular distributed load.
In 2014, Gallego [Gal14b] presented four more static tests on haunched beams with a varying shear span $a/d_{\max} = 2.1 - 5.0$ and an inclination angle of $\alpha = 3.8°$. Three beams presented a reinforcement ratio of $\rho = A_s/bd_{\max} = 0.76\%$ and the other one 2.35%. All beams failed in shear.
The available experimental evidence does not allow to generally accept a positive contribution of variable-depth members due to the inclination of a compression chord carrying shear. As pointed out by Gallego [Gal14b], a potential positive effect may be limited by a simultaneous decrease of the internal lever arm, that may lead to an increase of strains and crack openings.

2.4 Punching shear

Reinforced concrete slabs without shear reinforcement subjected to concentrated loads or supported by columns may exhibit a punching shear failure mode around the load/reaction introduction zone. Like shear failures, punching shear also exhibits a brittle behavior.
In 1960, Kinnunen and Nylander [Kin60] performed a series of punching tests and observed that higher reinforcement ratios are associated with higher punching shear strengths and reduced deformation capacities. Based on the test series, Kinnunen and Nylander [Kin60] presented a theory to determine the punching shear strength, assuming that failure occurs for a critical value of slab rotation ψ outside the punching cone. The slab behavior was determined by simplifying the slab kinematics and assuming a bilinear moment-curvature relationship.
Slabs supported on columns or subjected to concentrated loads differ from beams without shear reinforcement under point loads. While a beam presents constant shear force and linear varying moment (Figure 2.10(a)), slabs exhibit unitary shear forces and radial bending moments that increase rapidly close to the supported area (Figure 2.10(b)). The beam shear-transfer actions have enough strength where moderate shear has to be transferred. However, close to the support beam shear-transfer actions are disabled and arching action develops [Mut08b]. In contrast with beams, where the governing shear-transfer actions depend on the member slenderness, for slabs supported on columns, arching action is the governing shear-transfer action, defining an effective shear span a_{ef}

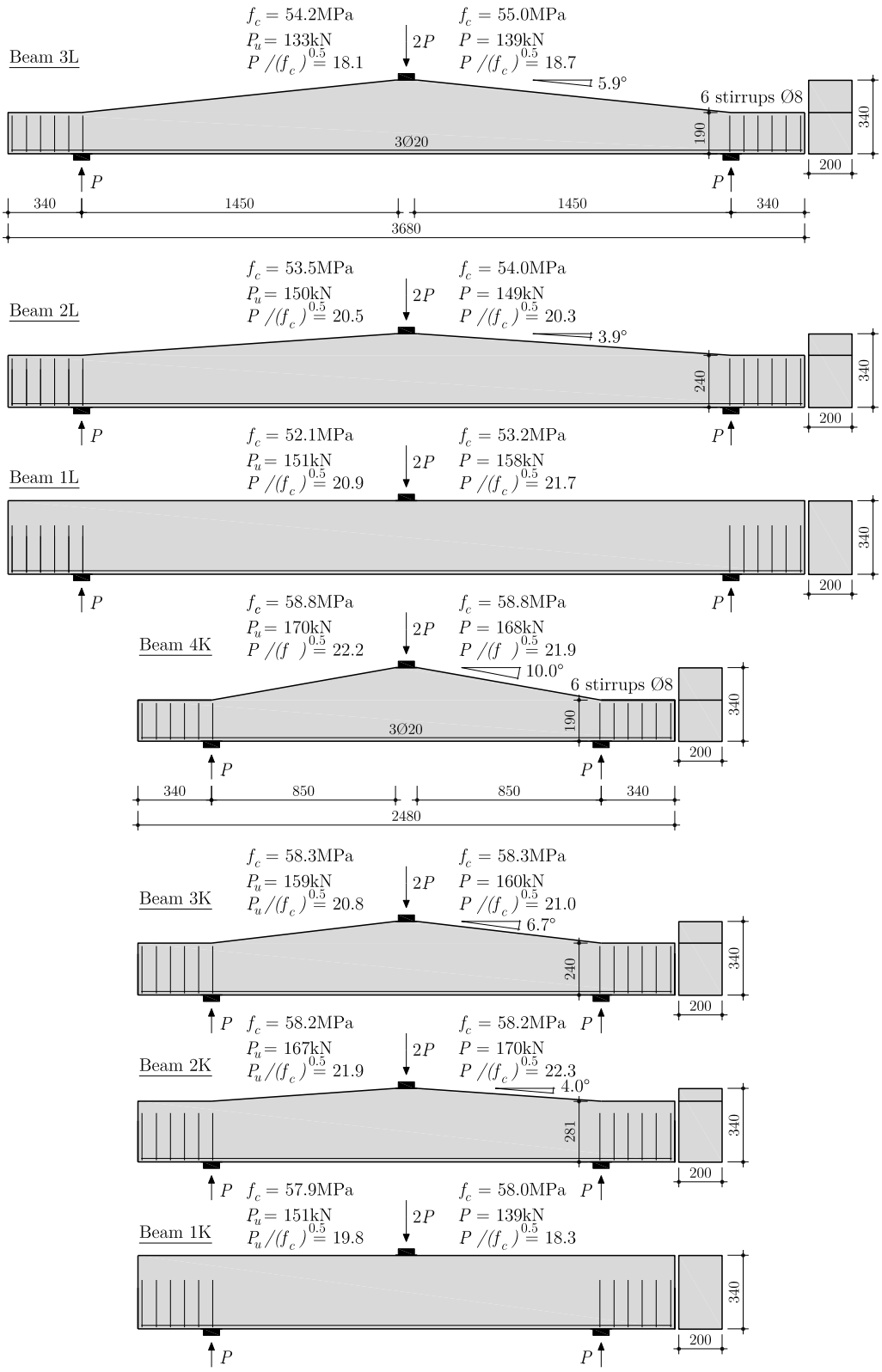

Figure 2.8: Tests on haunched beams performed by Rombach and Nghiep [Rom11] (dimensions in [mm])

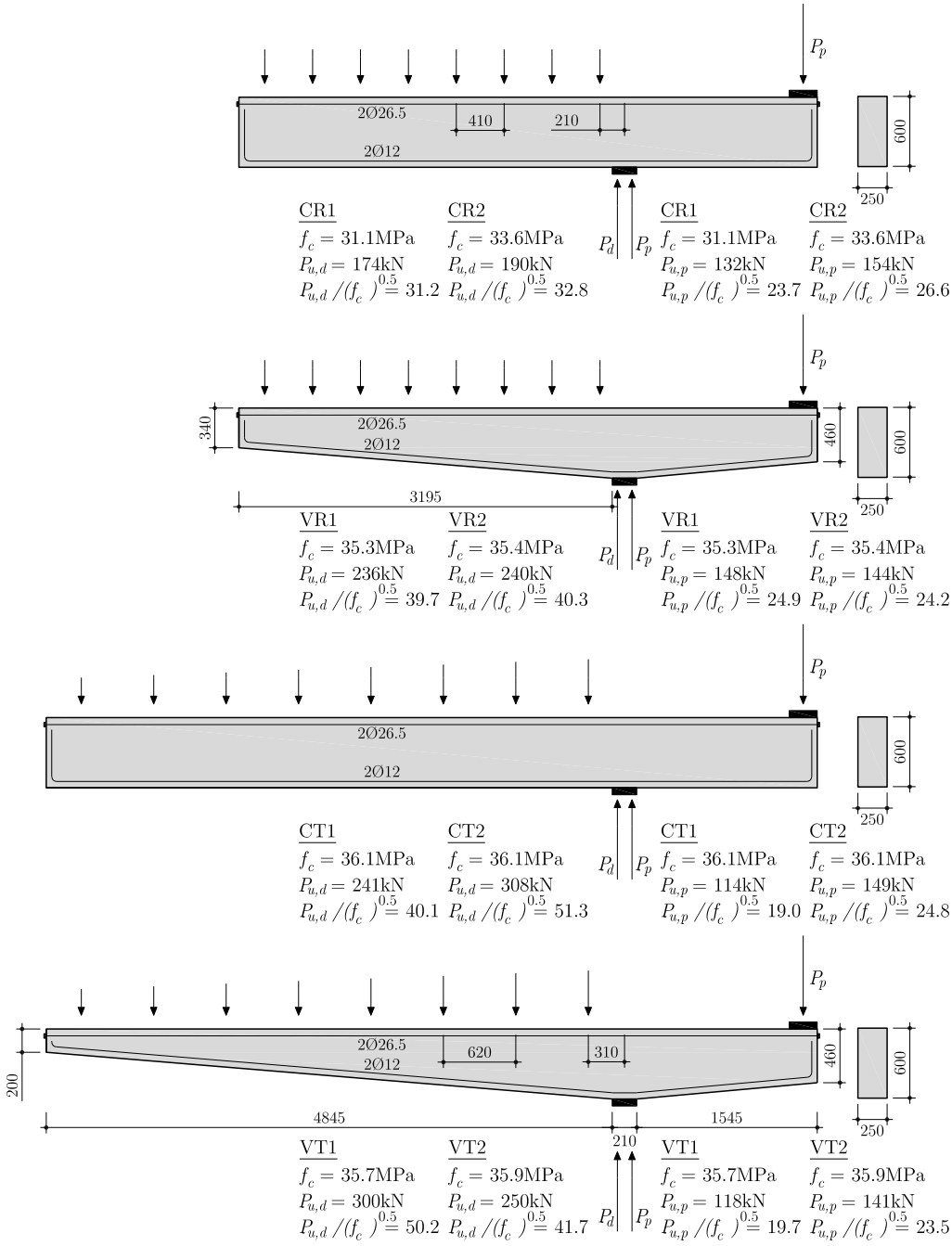

Figure 2.9: Tests on haunched beams performed by Pérez Caldentey et al. [Per12] (dimensions in [mm])

smaller than the geometric one [Mut10] (Figure 2.10(b)) and corresponding to that of beams on the left-side of Kani's valley.

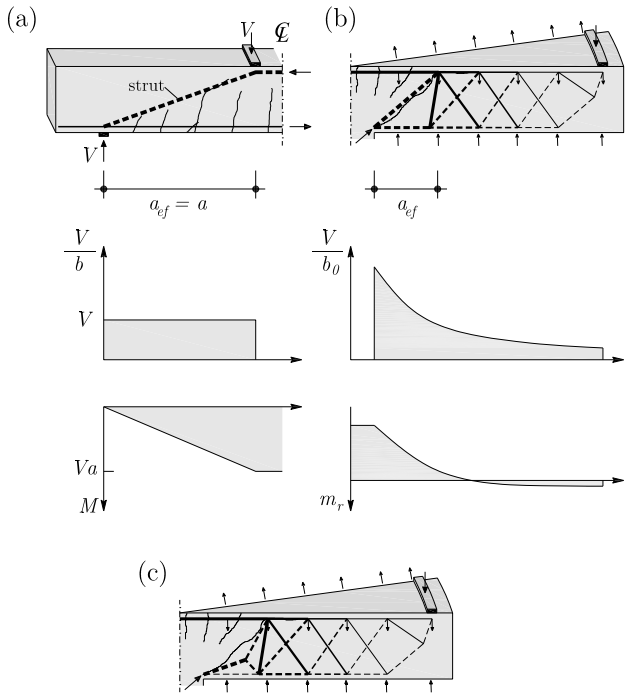

Figure 2.10: Arching action and beam shear-transfer actions in beams and slabs supported on columns: **(a)** shear forces and bending moments of a beam; **(b)** unitary shear forces and radial bending moments of a slab supported on columns; and **(c)** elbow-shaped strut [Mut10]

The observations performed by Kinnunen and Nylander [Kin60] that punching strength decreases with increasing slab rotations have been explained by Muttoni and Schwartz [Mut91], who have established a link between the reduction of punching shear strength with the presence of a critical shear crack that propagates into the inclined compression strut carrying the shear force to the column (Figure 2.10(b)).

Like beams, the arching action on slabs supported on columns also presents an elbow-shaped strut (Figure 2.10(c)). This strut is grounded on experimental evidence [Kin60, Gua09], which shows a decrease of the radial compression strain in the soffit of the slab near the column close to failure, after a maximum has been attained at lower load levels.

Reinforced concrete slabs without shear reinforcement have generally non-axis-symmetric conditions, *i.e.* where bending deformations are non-symmetric around the column or concentrated load. In general this can be consequence of [Sag11]:

— loading: load eccentricity (*i.e.* moment transfer) or one-way spanning with balanced moments;
— geometry: columns with irregular shapes (e.g. rectangular) or slabs with openings near the column;
— reinforcement layout: different flexural reinforcement layouts in each ortogonal direction.

Non-axis-symmetry conditions may result in a substantial different behavior when compared with symmetric conditions, as they might allow shear redistributions due to both bending and shear cracking [Sag11].
Actual flat slabs, even in axis-symmetric conditions are subjected to compressive membrane actions [Ein15], arising from the restraint against the slab expansion provided by stiff surrounding structural elements, but also due to the restraint against expansion of the hogging moment area, provided by the inplane stiffness of the sagging moment area. Due to this effect, the deflections of a continuous flat slab are smaller than the ones of a corresponding isolated specimen (more commonly tested), which leads to lower crack widths and potentially larger punching strengths.

2.5 Shear fields

The shear field is a vector field that comprises the direction ϕ_0 and magnitude v_0 of the principal shear force per unit length of a loaded slab [Mar90]. Considering a sandwich model (Figure 2.11(a)), the slab can be divided into a central core (Figure 2.11(b)) transferring shear forces and two outer panels (Figure 2.11(c)) carrying compression and tension forces due to both bending and torsional moments. The unitary shear forces (v_x,v_y) acting in the cross-section of the core are equilibrated by in-plane shear forces acting on the top and bottom faces of the core (Figure 2.11(b)). These in-plane shear forces are in their turn in equilibrium with force-increments acting in the outer panels (Figure 2.11(c)). The in-plane shear forces transferred between the core and the outer planes (v_x,v_y) have a resultant vector, the principal shear force, defined by its intensity v_0 and direction ϕ_0 (Figure 2.11(d)). This in-plane principal shear force is in equilibrium with the cross-section principal shear force, having the same magnitude v_0 and being comprised in a perpendicular plane to the in-plane principal shear force (Figure 2.11(d)). The magnitude v_0 and the angle ϕ_0 can be calculated as follows:

$$\phi_0 = \arctan\left(\frac{v_y}{v_x}\right) \tag{2.3}$$

$$v_0 = \sqrt{{v_x}^2 + {v_y}^2} \tag{2.4}$$

Vaz Rodrigues [Vaz07] developed an useful representation of the shear field that is used in this thesis, representing it by a set of lines parallel at each point to the shear field direction and whose thickness is proportional to its magnitude, refer to Figure 2.12.

2.6 Mechanical behavior of linearly supported slabs under concentrated loads

Reinforced concrete slabs subjected to concentrated loads near linear supports are commonly found in practice: bridge deck slabs (Figures 2.13(a,b)), slab bridges (Figure

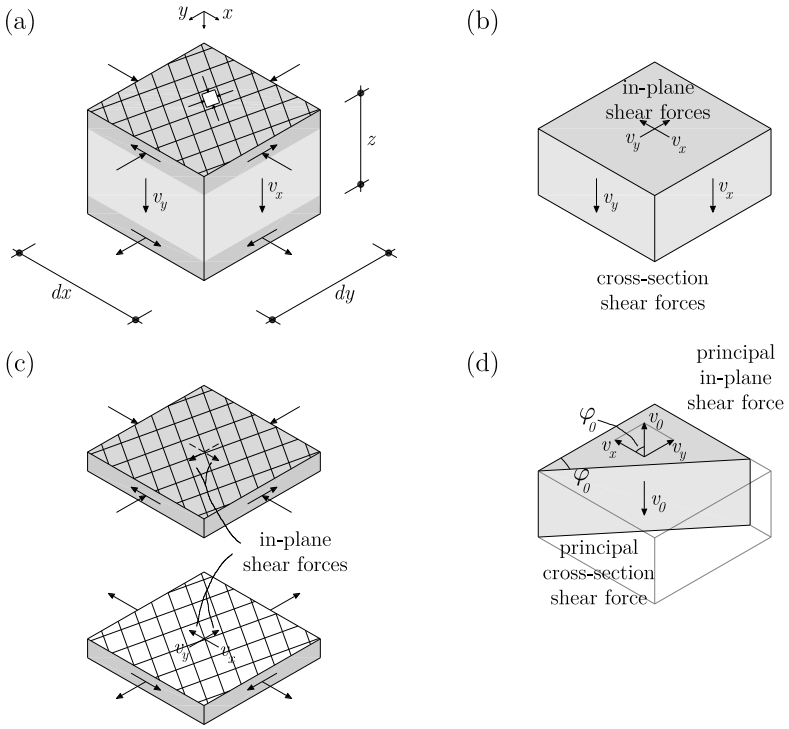

Figure 2.11: Sandwich model of a reinforced concrete slab [Vaz08]: **(a)** sandwich layers and forces; **(b)** forces acting on the core; **(c)** forces acting on the panels; and **(d)** magnitude and direction of principal shear force

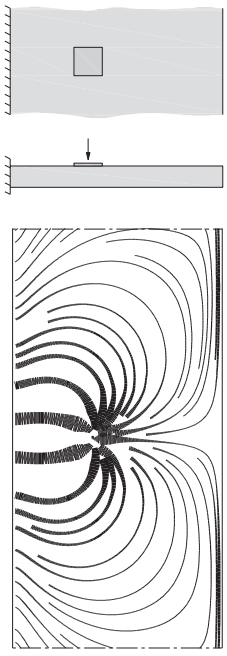

Figure 2.12: Shear flux representation for cantilever slab subjected to a concentrated load

2.13(c)), pile caps (Figure 2.13(d)) and flat slabs loaded by walls and supported on piles or columns (Figure 2.13(e)). These systems are characterized by high shear forces concentrated in the region between the concentrated loads and the linear support.

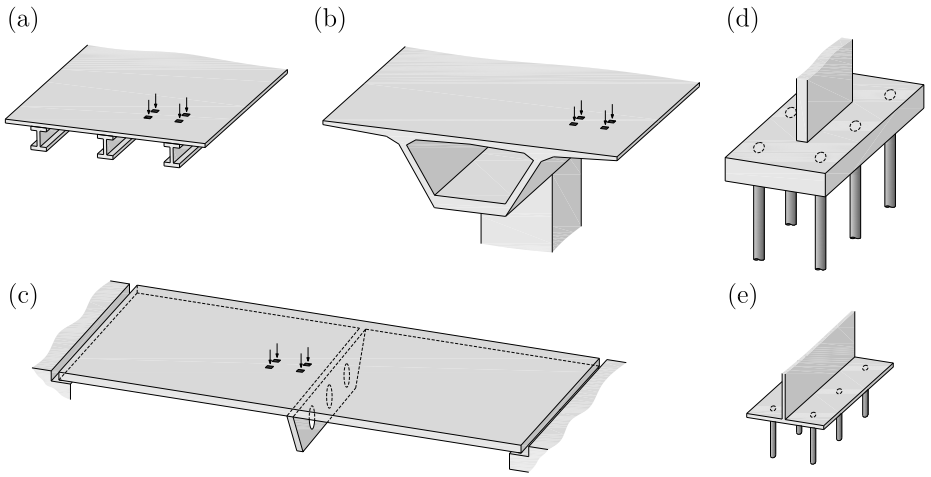

Figure 2.13: RC slabs subjected to concentrated loads near linear supports: **(a)** girder bridge; **(b)** box-girder bridge; **(c)** slab bridge; **(d)** pile cap; and **(e)** slab loaded by wall and supported by piles or columns

In a slab, with respect to the manner in which shear forces are transferred, several cases can be found. The first case is characterized by the development of parallel shear forces and is typically found on linearly supported one-way slabs subjected to distributed loading (Figure 2.14(a)). For two-way flat slabs supported on columns and subjected to distributed loads, the shear forces develop radially towards the columns (Figure 2.14(b)). Intermediate cases are also possible, with shear forces developing neither perfectly in a parallel or radial manner. This is generally the case of concentrated loads near linear supports (Figure 2.14(c)). Depending on the geometry and properties of the slab, as well as on its loading conditions, slabs subjected to concentrated loads may present different failure modes: shear near the line support [Reg82, Reg88, Coi07, Vaz08, Rom09, Rom13, Lan13a, Rei13a, Rei13b] (Figure 2.15(a)), punching shear around the concentrated loads [Reg82, Reg88, Coi07, Lan13a, Rei13a] (Figure 2.15(b)) or development of a flexural mechanism (Figure 2.15(c)).

The behavior of slabs subjected to concentrated loads near linear supports is different from the behavior of one-way and two-way flat slabs subjected to distributed loading. The first difference is found on the principal direction of the shear force, as previously seen (not perfectly parallel or radial). Another difference is related to the acting shear force and bending moment at the shear critical region, which may potentially vary as the level of load increases (due to redistributions on shear and moment fields after cracking and/or yielding of the flexural reinforcement). Moreover, the ratio between the maximum acting moment $m_{\max}$ and the maximum acting shear force $v_{\max}$ in cantilever slabs at the support is lower than for cantilever beams with the same shear span [Rom09] (Figure 2.16). Despite such different behavior, most available testing has only concen-

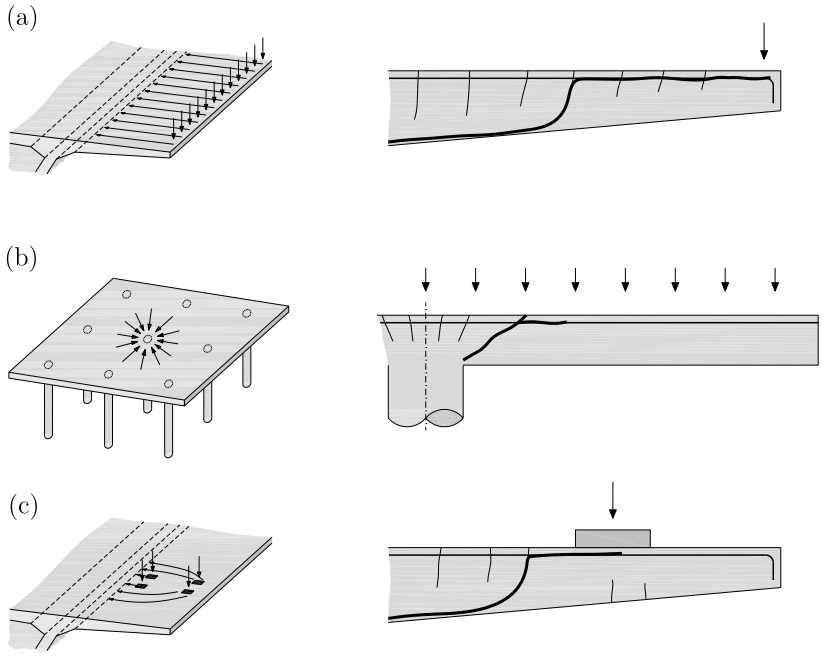

Figure 2.14: Shear transfer modes and typical failure crack patterns: **(a)** shear developing in a one-way slab; **(b)** two-way slab supported on columns; and **(c)** linearly supported slab subjected to concentrated loads

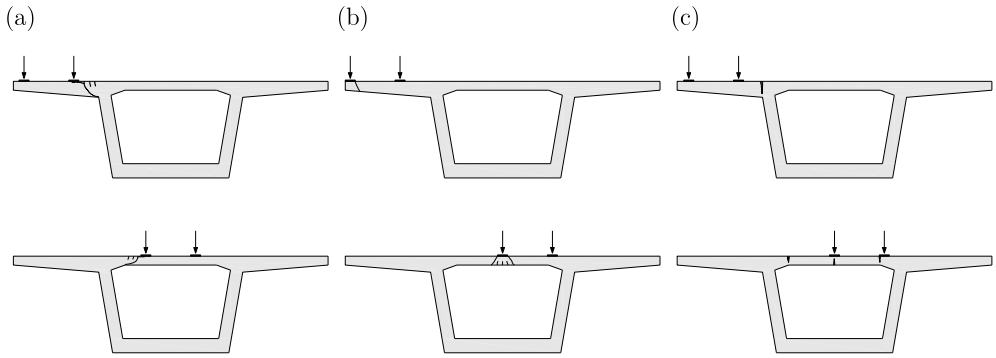

Figure 2.15: Failure modes of bridge deck slabs: **(a)** shear; **(b)** punching shear; and **(c)** flexural mechanism

trated on one-way slabs or beams loaded over the full width or two-way slabs with axis-symmetric punching conditions. Design codes reduce in the majority of cases shear design situations to these two limit cases.

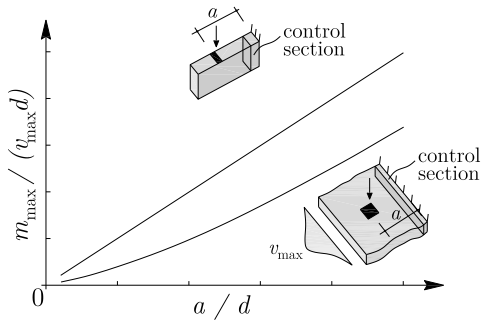

Figure 2.16: Comparison between the bending to shear ratio of a beam and a cantilever slab subjected to a concentrated load [Rom09]

The boundary conditions of the linear support play a significant role in the distribution of internal forces. This can for instance be observed in Figure 2.17, where the values of shear forces and bending moments of a simply supported slab (similar to the side span of Figure 2.13(a)) and a fully clamped slab (similar to Figure 2.13(b)) are presented. As Figure 2.17(c) shows, the maximum moment for a clamped slab is located close to the support, while for the simply supported slab, it is located under the load. In addition, these two maximum bending moments have opposite signs. For both types of slabs, the highest shear forces (Figure 2.17(c)) develop near the concentrated load, where the directions of the shear forces (Figure 2.17(b)) and the bending moments are similar to those in the column region of a flat slab (refer to Figure 2.14(b)). This means that non-symmetric punching might be a potential failure mode in this region.
With respect to the directions of the shear forces in the critical region between the load and the support, it can be observed that they in fact develop differently for both cases (Figure 2.17(b)). In the case of clamped slabs, the shear forces are practically perpendicular to the supported edge. This means that, in this region, the slab behaves similarly as a one-way strip with almost constant shear force in the x-direction (perpendicular to the edge), but with a high concentration on the symmetry axis and a rapid decrease along the y-direction (Figure 2.17(d)), as reported by Rombach and Velasco [Rom05]. As it is shown in Figure 2.17(d), clamped slabs present in this region higher shear forces compared to simply supported ones. The fact that most design codes propose to perform design in this situation by checking the shear strength at a control perimeter parallel to the line support and the punching strength at a perimeter around the concentrated loads might be suitable for cantilever slabs.
With respect to simply supported slabs, the shear behavior of the element has to be dependent of the the loading plate to specimen width ratio (c_y/b), refer to Figure 2.18. A slab strip with a ratio $c_y/b = 1$ is similar to a beam or a one-way slab loaded over the full width, and can only fail in shear (excluding flexure), as a punching shear perimeter around the load cannot develop. As it was discussed in Section 2.2, the control section

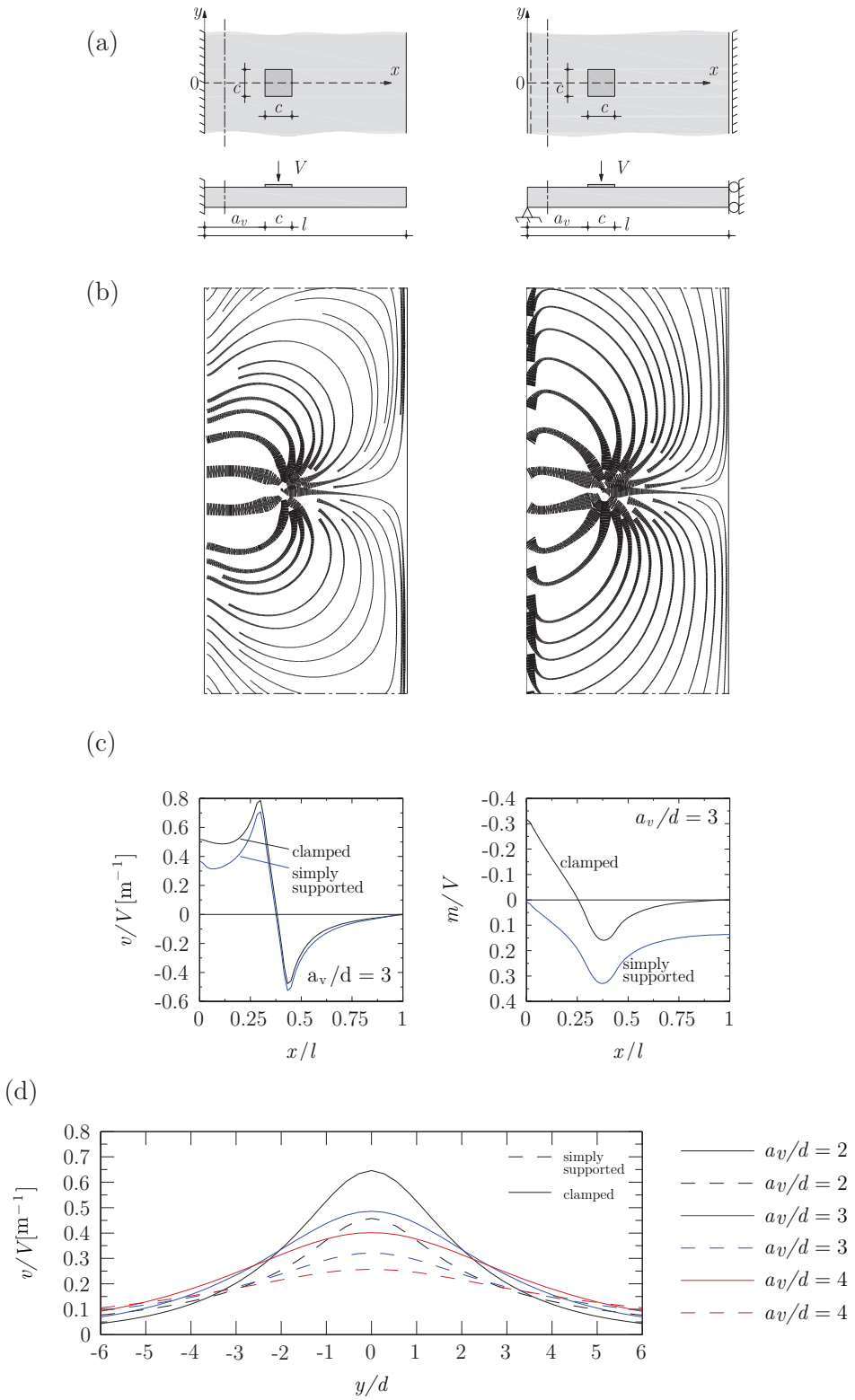

Figure 2.17: Comparison between slabs subjected to a concentrated load near a linear support (l = 3000 mm; h = 330 mm; d = 300 mm; c = 400 mm): **(a)** statical systems: clamped (left column) *vs* simply supported edge (right column); **(b)** shear fields ($a_v/d = 3$); **(c)** unitary shear forces and moments at load axis ($a_v/d = 3$); and **(d)** unitary shear distribution parallel to the edge as a function of a_v (internal forces calculated assuming a linear-elastic behavior of material and shell finite elements with shear deformation, considering $\nu = 0.2$)

has to be located close to the load and not close to the support, due to the larger acting bending moment close to the load, associated with larger critical shear crack opening and smaller shear strength (strain effect). It is reasonable to expect that the control section for shear has to be independent of the c_y/b ratio, and elements with $c_y/b = 1$ or $c_y/b \to 0$ should be treated in the same way for consistency. However some codes of practice [EC2-1, MC2010] consider that the shear control section is located close to the support. In this point the Canadian code CSA-A23.3-04 based on the Modified Compression Field Theory [Vec86] seems to be consistent, as it proposes for wide reinforced concrete members a punching shear check in a control perimeter around the load, and a shear check in a section close to the load [Lub06], refer to Figure 2.19. Lubell [Lub06] has investigated the shear behavior of wide members and has proposed to reduce the shear strength of these elements calculated over the full width by the factor $\beta_L = 0.8{+}0.2c_y/b_w$, based on experimental tests [Reg82, Reg88, Ser02, Lub06]. However, this approach does not take into account the three-dimensional force flow (associated with the punching shear mechanism) needed to achieve an uniform distribution over the full width.

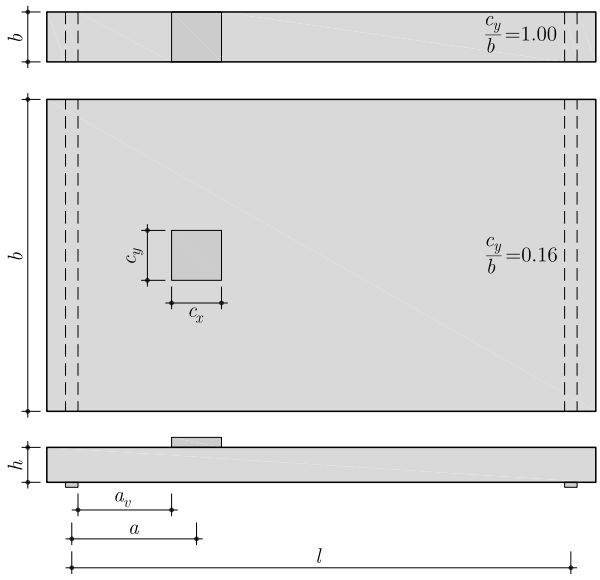

Figure 2.18: Loading plate to specimen width ratio (c_y/b) of simply supported slabs

The effective shear width assumed to participate in the shear strength mechanism usually depends on national practices [Lan14b], refer to Figures 2.20(a,b) for the Dutch and the French ones, respectively. *fib*-Model Code 2010 [MC2010] has recently proposed an effective width dependent of the degree of clamping of the support, refer to Figure 2.20(c). Besides these geometric rules, another approach commonly used in practice is the linear elastic effective width (b_w), refer to Figure 2.21. The effective width can be obtained from a linear elastic finite element analysis with shell elements by dividing the total shear force going through the control section (V) by the maximum unitary shear

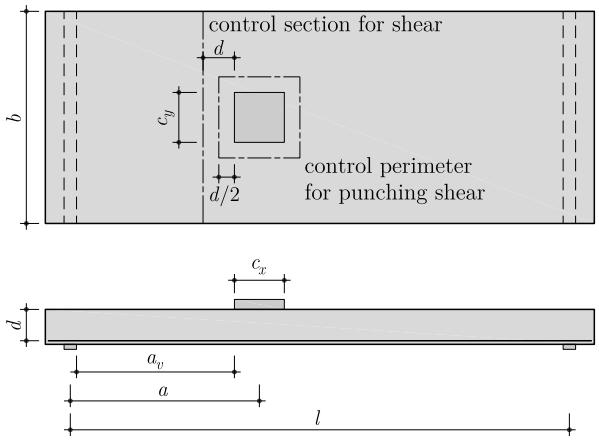

Figure 2.19: Control sections for shear and punching shear of wide reinforced concrete members under a concentrated load according to CSA-A23.3-04 [Lub06]

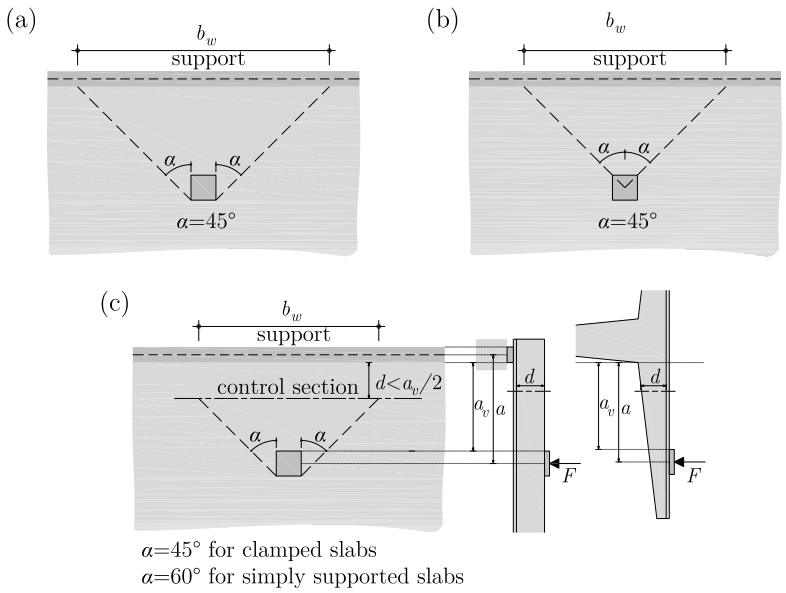

Figure 2.20: Effective shear widths according to the: **(a)** French practice; **(b)** Dutch practice; and **(c)** *fib*-Model Code 2010

force perpendicular to the control section ($v_{perp,\max}$).

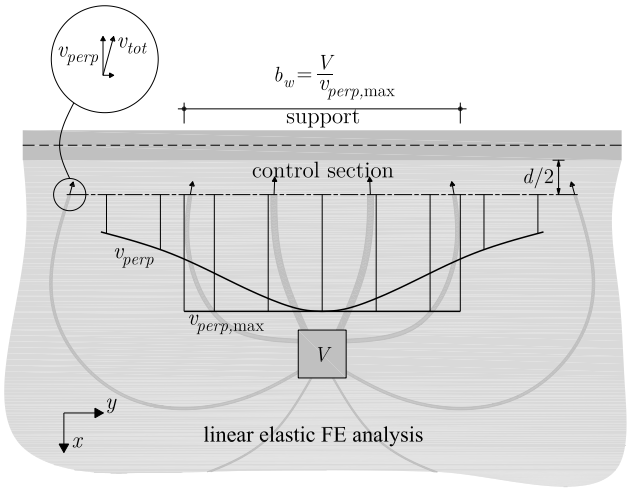

Figure 2.21: Determination of the linear elastic effective width

The location of the load also plays a significant role in the behavior of the slab. This is shown in Figure 2.17(d) where the shear force in the region between the load and the support is plotted for different locations of concentrated load (defined with the free shear span a_v, see Figure 2.17(a)) for clamped and simply supported slabs. For both cases, the maximum shear force depends on the clear shear span a_v, with smaller shear spans related to larger shear forces.

The location of the load does not only influence the internal forces in the slab, but also its shear strength. This fact, for beams without shear reinforcement was already demonstrated by Leonhardt and Walther [Leo62] and Kani [Kan66] (Figure 2.22(c)). An explanation of this phenomenon is given in [Mut08a] (Section 2.2): for small values of shear span, an inclined strut between the support and the load is less disturbed by the development of inclined cracks (Figure 2.22(a)). For larger shear span values, bending cracks develop through the inclined strut between the load and the support, thus decreasing the shear strength of the member (Figure 2.22(b)). This means that in members with short shear spans, larger shear strengths can be reached (Figure 2.22(c)). This dependency on the shear span is also observed in slabs subjected to concentrated loads close to linear supports, as it will be shown later in this thesis by analysis of test results. Contrary to beams, where the shear span is geometrically and statically defined, on slabs subjected to concentrated loads near a linear support, the shear span is generally defined as a geometric parameter: the (shorter) distance from the load to the support (even though the shear forces develop in various directions, and depending on the considered direction, different values of shear span are potentially found, as discussed by Lantsoght et al. [Lan13a]).

In addition to the boundary conditions and load location, another significant aspect influencing the design/assessment of two-way slabs subjected to concentrated loads is the presence of ducts (injected or not). Incorporating ducts is becoming increasingly popular

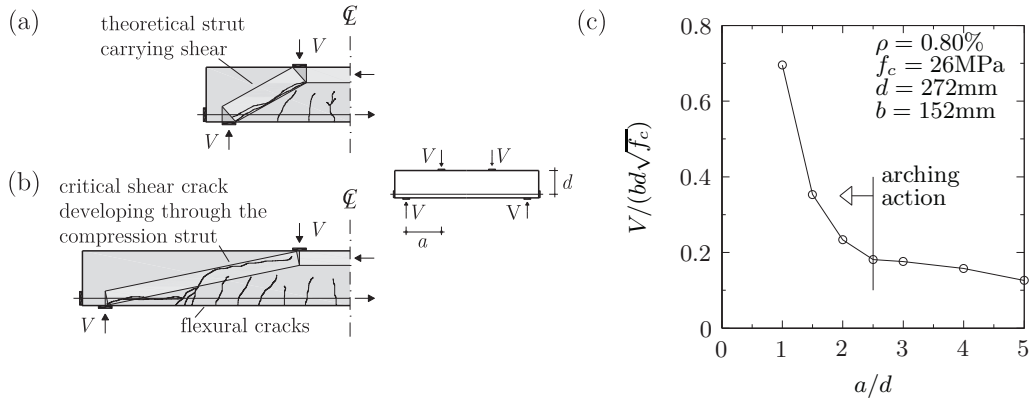

Figure 2.22: Comparison of cracking pattern and theoretical direct strut for: **(a)** small; and **(b)** larger shear span a (according to [Mut08a]); and **(c)** shear strength of beams without shear reinforcement tested by Kani [Kan66] as a function of the shear span

in flat slabs of residential buildings (water or heating pipes), as well as the classic case of deck slabs of bridges where it allows placing post-tensioning tendons (typically the case of deck slabs of bridges erected with a balanced cantilever construction method).
The influence of duct material and potential injection of the prestressing ducts on the strength of concrete girders subjected to in-plane shear is a well known phenomenon [Mut06, Fer08], as the ducts disturb the compressive field of the web, creating transverse tensile stresses and thus reduce the strength of concrete. In bridge deck slabs under concentrated loads near the supports, the inclined struts carrying shear also have to deviate at the location of the ducts, potentially reducing the shear strength. Although some researchers have investigated this problem for beams without shear reinforcement with circular and square openings [Han69, Som74, Sal77, Ars12], no previous research was found on two-way slabs with linear supports subjected to concentrated loads.

2.7 Static tests on cantilever slabs under concentrated loads

The existing experimental database on cantilever slabs without shear reinforcement under concentrated loads is somewhat limited.
Vaz Rodrigues [Vaz02] performed in 2002 a 1/3 scale test on a cantilever slab subjected to a concentrated load in the edge. The reinforcement ratio was $\rho = 1.19\%$ for the transversal top reinforcement over the clamped edge. The slab was haunched and its thickness varied from 110 mm to 140 mm. The free shear span to effective depth ratio was $a_v/d_{\max} = 6.0$. Punching shear was the reported failure mode.
Lu [Lu02] performed in 2003 a series of nine tests on reduced scale cantilevers with thicknesses of 50 mm and 60 mm. The main transversal reinforcement varied from $\rho = 0.15 - 1.00\%$. The author reported both flexural and brittle failures due to shear or punching shear. The author observed the positive influence of increasing the reinforcement ratio in both flexural and shear strengths, as well as adding an edge beam to

improve the slab load-carrying capacity.
Vaz Rodrigues et al. [Vaz08] performed six tests on two large-scale slabs, refer to Figure 2.23. Two main transversal reinforcement ratios in the clamped section were adopted, $\rho = 0.78\%$ and $\rho = 0.60\%$. Three different loading configurations were used, with four, two and one concentrated loads. The free shear span to effective depth ratio varied from $a_v/d_{\max} = 2.3 - 3.4$. All slabs (except DR1a) failed in shear in the region between the load and the linear support, while DR1a failed between the closest and farthest loads.

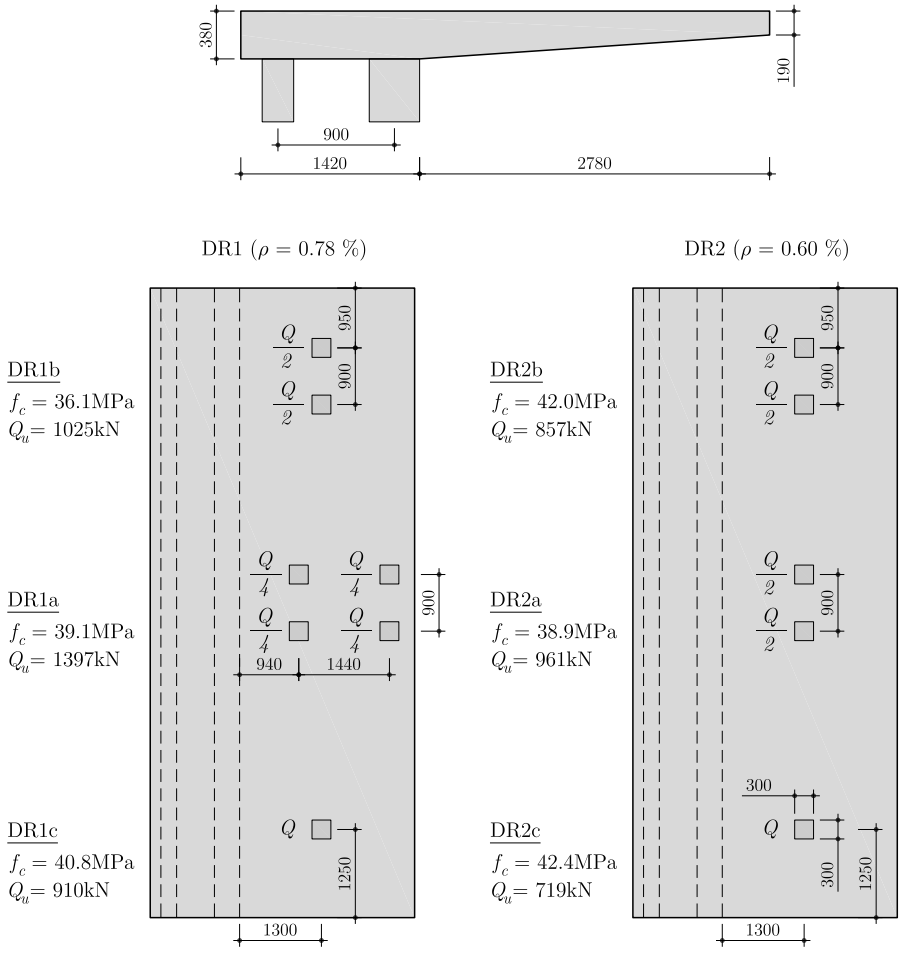

Figure 2.23: Tests on cantilevers slabs performed by Vaz Rodrigues et al. [Vaz08] (dimensions in [mm])

Rombach and Latte [Rom09] performed four tests on four slabs without shear reinforcement, refer to Figure 2.24. The main transversal reinforcement ratio in the clamped section varied from $\rho = 0.81 - 1.20\%$ and the free shear span to effective depth ratio from $a_v/d_{\max} = 2.1 - 3.1$. Three tests were preloaded with a linear load at the cantilever edge. All slabs failed in shear.
Reissen and Hegger [Rei13b] performed four tests on two slabs without shear reinforcement, refer to Figure 2.25. The main transversal reinforcement ratio in the clamped section was $\rho = 0.98\%$ and the free shear span to effective depth ratio $a_v/d_{\max} = 3.3$.

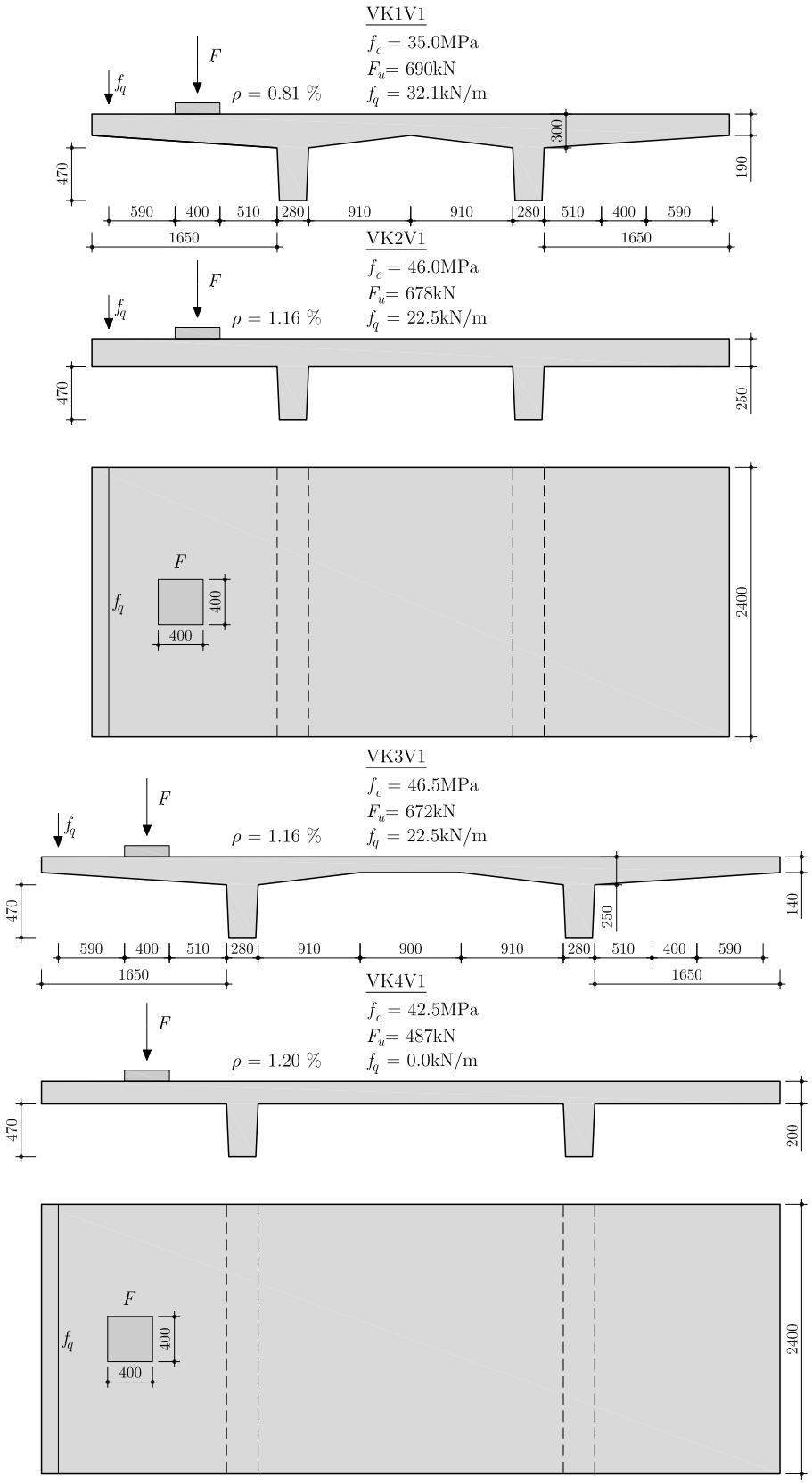

Figure 2.24: Tests on cantilevers slabs performed by Rombach and Latte [Rom09] (dimensions in [mm])

Two tests were preloaded with a linear load at the cantilever edge. All slabs failed in shear.

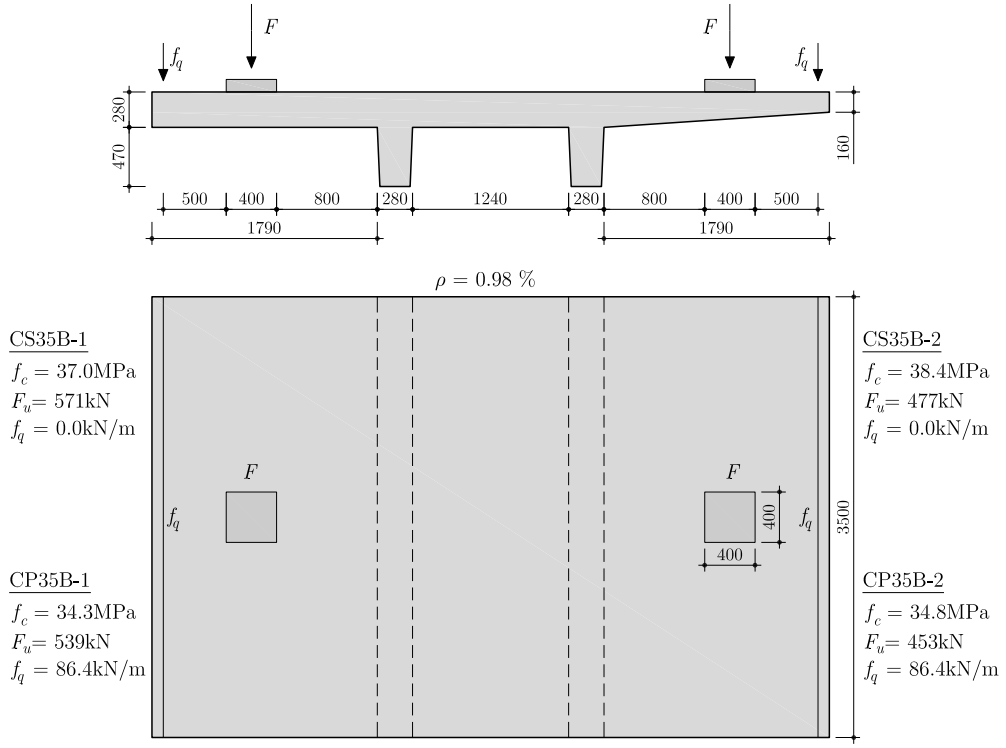

Figure 2.25: Tests on cantilevers slabs performed by Reissen and Hegger [Rei13b] (dimensions in [mm])

2.8 Static tests on simply supported one-way slabs under concentrated loads

Simply supported one-way slabs under concentrated loads received greater attention from the scientific community in the last century than cantilever slabs. A database of experimental tests on these elements has recently been compiled by Lantsoght et al. and can be found in references [Lan13b, Lan14a].

Among the first researchers to study these elements, Leonhardt and Walther [Leo62] performed a series of four-point bending tests on slab strips (500 mm wide) loaded by a concentrated load and a linear load, refer to Figure 2.26. Seven out of nine tests that failed in shear did so on the side with the concentrated load, suggesting that the shear strength of the slab strip diminishes proportionally to the loading plate to specimen width ratio (c_y/b). However, as it was observed by Lubell [Lub06], this influence could not be seen as a definite conclusion, as the results are within normal laboratory scatter.

An extensive test programme (29 tests) to study to a greater extent the influence of the loading plate to specimen width ratio (c_y/b) and to a lesser extent the influence of the load location on one-way slab strips was performed by Regan and Rezai-Jorabi [Reg88].

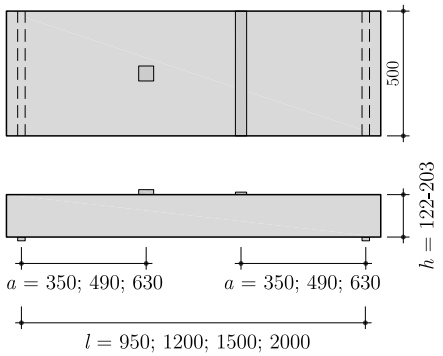

Figure 2.26: Tests on simply supported one-way slabs performed by Leonhardt and Walther [Leo62] (dimensions in [mm])

The width of the specimens varied from 400 mm to 1200 mm and the loading plate to specimen width ratio (c_y/b) from 0.06 to 1.00, refer to Figure 2.27. Reported failure modes included shear, punching shear around one concentrated load and punching shear around the two concentrated loads.

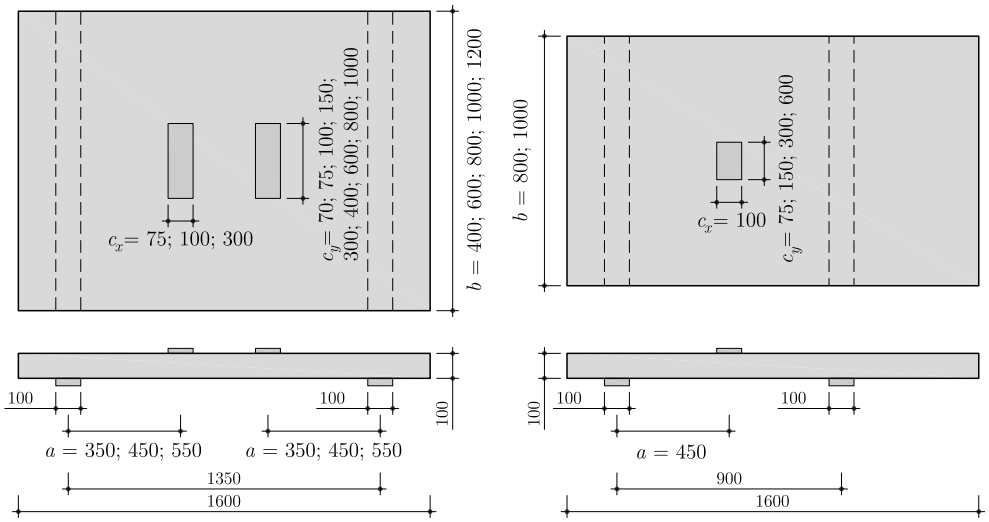

Figure 2.27: Tests on simply supported one-way slabs performed by Regan and Rezai-Jorabi [Reg88] (dimensions in [mm])

In order to study the influence of the load location on one-way slabs, as well as the influence of the transversal reinforcement, Ferreira [Ferr06] performed 12 tests, refer to Figure 2.28. All tests but one were reported to have failed in punching shear. The remaining one failed in flexural punching shear.

Damasceno [Dam07] performed a series of 8 tests on one-way slabs centrally loaded by monolithic rectangular columns. The transverse reinforcement and the column to specimen width ratio (c_y/b) have been varied, refer to Figure 2.29. Three tests are reported to have failed in punching shear, three others in flexural punching shear, and the remaining in flexure.

More recently, Reissen and Hegger [Rei13a] presented a series of 13 tests on one-way slab

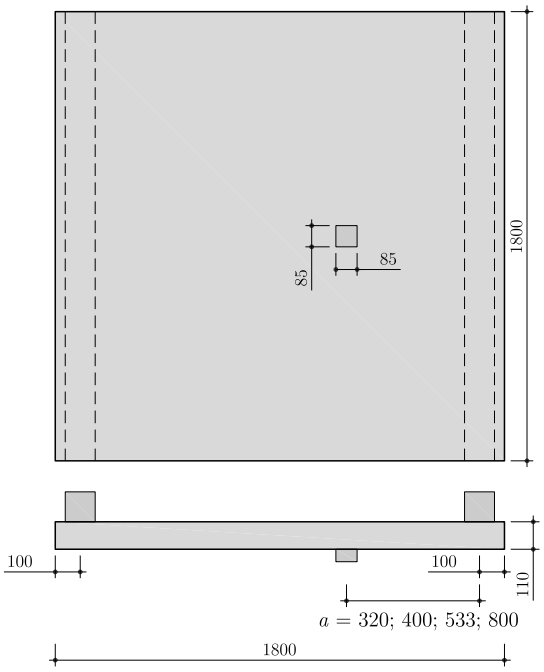

Figure 2.28: Tests on simply supported one-way slabs performed by Ferreira [Ferr06] (dimensions in [mm])

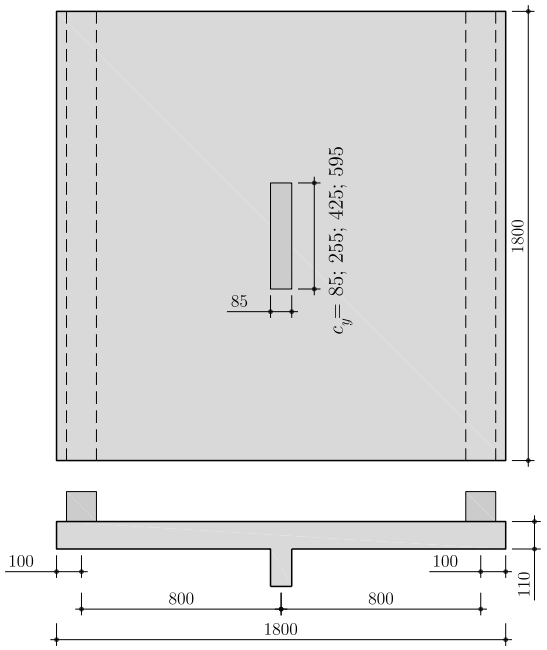

Figure 2.29: Tests on simply supported one-way slabs performed by Damasceno [Dam07] (dimensions in [mm])

strips to study to a greater extent the influence of the loading plate to specimen width ratio (c_y/b) and to a lesser extent the influence of the load location, refer to Figure 2.30. The width of the specimens varied from 500 mm to 3500 mm and the loading plate to specimen width ratio (c_y/b) from 0.11 to 0.80. Some tests failed in shear and others in punching shear.

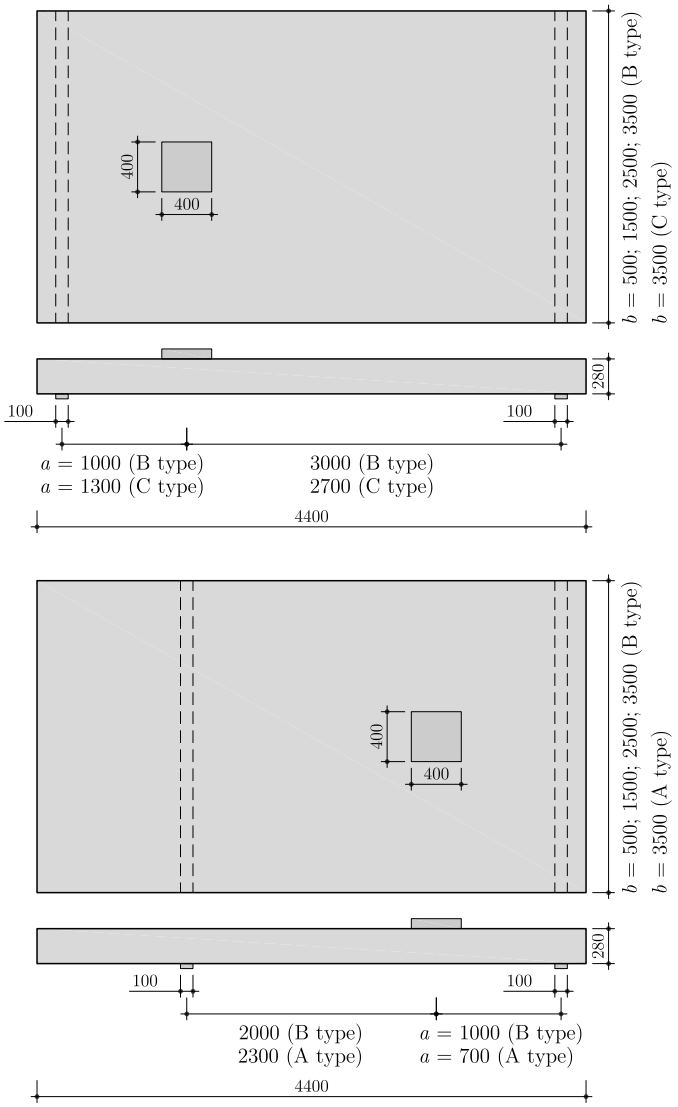

Figure 2.30: Tests on simply supported one-way slabs performed by Reissen and Hegger [Rei13a] (dimensions in [mm])

Many other tests exist in the database compiled by Lantsoght et al. [Lan13b, Lan14a]. However, some of them present extremely small shear spans ($a/d < 2.5$) and are thus suitable to be investigated with stress fields, or they present c_y/b ratios close to 1 and can be practically treated like beams.

2.9 Shear-fatigue of beams without shear reinforcement

Fatigue problems in reinforced concrete elements have traditionally been associated to rupture of the reinforcement bars, normally due to bending actions. Nevertheless, investigations on the fatigue behavior of some members such as bridge deck slabs (Figure 2.31(a)) have shown that shear-fatigue might be governing, particularly for high values of the maximum applied shear force. Shear-fatigue may be also governing for other structures exposed to large cyclic actions, such as wind towers and their foundations or offshore structures, refer to Figures 2.31(b,c). These cases related to structural engineering are usually governed by ratios of the minimum applied shear force to maximum applied shear force close to zero, or can even be subjected to reversal actions.

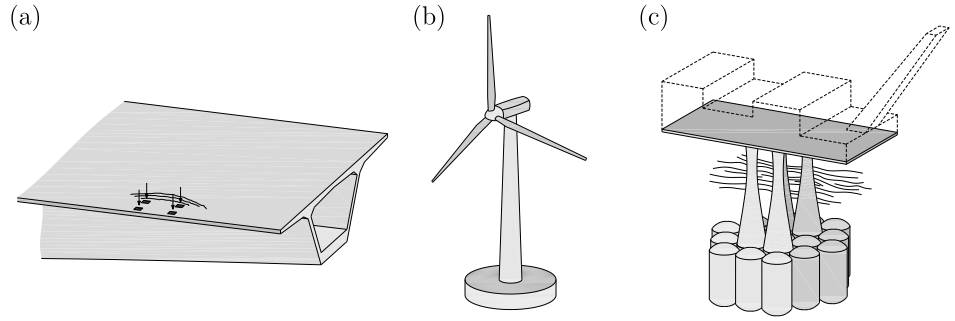

Figure 2.31: Examples of structural elements potentially sensitive to shear-fatigue failures: **(a)** bridge deck slabs; **(b)** wind towers; and **(c)** offshore platforms

In the past, most research on shear-fatigue failures of reinforced concrete members has concentrated on beams tested under three- or four-point bending configuration. An extensive summary on this topic can be found in reference [Gal14b]. These experimental programmes have focused on analysing the influence of parameters like the shear span-to-depth ratio (a/d), the flexural reinforcement ratio ($\rho = A_s/bd$), the concrete strength (f_c) or the influence of the maximum and minimum levels of shear forces ($V_{\max}$, $V_{\min}$). One of the first most comprehensive and systematic testing was carried out by Chang and Kesler [Cha58a, Cha58b] in the fifties. They tested 64 beams under fatigue loading with a constant value of shear slenderness ($a/d = 3.72$) and three different flexural reinforcement ratios ($\rho = 0.0102$, 0.0186 and 0.0289). According to their experimental results, Chang and Kesler identified two potential shear-fatigue failure modes (refer to Figure 2.32): shear-compression failure and diagonal cracking failure. Both were due to the development and propagation with the number of cycles of an eventually critical shear crack. In the former failure mode, the propagation of the crack limits the depth and strength of the compression zone near the load, which eventually crushes. In the latter, the critical shear crack propagates in an unstable manner leading to a sudden collapse of the member.

Stelson and Cernica [Ste58] tested 11 specimens with $\rho = 0.0290$ and similar cross section than those of Chang and Kesler, but higher shear slenderness ($a/d = 5.65$). Four specimens presented shear-fatigue failures by diagonal cracking at a very similar number

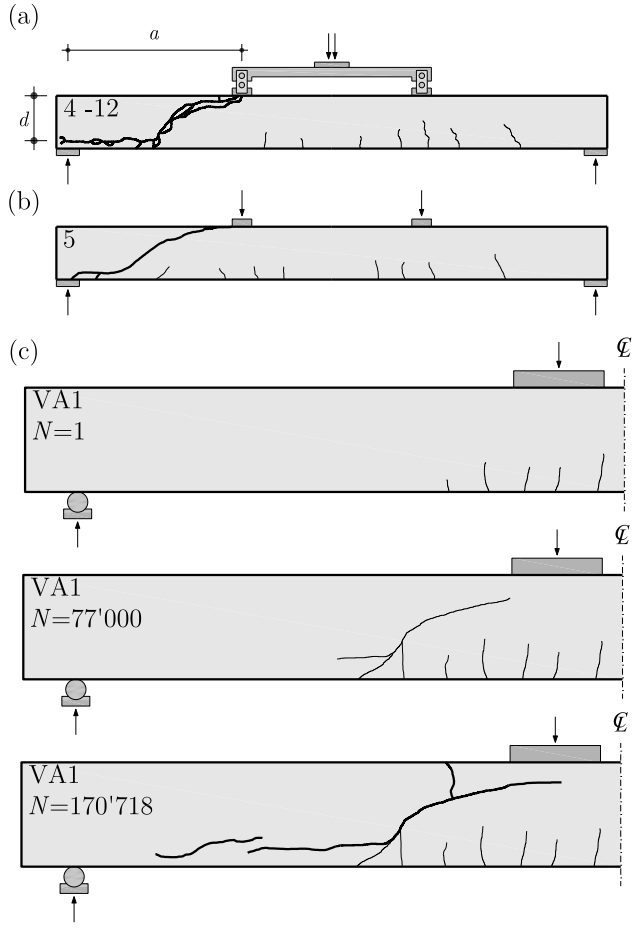

Figure 2.32: Failure modes by Chang and Kesler [Cha58a,Cha58b]: **(a)** shear-compression failure; **(b)** diagonal cracking failure; and **(c)** Zanuy [Zan08]: cracking evolution and shear-compression failure

of load cycles to the corresponding series of Chang and Kesler.

Verna and Stelson [Ver62] carried out 60 fatigue tests in reinforced concrete beams without stirrups. They focused on the description of fatigue failure and identified the following failure modes: shear-fatigue, fatigue of the reinforcement, fatigue of concrete in compression and fatigue of the anchorage. The latter failure mode was related to the propagation of a diagonal crack towards the support and at the level of the longitudinal reinforcement, similar to the delamination cracks due to dowel action [Mut08a]. Taylor [Tay59] investigated the influence of the type of reinforcement, by testing specimens with plain and ribbed bars with a constant value of the shear slenderness ($a/d = 4.1$) and for different amounts of flexural reinforcement. The results showed very similar fatigue strength of specimens with different reinforcement, even though the bond properties of reinforcement are known to play a significant role in the actions involved in resisting shear force [Mut08a].

Shear-fatigue tests carried out in Japan in late seventies focused on the influence of the shear slenderness and the load levels. Higai [Hig78] and Farghaly [Far79] tested reinforced concrete beams with shear slenderness ranging from 1.5 to 6.4. Their results showed that the diagonal crack developed in the first cycle for the shortest specimens, but the residual fatigue life after diagonal cracking was much larger than specimens with higher shear slenderness. Moreover, a higher sensitivity to diagonal cracking failure than to shear-compression was observed as the shear slenderness increased.

The influence of the ratio between the minimum and the maximum shear load ($R = V_{\min}/V_{\max}$) was investigated by Ueda [Ued82]. His tests showed that elements subjected to higher values of parameter R had higher fatigue life than elements tested with lower R values.

Rombach and Kohl [Rom12, Rom13] have recently tested 7 reinforced concrete beams with $a/d = 5.0$ and $\rho = 0.0157$, obtaining shear-fatigue failures (by shear-compression) in the beams where the maximum load exceeded 60% of static strength.

Other experimental works on lightly and normally reinforced beams (ρ varying from 0.0052 to 0.0160) [Sch98, Joh04] only presented some cases of shear-fatigue failures after rebar fractures, being fatigue of the reinforcement the most common failure mode.

A number of tests including shear-fatigue failures was also carried out by other researchers that focused on details like the shape of the section [Fre83, Mar84], the influence of large member size [Ten84] or the effect of high strength concrete [Kwa01].

Despite the significant efforts devoted to experimental programmes, most codes of practice still ground their provisions on empirical formulas [EC2-1, MC2010, SIA262:2013].

With respect to the previous experimental campaigns, it can be noted that shear-fatigue failures are due to the development and growth of an eventually critical shear crack, leading to the loss of the beam shear-transfer actions strength [Hig78]. Such failures are associated to members with moderate-to-high slenderness, where the shear strength depends on size and strain effects (governing the width of the critical shear crack [Mut08a]). However, for low slender members, arching action is prevalent, which seems to be less prone to failures under shear-fatigue (refer to [Hig78], Figure 2.33). Shear failures in

these cases are associated to the crushing of the compression strut carrying shear, which is sensitive to strain effects (transverse strains) but where size effect (localization of strains on a single crack) plays a more limited role [Zha07]. This fact has recently been accounted for by Gallego et al. [Gal14a] (Section 3.8), who proposed a consistent approach for shear-fatigue design of slender reinforced concrete members, including for the development and growth of a critical shear crack based on fracture mechanics applied to quasi-brittle materials. This approach has shown to lead to consistent and accurate estimates of the fatigue shear strength (number of cycles leading to failure) and failure modes. Its application for practical purposes remains yet complex.

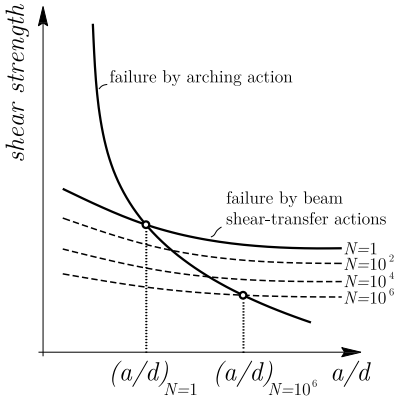

Figure 2.33: Influence of fatigue loading on the shear strength of compact members (governed by arching action) and slender members (governed by beam shear-transfer actions) [Hig78]

2.10 Shear-fatigue of slabs subjected to concentrated loads

As it was previously seen (Sections 2.6 and 2.7) and observed in this thesis (Chapters 4 and 5), shear is the most common governing failure mode of reinforced concrete cantilever slabs subjected to concentrated loads, under a quasi-static application of the load.
The concentrated loads resulting from heavy vehicles have a repetitive nature and may cause potential stiffness and strength reductions due to fatigue effects [CEB88]. Fatigue failure modes are the same as the static ones and can be due to rebar fracture and/or failure of concrete.
However, it should be noted that the results obtained for beams and one-way slabs (Figure 2.34(a)) are not directly applicable to cantilever slabs subjected to concentrated loads (Figure 2.34(d)), as beams do not exhibit a two-way action (Section 2.6).
With respect to fatigue testing of reinforced concrete slabs without shear reinforcement under concentrated loads, previous research has mainly focused on simply supported or inner slabs [Saw71, Haw76, Bat78, Oka78, Son82, Per88, Per89, You98, Tou01, Gra02, Hwa10] supported on two or four edges, refer to Figures 2.34(b,c). Table 2.1 presents some geometric properties of available experimental evidence. With respect to typical deck slabs of concrete bridges, it can be observed that several specimens have rela-

tively low thicknesses (< 100 mm) and others have low reinforcement ratios ρ ($\leqslant 0.2\%$, including specimens even with no flexural reinforcement) or fairly large ones ($> 1.5\%$). To the author's knowledge, no tests are available on cantilever deck slabs (Figure 2.34(d)), whose mechanical behavior may significantly differ from simply supported slabs (Section 2.6).

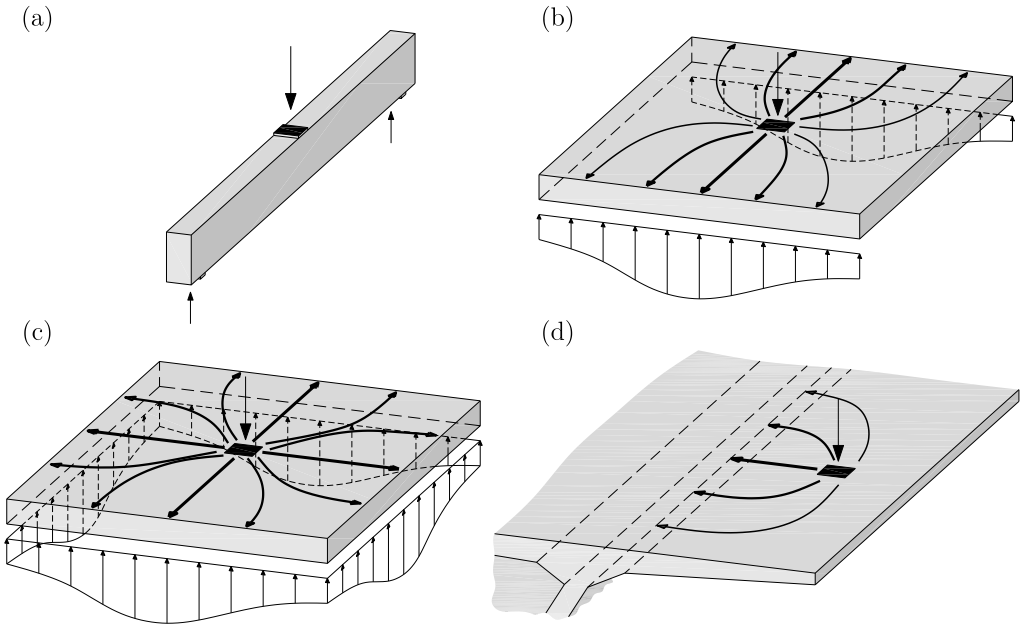

Figure 2.34: Structural reinforced concrete members failing in fatigue shear loading: **(a)** simply supported beam; **(b)** slab supported on two edges; **(c)** slab supported on four edges; and **(d)** cantilever slab

tests	ρ[%]	thickness [mm]	supports	spans [cm]	widths [cm]	type*
Sawko & Saha [Saw71]	-	38	two edges	229-152-114	152	PC
Sawko & Saha [Saw71]	1.7	76	two edges	114	152	RC
Hawkins [Haw76]	1.3	127	two edges	122	127	RC
Batchelor, Hewitt & Csagoly[Bat78]	0.0-0.2-0.4-0.6	22-18-12	two edges	30	305	RC
Okada, Okamura & Sonoda [Oka78]	1.1-1.3	170-180	four edges	235-360	-	RC
Sonoda & Horikawa [Son82]	1.3	60	four edges	80-250	-	RC
Perdikaris & Beim [Per88]	0.0-0.3-0.7	32	two edges	32	230	RC
Perdikaris, Beim & Bousias [Per89]	0.0-0.3-0.4-0.7	72	two edges	71	170	RC
Youn & Chang [You98]	1.0	60	two edges	70	210	RC
Toutlemonde & Ranc [Tou01]	1.2	180	two edges	250	500	RC
Graddy et al. [Gra02]	3.2	191	two edges	183	213	RC
Hwang et al. [Hwa10]	-	115	two edges	270	430	PC

* RC - reinforced concrete; PC - prestressed concrete

Table 2.1: Properties of slabs tested under concentrated fatigue loads

Chapter 3

Shear, punching shear and shear-fatigue modeling

3.1 Introduction

The present chapter aims to present mechanical models suitable to model shear, punching shear and shear-fatigue behavior of reinforced concrete members without shear reinforcement.
The chapter is organized as follows:

- Section 3.2 presents the Critical Shear Crack Theory (CSCT) for one-way shear and Section 3.3 the shear formulations of some design codes used in Europe;
- Section 3.4 and Section 3.5 present the CSCT for both axis-symmetric and non-axis-symmetric punching shear, respectively;
- The basics of linear elastic fracture mechanics are presented in Section 3.6 for both monotonic and fatigue loading. These concepts form the basis of nonlinear fracture mechanics applied to quasi-brittle materials presented in Section 3.7;
- Section 3.8 presents the mechanical model of Gallego et al. [Gal14a] to model shear-fatigue failures of beams without shear reinforcement.

3.2 The Critical Shear Crack Theory (CSCT) for shear

The CSCT was firstly presented by Muttoni and Schwartz [Mut91], and it is suitable to analyze slender reinforced concrete beams without shear reinforcement situated on the right-side of Kani's valley (Section 2.2).
According to this theory [Mut08a], the shear strength V_R depends on the member geometry (width b and effective flexural depth d), the square root of the concrete compressive strength $\sqrt{f_c}$ [Moo54], the critical shear crack width w_{cr} and its roughness (characterized by the maximum aggregate size d_g):

$$\frac{V_R}{bd} = \sqrt{f_c} f(w_{cr}, d_g) \tag{3.1}$$

Even though shear is a two-dimensional problem, sectional analysis are preferred by engineers. The CSCT assumes [Mut08a] that the shear strength is governed by a section (depending on the load configuration) where the width of the critical shear crack can be adequately represented by the strain at a depth of $0.6d$ from the compression face (Figure 3.1(a)), and that the critical crack width w_{cr} is proportional to the product of the longitudinal strain in the control depth ε times the effective flexural depth d:

$$w_{cr} \propto \varepsilon d \tag{3.2}$$

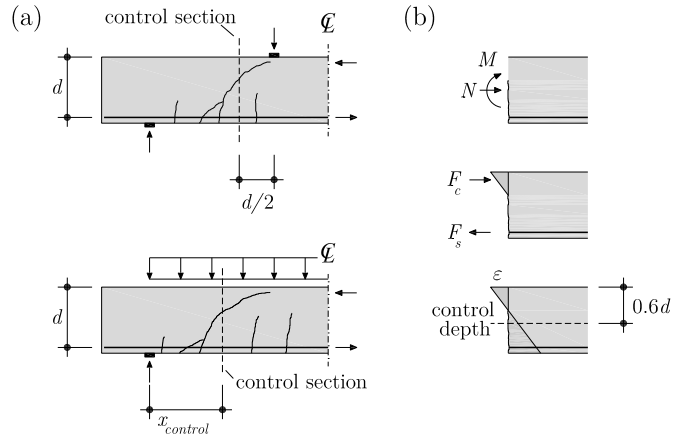

Figure 3.1: CSCT for reinforced concrete beams without shear reinforcement: **(a)** control section for point loading and distributed loading; and **(b)** determination of longitudinal strain in control depth using internal forces N and M [Mut08a]

The longitudinal strain ε is evaluated in the control section assuming that plane sections remain plane and a linear-elastic behavior of concrete in compression (neglecting its tensile strength), refer to Figure 3.1(b).
Assuming that no axial force is applied, the strain in the control depth is given by:

$$\varepsilon = \frac{M}{bd\rho E_s(d - c/3)} \frac{0.6d - c}{d - c} \tag{3.3}$$

and the depth of the compression zone c is:

$$c = d\rho \frac{E_s}{E_c} \left(\sqrt{1 + \frac{2E_c}{\rho E_s}} - 1 \right) \tag{3.4}$$

where M is the applied bending moment, ρ is the flexural reinforcement ratio, E_c is the Young's modulus of concrete and E_s is the Young's modulus of steel.
Equation 3.3 is only valid for a rectangular cross section without skin reinforcement on the side faces.
The CSCT proposes the following failure criterion [Mut08a]:

$$\frac{V_R}{bd\sqrt{f_c}} = \frac{1}{3} \frac{1}{1 + 120 \frac{\varepsilon d}{16 + d_g}} \quad \text{[MPa, mm]} \tag{3.5}$$

The shear strength is obtained by substituting Equation 3.3 in Equation 3.5 and solving the resulting quadratic equation. For high-strength concrete ($f_c > 60$ MPa) or light-weight concrete, d_g should be taken as zero, because the cracking surface develops through the aggregates.
The CSCT presents good agreement with tests results, as it is shown by Muttoni and Fernández Ruiz [Mut08a] with a database of 285 tests.

3.3 Code provisions on shear of beams without shear reinforcement

This section presents the shear formulations of some codes of practice for rectangular beams without shear and skin reinforcement.

3.3.1 *fib*-Model Code 2010

The shear strength formulation according to *fib*-Model Code 2010 [MC2010] is based on the Simplified Modified Compression Field Theory [Ben06, Sig13]. The shear strength ($V_{R,c}$) is given by:

$$V_{R,c} = k_v \sqrt{f_c} z b_w \quad [f_c \text{ in MPa}] \tag{3.6}$$

where the effective shear depth z can be taken as $0.9d$ (being d the effective flexural depth), b_w is the member width, f_c is the concrete compressive strength and $\sqrt{f_c}$ shall not be taken as greater than 8 MPa.
For a Level II approximation [Mut12], k_v is determined by:

$$k_v = \frac{0.4}{1 + 1500\varepsilon_x} \frac{1300}{1000 + k_{dg} z} \quad z \text{ in [mm]} \tag{3.7}$$

Parameter k_{dg} can be determined as:

$$k_{dg} = \frac{32}{16 + d_g} \geq 0.75 \quad d_g \text{ in [mm]} \tag{3.8}$$

For concrete compressive strengths larger than 70 MPa and light-weight concrete d_g shall be taken as zero in order to account for the loss of aggregate interlock in the cracks due to fracture of aggregates.
If no axial force is applied, the strain ε_x at the mid-depth of the effective shear depth in the control section is given by:

$$\varepsilon_x = \frac{1}{2E_s A_s} \left(\frac{M_E}{z} + V_E \right) \tag{3.9}$$

where E_s is the reinforcement modulus of elasticity, A_s is the tensile reinforcement area, and M_E and V_E the applied bending moment and shear force, respectively.

One may determine the static shear strength by substituting Equation 3.9 into Equation 3.7 and then Equation 3.6.
The control section for three or four-point bending tests on beams is located at d from the point load.

3.3.2 Eurocode 2

The shear strength formulation according to Eurocode 2 [EC2-1] was empirically calibrated with experimental data through a statistical approach. No mechanical model grounds Eurocode 2 formulation. The shear strength ($V_{R,c}$ in [N]) is given by:

$$V_{R,c} = 0.18k(100\rho_l f_c)^{1/3} b_w d \geq 0.035 k^{3/2} f_c^{1/2} b_w d \tag{3.10}$$

where f_c is the concrete compressive strength (in MPa), b_w is the member width (in mm), d is the effective flexural depth (in mm), and ρ_l is the reinforcement ratio (that shall not be taken larger than 0.02). Parameter k can be determined as:

$$k = 1 + \sqrt{\frac{200}{d}} \leq 2 \quad d \text{ in [mm]} \tag{3.11}$$

3.3.3 SIA262:2013

The Swiss code [SIA262:2013] shear formulation is based on the CSCT [Mut08a] (Section 3.2). The shear strength (v_R) is given by:

$$v_R = k_d \tau_c d_v \tag{3.12}$$

$$\tau_c = 0.3\sqrt{f_c} \tag{3.13}$$

$$k_d = \frac{1}{1 + \varepsilon_v d k_g} \quad d \text{ in [mm]} \tag{3.14}$$

$$k_g = \frac{48}{16 + D_{\max}} \quad D_{\max} \text{ in [mm]} \tag{3.15}$$

where d_v is usually equal to the effective flexural depth d, f_c is the concrete compressive strength and $D_{\max}$ is the maximum aggregate size. For concrete compressive strengths larger than 70 MPa and light-weight concrete $D_{\max}$ shall be taken as zero in order to account for the loss of aggregate interlock in the cracks due to fracture of aggregates.
If the main flexural reinforcement remains in the elastic domain, the specific deformation ε_v can be calculated as:

$$\varepsilon_v = \frac{f_s}{E_s} \frac{m}{m_R} \tag{3.16}$$

where f_s represents the yielding stress of the rebar steel, E_s is the reinforcement modulus of elasticity, m is the acting moment in the control section and m_R is the yielding moment. Assuming a plastic behavior of the reinforcement after yielding, a rectangular stress diagram in the concrete compression zone and neglecting the compressive reinforcement contribution, the yielding moment can be calculated as:

$$m_R = \rho f_s b d^2 \left(1 - \frac{\rho f_s}{2 f_c}\right) \tag{3.17}$$

where ρ is the reinforcement ratio and b the beam width.
If the reinforcement enters the plastic domain, ε_v is given by:

$$\varepsilon_v = 1.5 \frac{f_s}{E_s} \tag{3.18}$$

The control section for three or four-point bending tests on beams is located at $d_v/2$ from the point load.

3.4 The Critical Shear Crack Theory (CSCT) for axis-symmetric punching shear

Muttoni and Schwartz [Mut91] observed that the width of the critical shear crack w_{cr} that reduces the strength of the compression strut carrying shear (Section 2.4) can be assumed to be proportional to the product between the slab rotation ψ and the effective flexural depth d (Figure 3.2).

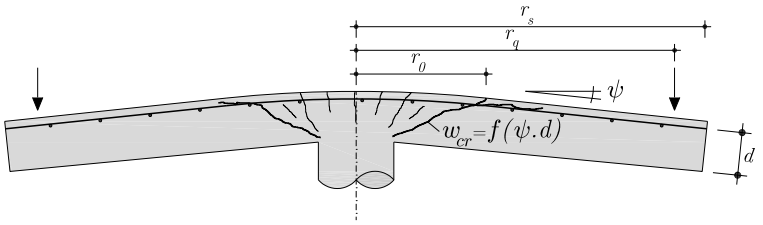

Figure 3.2: Correlation between the opening of the critical shear crack, slab thickness and rotation [Mut08b]

Muttoni [Mut08b] proposed the following failure criterion for punching shear:

$$\frac{V_R}{b_0 d \sqrt{f_c}} = \frac{3/4}{1 + 15 \frac{\psi d}{16 + d_g}} \quad \text{[MPa, mm]} \tag{3.19}$$

where b_0 is the control perimeter located at $d/2$ from the face of the column, $\sqrt{f_c}$ is the square root the concrete compressive strength and d_g is the maximum aggregate size.
The load-rotation relationship of the slab is needed to determine its punching shear strength, given by the intersection between the failure criterion and the load-rotation relationship (Figure 3.3). The axis-symmetric case of an isolated slab can be treated analytically after some simplifications [Mut08b]. For practical purposes Muttoni [Mut08b]

proposes the following simplified load-rotation relationship (refer to Figure 3.3):

$$\psi = 1.5 \frac{r_s}{d} \frac{f_y}{E_s} \left(\frac{V}{V_{flex}} \right)^{3/2} \tag{3.20}$$

where V_{flex} represents the flexural strength of the slab.

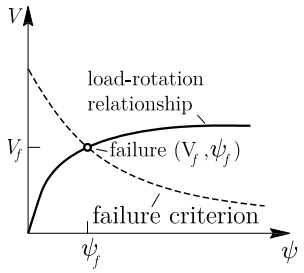

Figure 3.3: Punching strength given by the intersection between the failure criterion and the load-rotation relationship

The CSCT presents good agreement with test results, as it is shown by Muttoni [Mut08b] with a database of 99 tests.

3.5 The Critical Shear Crack Theory (CSCT) for non-axis-symmetric punching shear

Based on the shear field representation (Section 2.5), in order to account for non-uniform distribution of shear forces along the control perimeter, Vaz Rodrigues et al. [Vaz08] have proposed to reduce the control perimeter as follows:

$$b_{0,el} = \frac{V}{v_{el,perp,\max}} \tag{3.21}$$

where V is the applied shear force and $v_{el,perp,\max}$ is the maximum perpendicular unitary shear force acting in the control perimeter, given by a linear elastic finite element analysis with shell elements, refer to Figure 3.4.
This approach is equivalent to the one considering a constant shear force of $v_{el,perp,\max}$ along the reduced control perimeter $b_{0,el}$. Using this reduced control perimeter $b_{0,el}$ to calculate the punching shear strength for a given failure criterion corresponds to consider that failure occurs when the maximum applied unitary shear force at one point of the control perimeter reaches the unitary punching shear strength. As $b_{0,el}$ is calculated with linear elastic finite element analysis, no redistributions due to bending cracking or reinforcement yielding are considered.
Vaz Rodrigues [Vaz07] has used Muttoni's [Mut08b] punching shear failure criterion (Equation 3.19) combined with nonlinear finite element analysis to account for bending cracking and reinforcement yielding. By establishing the load-rotation relationship between two points (one placed in the center of the punching loads or columns, and the

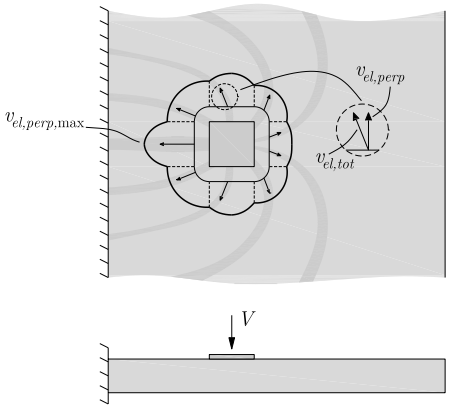

Figure 3.4: Shear forces perpendicular to the control perimeter

other placed in the slab in order to get approximately the maximal relative rotation), Vaz Rodrigues was able to calculate the unitary punching shear strength as a function of the applied load. With increasing load levels, at a certain point the applied unitary shear force perpendicular to the control perimeter reaches the unitary punching shear strength and failure occurs. This corresponds to assuming that failure is governed by the maximal crack width along the control perimeter, not allowing shear redistributions due to shear cracking. The same procedure can be performed with other load-rotation relationships (e.g. Equation 3.20 for internal columns in axis-symmetric conditions) and using the same reduced elastic control perimeter $b_{0,el}$ (Equation 3.21). Considering the maximum crack width (dependent of the maximum rotation $\psi_{\max}$) as the governing parameter for punching shear strength is known as the CSCT($\psi_{\max}$) method [Sag11].

Sagaseta et al. [Sag11] presented a new approach to account for shear redistributions along the control perimeter for non-axis-symmetrical punching shear around internal columns. Due to the non-axis-symmetric conditions, the slab rotations depend on the considered direction and are uneven along the control perimeter, meaning that some parts of the slab reach their ultimate strength while others still have a potential strength capacity. However this does not imply the slab collapse, as the areas which reached its strength can develop a softening process (side A of Figure 3.5) while others continue increasing its shear force (side B of Figure 3.5, assuming that shear forces along each side of the control perimeter are roughly constant [Sag11]). This redistribution results in higher punching shear strengths and rotations when compared with the CSCT($\psi_{\max}$) method, provided that the shear increase in side B (Figure 3.5) balances the shear softening in A.

Based on these considerations Sagaseta et al. [Sag11] have presented the so-called CSCT (ψ_x-ψ_y) method (Figure 3.6). Dividing the control perimeter into four segments (Figure 3.6(a)) and assuming constant rotations ψ_x-ψ_y and unitary strengths $v_{R,x}$-$v_{R,y}$ for each segment, the punching shear strength V_R is given by:

$$V_R = v_{R,x} b_x + v_{R,y} b_y = \frac{V_{R,x}}{b_0} b_x + \frac{V_{R,y}}{b_0} b_y \tag{3.22}$$

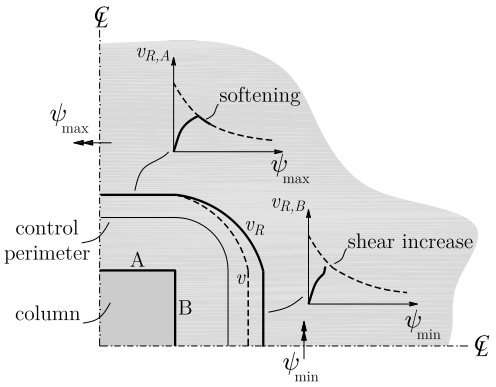

Figure 3.5: Shear stress redistributions along the control perimeter [Sag11]

where $v_{R,x}$ and $v_{R,y}$ are calculated according to Muttoni's failure criterion (Equation 3.19) with the ψ_x-ψ_y rotations, $V_{R,x}$ and $V_{R,y}$ represent the strength of segments b_x-b_y (Figure 3.6(a)), and $b_0 = b_x + b_y$. Lengths b_x-b_y are generally taken as $b_0/2$ in square columns ($\theta_{limit} = 45°$, Figure 3.6(a)). However reduced lengths of b_x-b_y are recommended to be taken ($\theta_{limit} = 90°$) for punching loads close to the flexural loads [Sag11], as wide crack openings may limit the redistribution capacity of the slab.

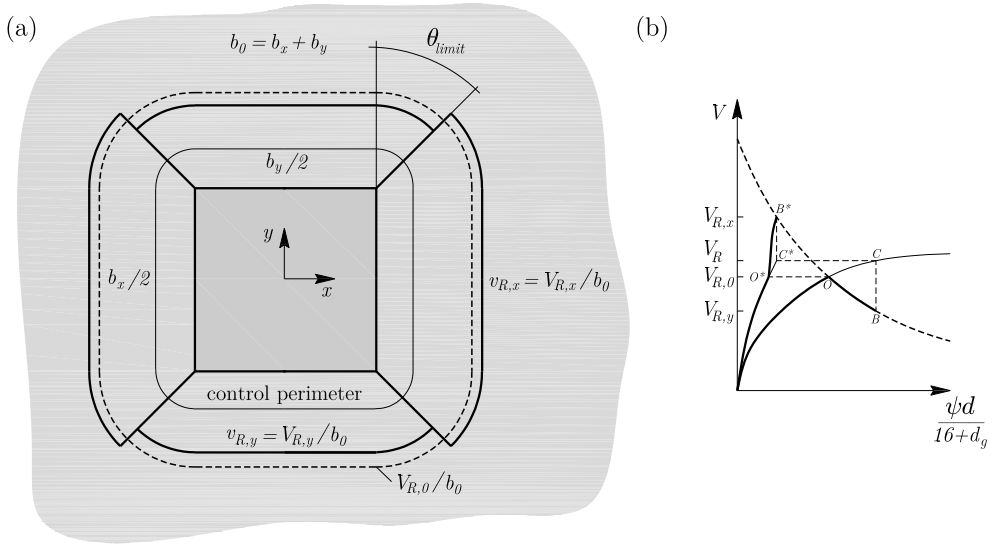

Figure 3.6: Shear redistributions according to CSCT(ψ_x-ψ_y) method: **(a)** discretisation of control perimeter and distribution of unitary shear strength; and **(b)** redistribution process [Sag11]

The redistribution process can be seen in Figure 3.6(b) according to the CSCT(ψ_x-ψ_y) method. Point O corresponds to the punching shear strength $V_{R,0}$ of the CSCT($\psi_{\max}$) method, point B to the force component in the segment b_y after redistribution, and point C to the predicted punching shear strength V_R and maximum rotation. The redistribution process ends when the shear force being redistributed from segment b_y to b_x reaches the failure criterion in the x direction.

The work developed by Sagaseta et al. [Sag11] for square columns has also been extended for flat slabs supported on rectangular columns [Sag14].

3.6 Linear elastic fracture mechanics

The present section aims at providing the basics of Linear Elastic Fracture Mechanics (LEFM), and its content is based on the book of Wang [Wan96]: *Introduction to Fracture Mechanics*.

3.6.1 Linear elastic materials

Wang [Wan96] defines Fracture Mechanics (FM) as a set of theories that describe the behavior of solids or structures with geometrical discontinuities at the scale of the structure, as notches or cracks.
A notch can be defined as a geometric discontinuity which has a definite depth (D) and root radius (ρ), and a crack can be seen as a notch with a root radius $\rho \to 0$. Let us consider the plate of Figure 3.7 containing a notch and uniaxially loaded (stress σ). The linear elastic analysis of this plate (analytically, numerically or experimentally) allows to study the severity of the notch, *i.e.*, how disturbed the stress field is in the vicinity of the notch compared with the uniform distribution. The maximum applied stress $\sigma_{\max}$ is related with the nominal stress σ_N by the stress concentration factor K_T, which can be approximated for elliptical notch shapes as follows:

$$K_T = \frac{\sigma_{\max}}{\sigma_N} = 1 + 2\sqrt{\frac{D}{\rho}} \tag{3.23}$$

When $\rho \to 0$, $K_T \to \infty$, and as a result $\sigma_{\max} \to \infty$. The stress concentration factor is thus not suitable to distinguish between different crack lengths and applied stress levels.

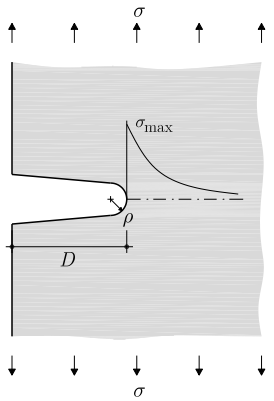

Figure 3.7: Notch on uniaxially loaded plate [Wan96]

The basic concept proposed by Griffith [Gri21] in 1921 to formulate the linear elastic theory of crack propagation is the following: whether a stressed cracked body remains stable or becomes unstable is dependent on whether the cracked body contains sufficient

energy to afford creating additional surface maintaining equilibrium. Let us consider the stressed cracked thin plate with a crack length of $2a$ and thickness B of Figure 3.8.

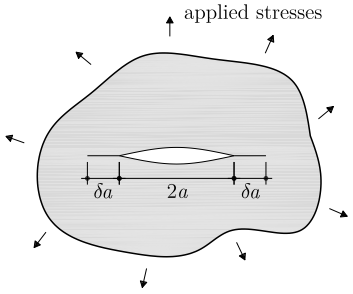

Figure 3.8: Stressed cracked plate [Wan96]

According to the law of conservation of energy the work performed per unit time by the applied loads $\dot{W}$ must be equal to the rates of change of the internal elastic energy $\dot{U}_E$, plastic energy $\dot{U}_P$ and kinetic energy $\dot{K}$ of the body, and the energy per unit time $\dot{\Gamma}$ spent in increasing the crack area:

$$\dot{W} = \dot{U}_E + \dot{U}_P + \dot{K} + \dot{\Gamma} \tag{3.24}$$

Assuming a slow crack growth, the kinetic energy can be neglected ($K = \dot{K} = 0$). Since all changes with respect to time are caused by changes in crack size, the differential operator with respect to time $\delta/\delta t$ can be given by:

$$\frac{\delta}{\delta t} = \frac{\delta}{\delta A}\frac{\delta A}{\delta t} = \dot{A}\frac{\delta}{\delta A} \tag{3.25}$$

where $A = 2aB$ represents the crack area. However the total crack surface area is twice the crack area. Therefore Equation 3.24 can be rewritten as:

$$-\frac{\delta \Pi}{\delta A} = \frac{\delta U_P}{\delta A} + \frac{\delta \Gamma}{\delta A} \tag{3.26}$$

where

$$\Pi = U_E - W \tag{3.27}$$

represents the potential energy of the system. Equation 3.26 shows that the reduction of the potential energy is equal to the energy dissipated in plastic work and surface creation.
For an ideally brittle material $U_P = 0$, *i.e.*, the dissipated energy in plastic energy is negligible. The law of conservation of energy of Equation 3.26 can once again be rewritten as

$$-\frac{\delta \Pi}{\delta A} = \frac{\delta \Gamma}{\delta A} = 2\gamma \tag{3.28}$$

where γ represents the energy required to form unit new material surface (material

property) and factor 2 to the two new material surfaces formed during crack growth. Equation 3.28 obliges that sufficient available potential energy is available in the system to overcome the surface energy of the material in order to have crack growth. A crack-extension force G can be defined as

$$G = -\frac{\delta \Pi}{\delta A} \tag{3.29}$$

The total energy of the system can be defined as:

$$U_{total} = (-W + U_E) + \Gamma \tag{3.30}$$

According to Clapeyron's theorem of linear elastostatics that states that the potential energy of deformation of a body, which is in equilibrium under a given load, is equal to half the work done by the external forces, and assuming these forces remained constant from the initial state to the final state, we have:

$$W = 2U_E \tag{3.31}$$

The crack-extension force can be rewritten as:

$$G = \frac{\delta U_E}{\delta A} \tag{3.32}$$

and the total energy of the system:

$$U_{total} = -U_E + \Gamma \tag{3.33}$$

Griffith [Gri21] applied the stress solutions of Inglis [Ing13] to show that the increase in strain energy due to the elliptic cavity (zero radius) in an infinite plane of thickness B is given by:

$$U_E = \frac{\pi a^2 \sigma^2 B}{E} \tag{3.34}$$

where E is Young's modulus of the material. The energy spent increasing the crack area is given by:

$$\Gamma = 4aB\gamma \tag{3.35}$$

Thus, the total system energy of the thin plate becomes

$$U_{total} = -\frac{\pi a^2 \sigma^2 B}{E} + 4aB\gamma \tag{3.36}$$

which exhibits a maximum at the following crack length:

$$a_c = \frac{2\gamma E}{\pi \sigma^2} \tag{3.37}$$

meaning that the critical crack length below which the crack would remain stable de-

creases with the applied stress. Alternatively, the critical stress level that the plate can sustain for a given crack length a is

$$\sigma_c = \sqrt{\frac{2E\gamma}{\pi a}} \tag{3.38}$$

All the presented equations are only valid for linear elastic materials.
The energy release rate G characterises the amount of energy released if the crack advances a unit length. When this value is greater than the surface energy of the material the crack can grow, otherwise no crack propagation is possible.
The energy release rate G can be determined from experimental tests. Figure 3.9(a) presents a cracked specimen made of a linear elastic material subjected to a load P and/or a displacement u. When the crack length is a, the specimen is less compliant than when the crack length is $a + \delta a$. The compliance C of the specimen (geometry dependent) is given by:

$$C = \frac{u}{P} \tag{3.39}$$

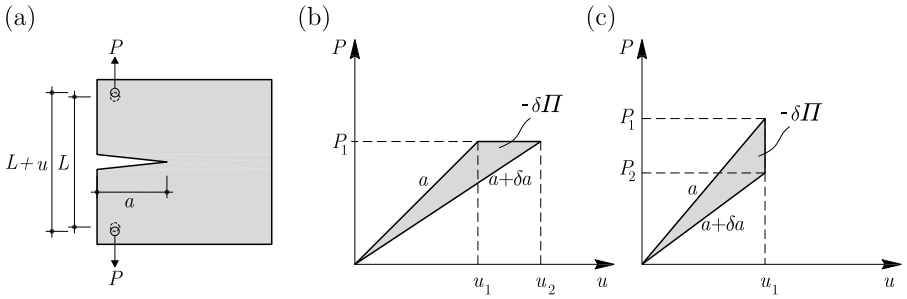

Figure 3.9: Edge stressed cracked plate and load displacement characteristics [Wan96]: **(a)** geometry; **(b)** constant load crack extension; and **(c)** crack extension under constant displacement

If we consider a test performed at constant load conditions (Figure 3.9(b)), an increase of crack length of δa results in a potential energy change of $\delta\Pi$ (difference between the external work and the stored but recoverable elastic strain energy). The increase of elastic strain energy δU_E is given by:

$$\delta U_E = \frac{1}{2}P_1 u_2 - \frac{1}{2}P_1 u_1 \tag{3.40}$$

and the work performed by the load P in the distance $(u_2 - u_1)$ as:

$$\delta W = P_1(u_2 - u_1) \tag{3.41}$$

The energy spent in increasing crack surfaces is given by:

$$-\delta\Pi = \delta W - \delta U_E = P_1(u_2 - u_1) - \frac{1}{2}P_1(u_2 - u_1) = \frac{1}{2}P_1(u_2 - u_1) = \frac{1}{2}P_1\delta u \tag{3.42}$$

which means that the energy spent in crack development was supplied by the work of the external load.

In a similar way, if we consider a test performed at constant displacement conditions (Figure 3.9(c)), an increase in crack length causes a decrease in the stored elastic strain energy of:

$$\delta U_E = \frac{1}{2}(P_1 - P_2)u_1 = \frac{1}{2}u_1\delta P \tag{3.43}$$

which is spent in increasing crack surface since no external work is done.

When an increase in crack area δA tends to zero, the compliance C is the same for both constant load and constant displacement conditions, which means that the difference between the energy spent in crack growth in both cases tends to zero:

$$\frac{1}{2}P_1\delta u = \frac{1}{2}u_1\delta P \Leftrightarrow \delta u = \frac{u}{P}\delta P = C\delta P \tag{3.44}$$

and the energy release for both cases is given by:

$$G = \frac{1}{2}CP\delta P \tag{3.45}$$

The strain or potential energy release rate with respect to crack length for small crack area increases $\delta A = B\delta a$ can be found experimentally in a plate of uniform thickness B as:

$$G = \frac{1}{2}P\frac{\delta u}{\delta A} = \frac{P^2}{2}\frac{\delta C}{\delta A} \tag{3.46}$$

G can be determined by means of measurements of the compliance of a specimen with different crack lengths.

There are three different stressing modes of a crack. The opening mode or mode I (Figure 3.10(a)) corresponds to normal separation of crack surfaces under tensile stresses. The sliding mode or mode II corresponds to a crack propagation normal to the crack front under shear stresses. Finally, the tearing mode or mode III corresponds to a crack propagation parallel to the crack front, also when subjected to shear stresses. A stressed body can experience one or a combination of these modes.

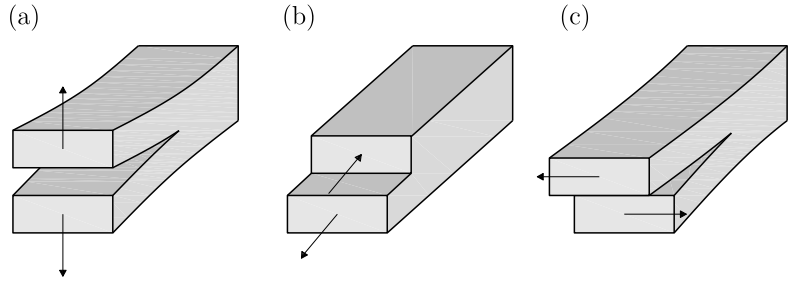

Figure 3.10: Stressing modes of a crack [Wan96]: **(a)** opening mode or mode I; **(b)** sliding mode or mode II; and **(c)** tearing mode or mode III

The stress, strain and displacement fields of a cracked linear elastic body can be calculated analytically by using the Westergaard method [Wes39], for example. Solving this problem yields these fields in the vicinity of a crack as a linear proportional function of the stress intensity factors K, which embody the loading and geometry conditions. The stress intensity factors and the searched fields can be found in many handbooks. In general the stress intensity factor depends on the applied stress, crack size and geometry:

$$K = Y\sigma\sqrt{\pi a} \tag{3.47}$$

where Y is the so-called geometry factor, dependent of the body and crack geometries. For a center crack in an infinite plate, $Y = 1$. Y can be found in many handbooks for various practical situations, but in general, Y can be obtained from linear elastic finite element analysis.

As the stress and displacement fields are linearly proportional to the stress intensity factor, the superposition principle is applicable in LEFM.

Let us now recall Griffith's energy concept to show that it is related with the stress intensity factor. Figure 3.11 shows the forces needed to close a crack over an infinitesimal distance δ in a plate of thickness B. The work done by these forces is equal to the energy needed to make the crack grow this δ distance:

$$\delta U_E = 2B\int_0^{\delta}\frac{1}{2}\sigma_y u_y \mathrm{d}x = 2B\int_{a-\delta}^{a}\frac{1}{2}\sigma_y u_y \mathrm{d}x \tag{3.48}$$

where factor 2 is related to the two surfaces of the crack and factor 1/2 is the assumed proportionality between tractions and the corresponding displacement u_y. Using the expressions for σ_y and u_y that can be found in many handbooks and adopting polar coordinates with origin at the crack tip (r,θ), we get:

$$G = \lim_{\delta\to 0}\frac{2K_I^2}{\pi E\delta}\int_0^{\delta}\sqrt{\frac{\delta - r}{r}}\mathrm{d}r = \lim_{\delta\to 0}\frac{2K_I^2}{\pi E}\int_0^{\pi/2}\sqrt{\frac{\cos^2\theta}{\sin^2\theta}}2\delta\sin\theta\cos\theta\mathrm{d}\theta \tag{3.49}$$

yielding:

$$G = \frac{K_I^2}{E} \tag{3.50}$$

for plane stress conditions and:

$$G = \frac{K_I^2}{E}(1-\nu^2) \tag{3.51}$$

for plane strain conditions. Subscript I stands for mode I.

3.6.2 Linear elastic-perfectly plastic materials

Linear elastic-perfectly plastic materials cannot exhibit very high elastic stresses in the vicinity of a crack tip, because the maximum admissible stress is the material's yield

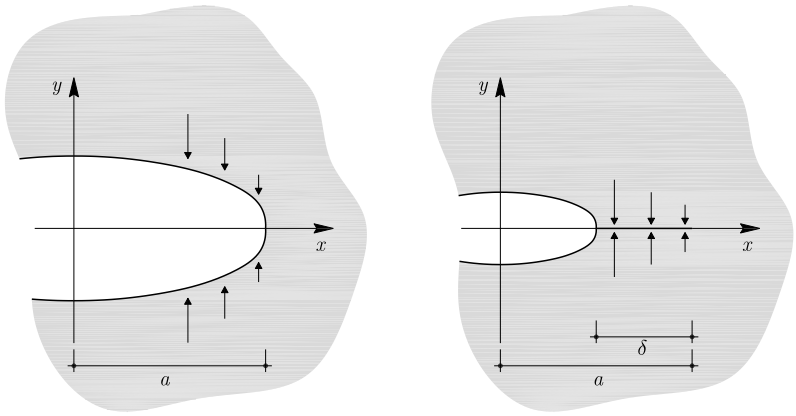

Figure 3.11: Forces applied to close a crack over an infinitesimal distance [Wan96]

condition. As a consequence local plastic yielding occurs. Let us consider the elastic stress distribution in the crack tip of Figure 3.12, given by:

$$\sigma_{yy} = \frac{K_I}{\sqrt{2\pi r}} \tag{3.52}$$

where r is the distance from the crack tip. As a first approximation the boundary between the elastic and plastic behavior occurs when the elastic stress is equal to the yielding stress σ_{ys}, and the so-called first-order plastic zone size is given by:

$$r_l = \frac{K_I^2}{2\pi {\sigma_{ys}}^2} \tag{3.53}$$

However, when yielding occurs, stress redistributions must be present in order to satisfy equilibrium. Assuming that the force carried by the elastic stress distribution is the same before and after plastic yielding, force equilibrium yields the second-order plastic zone size [Irw68]:

$$\sigma_{ys} r_p = \int_0^{r_l} \sigma_{yy} \mathrm{d}r = \int_0^{r_l} \frac{K_I}{\sqrt{2\pi r}} \mathrm{d}r \Rightarrow r_p = \frac{1}{\pi} \left(\frac{K_I}{\sigma_{ys}} \right)^2 \tag{3.54}$$

It can be shown that according to the Von Mises yield criterion the effective yield stress σ_y is given by [Wan96]:

$$\sigma_y = \begin{cases} \frac{\sigma_{ys}}{1-2\nu} & \text{plane strain} \\ \sigma_{ys} & \text{plane stress} \end{cases} \tag{3.55}$$

where σ_{ys} is the uniaxial yield stress. Considering $\nu = 1/3$ and $\sigma_y = 3\sigma_{ys}$, the plastic zone under plane strain condition is approximately 1/9 of that under plane stress condition.

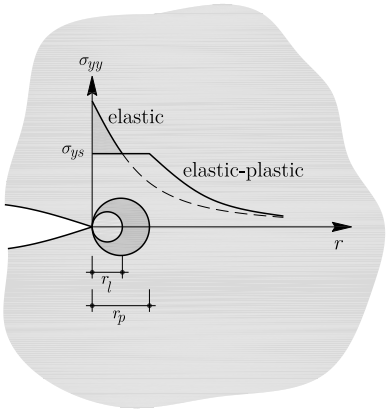

Figure 3.12: First-order and second-order estimates of plastic zone size [Wan96]

3.6.3 Fracture toughness as a failure criterion

As it was discussed in Section 3.6.2, materials may exhibit plasticity at the crack tip. If the stress redistribution associated with the yielding has a minimal effect on the crack tip elastic stress field, LEFM (Section 3.6.1) can still be applied and the stress intensity factor K is enough to describe the stress field of a cracked body. In these conditions, there is a critical stress and strain state at the crack tip that causes the crack to propagate in a brittle manner, described by the critical stress intensity factor or fracture toughness K_c.

Tests show that the fracture toughness K_c depends on the thickness B of the tested specimens. Plane strain conditions are associated with small plastic regions in the crack tip, and plastic contraction is restrained by the surrounding elastic material. On the other hand, plane stress conditions associated with negligible stresses normal to the specimen's plane are able to dissipate more energy as a result of plastic deformation near the specimen surface, resulting in higher fracture toughness than the one associated with plane strain conditions. Figure 3.13 represents schematically the dependency of the specimen's thickness on the measured fracture toughness. With increasing thickness the measured fracture toughness approaches the fracture toughness under plane strain conditions K_{Ic} (mode I), which is a material property.

Knowing the fracture toughness allows us to calculate the residual strength of a cracked element as:

$$\sigma_c = \frac{K_c}{Y\sqrt{\pi a}} \tag{3.56}$$

where Y is the geometry correction factor (dependent of the body and crack geometries). Conservatively $K_c = K_{Ic}$ can be assumed. If the stress state is known, the critical crack size can be calculated as:

$$a_c = \frac{1}{\pi}\left(\frac{K_c}{Y\sigma}\right)^2 \tag{3.57}$$

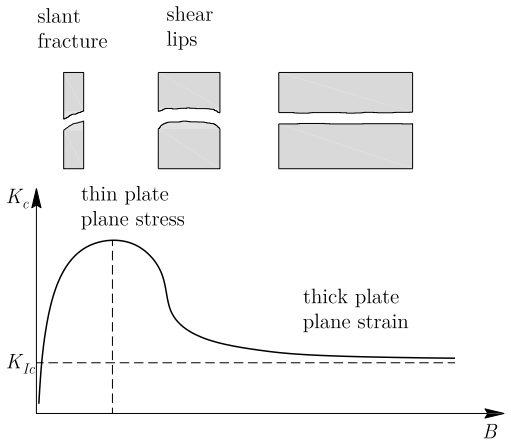

Figure 3.13: Effect of thickness on fracture toughness [Wan96]

Equations 3.56 and 3.57 form the basis of the LEFM based design methodologies.

3.6.4 Fatigue crack growth

When a structure is subjected to a constant range of cyclic stresses, stable fatigue crack growth can occur at stress levels well below the yield stress of the material. The propagation of a crack with the load cycles ($\mathrm{d}a/\mathrm{d}N$) depends on the stress intensity factor amplitude at the crack tip (ΔK), refer to Figure 3.14. Three regimes can then be distinguished: (a) initiation of crack propagation; (b) stable crack propagation or linear regime; and (c) unstable crack propagation. The former is governed by a threshold (ΔK_0) below which no propagation occurs. The latter leads to a fast and unstable crack propagation resulting in failure. With respect to the stable crack propagation regime, it can be characterized by the empirical law observed by Paris-Erdogan [Par63]:

$$\frac{\mathrm{d}a}{\mathrm{d}N} = C\Delta K^n \tag{3.58}$$

where C and n are constants depending on the material properties. This law depends on the ratio R between minimum and maximum applied stresses, and its validity has been largely verified for metallic materials.

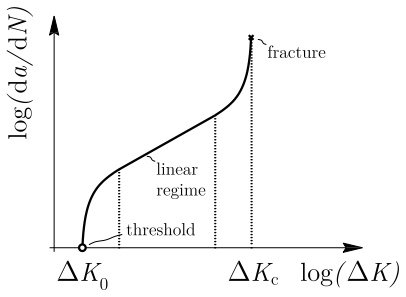

Figure 3.14: Crack growth rate as a function of the stress intensity factor

The Wöhler diagrams (also known as S-N curves, refer to Figure 3.15) can be determined by calculation of the number of cycles to failure N under a constant range of cyclic stresses (S):

$$N = \int_{a_0}^{a_f} \frac{\mathrm{d}a}{C\Delta K^n} \tag{3.59}$$

where a_0 is the initial crack length and a_f is the critical crack length leading to unstable crack growth, which may be calculated from the fracture toughness (Section 3.6.3).
If the structure is loaded with different stress ranges, damage sum can be performed according to the Palmgren-Miner's rule [Min45]:

$$\sum_i \frac{n_i}{N_i} \tag{3.60}$$

where n_i represents the number of cycles of amplitude S_i, and N_i is the number of cycles to failure if the only applied stress range is S_i, refer to Figure 3.15. Failure theoretically occurs when the damage sum reaches 1. However, it cannot be seen as an universal law.

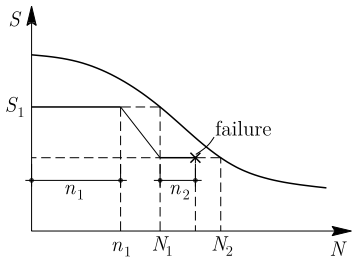

Figure 3.15: Typical S-N curve and damage cumulation [Min45]

3.7 Nonlinear fracture mechanics for quasi-brittle materials

This section presents the basics of nonlinear fracture mechanics (NLFM) applied to quasi-brittle materials, like concrete. Size-effect laws are presented to study both monotonic and fatigue loading.

3.7.1 Hillerborg's fictitious crack model

This section presents Hillerborg's [Hil76, Hil83] fictitious crack model aimed at studying the nonlinear fracture process of concrete. This model is based on Dugdale's strip-yield model [Dug60].
The fracture behavior of concrete in tension is different from metallic materials, due to the fact that the fracture of concrete is preceded by micro-cracking instead of yielding. Micro-cracking allows stress decrease with increasing deformation. When micro-cracks grow and form a crack, stress transfer is still possible through the crack. Figure 3.16

presents a three-point bending test of an unreinforced concrete notched element and the typical stress distribution ahead of the crack tip. The relatively large depth of the fracture process zone (FPZ) does not allow for a clear definition of the crack tip like metallic materials do.

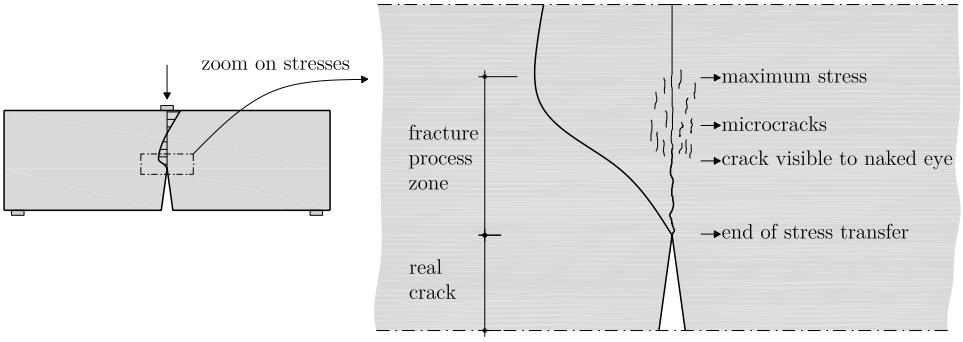

Figure 3.16: Three-point bending test of an unreinforced concrete notched element and typical tensile stress distribution [Hil83]

In concrete microcracking no substantial contraction occurs (compared with the one occurring when metal yields). Consequently the influence of plane stress or strain conditions is expected to be the same, *i.e.*, the concrete behavior is expected to be independent of the specimen width.
The tensile behavior of concrete can be described by stress-strain and post-peak stress-displacement diagrams obtained by displacement-controlled tests, refer to Figure 3.17. The region A where fracture occurs has a certain width. However, Hillerborg [Hil83] proposes to adopt an original width of the fracture zone equal to zero and to concentrate all the post-peak displacements in a line crack, reason why the model is named as fictitious crack model.

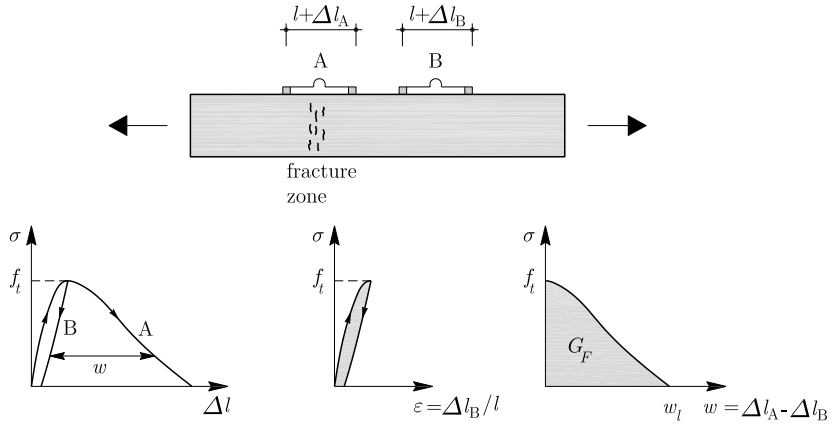

Figure 3.17: Uniaxial tensile test of an unreinforced concrete element and determination of stress-strain and post-peak stress-displacement diagrams [Hil83]

The energy per unit area spent to perform a complete separation of the two halves of the uniaxial tensile test in the fracture zone is given by:

$$G_F = \int_0^{w_l} \sigma \mathrm{d}w \tag{3.61}$$

where $w_l = w(\sigma = 0)$. The energy absorbed outside the fracture zone can be calculated based on the stress-strain diagram, but a purely elastic material does not exhibit energy absorption outside the fracture zone.
The fictitious crack model can be implemented in a finite element code in order to study the stability and crack growth, refer to Figure 3.18. The simplest possible assumptions regarding the stress-strain and post-peak stress-displacement relations are those of Figure 3.19, which depend on the material properties f_t and G_F (besides the Young's modulus E). These values can be combined into a characteristic length:

$$l_{ch} = \frac{EG_F}{f_t^2} \tag{3.62}$$

The characteristic length is a material property, and the length of the fracture zone during crack growth is of the order 0.3-0.5l_{ch} [Hil83].

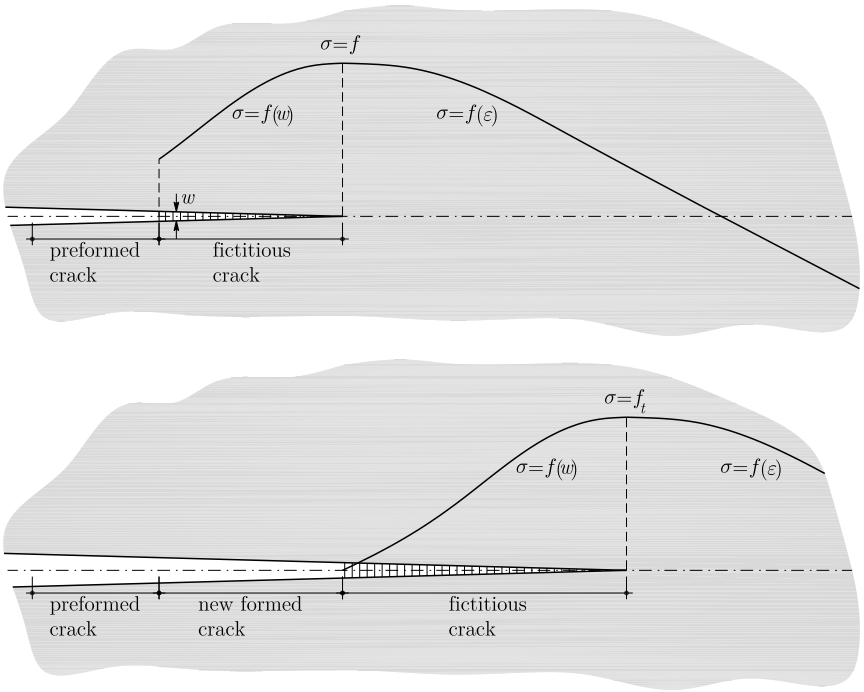

Figure 3.18: Stress distribution in front of a crack tip before and after growth of the real crack [Hil83]

The post-peak stress-displacement can be determined by an uniaxial tensile test. However this kind of tests is difficult to perform, because it requires a very stiff test rig. But other tests can be performed in order to determine G_F, like the three-point bend test, the compact tension test or the wedge splitting test.
LEFM (Section 3.6) assumes that there is no fracture zone ahead of the crack tip. Even though this assumption is only true for concrete when the specimen dimensions are much

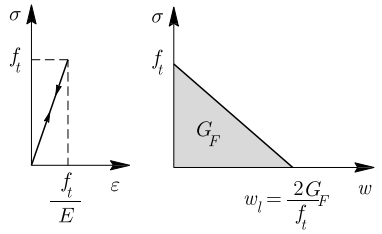

Figure 3.19: Simplest possible assumptions regarding the stress-strain and post-peak stress-displacement relations for finite element implementation [Hil83]

larger than the fracture zone, Hillerborg [Hil83] has used the fracture toughness failure criterion (Section 3.6.3) to study how great are the errors of using LEFM compared with a finite element implementation of the fictitious crack model. In order to perform this study, Hillerborg [Hil83] assumed that the fracture toughness K_c (and the corresponding critical energy rate (Equation 3.50)) correspond to K (and G) when the maximum load in a test is attained. As for concrete there is no well defined crack tip, a notched beam can be used to perform this study. Figure 3.20 shows the result of such a test. It can be observed that K_c and G_c depend on the geometry and are not material properties. They only become material properties when the specimen dimensions become large enough and G_c approaches G_F.

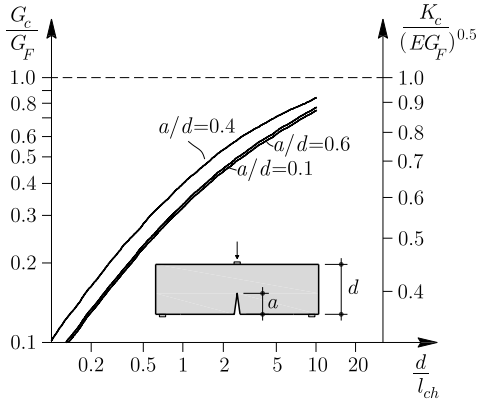

Figure 3.20: Theoretical variation with beam depth of K_c and G_c for a three-point bending test and application of LEFM [Hil83]

3.7.2 Bažant's size effect law

As discussed in Section 3.7.1, the global response of concrete structures depends on the dimensions of the structure. This phenomenon is known as the deterministic size effect, and it shall not be misinterpreted as the statistical site effect [Wei51]. In this section the Bažant's [Baz84] size effect law is presented, which is valid for structures with geometrically similar shapes, like beams of the same span-to-depth ratio and the same notch-to-depth ratio, for example.

According to the strength of materials (SOM) standard criterion, failure occurs when the nominal applied stress σ_N reaches the direct tensile strength of concrete f'_t. The nominal applied stress σ_N can be expressed as:

$$\sigma_N = c_N \frac{P}{bd} \tag{3.63}$$

where P represents the load (or loading parameter), b is the thickness of the element, d is the characteristic dimension, and c_N is independent of size and characterizes the structure shape and type of loading.

If we consider the LEFM failure criterion (Section 3.6.3), it can be shown that σ_N is inversely proportional to $\sqrt{d}$.

The SOM and the LEFM failure criteria are plotted schematically in Figure 3.21. However, concrete structures exhibit a gradual transition from the SOM to the LEFM criteria, the so-called nonlinear fracture mechanics (NLFM) criterion.

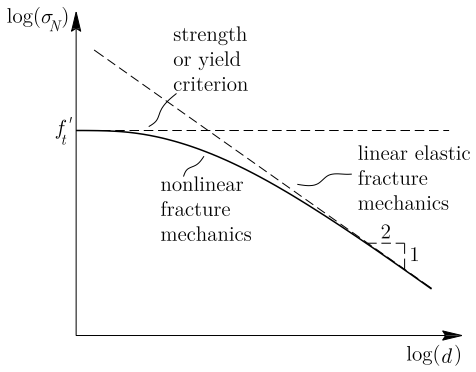

Figure 3.21: Deterministic size effect according to SOM, LEFM and NLFM criteria [Baz84]

In concrete, the thickness of the fracture zone w_c can be assumed to be related to the maximum aggregate size d_a by an empirical constantly n ($w_c = nd_a$), which can be taken as 3 [Baz83]. Bažant and Oh [Baz83] state that w_c has to be a material property in order to obtain consistent numerical results when implementing their crack band theory for fracture of concrete.

The uniaxial tensile behavior of concrete can be described by the stress-strain relation of Figure 3.22, characterized by the elastic modulus E_c, the tensile stress f'_t and the strain-softening modulus E_t (negative value).

The fracture energy per unit thickness may be calculated as:

$$G_F = w_c \left(1 - \frac{E_c}{E_t}\right) \frac{f_t'^2}{2E_c} \tag{3.64}$$

Bažant and Oh [Baz83] analysed numerous test data and proposed the following empirical expression:

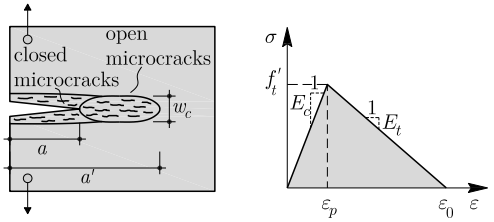

Figure 3.22: Crack band fracture and idealized tensile stress-strain diagram for fracture process zone [Baz84]

$$G_F = (2.72 + 0.0214 f'_t)\, f'^2_t \frac{d_a}{E_c} \quad \text{in [psi]} \tag{3.65}$$

More recently Bažant and Becq-Giraudon [Baz02] proposed updated expressions for G_F based on more tests.

Considering the uniaxial tensile test of the concrete panel of Figure 3.23, before cracking the strain energy density in the panel is uniform and equals $\sigma^2/2E$. When cracking occurs, we can assume that the crack band forces both strain energy and stress relief in the area delimited by points 123456, where line $\overline{16}$, $\overline{56}$, $\overline{23}$ and $\overline{43}$ have a certain fixed slope k_1 close to 1. The total energy release can be approximated as:

$$W = W_1 + W_2 = 2k_1 a^2 b \frac{\sigma^2}{2E_c} + 2n d_a a b \frac{\sigma^2}{2E_c} \tag{3.66}$$

where W_1 is the energy contained in volumes $\overline{156} + \overline{243}$ and W_2 the energy contained in volume $\overline{1245}$.

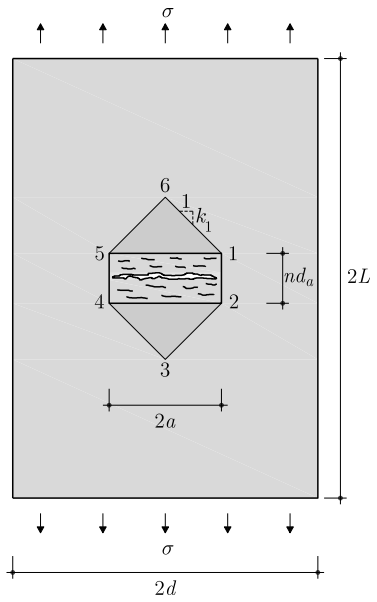

Figure 3.23: Uniaxial tensile test of a concrete panel and crack band propagation [Baz84]

Assuming the top and bottom boundaries to be fixed during cracking, the external work is zero. The potential energy release rate of the panel is thus:

$$\frac{\delta W}{\delta a} = 2\left(2k_1 a + n d_a\right) b \frac{\sigma^2}{2E_c} \tag{3.67}$$

which has to be equal to the energy consumed per unit crack band extension:

$$\frac{\delta W}{\delta A} = G_F b \tag{3.68}$$

Substituting G_F from Equation 3.65 in Equation 3.68, one may obtain an equation with the following solution:

$$\sigma_N = \frac{B f_t'}{\sqrt{1 + \frac{\lambda}{\lambda_0}}} \tag{3.69}$$

$$B = \sqrt{1 + \frac{E_c}{-E_t}} \tag{3.70}$$

$$\lambda_0 = \frac{n}{2k_1}\frac{d}{a} \tag{3.71}$$

where $\lambda = d/d_a$. B and λ_0 are constants when geometrically similar specimens are considered.

Assuming that the total potential energy release W caused by fracture is a function of both the fracture length a (crack band) and the cracked zone area $nd_a a$, Equation 3.69 can be generalized for various geometries and loading configurations:

$$\sigma_N = \frac{B f_t'}{\sqrt{1 + \frac{d}{\lambda_0 d_a}}} \tag{3.72}$$

where once again B and λ_0 are constants when geometrically similar specimens are considered.

Dam concrete or other concretes with crushed aggregates can exhibit cracks predominantly going through the aggregates. Based on this observation, Brühwiler and Roelfstra [Bru89] reached the conclusion that maximum aggregate size cannot be alone the sole material parameter to describe fracture. Instead they propose Hillerborg's characteristic length [Hil83] (Section 3.7.1, Equation 3.62) to be considered as the appropriate material parameter. Bažant's size effect law may be thus formulated by a more general expression:

$$\sigma_N = \frac{B f_t'}{\sqrt{1 + \frac{H}{H_0}}} \tag{3.73}$$

where H_0 is a characteristic property of the concrete (related to l_{ch}) and H is a characteristic dimension of the concrete structure (the fracture ligament length in compact

tension tests, for instance).

3.7.3 Hu and Wittmann's size effect law

Hu and Wittmann [Hu92] have observed that there is an influence of the free boundary of specimens in the FPZ ahead of real crack in a concrete structure. The energy required to propagate the crack decreases as the crack becomes closer to a free boundary [Hu00]. The change in the local fracture energy g_f can be approximated by a bilinear function [Hu92], refer to Figure 3.24. The transition from the constant value G_F to the descending branch occurs at the transition ligament length a_l, dependant of the material properties and specimen size and shape. The global fracture energy G_f measured in tests is the average of the local fracture energy g_f distribution:

$$G_f(a,W) = \frac{\int_0^{W-a} g_f(x)\mathrm{d}x}{W-a} \tag{3.74}$$

$$G_f(a,W) = \begin{cases} G_F\left(1 - \frac{a_l/W}{2(1-a/W)}\right) & 1 - a/W > a_l/W \\ G_F\frac{1-a/W}{2a_l/W} & 1 - a/W \leq a_l/W \end{cases} \tag{3.75}$$

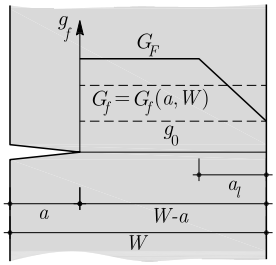

Figure 3.24: Local fracture energy distribution ahead of real crack [Hu04]

In order to obtain G_F and a_l for a certain concrete mix, the G_f value of at least four specimens with single size and a full range variation of the notch depth must be previously determined [Hu04], one can then apply the least squares method. This procedure leads to a G_F value that is essentially independent of the specimen size W and relative notch depth $\alpha = a/W$ [Hu07, Cif13].

A first approach performed by Hu and Wittmann [Hu00] to obtain a size-effect law was based on the fracture properties of a large plate with an edge crack of various lengths. A simple asymptotic function was proposed to model the transition between the SOM and the LEFM criteria (Figure 3.25), as a function of the ratio between the crack length a and the reference crack $a^* \propto l_{ch}$:

$$\sigma_N = \frac{Bf_t'}{\sqrt{1+\beta\frac{a}{l_{ch}}}} \tag{3.76}$$

where B and β are dimensionless constants to account for variations in loading conditions

and specimen geometry. β depends on the α ratio, being constant for geometrically similar specimens of different sizes with a constant α.

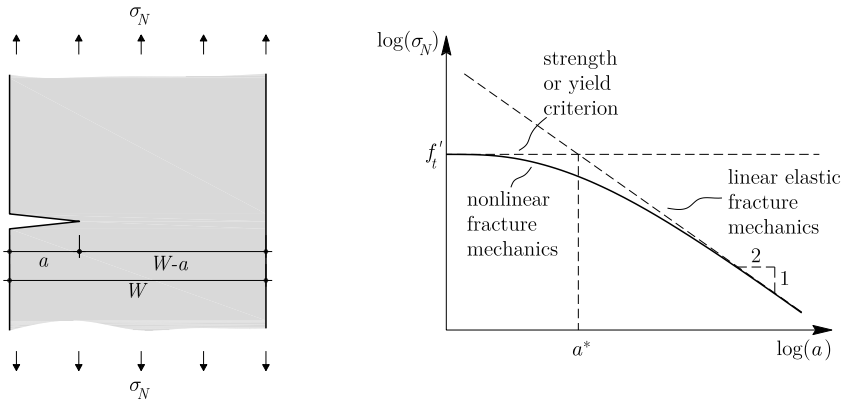

Figure 3.25: Tensile failure of a large plate with a short edge crack [Hu00]

A second approach developed by Duan, Hu and Wittmann [Dua02] has adopted the bilinear function to approximate the distribution of fracture energy along the ligament [Hu92] (Figure 3.24) and the transitional ligament $a_l{}^*$ was introduced to define the intersection of the two linear functions. This model revealed the role of specimen back free surface in determining the FPZ fracture energy, relating it to the crack length ratio a/a_l^*.
The two approaches previously presented differ from size-effect laws based on the specimen size. The first difference lies on the fact that the size-effect may occur in a large specimen if the edge crack or ligament is not long enough. Another difference is that the reference crack length a^* or the transitional ligament $a_l{}^*$ and the ratios a/a^* and $a/a_l{}^*$ determine the size effect rather than the physical size W.
The transition between the SOM and the LEFM criteria (Figure 3.25) can be expressed as a function of the ratio between the crack length a and the reference crack a^*, and Equation 3.76 can be rewritten as:

$$\sigma_N = \frac{A(\alpha) f_t'}{\sqrt{1 + \frac{a}{a^*}}} \tag{3.77}$$

where $\alpha = a/W$ and $A(\alpha)$ is a factor depending on the loading configuration. The intersection between the SOM and LEFM criteria yields:

$$K_{Ic} = A(\alpha^*) f_t' Y(\alpha^*) \sqrt{\pi a^*} \tag{3.78}$$

where K_{Ic} is the fracture toughness, $Y(\alpha^*)$ is a geometric factor that depends on the reference crack ratio $\alpha^* = a^*/W$.
For a large plate with an edge crack where $W \gg a$, $\alpha = 0$, $A = 1$ and $Y = 1.12$. The reference crack size $a_\infty{}^*$ is a material constant given by:

$$a_\infty{}^* = \frac{1}{1.12^2 \pi} \left(\frac{K_{Ic}}{f_t'} \right)^2 = \frac{l_{ch}}{1.12^2 \pi} \tag{3.79}$$

with

$$l_{ch} = \frac{EG_F}{f_t'^2} = \left(\frac{K_{Ic}}{f_t'^2}\right)^2 \tag{3.80}$$

For specimens with a given α-ratio, the reference crack size a^* is influenced by α as follows:

$$a^* = \frac{1}{\pi Y^2 A^2}\left(\frac{K_{Ic}}{f_t'}\right)^2 = \left(\frac{1.12}{Y(\alpha)A(\alpha)}\right)^2 {a_\infty}^* = \frac{{a_\infty}^*}{B(\alpha)} \tag{3.81}$$

$$B(\alpha) = \left(\frac{Y(\alpha)A(\alpha)}{1.12}\right)^2 \tag{3.82}$$

The size-effect law is thus given by:

$$\sigma_N = \frac{A(\alpha)f_t'}{\sqrt{1 + B(\alpha)\frac{a}{a_\infty^*}}} \tag{3.83}$$

Equation 3.83 shows that the transition between the SOM and the LEFM criteria is significantly affected by the specimen geometry and size.

3.7.4 Jenq and Shah's two parameter fracture model

Jenq and Shah [Jen85] developed a two parameter fracture model to be used with LEFM (Section 3.6) in order to reproduce the nonlinear fracture behavior of concrete. The critical stress intensity factor K_{Ic}^S in mode I is calculated at the tip of the effective crack and the critical effective crack extension is dictated by the elastic critical crack tip opening displacement $CTOD_c$. The proposed model has been shown to be size independent in tests on notched beam specimens. Moreover the model is able to predict size effects on notched and unotched beams and tensile specimens.

The concept of Jenq and Shah's model can be explained with Figure 3.26. In the beginning the relation between the load P and the crack mouth opening displacement ($CMOD$) is linear up to about the load corresponding to approximately half the maximum load. In this stage, the intensity factor $K_I < 0.5K_{Ic}^S$. This phase is followed by another one where inelastic displacement occurs. Failure occurs when the $CTOD$ reaches a critical level $CTDO_c$ and $K = K_{Ic}^S$.

The model was validated through three-point bending tests on geometric similar notched beams. In these tests, from the measured maximum loads and corresponding elastic component of $CMOD$, the value of the effective elastic crack was determined such that the calculated $CMOD$ was equal to the measured one. For that value of crack length, K_{Ic}^S and $CTOD_c$ were determined. The obtained values are essentially independent of the size of the beams.

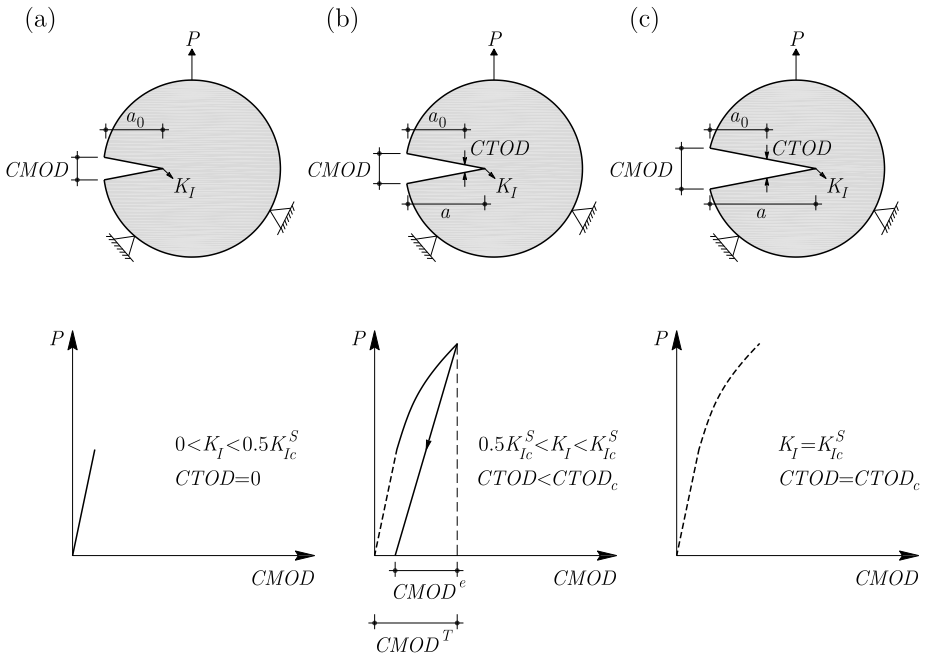

Figure 3.26: Fracture resistance stages of plain concrete [Jen85]: **(a)** $K_I < 0.5K_{Ic}^S$; **(b)** nonlinear range; and **(c)** critical point

3.7.5 Bažant and Xu's size effect in fatigue fracture of concrete

Bažant and Xu [Baz91] performed a series of monotonic and fatigue tests on geometrically similar notched beams (Figure 3.27). Three different characteristic sizes were used ($d = 38, 76, 152$mm) and the notch size and span were $a_0 = d/6$ and $L = 2.5d$, respectively. As it was already discussed (Section 3.7.1) it is difficult to clearly define the crack length in concrete. In order to do it, the indirect method $CMOD$-compliance C method can be used. This method consists in applying a small load in a notched beam a certain number of cycles and measuring the compliance, and subsequently increasing the notch depth and measuring the new compliance, refer to Figure 3.28. The applied load has to be small to ensure that the increment in the notch size with a saw completely removes the fracture process zone, and that the beam can be considered as virgin for the next notch depth.

All the fatigue tested specimens were loaded between zero and 80% of the monotonic static strength.

In order do determine the crack evolution law as a function of the stress intensity factor, based on the load P - $CMOD$ diagrams of the fatigue tests, one can calculate for each cycle the compliance of the unloading branch (C_N, refer to Figure 3.29(a)). Knowing the compliance C_N, it is possible to determine the crack length (a_N/d, refer to Figure 3.29(b)) from the previously determined compliance-notch depth diagrams of Figure 3.28 and to plot the crack growth as a function of the loading cycles N (Figure 3.29(c)). One can also calculate the stress intensity factor K_I (as we know the applied stress and the crack length) and plot in logarithmic scale the rate of crack increment with the number

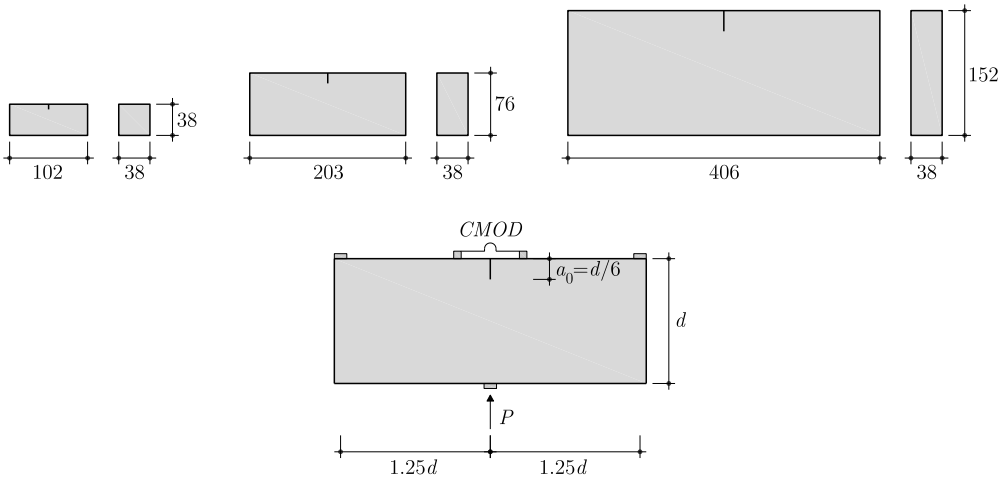

Figure 3.27: Geometry of the fatigue and static tests performed by Bažant and Xu [Baz91] (dimensions in [mm])

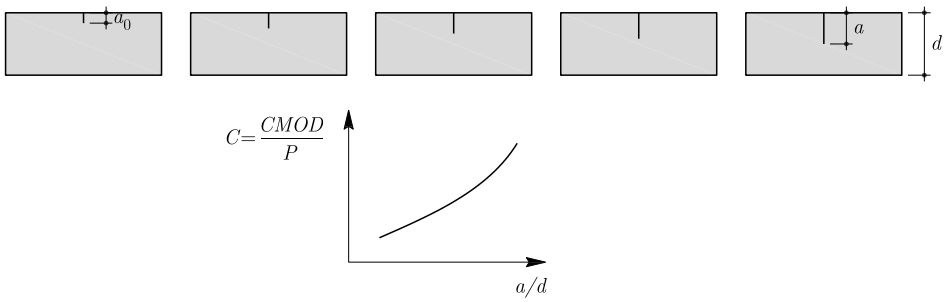

Figure 3.28: $CMOD$-compliance method: experimental determination of the relationship [Baz91]

of cycles as a function of the variation of the stress intensity factor normalised by the fracture toughness of concrete K_{If}, refer to Figure 3.29(d).

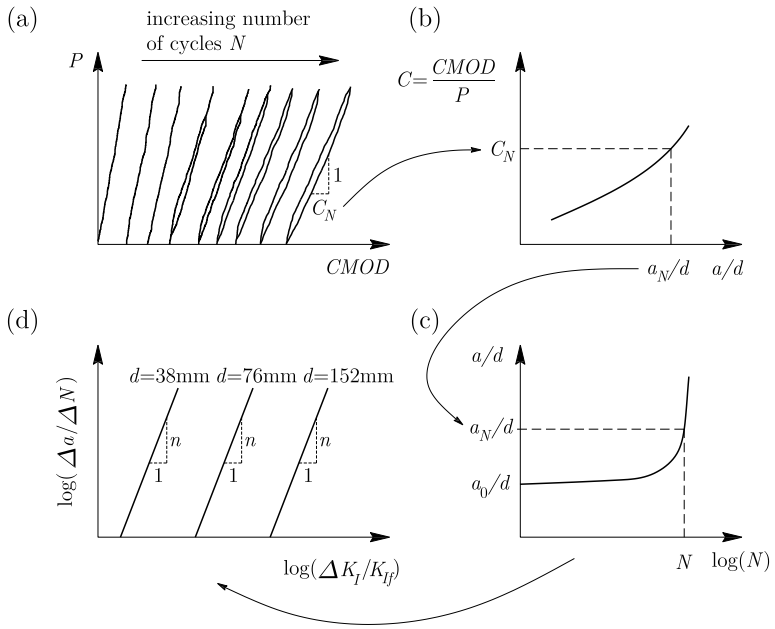

Figure 3.29: Determination of crack evolution law as a function of the stress intensity factor [Baz91]: **(a)** $P - CMOD$ diagram; **(b)** $C - a/d$ diagram; **(c)** $a/d - N$ diagram; and **(d)** $\Delta a/\Delta N - \Delta K_I/K_{If}$ diagram

Figure 3.29(d) shows that depending on the size of the specimen we get different best-fit lines, even though with the same slope. Comparing Figure 3.29(d) with the typical materials that can be described by LEFM (Section 3.6.4 and Figure 3.14), it can be seen that Paris law (Equation 3.58) is invalid for concrete, because according to it there should only exist one line, dependent of material properties and not on the specimen dimensions.

Bažant's size effect law for monotonic loading (Section 3.7.2 and Equation 3.69) can be rewritten as follows:

$$\sigma_N = \frac{Bf'_t}{\sqrt{1+\beta}} \tag{3.84}$$

where $\beta = d/d_0$ is the so-called brittleness number and (B, d_0) are empirical constants characterizing both the material properties and structure shape. It was previously discussed that the size effect law coincides with LEFM when $\beta \to \infty$. Due to these deviations from the LEFM, the critical value of K_{Ic} of stress intensity factor K_I at which the crack can propagate at monotonic loading depends on the specimen size and geometry. When $\beta \to \infty$, $K_{Ic} \to K_{If}$.

Recalling the general expression for the nominal stress σ_N (Equation 3.63), it can be shown that the stress intensity factor K_I is a function of the ratio crack length / beam depth a/d:

$$K_I = \sigma_N \sqrt{d} \frac{f\left(\frac{a}{d}\right)}{c_N} \tag{3.85}$$

In order to determine the size-dependency of K_{Ic}, we can introduce Equation 3.84 in Equation 3.85:

$$K_{Ic} = \frac{B f_t' \sqrt{\beta d_0}}{\sqrt{1+\beta}} \frac{f\left(\frac{a}{d}\right)}{c_N} = K_{If} \sqrt{\frac{\beta}{1+\beta}} \tag{3.86}$$

$$K_{If} = B f_t' \sqrt{d_0} \frac{f\left(\frac{a}{d}\right)}{c_N} \tag{3.87}$$

where K_{If} is the fracture toughness because $K_{Ic} \to K_I f$ when $\beta \to \infty$. The fracture toughness can thus be calculated from parameters B and d_0, which in their turn can be calculated from the monotonic tests.

To take into account the size-dependency of K_{Ic}, Bažant and Xu [Baz91] proposed the following modified Paris law:

$$\frac{\Delta a}{\Delta N} = C \left(\frac{\Delta K_I}{K_{Ic}}\right)^n \tag{3.88}$$

Constant d_0 (also known as transition size from SOM to LEFM) applies only to peak-load states at monotonic loading. Bažant and Xu [Baz91] raised doubts on whether it is correct to consider it constant and with the same value as the monotonic one for fatigue testing. In order to obtain a size-independent plot of the $\Delta a/\Delta N - \Delta K_I/K_{If}$ diagram for all specimen dimensions, Bažant and Xu [Baz91] proposed to use a d_0 ten times larger than the monotonic one. As the fracture process zone seems to be proportional to d_0 [Baz90], this would mean that the fracture process zone is greatly enlarged by cyclic loading.

The size-adjusted Paris law from Equation 3.88 can be rearranged by introducing ΔK_I from Equation 3.85, yielding:

$$\frac{\Delta a}{\Delta N} = \overline{C} \left(\sqrt{1+\beta} \Delta \sigma_N\right)^n \tag{3.89}$$

$$\overline{C} = C \left(\sqrt{d_0} \frac{f\left(\frac{a}{d}\right)}{c_N K_{If}}\right)^n \tag{3.90}$$

3.8 Gallego, Zanuy and Albajar's shear-fatigue mechanical model

In this section the mechanical model developed by Gallego, Zanuy and Albajar [Gal14a, Gal14b] to study shear-fatigue failures of reinforced concrete beams without shear reinforcement is presented.

One of the basic assumptions of the model is that the diagonal crack develops from

a flexural crack at an initiation section located at d (flexural depth) from the point load, refer to Figure 3.30(a). This assumption is taken from the average position of the crack in several experimental tests. The strain and stress states at the initiation section are shown in Figures 3.30(b-d) and the stress states at points A (neutral axis), B (tip of the flexural crack) and in between line $\overline{\text{AB}}$ are shown in Figures 3.30(e-g). Before the diagonal crack formation, aggregate interlock and dowel action are assumed to be not yet activated, and the shear force is fully carried by the the uncracked zone. The shear stress distribution is assumed to be parabolic with a maximum at the neutral axis (Figure 3.30(d)). Vertical stresses are considered to be zero in order to preserve the strain compatibility condition between both sides of the flexural crack (Figures 3.30(h-i)).

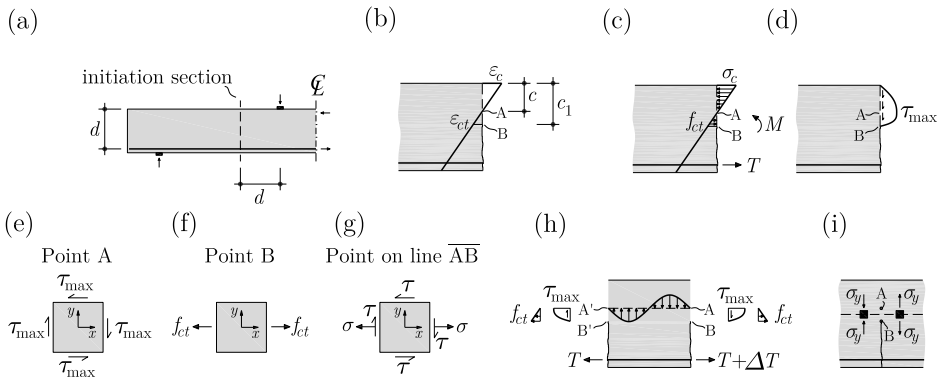

Figure 3.30: Determination of stress state at the initiation section and on the boundaries of a concrete tooth [Gal14a]: **(a)** location of the initiation section; **(b)** strain distribution; **(c)** normal stress distribution; **(d)** shear stress distribution; **(e)** stress state at point A; **(f)** stress state at point B; **(g)** stress state at a point on line $\overline{\text{AB}}$; **(h)** stress state on the boundaries of a concrete tooth; and **(i)** distribution of vertical stresses on concrete teeth borders

The diagonal crack is assumed to start from point A. Mohr's circle in point A shows that that the principal stress σ_I is:

$$\sigma_I = \tau_{\max} \tag{3.91}$$

Recalling that the assumed shear stress distribution is a second order parabolic function, the shear force is given by:

$$V = \frac{2}{3}\tau_{\max} b c_1 \tag{3.92}$$

where b is the beam width and c_1 the depth of the flexural crack tip (Figure 3.30(b)). The principal stress is thus:

$$\sigma_I = \frac{3}{2}\frac{V}{b c_1} \tag{3.93}$$

Comparing the values of σ_I and the number of cycles to diagonal crack formation N_{diag} of 72 tests from 9 different experimental campaigns, Gallego et al. [Gal14a] proposed the following equation:

$$\log N_{diag} = A(1-R)^B \left(\frac{\sigma_{I,\max}}{f^*_{ct,fl}}\right)^C \tag{3.94}$$

$$f^*_{ct,fl} = f_{ct,C-T}\left(1.6 - \frac{h}{1000}\right) \geq f_{ct,C-T} \quad h \text{ in [mm]} \tag{3.95}$$

$$f_{ct,C-T} = f_{ct}\left(1 - \frac{\sigma_{II}}{f_c}\right) \tag{3.96}$$

where f_{ct} is the concrete tensile strength, $f^*_{ct,fl}$ [EC2-1] incorporates the size effect in the normalization of the flexural concrete tensile strength, $f_{ct,C-T}$ [Kup69] refers to the influence of the biaxial stress state at the tip of the flexural crack, R is the ratio between minimum and maximum applied stresses, and $A = 3.01$, $B = -0.08$ and $C = -0.99$ are constants fitted with the least squares method.

After the sudden development of the diagonal crack, the fatigue loading will contribute to the crack propagation, that will diminish the available compression depth. Failure finally occurs when the required depth of the compression zone to resist the applying bending moment equals the available compression zone depth, refer to Figure 3.31. The decrease in the available compression zone depth is the result of the fatigue damage of the concrete compression zone. The residual compressive strength of a concrete specimen subjected to a fatigue process of constant stress limits $f_{c,N}$ is given by [Hsu81]:

$$f_{c,N} = f_c[1 - 0.0662(1 - 0.556R)\log N - 0.0294\log T] \quad N > 1000 \tag{3.97}$$

$$f_{c,N} = f_c[1.2 - 0.2R - 0.133(1 - 0.779R)\log N - 0.053(1 - 0.445R)\log T] \quad N \leq 1000 \tag{3.98}$$

where f_c is the concrete monotonic compressive strength and T is the load period. According to the proposed sectional equilibrium of Figure 3.31 and assuming $z = 0.9d$, the required compression zone depth is given by:

$$\frac{x_N}{d} = \frac{1 - \sqrt{1 - \frac{1.6M_{\max}}{0.68bd^2 f_{c,N}}}}{0.8} \leq \frac{A_s f_y}{0.68bdf_{c,N}} \tag{3.99}$$

where $M_{\max}$ is the maximum applied bending moment, f_y is the reinforcement yield stress and A_s is the longitudinal reinforcement sectional area.

The evolution of the available compression zone depth is performed with a model based on Jenq and Shah's two parameter fracture model [Jen85] (Section 3.7.4).

Even though the diagonal crack propagation is a mixed-mode propagation problem due to the interaction between shear and bending, it is assumed that the crack propagates exclusively in mode I.

The geometry of the development of the diagonal crack is shown in Figure 3.32, inspired from the work of Carpinteri et al. [Car11] for monotonic loaded beams. The diagonal

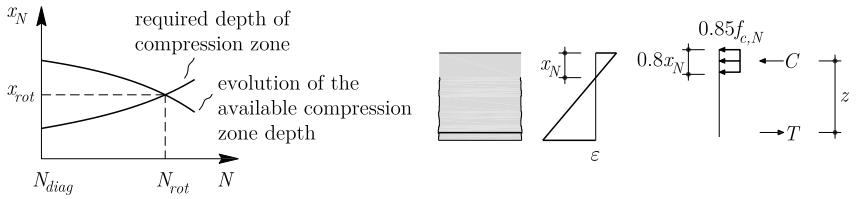

Figure 3.31: Evolution of the available and required compression zone depth after diagonal cracking, and proposed sectional equilibrium [Gal14a]

crack is assumed to be composed of a vertical part of height L_0 and a second part starting at the tip of the flexural crack and extending towards the load application point.

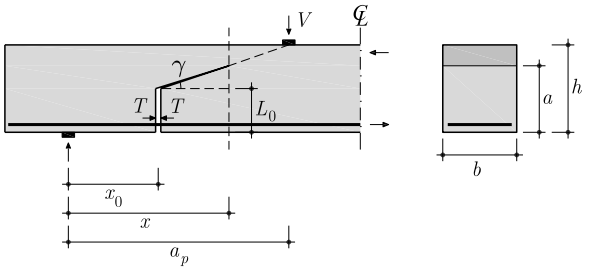

Figure 3.32: Geometry of the development of the diagonal crack [Gal14a]

The determination of the stress intensity factor K_I^S at the shear crack tip can be performed using the following equation (refer to Figure 3.33):

$$K_I^S = K_{I,Mom}^S + \beta K_{I,Steel}^S \tag{3.100}$$

where β is a factor dependent on the inclination angle of the diagonal crack.

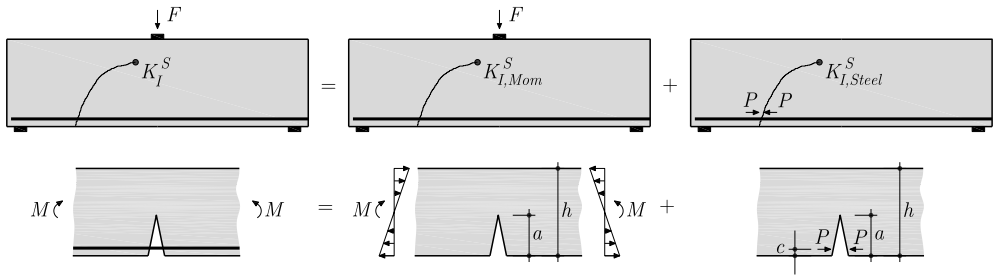

Figure 3.33: Estimation of the stress intensity factor at the tip of the effective diagonal crack [Gal14a]

The stress intensity factor due to the applied moment $K_{I,Mom}^S$ can be expressed as [Gal14a]:

$$K_{I,Mom}^S = \frac{6M}{bh^2}\sqrt{\pi a}F\left(\frac{a}{h}\right) \tag{3.101}$$

where M is the applied moment, h is the beam height, a is the sectional projected height of the shear crack and $F\left(\frac{a}{h}\right)$ is a geometric factor that can be found in reference [Gal14a]. The stress intensity factor due to the closure effect of the steel reinforcement $K_{I,Steel}^S$ is

given by:

$$K^S_{I,Steel} = \frac{2P}{b\sqrt{\pi a}} \frac{G\left(\frac{c}{a}, \frac{a}{h}\right)}{\left(1-\frac{a}{h}\right)^{3/2}\sqrt{1-\left(\frac{c}{a}\right)^2}} \tag{3.102}$$

where P is the force in the steel reinforcement, c is the concrete cover and $G\left(\frac{c}{a}, \frac{a}{g}\right)$ is a geometric factor that can be found in reference [Gal14a].

The stress intensity factor due to the closure effect of the steel reinforcement is affected by a factor β dependent on the inclination angle of the diagonal crack, that reduces the closure effect of the reinforcement when the diagonal crack diminishes its inclination. The following β expression has been proposed by Carpinteri et al. [Car11]:

$$\beta = \left(\frac{\gamma}{90}\right)^{0.2} \quad \gamma \text{ in degrees} \tag{3.103}$$

The study of the capabilities of the model has been performed by Gallego et al. [Gal14a] on the beams tested by Chang and Kesler [Cha58a, Cha58b] and beam VA1 tested by Zanuy [Zan08], adopting the Paris law proposed by Toumi et al. [Tou98]:

$$\frac{\mathrm{d}a}{\mathrm{d}N} = C\left(\frac{\Delta K^S_I}{K^S_{Ic}}\right)^m \tag{3.104}$$

$$\frac{F_{\max}}{F_u} = 4.58\ln C + 87.7 \tag{3.105}$$

where parameter m was taken as 2.5 and F_u was calculated according to [EC2-1]. The fracture toughness of concrete K^S_{Ic} was assumed to be 1.52 MPa$\sqrt{\text{m}}$. As the Jenq and Shah's two parameter fracture model [Jen85] (Section 3.7.4) is used, the stress intensity factor variation and the concrete toughness to apply the Paris law are those referred to the tip of the effective diagonal crack.

The study of the propagation of the diagonal crack can be performed through a step-by-step analysis with a predetermined number of cycles.

The evolution of the maximum applied stress intensity factor at the tip of the effective diagonal crack with the crack length is schematically plotted in Figure 3.34.

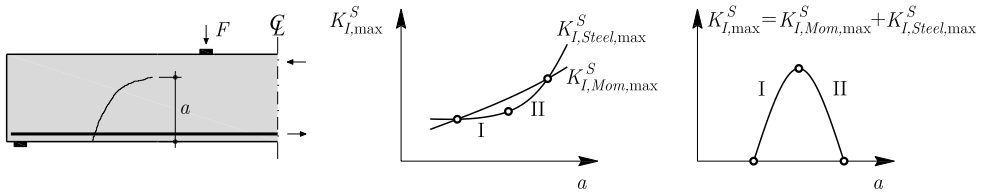

Figure 3.34: Evolution of the maximum applied stress intensity factor at the tip of the effective diagonal crack with the crack height [Gal14a]

Failure due to shear-compression fatigue occurs when the required compression zone depth to resist the applied bending moment equals the available compression zone depth, refer to Figure 3.35(a). However, if after diagonal cracking the stress intensity factor at

the effective diagonal crack tip reaches the fracture toughness of concrete, an unstable crack propagation occurs and a diagonal shear-fatigue failure is produced, refer to Figure 3.35(b).

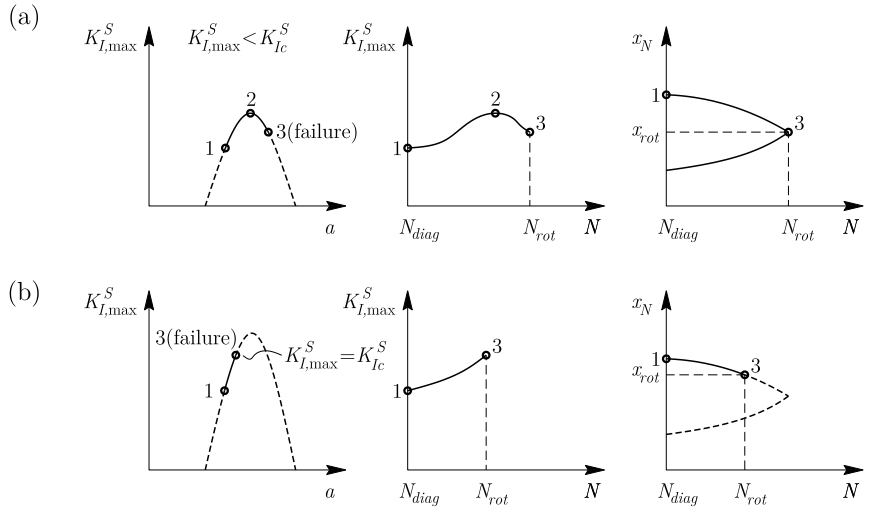

Figure 3.35: Scheme of the process of shear-fatigue failures [Gal14a]: **(a)** shear-compression; and **(b)** diagonal-cracking

Chapter 4

Static Experimental Campaign

4.1 Introduction

This chapter describes the main aspects and results of one experimental static campaign on cantilever slabs under concentrated loads near linear supports, carried out within the framework of this thesis.
The campaign comprises twelve static tests on six full scale slabs (3.00 m x 3.00 m x 0.18 m), corresponding to three different loading locations, three types of longitudinal ducts and a slab type with no ducts.
Detailed test results are available in a specific test report. A summary of the main aspects and results of this test campaign can be found in reference [Nat14a].

4.2 Campaign

Prestressed concrete cantilever bridges usually have longitudinal ducts with prestressing cables in the deck slab, as it is the top flange of a concrete box girder. In addition to the previously discussed influences (Section 2.6) of boundary conditions and load location, another significant aspect influencing the design of deck slabs is the presence of ducts (injected or not) in the slab. The incorporation of ducts is not only limited to the classic case of balanced cantilever bridges, as nowadays water and heating pipes are commonly inserted in reinforced concrete flat slabs.

4.2.1 Specimens

Twelve tests were performed on six full scale slabs (3.00 m x 3.00 m x 0.18 m) with a central line support. Four parameters were varied, namely the concentrated load location, the material, the diameter and the filling of the longitudinal ducts. The slab geometry (Figure 4.1(b)) was adapted from an existing viaduct built in Switzerland in the late $60's$ [Pig71] (Figure 4.1(a)). The slab's central region over the support was thicker in order to reproduce gussets near bridge webs.

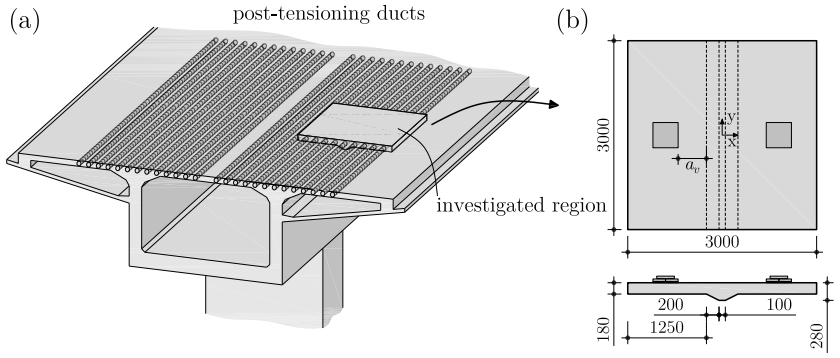

Figure 4.1: Tested slabs: **(a)** investigated region; and **(b)** geometry (dimensions in [mm])

The geometry and reinforcement layout was the same for all slabs. Also concrete properties were kept as constant as possible. The bending top reinforcement in transverse x-direction (perpendicular to the support) consisted of 16 mm diameter bars spaced 100 mm with a nominal effective depth $d_{xt} = 152$ mm (reinforcement ratio $\rho = 1.32\%$), and the bottom one 14 mm diameter bars spaced 125 mm with a nominal effective depth $d_{xb} = 153$ mm. In the longitudinal direction, the top reinforcement consisted of 12 mm diameter bars spaced 125 mm ($d_{yt} = 138$ mm) and the bottom one 10 mm diameter bars spaced 300 mm, as well as 12 mm diameter bars spaced 300 mm ($d_{yb} = 140$ mm), refer to Figure 4.2. Three tests have been performed on slabs without ducts (side A), three on slabs with empty ducts (side C), three on slabs with injected steel ducts (side D) and three on injected polypropylene ducts (side B) (refer to Table 4.1).
The case with empty steel ducts was investigated in order to simulate a deficient injection, unbonded prestressing or the presence of pipes in a building slab. The duct diameter (ϕ_{duct}) was 63 and 72 mm (refer to Table 4.1), which represents 41% and 47% respectively of the nominal effective flexural depth ($d = d_{xt}$). All specimens presented a duct located at d (its center) from the gusset edge. The spacing between axes of ducts was equal to 167 mm ($\approx d$) thereafter. For the injected ducts, 7 prestressing tendons (0.6") were arranged, but no longitudinal prestressing force was applied to allow comparisons with the reference specimen without ducts.

Slab	Side	Test	a_v [mm]	a_v/d	Ducts	ϕ_{duct} [mm]	Age [days]	Concrete f_c [MPa]	E_c [MPa]	Injection Age [days]	Mortar f_m [MPa]
SN1	A	SN1A	304	2	no ducts		250	30.3	27'500		
SN2	A	SN2A	456	3	no ducts		220	30.1	27'400		
SN3	A	SN3A	608	4	no ducts		286	30.4	27'600		
SN1	B	SN1B	304	2	injected, polypropylene	63	81	28.3	26'600	62	50.3
SN2	B	SN2B	456	3	injected, polypropylene	63	150	29.5	27'100	131	67.1
SN3	B	SN3B	608	4	injected, polypropylene	63	164	29.7	27'200	145	67.8
SN4	D	SN4D	304	2	injected, steel	72	270	28.8	26'900	249	53.6
SN5	D	SN5D	456	3	injected, steel	72	234	28.7	26'700	213	48.8
SN6	D	SN6D	608	4	injected, steel	72	291	28.9	27'000	270	54.2
SN4	C	SN4C	304	2	non-injected, steel	72	182	28.4	26'200		
SN5	C	SN5C	456	3	non-injected, steel	72	199	28.5	26'400		
SN6	C	SN6C	608	4	non-injected, steel	72	171	28.3	26'100		

Table 4.1: Properties of test specimens

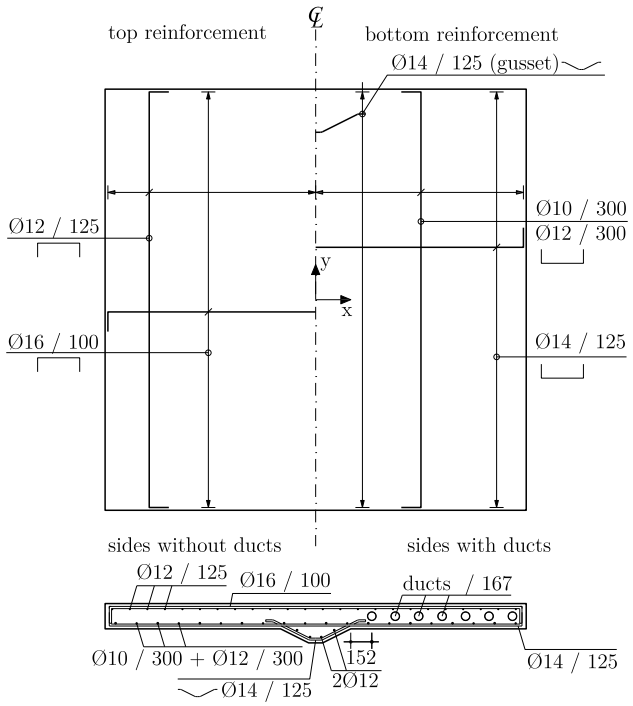

Figure 4.2: Reinforcement layout (dimensions in [mm])

4.2.2 Material properties

Normal strength concrete was used in all slabs. Table 4.1 presents the compressive strength and modulus of elasticity (measured on concrete cylinders, 320 mm high, 160 mm diameter), as well as the concrete age at the time of slab testing, calculated from evolution curves of the concrete strength and modulus of elasticity with time (14 concrete strength tests performed from 14 to 300 days and 9 modulus of elasticity tests from 28 to 200 days). The compressive strength ranged from 28.3 MPa to 30.4 MPa and the modulus of elasticity from 26′100 MPa to 27′500 MPa. One cubic meter of concrete was made of 887 kg of sand, 98 kg of gravel ranging from 4 to 8 mm, 405 kg of gravel ranging from 8 to 16 mm, 681 kg of gravel ranging from 16 to 32 mm, 300 kg of Portland cement and 129 kg of water. The maximum aggregate size d_g was 32 mm for all specimens. The average compressive strength of the injection mortar is also presented in Table 4.1, obtained from 4 compression tests performed the day the specimen was tested and according to EN196-1 [EN196-1]. The measured compressive strength at the age of testing varied between 48.8 and 67.8 MPa.

The average reinforcement mechanical properties of 3 tests per diameter are presented in Table 4.2 and the stress-strain relationships in Figure 4.3 (quenched and self-tempered steel for 16 mm-diameter bars and cold-worked steel for the others).

ϕ_{rebar} [mm]	f_y [MPa]*	f_u [MPa]	Type
16	547	601	quenched and self-tempered
14	550	602	cold-worked
12	548	604	cold-worked
10	570	640	cold-worked

* Offset yield-point at 0.2% strain for cold-worked rebar

Table 4.2: Mechanical properties of the reinforcement

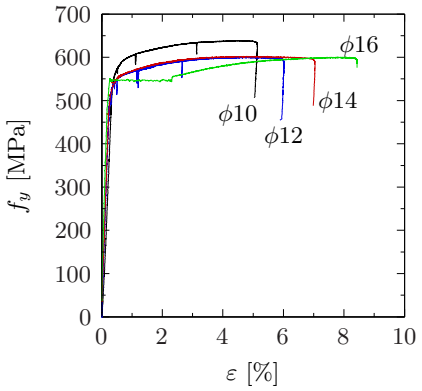

Figure 4.3: Measured stress-strain relationships of reinforcement bars

4.2.3 Test setup

The test setup is shown in Figure 4.4. The specimen was supported on the bottom of its gusset by means of a 80 mm high I-shaped aluminium profile. On each side of the profile web, 30 strain gauges were glued with a 100 mm spacing to record the vertical strains, as shown in Figures 4.4(c,d).

At the interface between the aluminium profile and the tested slab there was a thin layer of plaster of about 3 mm, in order to get leveled surfaces. The loads were introduced by means of two hydraulic jacks supported on a steel frame connected to the strong floor of the laboratory. The loading area had the dimensions of 400 mm × 400 mm in-plane and load was applied through a 10 mm thick neoprene pad. Each load was introduced in this area by means of four 200 mm × 200 mm × 40 mm steel plates, loaded in their turn by a 280 mm × 280 mm × 40 mm steel plate. Between top and bottom plates steel spheres (30 mm diameter) were placed at the center of the bottom plates (Figure 4.4(b)). This device was designed in order to distribute the load as uniformly as possible over the square contact area and is consistent to the load model of EN1991-2 for road bridges [EC1-2].

Two HEB120 steel profiles linked to the loading frame and connected to the gusset over the support by means of two embedded rods (embedment length of 350 mm) prevented the horizontal displacement of the specimens (Figure 4.5). The rods had a 400 mm spacing between them.

Three different loading locations were investigated, corresponding to a clear distance from the end of the gusset (a_v) of $2d$, $3d$ and $4d$, where $d(= d_{xt})$ is the flexural effective

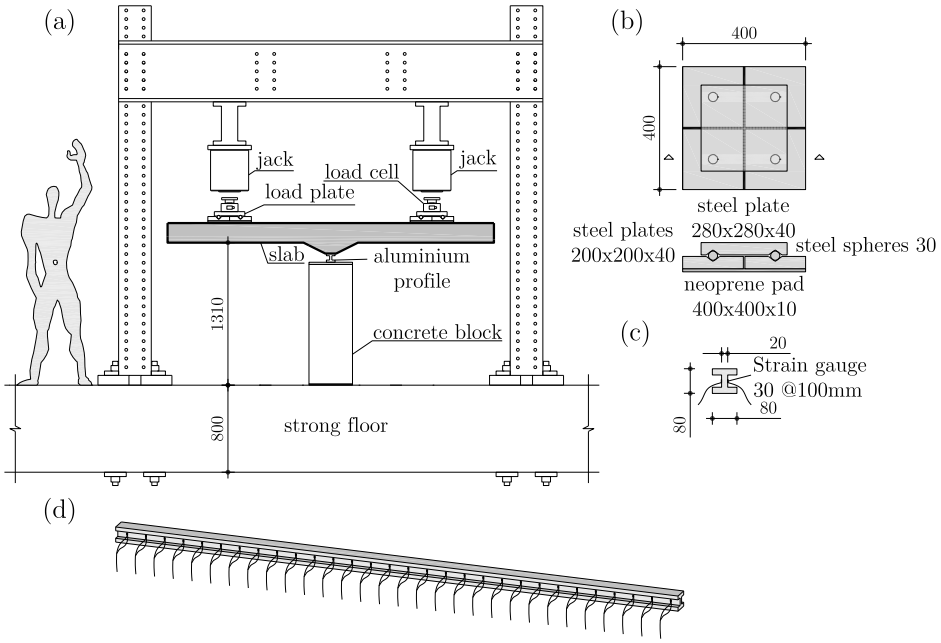

Figure 4.4: Test setup (dimensions in [mm]): **(a)** view; **(b)** loading plates; **(c)** cross-section; and **(d)** 3-d view of aluminium profile

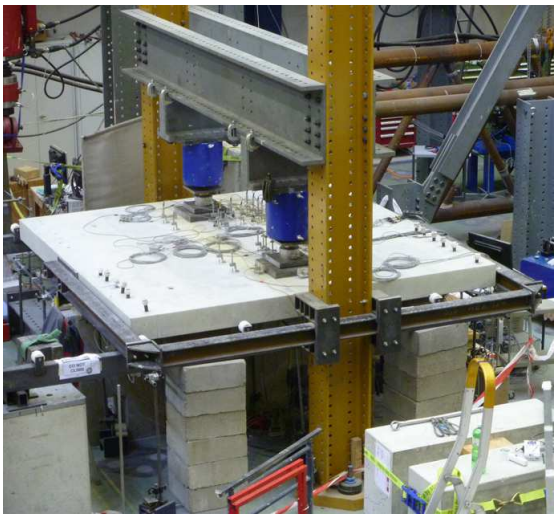

Figure 4.5: Test setup picture

depth of the slab (Figure 4.1(b)).
After failure was achieved on one side of the slab, that side was strengthened using steel external profiles and plates bolted on top and bottom faces, by means of prestressed bars. After strengthening, the slab was reloaded leading to a second failure on the other side (Figure 4.6).

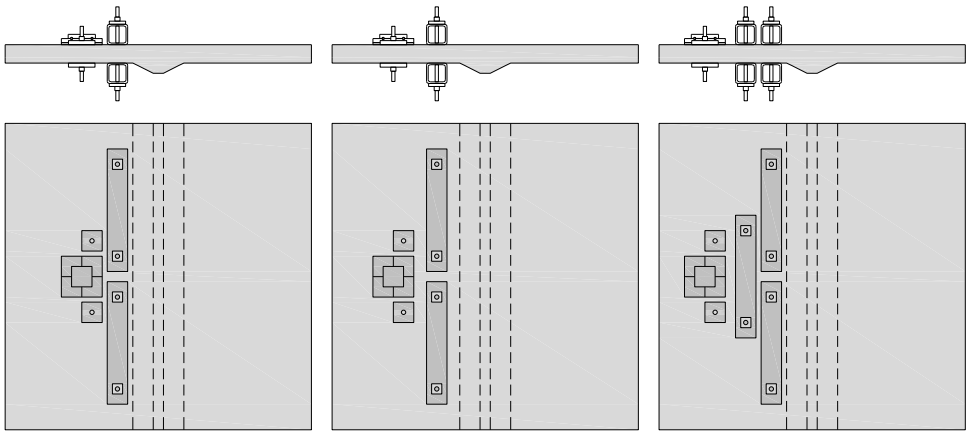

Figure 4.6: Slab repair

4.3 Test results

The main results of the test campaign are shown in the following sections.

4.3.1 Load-displacement

Figure 4.7 plots the load-deflection curves for all tests, where the deflection δ was measured at the center of the loading plates. For all cases, except for the slabs with non-injected steel ducts, once the maximum load was attained, the slabs presented a softening behavior, with a significant decrease of the applied load for increasing displacements. For the slabs with non-injected ducts, the load reached a plateau and the displacements could be significantly increased for a fairly constant applied load.

4.3.2 Crack patterns

The crack patterns as well as the saw-cuts at the center of all slabs are presented in Figures 4.8 and 4.9. All slabs presented a crack pattern on the top surface that developed parallel to the linear support in the central region. On the bottom surface, cracking was however mostly perpendicular to the line support and concentrated in the loading area. The observed failure crack in the central section of the saw-cuts of slabs without ducts or with injected ducts was similar to typical shear cracks of beams without shear reinforcement. For large shear spans ($a_v/d = 3$ and 4), the shear crack developed almost horizontally in the compression zone (slab soffit) near the gusset edge. For these cases,

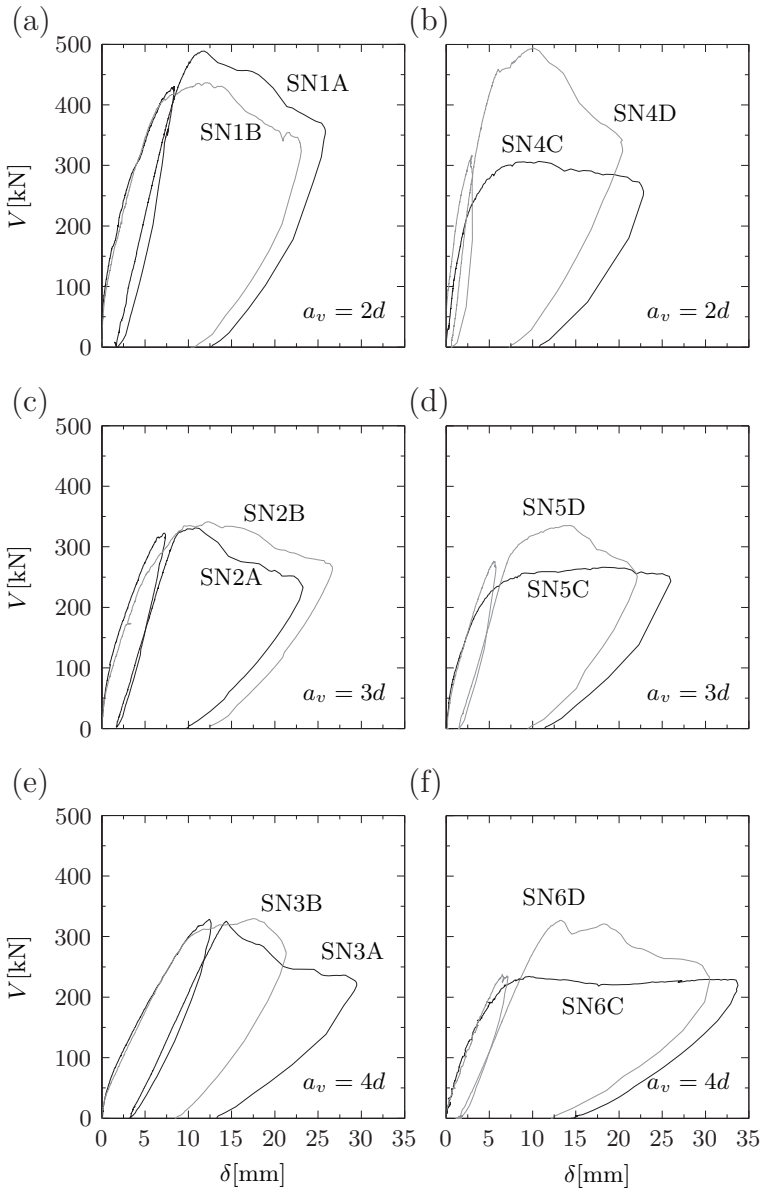

Figure 4.7: Load-deflection curves (at the center of the loading plates)

the shear crack intercepted the top transverse reinforcement with a steep angle at a distance approximately equal to d from the loading plate edge. Cover spalling in this region was due to dowel action of the main reinforcement. For shorter shear spans ($a_v/d = 2$), the shear crack was steeper and more straight on average, and intercepted the upper main reinforcement near the loading plate edge. For slabs with empty ducts, the failure cracking pattern was different and developed horizontally along the bottom and the top reinforcements.

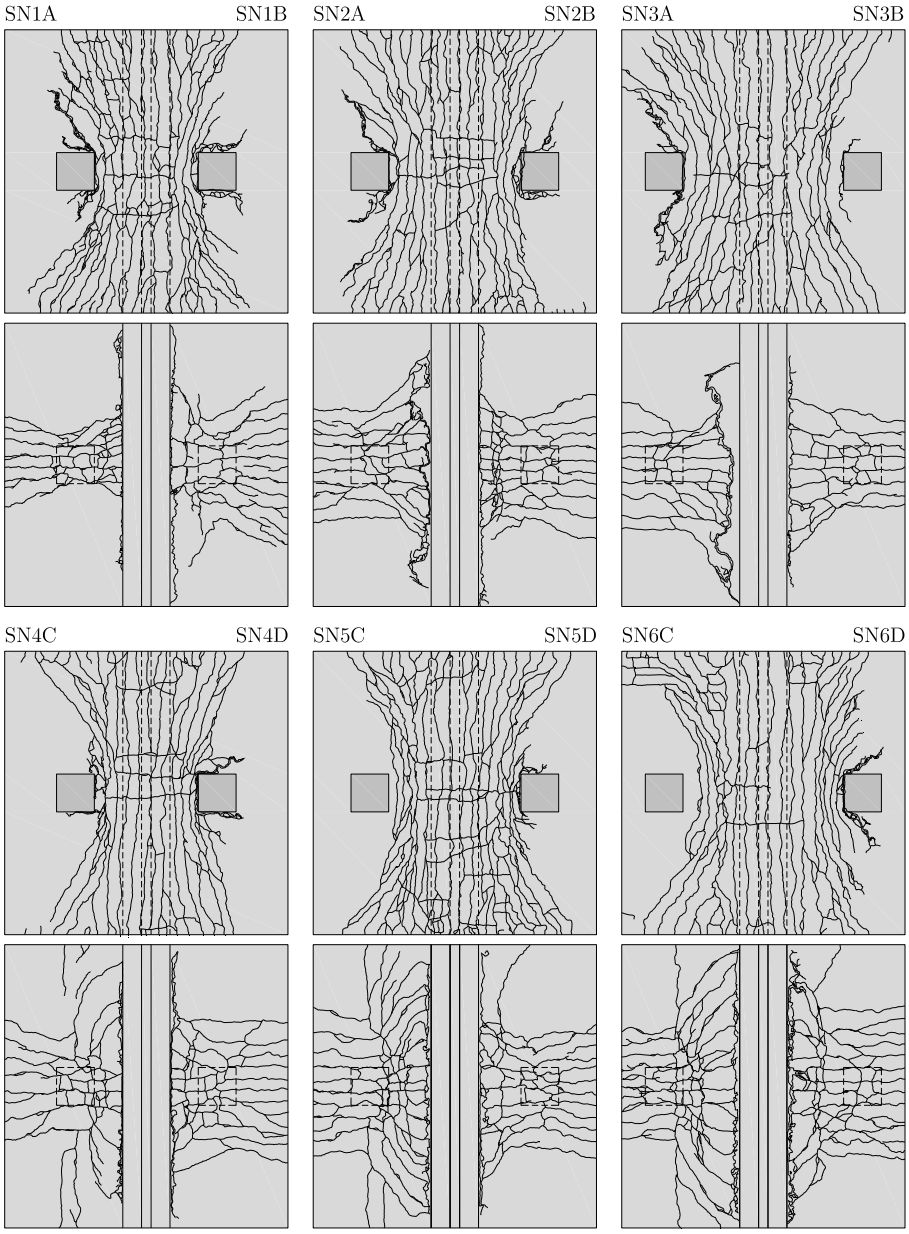

Figure 4.8: Crack patterns after failure: top and bottom faces

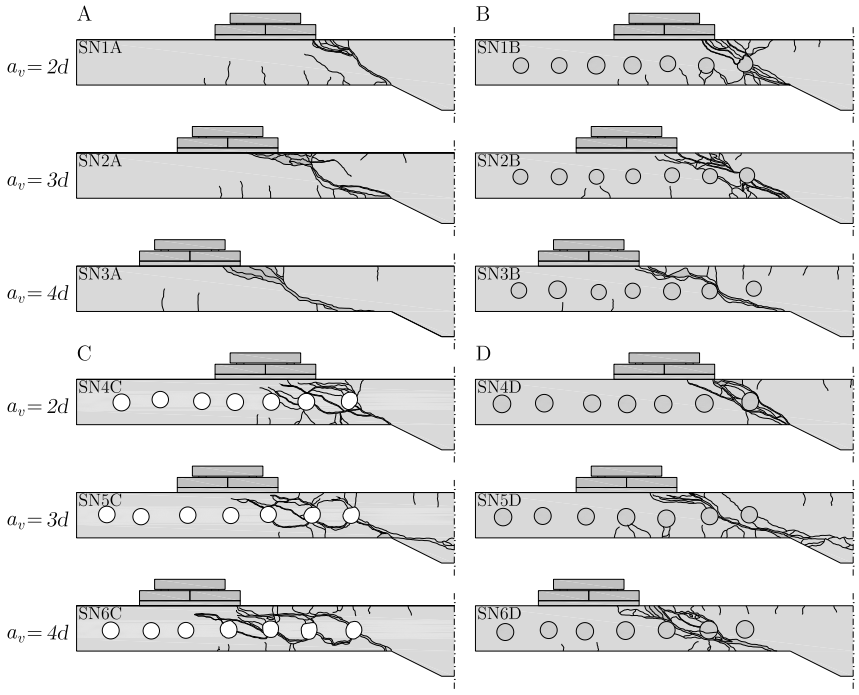

Figure 4.9: Crack patterns after failure: central cuts

4.3.3 Strength

Table 4.3 presents the maximum loads for all tests. No significant differences were observed between the strength of slabs with injected ducts and those without ducts. On the contrary, the strength of slabs with empty ducts was in average 26% smaller than those of reference slabs without ducts. A comparison between the strengths of all tests is shown in Figure 4.10, normalized by the square-root of f_c and the square of d. The results show that the normalized shear strength reduces for larger values of the a_v/d ratio despite the fact that the unitary shear force should be larger for lower values of the ratio a_v/d (refer to Figure 2.17). This result is interesting as it denotes a significant influence of the arching action (refer to the relatively large strength of tests with $a_v/d = 2$) but also a potential influence of the bending moments on the shear strength. This latter influence can further be observed by comparing the results of $a_v/d = 3$ and 4 (both with limited arching action).

4.3.4 Thickness variation

The thickness increase of slabs (which is related to the vertical opening of the inclined shear crack, refer to Figure 4.11) was recorded during the tests. The maximum measured thickness increases for all tests at maximum load $V_{\max}$ are presented in Figure 4.12. Figure 4.13 shows the interpolated records for one representative test (using a cubic function for this purpose). Significant thickness increases were observed before the maximum load was reached (with values up to 8 mm). It can also be noted that the

Test	a_v/d	Ducts	$V_{\max}$ [kN]	$V_{\max}/(d^2\sqrt{f_c})$	ratio to reference test*
SN1A	2	no ducts	489	3.85	
SN2A	3	no ducts	330	2.60	
SN3A	4	no ducts	328	2.57	
SN1B	2	injected, polypropylene	437	3.56	0.92
SN2B	3	injected, polypropylene	341	2.72	1.04
SN3B	4	injected, polypropylene	330	2.62	1.02
SN4D	2	injected, steel	494	3.98	1.03
SN5D	3	injected, steel	335	2.71	1.04
SN6D	4	injected, steel	327	2.63	1.02
SN4C	2	non-injected, steel	307	2.49	0.65
SN5C	3	non-injected, steel	266	2.16	0.83
SN6C	4	non-injected, steel	234	1.90	0.74

* ratio between the normalized load of the specimen ($V_{\max}/(d^2\sqrt{f_c})$) and the one corresponding to the reference specimen with same load location

Table 4.3: Maximum loads for all tests

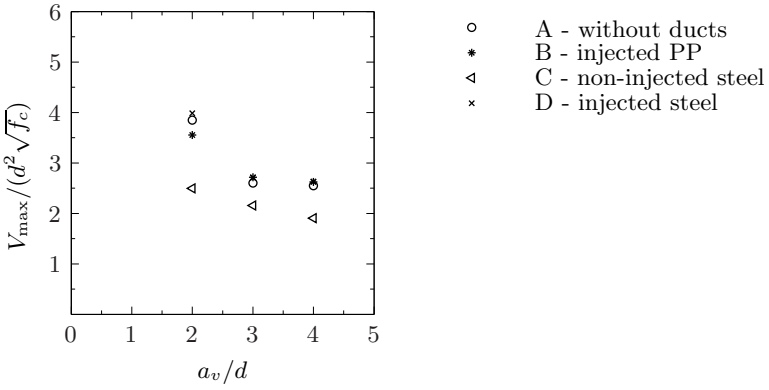

Figure 4.10: Maximum loads for all tests

thickness increase was almost negligible up to about 60% of the maximum load, growing at an increasing rate thereafter (Figure 4.13(e)).

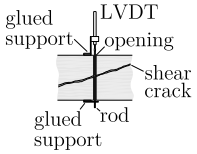

Figure 4.11: Measurement of thickness increase related to critical shear crack opening

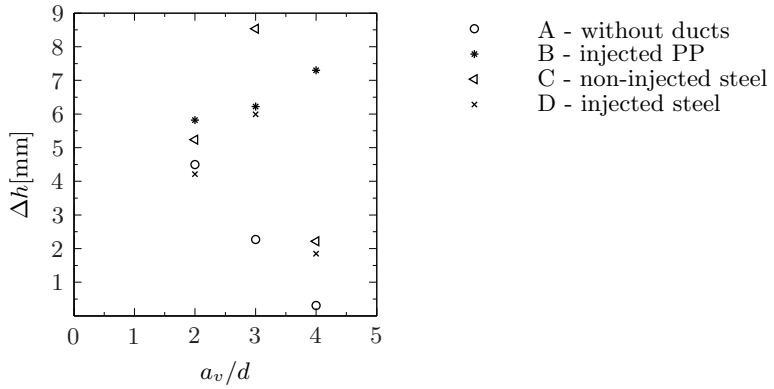

Figure 4.12: Maximum measured thickness increase at $V_{\max}$

Figure 4.14 presents the interpolated values of thickness variation at the moment of maximum applied load $V_{\max}$ for all tests.

4.3.5 Line reaction

The reaction along the line support could be calculated based on the average strain at each of the 30 strain gauge locations of the I-shaped aluminium profile, assuming an elastic behavior of the aluminium and considering a constant strain at the contributing area of each gauge. Good agreement was found between the total measured reaction R_{tot} and the total applied force V_{tot}, with relative errors at maximum load of less than 5% for all tests, except SN6 (where it remained below 10%). Measurements on the reaction along the support line were not performed for the second loading (after strengthening) since the shear field in the strengthened zone is potentially influenced by the strengthening elements. The results for all tests are plotted in Figures 4.15 and 4.16. They show clear and rather significant redistributions of the reactions. For low load levels, the reaction concentrates mostly in the zone close to the load (refer to Figure 2.17). As the level of applied load increased (particularly above 60% of the maximum applied load), the reaction in the region close to the load increased at a slower rate and eventually decreased transferring the load to the adjacent regions. The load levels at which this phenomena was observed are consistent with those observed for the development of the

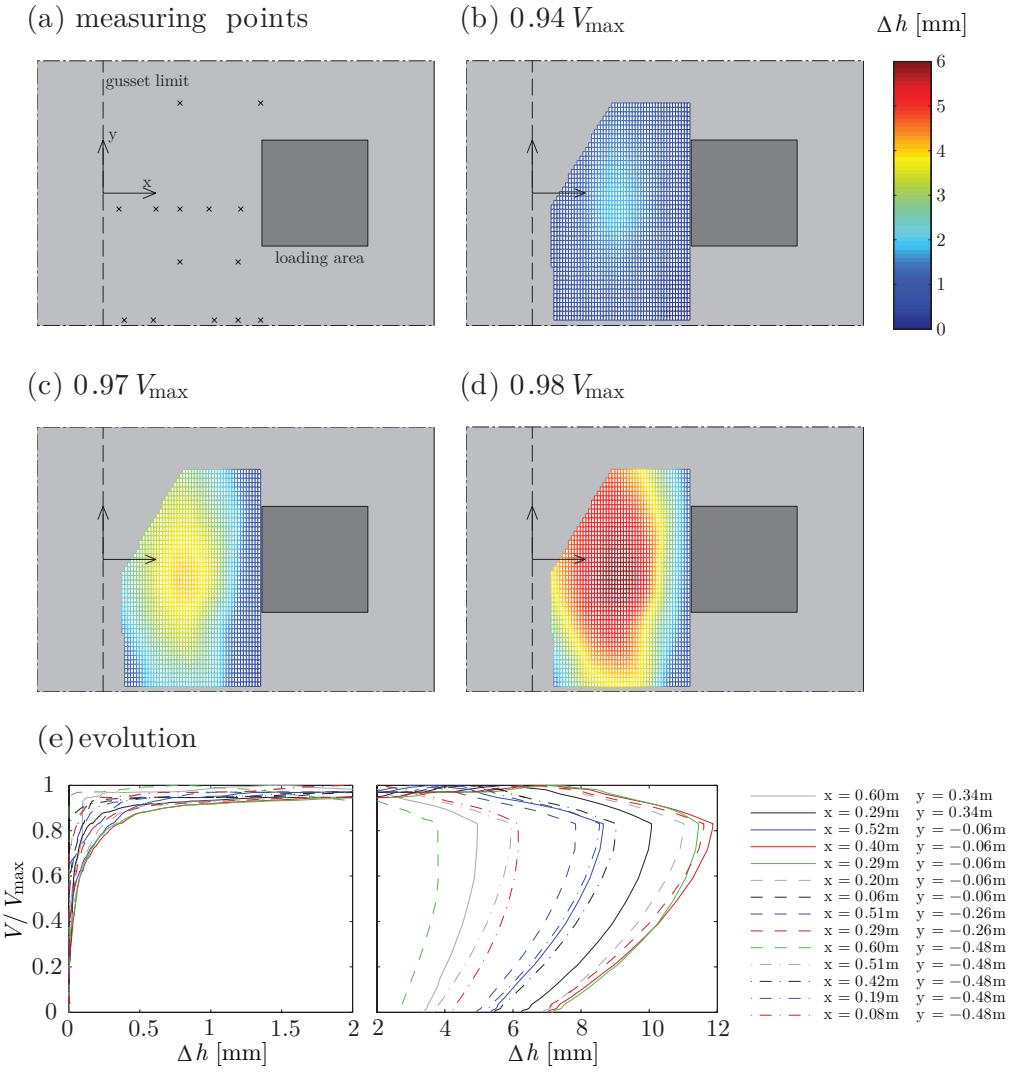

Figure 4.13: Thickness variation in test SN3B ($a_v = 4d$) with injected plastic ducts: **(a)** measuring points; **(b,c,d)** interpolated surfaces of thickness increases; and **(e)** evolution of thickness increase with applied load

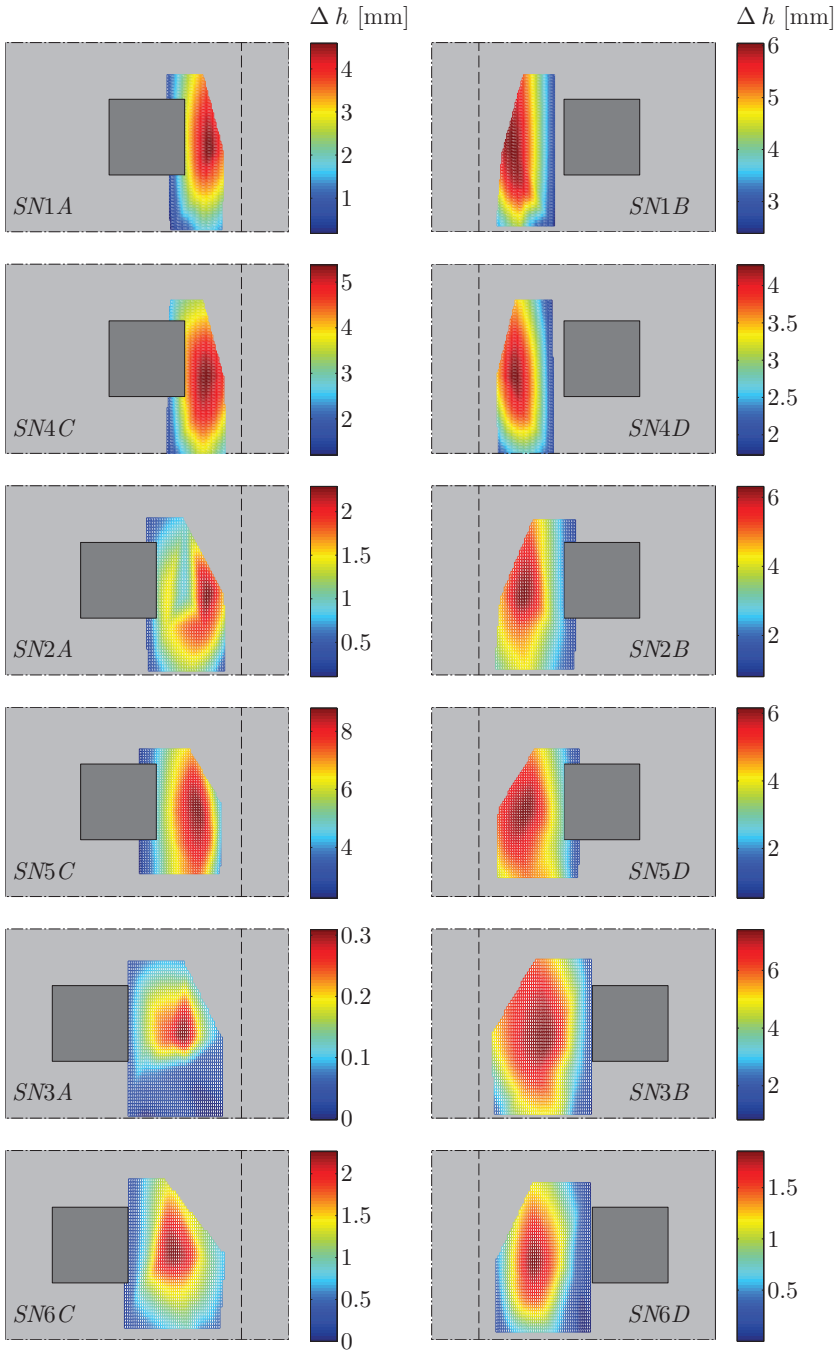

Figure 4.14: Thickness variation at $V_{\max}$ (in [mm])

inclined shear cracks previously presented. The region influenced by this softening behavior is also in accordance with the region where most significant variation of thickness was observed (Figure 4.13).

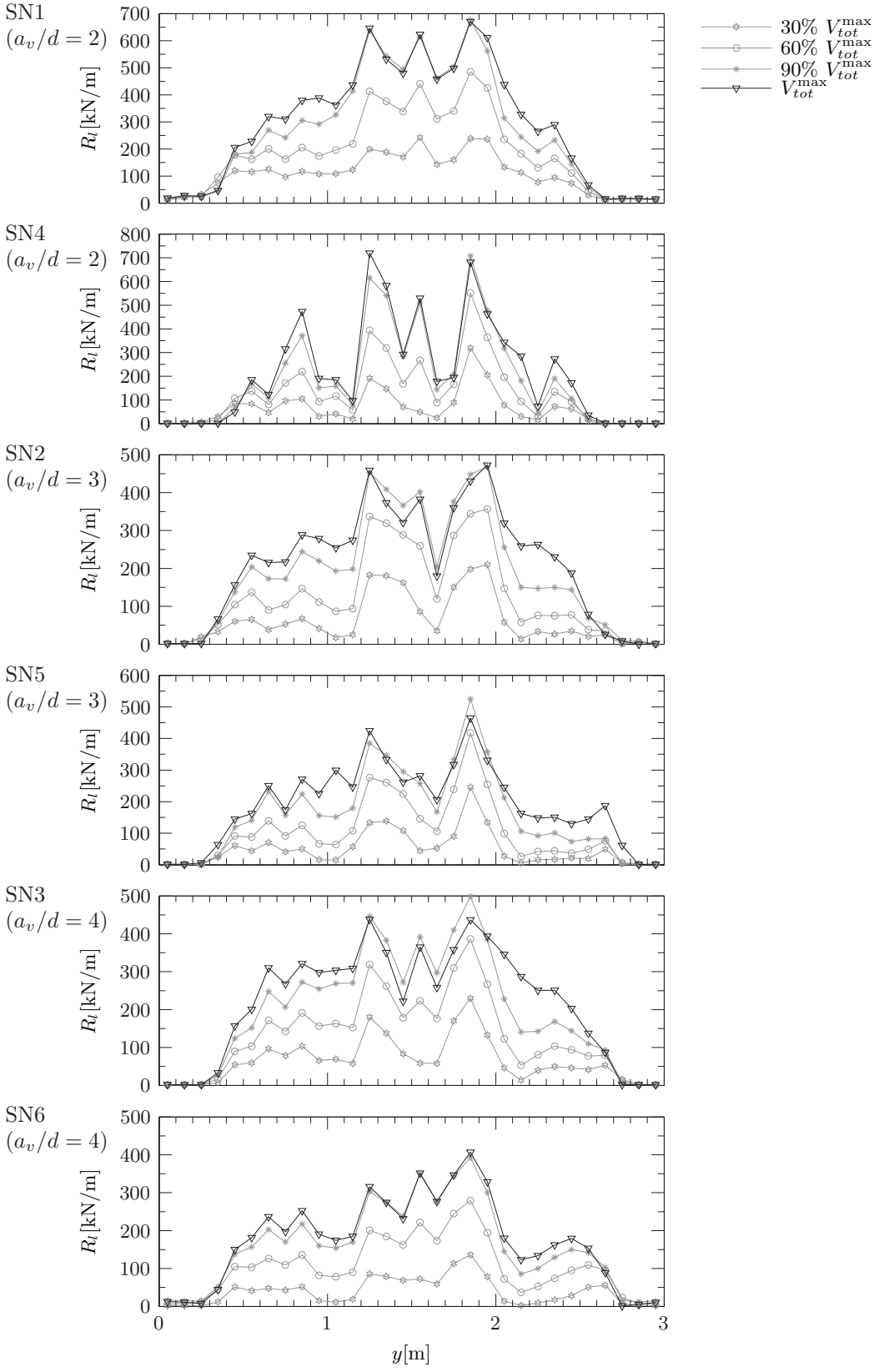

Figure 4.15: Measured line reactions

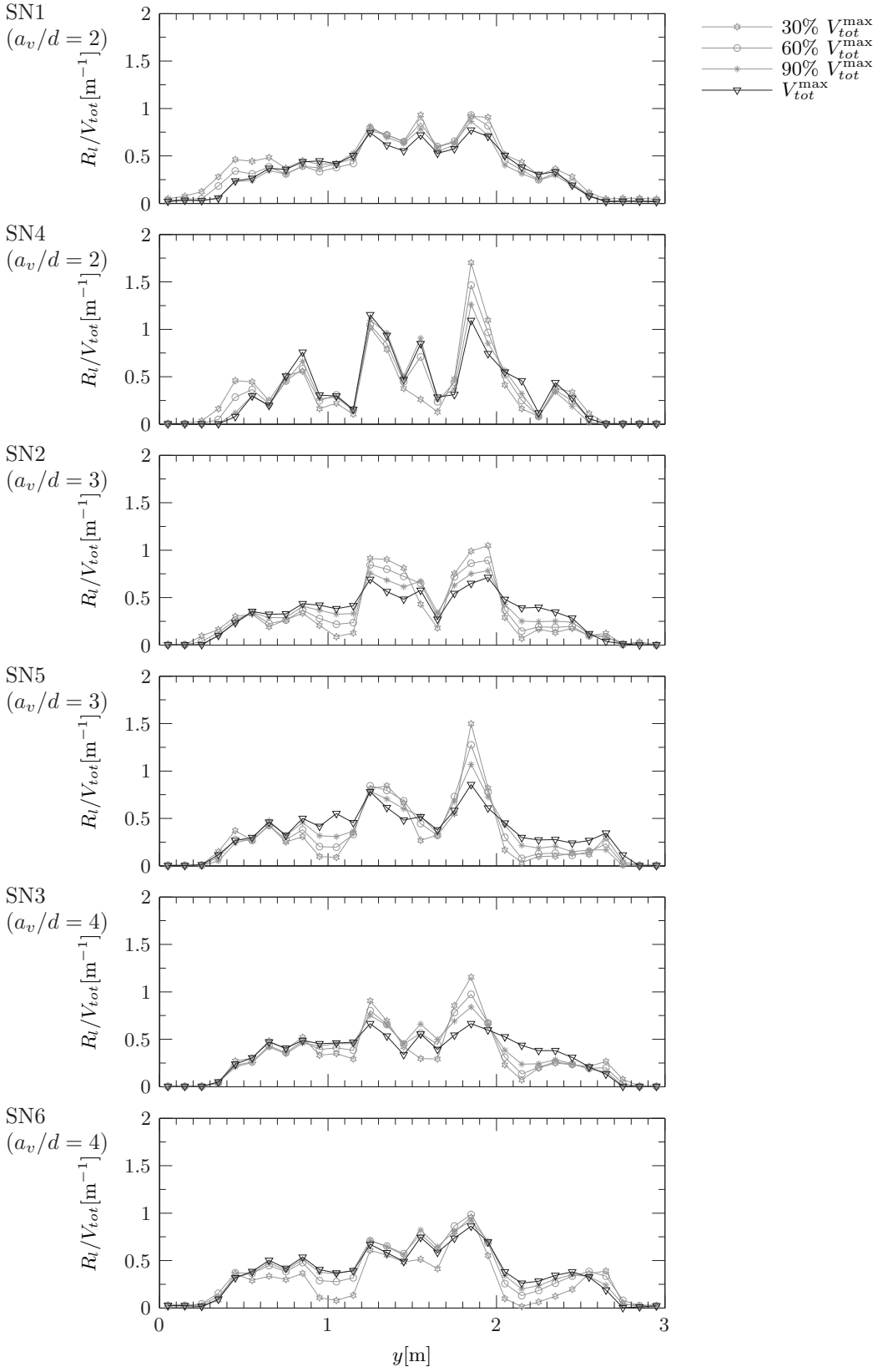

Figure 4.16: Normalized measured line reactions

Chapter 5

Fatigue Experimental Campaign

5.1 Introduction

This chapter describes the main aspects and results of one experimental fatigue campaign on cantilever slabs under concentrated loads near linear supports carried out within the framework of this thesis.
The campaign comprises four static tests on two full scale slabs (3.00 m x 3.00 m x 0.25 m) and eleven other fatigue tests on eight slabs, corresponding to two different loading locations.
Detailed test results are available in a specific test report. The summary of the main aspects and results of this test campaign presented in this thesis can also be found in references [Nat14b, Nat15a, Nat15b].

5.2 Campaign

To the author's knowledge no fatigue tests are available in the literature on cantilever slabs under concentrated loads, whose mechanical behaviour may significantly differ from simply supported slabs (Section 2.10). In order to provide such experimental evidence, an experimental programme has been performed within the framework of this thesis. The specimens were full-scale slabs (3.00 m x 3.00 m x 0.25 m) with a central line support and subjected to a single concentrated load on both sides of the support. Four static tests were performed on two slabs (two tests per slab and load location) and eleven fatigue tests on eight slabs (four slabs per load location).
Other topics as the influence of moving loads [Per88, Per89, Hwa10] or the influence of impact loading on shear strength [Mic14] are not investigated within this thesis.

5.2.1 Specimens

Ten slabs (FN1-FN10) were tested. The slabs had 3.00 m x 3.00 m x 0.25 m dimensions and contained only flexural reinforcement.

The geometry and reinforcement layout were the same for all slabs (Figure 5.1). The bending top reinforcement in the x-transverse direction (perpendicular to the support) consisted of 20 mm diameter bars spaced 150 mm with a nominal effective depth $d_{xt} =$ 210 mm (nominal reinforcement ratio $\rho_{xt} = 1.00$ %), and the bottom one 16 mm diameter bars spaced 150 mm with a nominal effective depth $d_{xb} = 212$ mm ($\rho_{xb} = 0.63$ %). In the longitudinal direction, the top reinforcement consisted of 12 mm diameter bars spaced 150 mm ($d_{yt} = 194$ mm, $\rho_{yt} = 0.39$ %) and the bottom one 10 mm diameter bars spaced 150 mm ($d_{yb} = 199$ mm, $\rho_{yb} = 0.26$ %), refer to Figure 5.1.

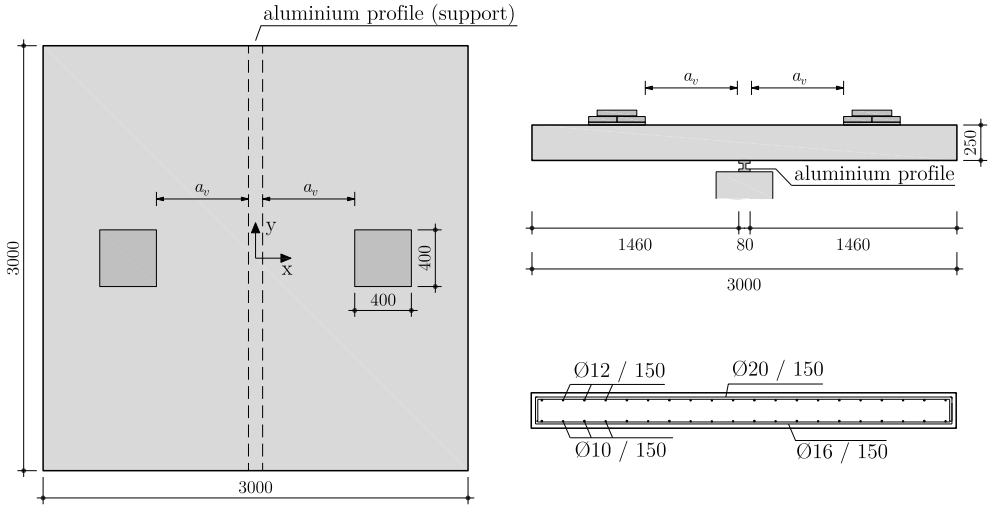

Figure 5.1: Geometry and reinforcement layout of tested slabs (dimensions in [mm])

5.2.2 Material properties

Normal strength concrete was used in all slabs. Table 5.1 presents the compressive strength and modulus of elasticity (measured on concrete cylinders, 320 mm high, 160 mm diameter), as well as the age of concrete at the time of slab testing. The compressive strength ranged from 32.3 MPa to 46.6 MPa and the modulus of elasticity from 28′000 MPa to 35′000 MPa. One cubic meter of concrete had a nominal composition of 832 kg of sand, 378 kg of gravel ranging between 4 to 8 mm, 681 kg of gravel ranging from 8 to 16 mm, 310 kg of Portland cement and 111 kg of water. The maximum aggregate size d_g was 16 mm for all specimens.
Conventional reinforcing bars were used in the specimens. The average reinforcement mechanical properties of 3 tests per diameter are presented in Table 5.2 and the stress-strain relationships in Figure 5.2.

5.2.3 Test setup

The test setup is shown in Figure 5.3. The test setup is similar to the one of the static campaign (Section 4.2.3), just differing on the size of the loading frame and on the used

slab	side	a_v [mm]	type of test	age (start-end)	f_c [MPa] (start-end)	E_c[MPa] (start-end)
FN1	W	440	static	129	45.2	33'000
FN1	E	440	static	186	46.6	34'000
FN2	W	440	fatigue	97-112	38.2-38.7	30'500
FN2	E	440	fatigue	97	38.2	30'500
FN3	W and E	440	fatigue	96-98	36.2	30'000
FN4	W	440	fatigue	102-110	38.4-38.6	30'500
FN4	E	440	fatigue	102	38.4	30'500
FN5	W and E	440	fatigue	34-63	32.3-34.8	28'000-29'500
FN6	W	680	static	144	45.7	33'000
FN6	E	680	static	178	46.5	34'000
FN7	W and E	680	fatigue	322	44.8	35'000
FN8	W	680	fatigue	298-325	43.5-43.7	34'500
FN8	E	680	fatigue	298-476	43.5-44.6	34'500-35'000
FN9	W and E	680	fatigue	305-316	44.7	35'000
FN10	W and E	680	fatigue	328-396	43.7-44.2	34'500-35'000

Table 5.1: Properties of test specimens

slab	ϕ_{rebar}[mm]	f_y[MPa]*	f_u[MPa]	type
FN1, FN6, FN7, FN8, FN9, FN10	20	579	680	quenched & self-tempered
	16	553	650	quenched & self-tempered
	12	520	620	quenched & self-tempered
	10	504	595	quenched & self-tempered
FN2, FN3, FN4, FN5	20	600	700	quenched & self-tempered
	16	595	709	quenched & self-tempered
	12	523	591	cold-worked
	10	543	606	cold-worked

* Offset yield-point at 0.2% strain for cold-worked rebar

Table 5.2: Mechanical properties of the reinforcement

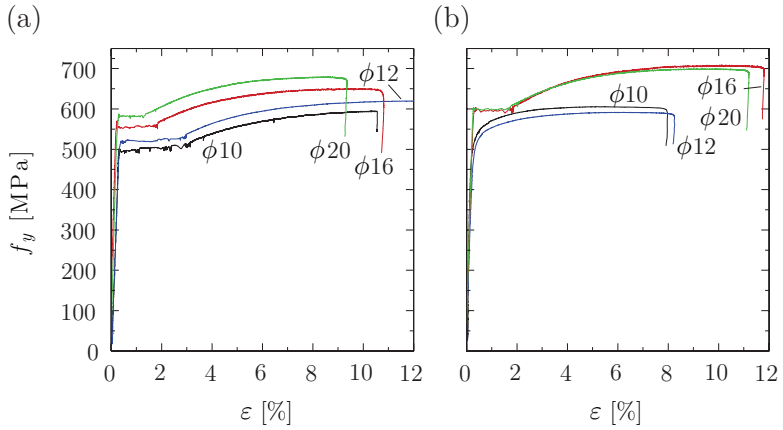

Figure 5.2: Measured stress-strain relationships of reinforcement bars: **(a)** FN1, FN6, FN7, FN8, FN9 and FN10; and **(b)** FN2, FN3, FN4 and FN5

actuators.
Two different loading locations were investigated, corresponding to a clear distance from the line support (a_v) of 440 mm and 680 mm (Figure 5.1) (2.1d and 3.2d respectively, where $d(= d_{xt})$ is the nominal effective depth of the slab).
After failure occurred on one side of the slab, that side was strengthened using steel external profiles and plates bolted on top and bottom faces, by means of prestressed bars (Figure 4.6). After strengthening, the test was continued, leading to a second failure on the other side.

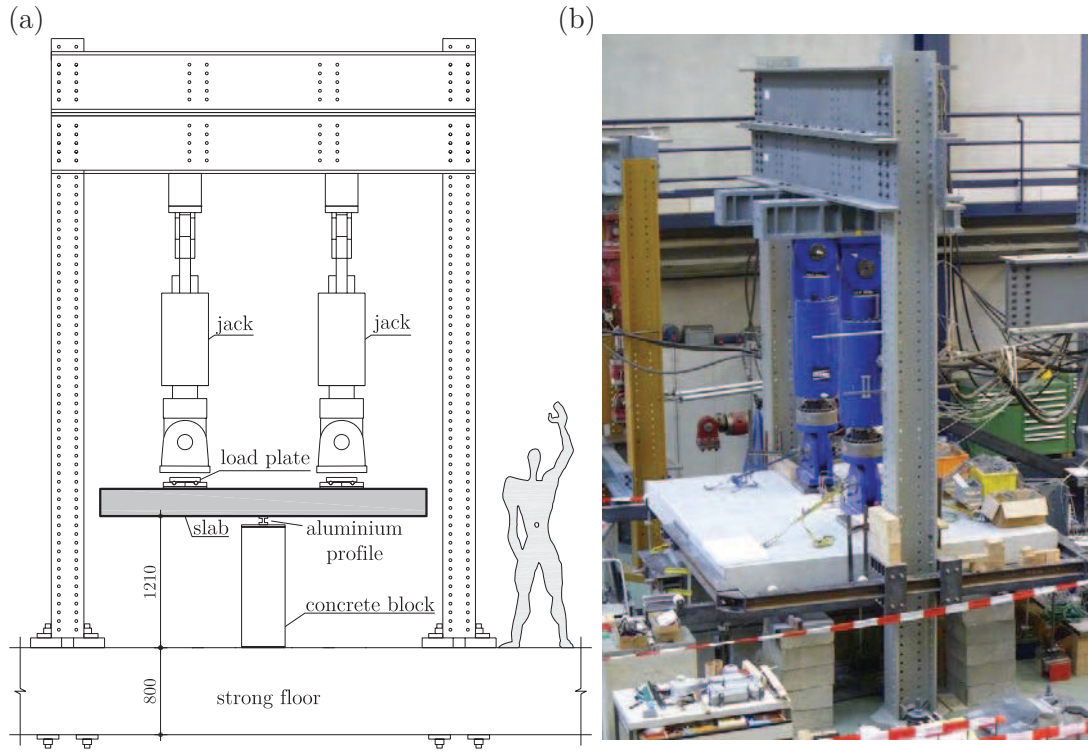

Figure 5.3: Test setup (dimensions in [mm]): **(a)** side view; and **(b)** picture

5.2.4 Test procedure

Two slabs were tested quasi-statically in order to obtain the reference static strengths (V_{Ref}) for each load location. Each slab provided two reference tests (duplicated values). The fatigue loading was done in a combined force-displacement control mode. The forces of the two actuators were controlled taking partially advantage of test setup symmetric conditions. The average force of both jacks was kept constant and both forces corrected to keep the relative displacement between them lower than 10 mm. Differences between maximum applied forces on both sides were lower than 1% for five tested slabs (FN3 and FN7-FN10), between 2-3% for two other slabs (FN2 and FN4), and 3.1% for the remaining one (FN5).
The target ratio R between the minimum ($V_{\min}$) and the maximum ($V_{\max}$) applied forces

was 0.10, and the actual values varied between 0.09 - 0.12, refer to Table 5.3. These values are reasonable as in actual bridge deck slabs the ratio R of the traffic load is 0.0, yet dead load is also acting. A qualitative representation of the fatigue loading history is given in Figure 5.4.

For each load location four different levels (LL) of maximum applied load were used. The maximum applied load was corrected in order to account for small differences of concrete compressive strength between fatigue and reference tests, as follows:

$$V_{\max} = LL \cdot V_{Ref} \sqrt{\frac{f_c}{f_{c,Ref}}} \tag{5.1}$$

where V_{Ref} is the average static strength of the two reference tests, f_c is the concrete compressive strength at the day when testing started and $f_{c,Ref}$ is the average concrete strength of the two reference tests. For the free shear span $a_v = 680$ mm, the target loading levels LL were 60, 70, 80 and 90%, and for $a_v = 440$ mm 80, 85, 90 and 95%.

The sinusoidal fatigue loading was applied with a loading frequency of 1 Hz, and for some specimens with 0.75 Hz and 0.5 Hz close to failure (FN9 and FN10, due to the required hydraulic debit of the actuators (related to the large displacements experienced by the slabs)).

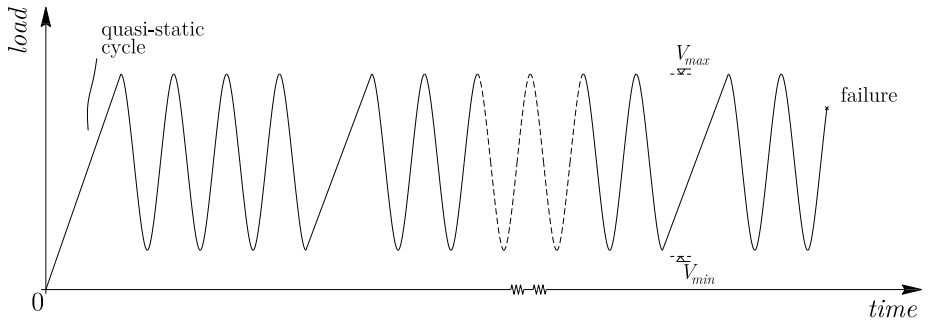

Figure 5.4: Qualitative fatigue loading history

5.2.5 Measurements

Continuous measurements were performed during the fatigue tests, namely the applied forces and the displacements measured by the actuators, thickness variation (up to fifteen points around each loading plate), the strains of selected rebars at some locations using strain gauges, and crack openings (up to ten locations) after the first loading cycle. In addition, measurements were taken in quasi-static tests at selected loading cycles (refer to Figure 5.4), namely the aluminium profile strains (distribution of reaction forces) and the vertical displacements (up to fourteen points).

5.3 Test results

5.3.1 Static reference tests

The quasi-statically tested slabs (reference specimens) failed in shear, in a similar manner as the tests of the static campaign (Chapter 4). Table 5.3 presents the maximum loads for all static tests. For both loading locations, once the maximum load was attained, the slabs presented a softening behavior, with a significant decrease of the applied load for increasing displacements (Figures 5.5(a,c)).

The crack patterns on the top surfaces developed parallel to the linear support in the central region, while on the bottom surface, cracking was mostly perpendicular to the support line and concentrated near the loading area, refer to Figures 5.5(b,d). The observed failure crack in the central section of the saw-cuts (refer to Figures 5.5(a,c)) was similar to shear cracking of beams (or one-way slab strips loaded over the full width) without shear reinforcement. For the largest shear span, the shear crack developed almost horizontally in the compression zone (slab soffit) near the support edge. In this case, the shear crack intercepted the top transverse reinforcement with a steep angle and at a distance approximately equal to d from the loading plate edge. The concrete cover spalled in this region due to dowel action of the main reinforcement. For the shorter shear span, the shear crack was steeper and straighter on average, also intercepting the upper main reinforcement at a distance approximately equal to d from the loading plate edge. The critical shear crack of both slabs seems to develop from a flexural crack at a certain distance from the loading plate (and not from the tip of the loading plate). Additionally it exhibits a horizontal branch close to the load due to dowel action, allowing to classify these failures as typical shear failures and not as punching failures around the load.

The reaction along the support line could be estimated (refer to Figures 5.6(a,b)) based on the strain at each of the thirty locations of strain gauges of the I-shaped aluminium profile. As previously observed in the static campaign (Section 4.3.5), close to failure the reaction in the central region increased at a lower rate or even decreased transferring the load to the adjacent regions. The level of load at which this phenomenon was observed is consistent with those observed for the development of the inclined shear crack, whose vertical opening is related with the increase of thickness of the slabs recorded during the tests, refer to Figure 5.7 for a representative case. The figure also shows that the reaction tends to concentrate in the middle part of the support line as the applied force at the concentrated load increases (associated to the uplift of the extremities).

5.3.2 Fatigue tests

All slabs except FN5 (a_v = 440 mm; target LL = 80%), FN9 (a_v = 680 mm; target LL = 70%) and FN10 (a_v = 680 mm; target LL = 60%) failed in shear-fatigue without rebar fractures. Table 5.3 presents the main results of the test campaign. Figure 5.8 depicts the Wöhler diagrams for each loading location normalized by the average failure loads of the static reference tests. The ratio between the maximum applied loads (fatigue

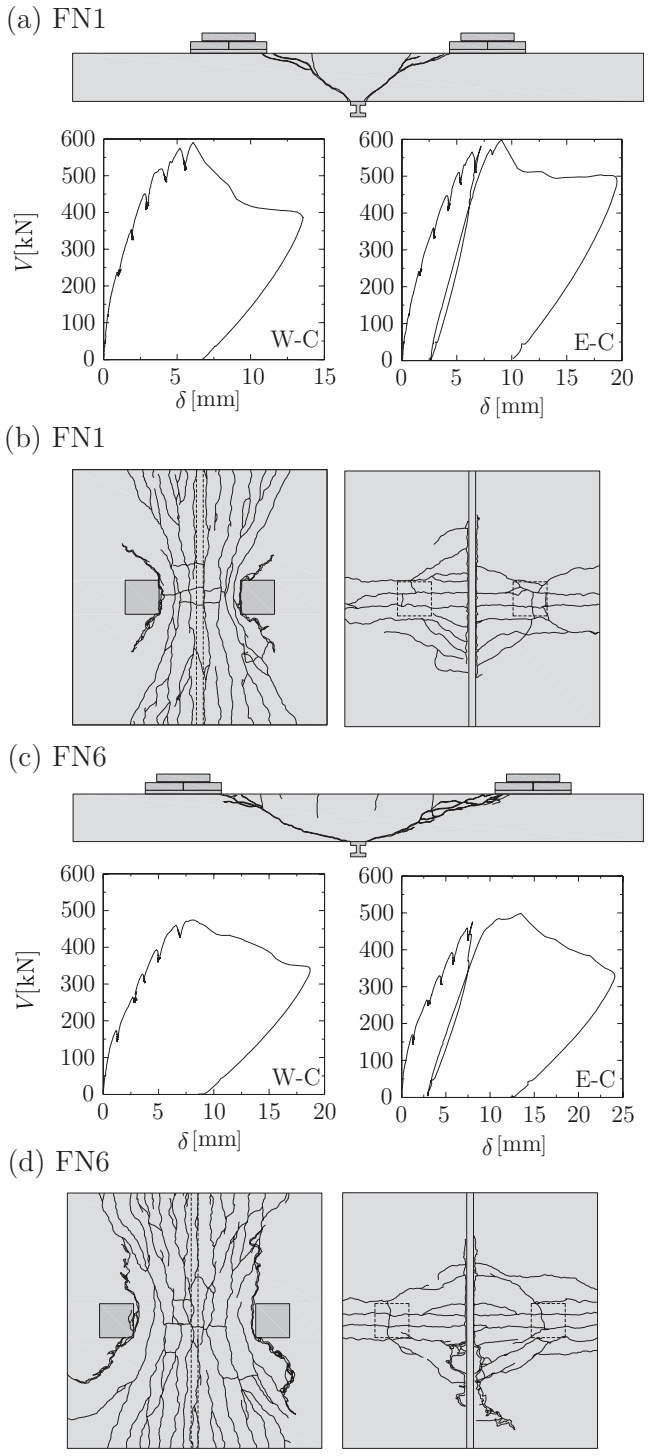

Figure 5.5: Reference static tests: **(a)** central saw-cut and load deflection-curves at the center of the loading plates of slab FN1 ($a_v = 440$ mm); **(b)** top and bottom crack patterns of slab FN1; **(c)** central saw-cut and load deflection-curves at the center of the loading plates of slab FN6 ($a_v = 680$ mm); and **(d)** top and bottom crack patterns of slab FN6

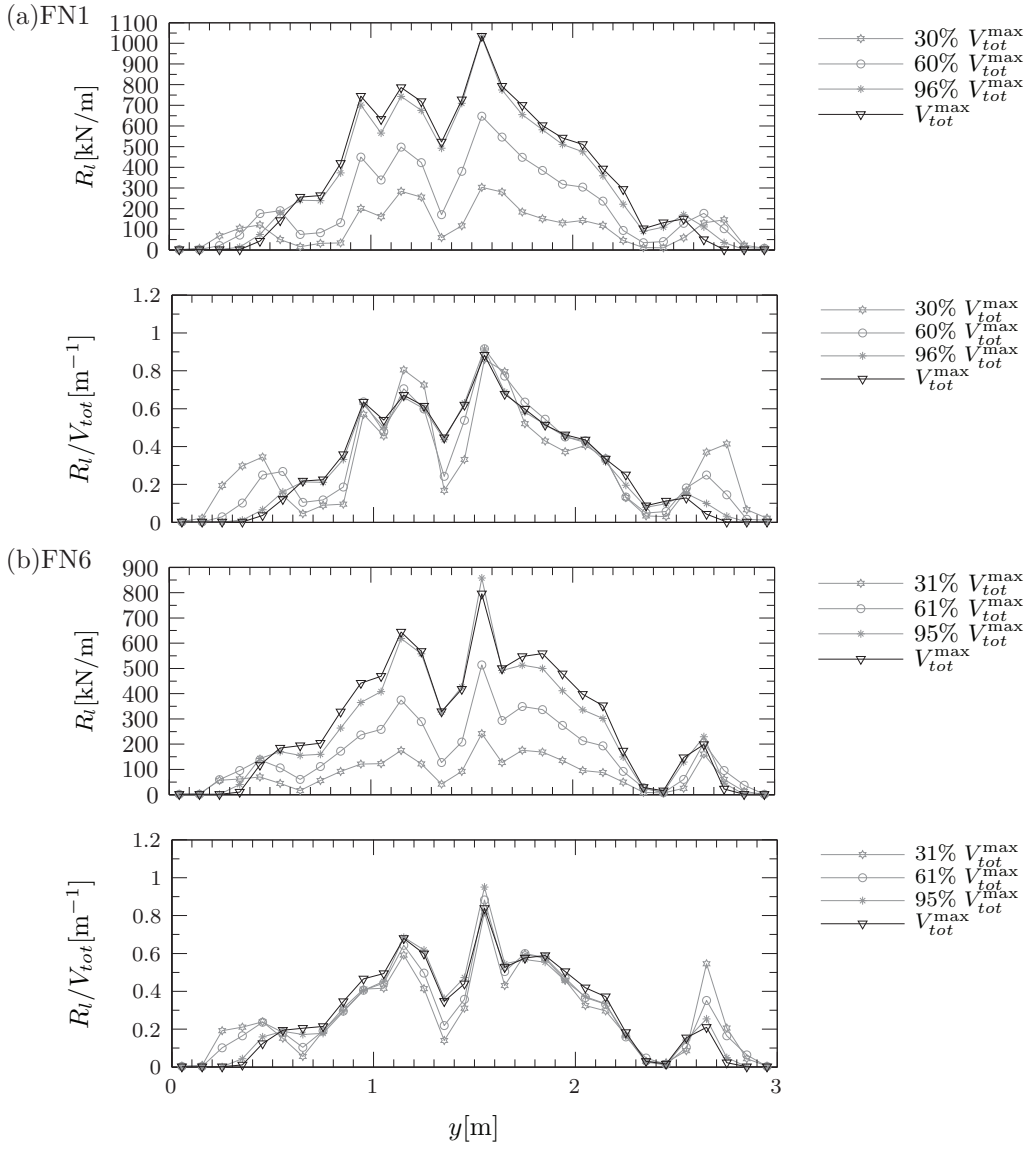

Figure 5.6: Reference static tests: **(a)** measured and normalized linear reaction evolution in the first test of slab FN1 ($a_v = 440$ mm); **(b)** measured and normalized linear reaction evolution in the first test of slab FN6 ($a_v = 680$ mm)

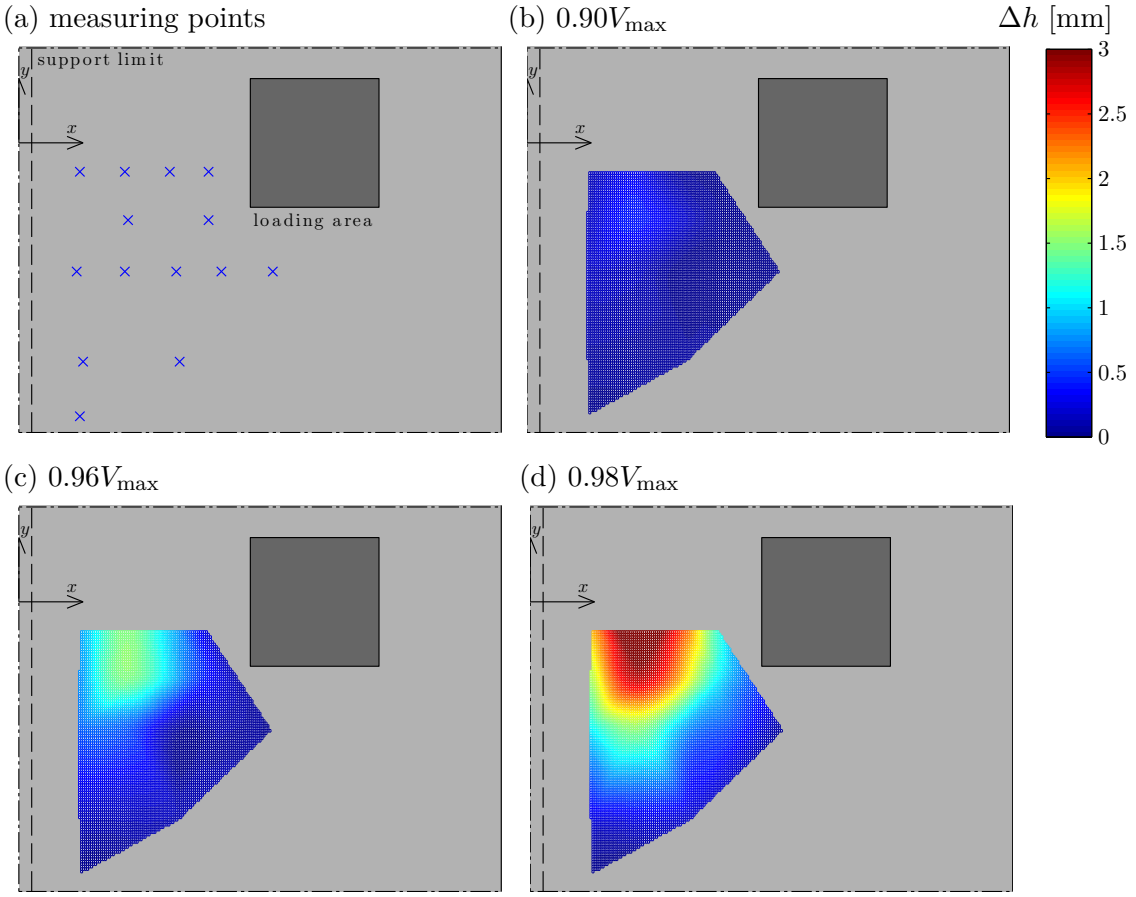

Figure 5.7: Thickness variation in slab FN6 (a_v = 680 mm) side E: **(a)** measuring points; and **(b-d)** interpolated surfaces of thickness increases (in [mm])

slab	side	a_v [mm]	type	V_{max} [kN]	V_{min} [kN]	R	actual LL [%]	cycles N	measured d_{xt} [mm]*	measured d_{yb} [mm]**	FM***
FN1	W	440	static	591	-	-	-	1	203	201	S
FN1	E	440	static	597	-	-	-	1	203	201	S
FN2	W	440	fatigue	520	53	0.10	96	1'350	212	209	S
FN2	E	440	fatigue	506	54	0.11	93	990	212	209	S
FN3	W	440	fatigue	473	48	0.10	90	72'340	214	203	S
FN3	E	440	fatigue	472	48	0.10	90	72'340	214	203	S
FN4	W	440	fatigue	467	47	0.10	86	17'300	208	209	S
FN4	E	440	fatigue	456	49	0.11	84	15'560	208	209	S
FN5	W	440	fatigue	394	36	0.09	79	501'810	210	209	RF
FN5	E	440	fatigue	382	44	0.12	77	501'810	210	209	RFFS
FN6	W	680	static	474	-	-	-	1	190	201	S
FN6	E	680	static	499	-	-	-	1	190	201	S
FN7	W	680	fatigue	427	46	0.11	89	824	197	201	S
FN7	E	680	fatigue	427	46	0.11	89	824	197	201	S
FN8	W	680	fatigue	378	42	0.11	80	5'007	210	201	S
FN8	E	680	fatigue	376	42	0.11	80	5'193	210	201	S
FN9	W	680	fatigue	333	35	0.11	70	311'200	200	201	RF
FN9	E	680	fatigue	334	38	0.11	70	311'200	200	201	RFFS
FN10	W	680	fatigue	281	30	0.11	59	734'760	199	199	RFFS
FN10	E	680	fatigue	282	30	0.11	60	734'760	199	199	RFFS

* average value measured in the middle region of the center transversal saw-cut
** average value measured in the region under the loading plates in the center transversal saw-cut
*** FM - failure mode; S - shear; RF - rebar fracture; RFFS - rebar fracture followed by shear

Table 5.3: Main properties of tested specimens

strength) and the static shear strengths are normalized with the square-root of the concrete compressive strength ($\sqrt{f_{c,Ref}/f_{c,fat}}$).

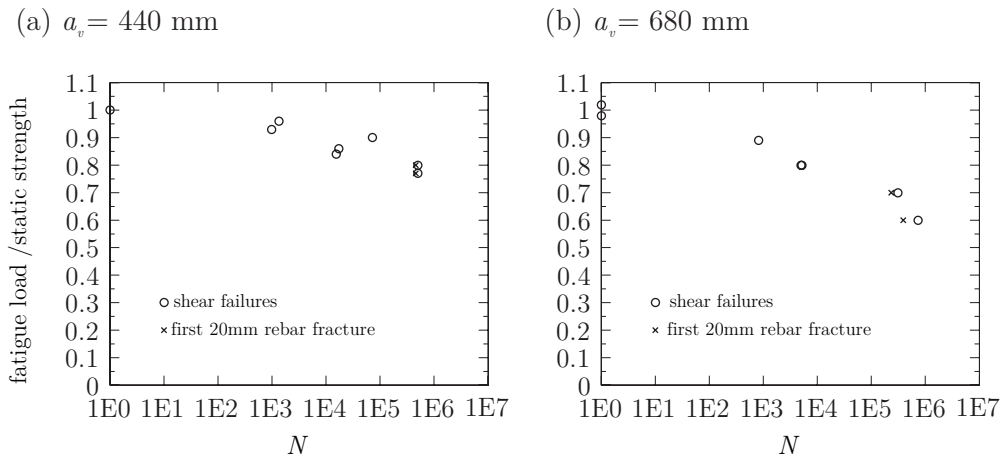

Figure 5.8: Wöhler diagrams of tested slabs: **(a)** $a_v = 440$ mm; and **(b)** $a_v = 680$ mm

The slabs that failed in shear-fatigue presented similar crack patterns to the static reference specimens (Figures 5.9 and 5.10). The slabs which exhibited rebar fractures eventually failed in shear as well (except FN9-W), due to excessive flexural crack openings that propagated into critical shear cracks. This failure mode is similar to the shear failure observed after yielding of longitudinal reinforcement described in reference [Vaz10]. Tests with a free shear span $a_v = 680$ mm that failed with rebar fractures presented eight transversal 20 mm rebar fractures located at the top surface in the center line, as well as some 10 mm longitudinal rebar fractures on the bottom surface, developing a full flexural mechanism, refer to Figure 5.11. The 10 mm bars were located at the transversal section that passes through the middle of the loading plates, between the load and the free edge.

The test with free shear span $a_v = 440$ mm which presented rebar fractures is somewhat different from previous cases. Three 20 mm rebars failed between the center line and one loading plate, at the intersection between the critical shear crack that developed from a flexural crack and the main flexural reinforcement, not developing a flexural mechanism. Dowel action might have generated additional stresses in the rebars due to local bending. This might have potentially contributed to an increase of the fatigue damage of the bars in this region.

All bars failing under fatigue loading were extracted from the tested specimens after failure to confirm the fatigue failures, refer to Figure 5.12.

Determining the cycle when the first 20 mm rebar failure took place was performed through cross-interpretation of the strain evolution measured in strain gauges placed at the center of some selected 20 mm rebars and the evolution of crack openings (devices to track crack opening evolution were placed at selected cracks after the first loading cycle), refer to Figure 5.13 for two representative cases. When a top transversal 20 mm

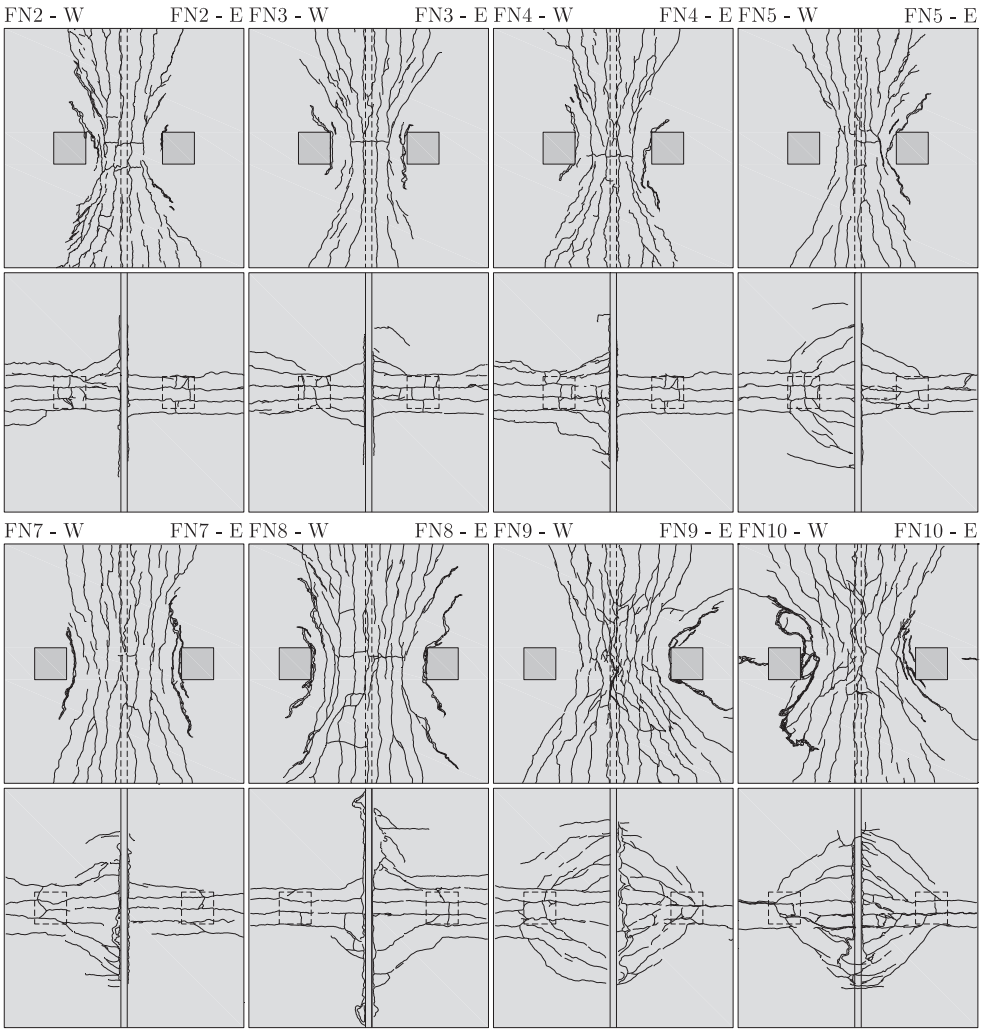

Figure 5.9: Crack patterns: top and bottom faces

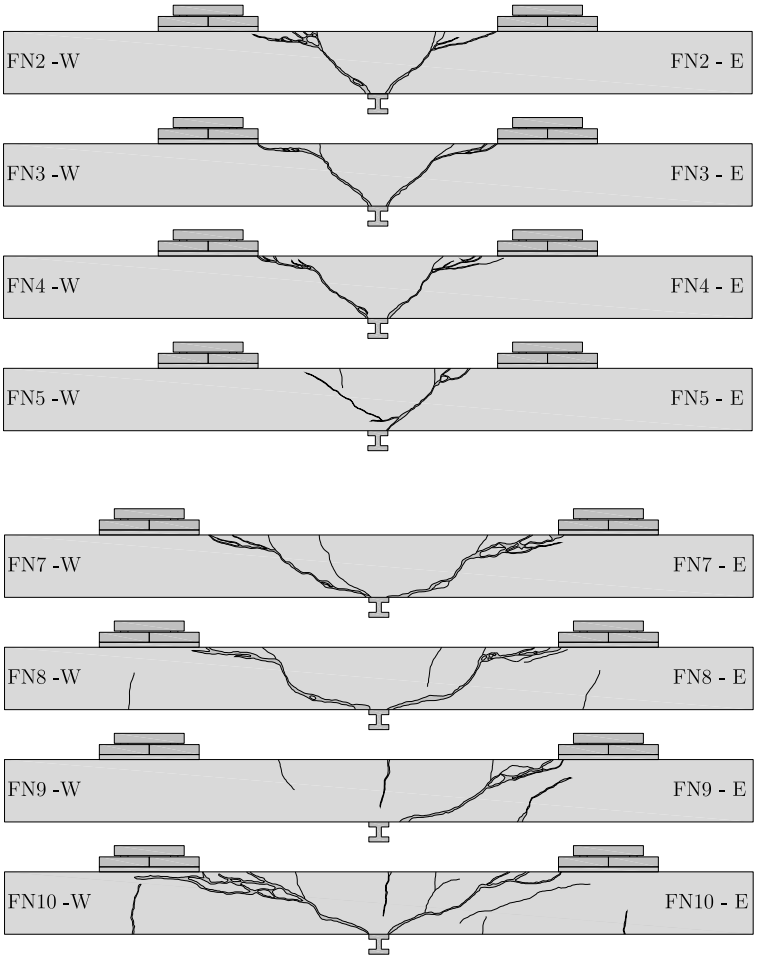

Figure 5.10: Crack patterns: central saw-cuts

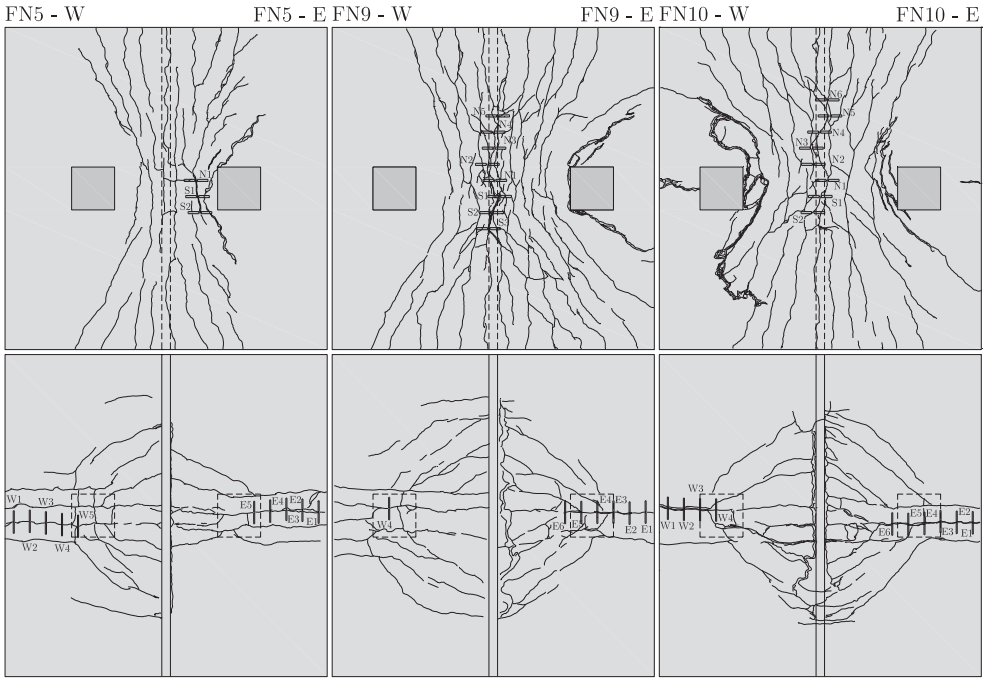

Figure 5.11: Crack patterns and location of rebar fractures

Figure 5.12: Failed rebars due to fatigue

diameter rebar failed, the measured strain in the failed rebar diminished abruptly and the strain measurement in adjacent bars increased noticeably. This phenomenon could also be tracked by devices which measured crack openings in the vicinity of the failed bar, as a rebar failure contributes to larger crack openings. The determination of the cycle when the 10 mm bars failed was not possible. All slabs that failed due to rebar fractures presented a remaining life after the first 20 mm rebar fracture occurred. The slabs FN9 and FN10 ($a_v = 680$ mm) that developed a full flexural mechanism exhibited a significant one, 24.5% and 46.9% of the total endurance in this regime respectively, while FN5 ($a_v = 440$ mm) whose bars failed due to dowel action only had an additional 8.3% of the endurance in this state. It is relevant to note that the number of cycles until the first 20 mm rebar fracture for FN5 was approximately twice the number of FN9.

The fatigue loading led to progressive stiffness reductions for all tests. This phenomenon could be observed in the load-deflection evolution curves, refer to Figures 5.14 and 5.15 for a representative case.

The linear reaction also varied with the fatigue loading. Close to failure, for both test types failing with or without rebar fractures, load transfer from the central region to the adjacent ones was observed, refer to Figure 5.16 and Figures 5.17 and 5.18 for representative cases of both types. This is consistent with the observed results for quasi-static (reference) specimens near failure and confirms the capacity of these members to redistribute internal forces near failure.

The slab thickness increase of some tests failing in shear-fatigue without rebar fractures is shown in Figures 5.19 and 5.20. It is interesting to note that important thickness variations of more than 3 mm occurred many cycles before failure in the region between the loading plate and the support. At failure these values can be larger than 10 mm, what explains the important line reaction redistributions previously discussed.

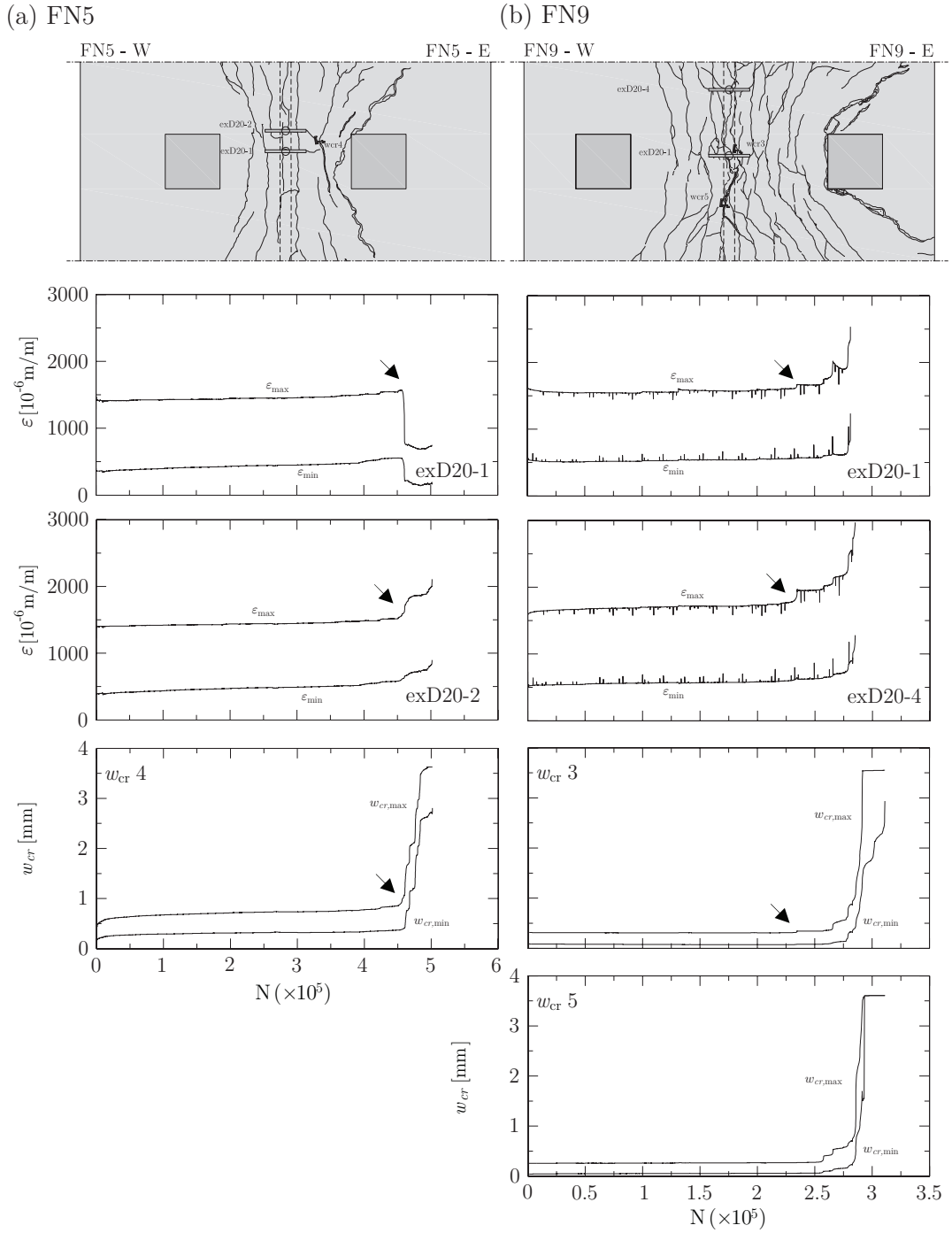

Figure 5.13: Minimum and maximum measured strain evolution in the main transversal reinforcement and crack opening evolutions (maximum measurable value of approximately 3.5 mm): **(a)** FN5 ($a_v = 440$ mm); and **(b)** FN9 ($a_v = 680$ mm)

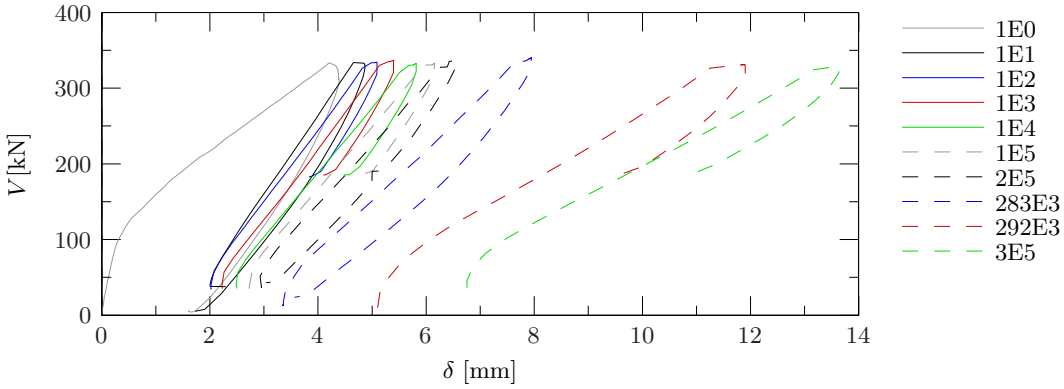

Figure 5.14: Load-deflection evolution measured at the center of the loading plate of tested slab FN9-E ($a_v = 680$ mm)

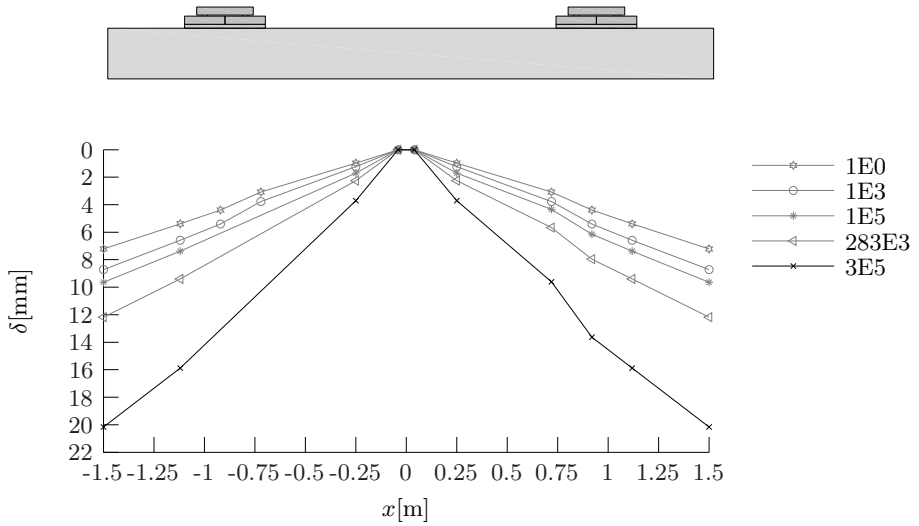

Figure 5.15: Displacements in central section of slab FN9 ($a_v = 680$ mm)

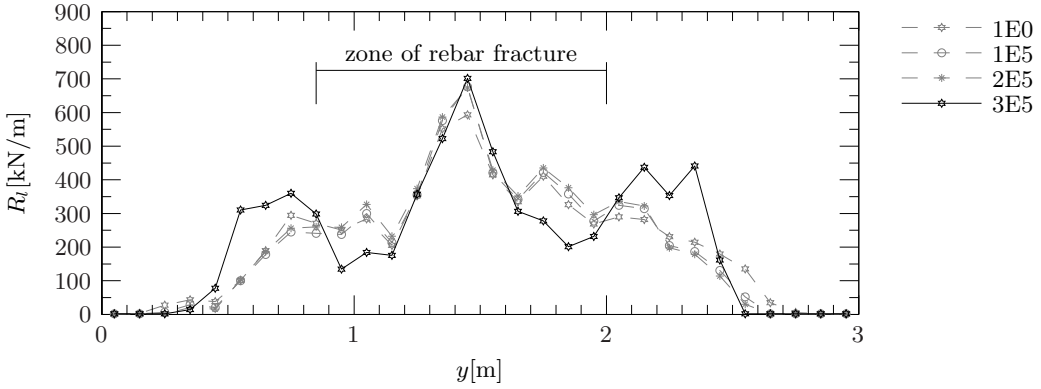

Figure 5.16: Line reaction evolution of tested slab FN9 ($a_v = 680$ mm) that failed with rebar fractures

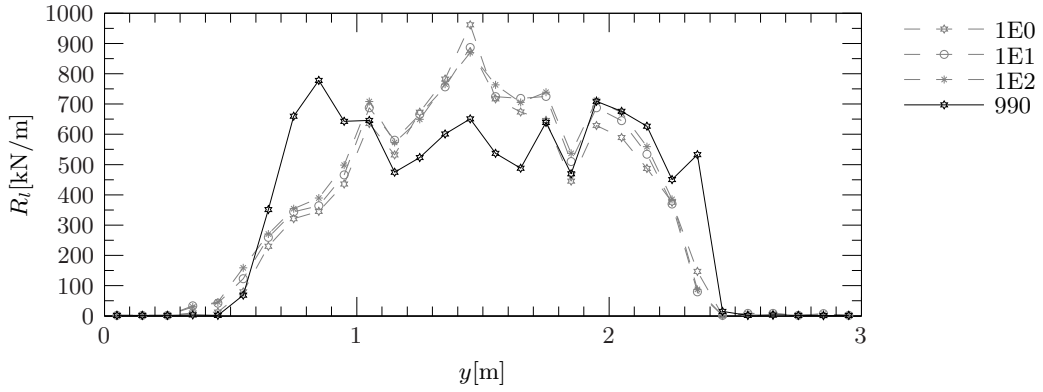

Figure 5.17: Line reaction evolution of tested slab FN2 ($a_v = 440$ mm) that failed in shear-fatigue without rebar fractures

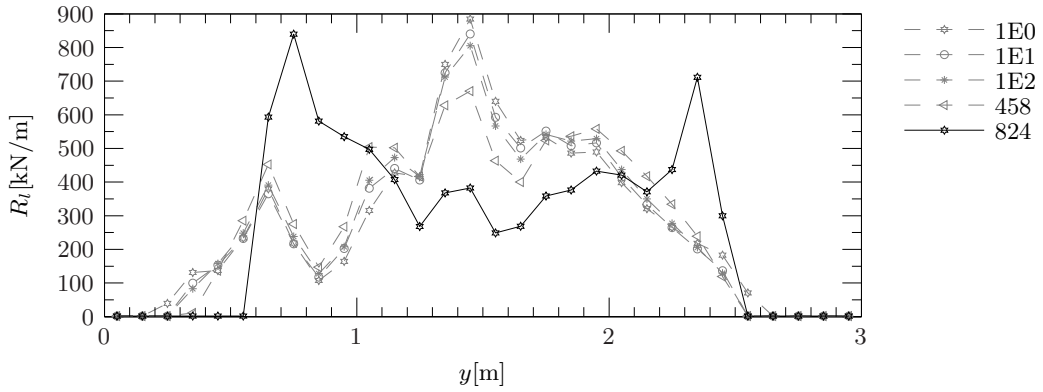

Figure 5.18: Line reaction evolution of tested slab FN7 ($a_v = 680$ mm) that failed in shear-fatigue without rebar fractures

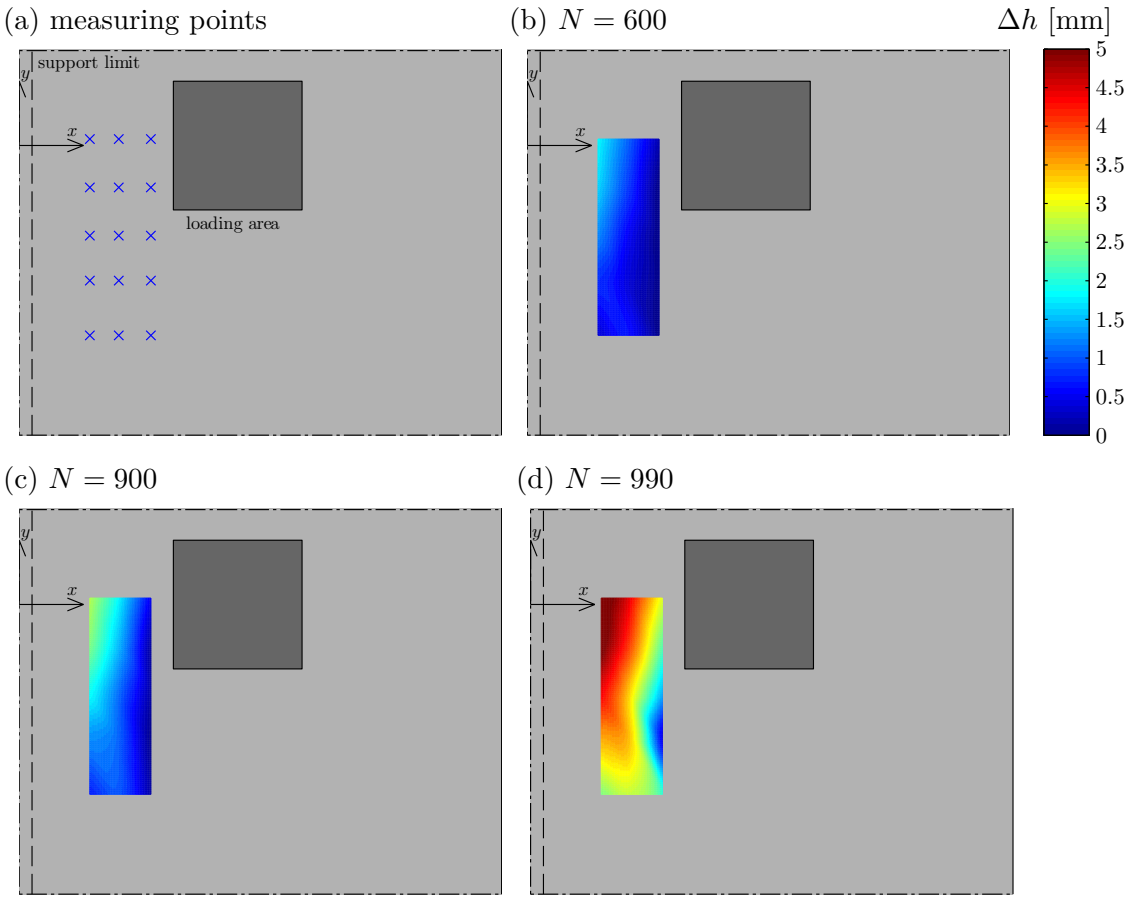

Figure 5.19: Thickness variation in slab FN2-E (a_v = 440 mm): **(a)** measuring points; and **(b-d)** interpolated surfaces of thickness increases (in [mm])

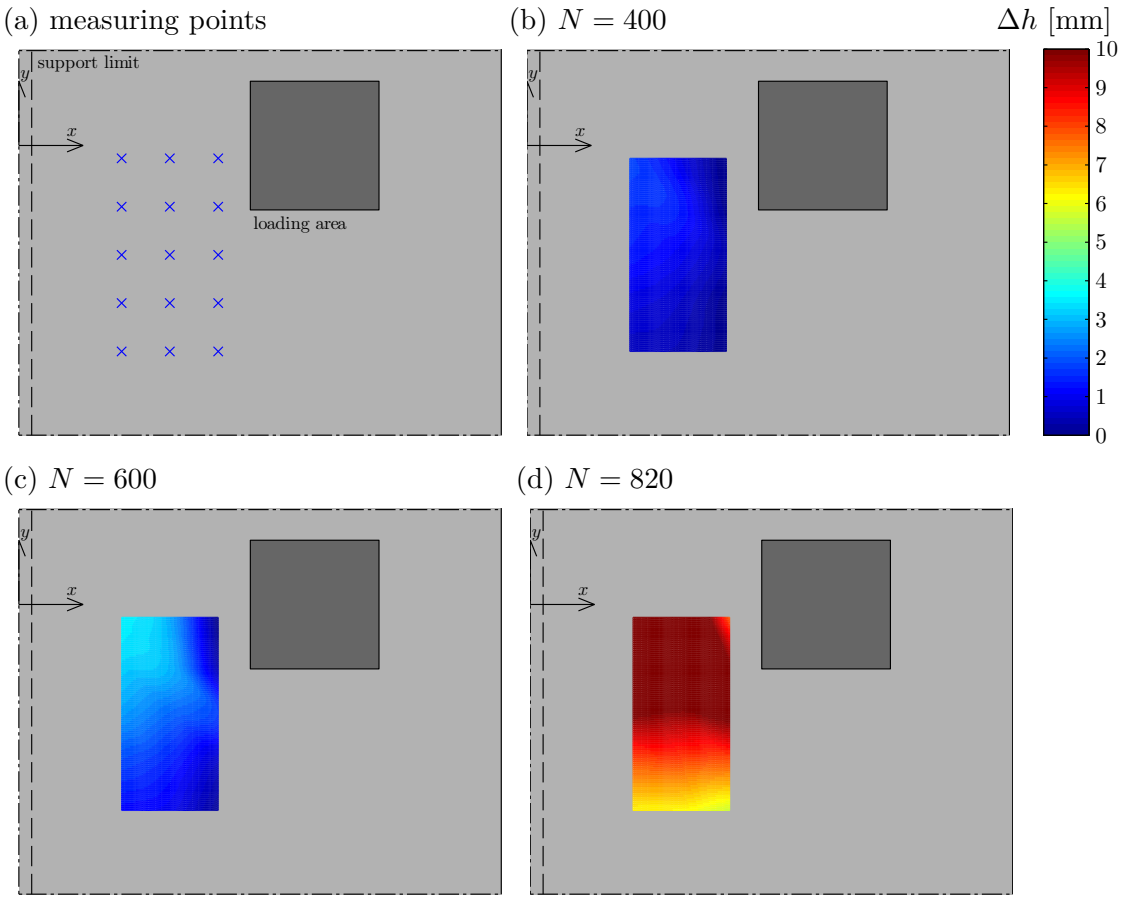

Figure 5.20: Thickness variation in slab FN7-E (a_v = 680 mm): **(a)** measuring points; and **(b-d)** interpolated surfaces of thickness increases (in [mm])

Chapter 6

Shear and punching shear assessment

6.1 Introduction

The present chapter presents several proposals on how to apply the Critical Shear Crack Theory (CSCT) for both shear and punching shear on slabs under concentrated loads near linear supports. With the aim of keeping the proposals at a complexity level comparable to Level III of *fib*-Model Code 2010 [MC2010], the following points are discussed within this chapter:

- Which assumptions can be made in order to use linear elastic finite elements to model reinforced concrete slabs, known by their highly nonlinear behavior;
- How to account for internal forces redistributions due to bending and shear cracking;
- Where to locate the control sections;
- How to account for arching action;
- How to account for empty ducts or pipes placed in the slab core.

The proposals presented in this chapter are assessed on their suitability by performing comparisons with the experimental static tests of this thesis (Chapters 4 and 5) and those found in the literature as presented in Section 2.7 and Section 2.8.
Membrane action (which is known to enhance shear strength [Ein15]) influence was not considered in this thesis.

6.2 Cantilever slabs

In this section the shear assessment of cantilever slabs subjected to concentrated loads near linear supports is investigated, based on the CSCT. As it was shown in Section 2.7, shear is often the governing failure mode of these structures. However, punching shear associated with the peak of shear force near the edge of the loading plate (Figure 2.17) has been reported to be governing in some cases, typically those where the concentrated

loads acts near the cantilever edge [Vaz07].
In comparison with classic punching failures, cantilever slabs under concentrated loads are somewhat different. Figure 6.1 shows the transverse bending moment and shear diagrams in the central section of the statically tested slabs of Chapter 4. In the bridge's longitudinal direction there are positive moments in the concentrated load region, which means that the bottom longitudinal reinforcement is in tension. On the contrary, in the transversal direction, the acting bending moment in the loading plate edge is negative for most of the possible loading configurations, which means that the bottom transversal reinforcement is in compression and the top one is in tension. As a consequence, the shape of the critical shear cracks seems to develop from a flexural crack at the top of the slab, refer to Figure 6.1 and Section 4.3.2.
Slab DR1-a tested by Vaz Rodrigues et al. [Vaz08] (Section 2.7 and Figure 2.23) under four concentrated loads exhibited a detachment of the region around the two farthest loads from the linear support, refer to Figure 6.2. This aspect may lead to the idea that it was a punching failure. However, as it has been previously noticed, in the transversal direction the shear surface seems to develop from a flexural crack associated with negative bending moments. As discussed by Latte [Lat10], if the failure region is not situated between the linear support and the closest loading plates (like in most existing tests), it might be due to the fact that the transversal top reinforcement in the clamped region is twice the one between the closest and farthest loads. However, a second shear crack was also developing between the linear support and the closest loading plates, indicating that failure in this region was imminent.
Real bridge cantilever deck slabs are subjected to important uniform dead loads (besides the self-weight) and linear loads at the cantilever tip, which contribute to even more important transversal negative bending moments, compared with the experimental tests of this thesis and others presented in Section 2.7. Punching shear failures are thus unlikely to occur in cantilever slabs subjected to concentrated loads, and therefore they are not investigated hereafter.

6.2.1 Finite element modeling

Finite element (FE) modeling is a widely spread tool nowadays. Isotropic linear elastic FE analyses (LEFE) are commonly used by engineers to model reinforced concrete structures like bridge deck slabs. Shell finite elements with or without shear deformation are used to model these structures. However, reinforced concrete is highly nonlinear. Nonlinear FE analyses can be performed, but they require larger computation times. Their complexity can vary enormously, depending on the base assumptions. Commercial softwares normally require an important number of parameters which are often difficult to be estimated by engineers. Moreover these softwares are sometimes highly sensitive to some of these parameters.
LEFE analyses offer the advantages of short calculation times and limited number of input parameters. However, in order to account for the slab behavior after flexural cracking and the fact that tensile forces are resisted by an orthogonal layout of reinforcement bars

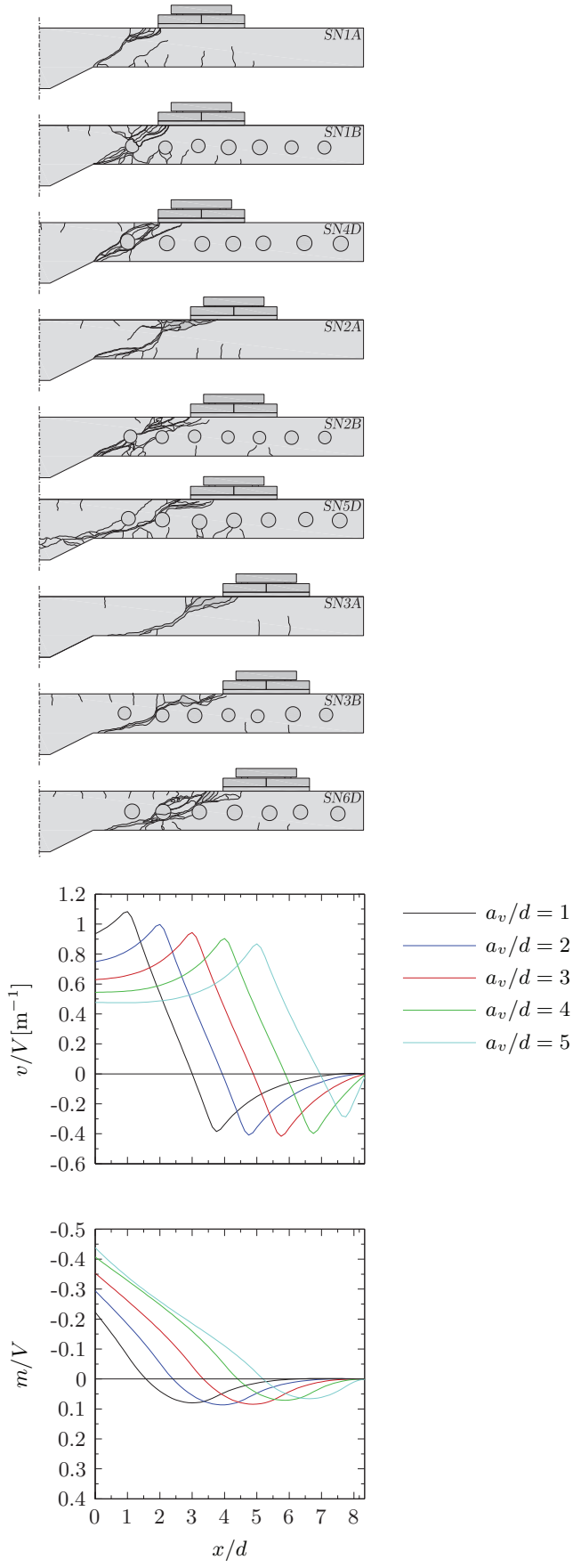

Figure 6.1: Central saw-cuts of SN series and corresponding shear and bending moment diagrams

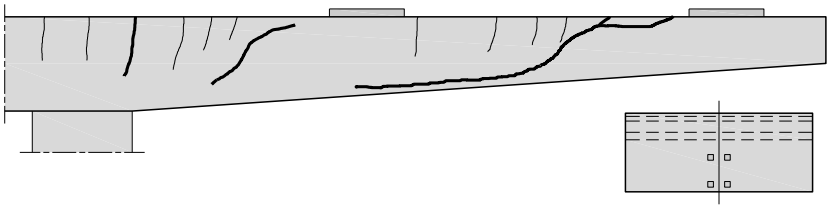

Figure 6.2: Central saw-cut of slab DR1-a tested by Vaz Rodrigues et al. [Vaz08]

that does not correspond to the principal directions of bending moments, an appropriate selection of Poisson's ratio ν and shear modulus G has to be done.

Figure 6.3 shows the comparison between the measured line reactions of the static tests performed in the framework of this thesis (Chapters 4 and 5) and the ones obtained with certain LEFE analyses. Shell finite elements with shear deformation were used (SHELL43 elements of ANSYS ®Academic Research [ANSYS] software). The supports were modeled as linear elastic compression-only supports (axial stiffness of profile's web), refer to Figure 6.4. Four hypothesis were tested:

- $\left(\nu = 0.2; G = \frac{E}{2(1+\nu)}\right)$, where ν is Poisson's coefficient of concrete, E is the Young's modulus of concrete and G is the shear modulus;
- $\left(\nu = 0.2; G = \frac{1}{8}\frac{E}{2(1+\nu)}\right)$;
- $\left(\nu = 0; G = \frac{E}{2(1+\nu)} = \frac{E}{2}\right)$;
- $\left(\nu = 0; G = \frac{1}{8}\frac{E}{2(1+\nu)} = \frac{E}{16}\right)$.

The use of $\nu = 0$ is pertinent for cracked concrete. However, slabs always present compression zones where concrete is not cracked. In order to design these structures Rombach [Rom04] proposes the use of any value between $\nu = 0.0 - 0.2$, provided that at least 20% of the main flexural reinforcement is adopted in the perpendicular direction. The use of $\frac{1}{8}G$ in the slab plane to account for cracking in the torsional stiffness had already been proposed by Vaz Rodrigues [Vaz07]. This reduction is justified by the fact that the bending stiffness is more important in the directions of reinforcement bars, compared to diagonal directions. For this assumption to be valid, the local axis of the finite elements must coincide with the directions of the orthogonal reinforcement bars.

Adopting $\left(\nu = 0; G = \frac{E}{16}\right)$ seems to be the investigated approach that best-fits the measured line reactions at failure.

All the LEFE calculations at failure performed hereafter were done with shell finite elements (SHELL43 elements of ANSYS ®Academic Research [ANSYS] software) with shear deformation and $\left(\nu = 0; G = \frac{E}{16}\right)$, which yields the following material constitutive law for the used element:

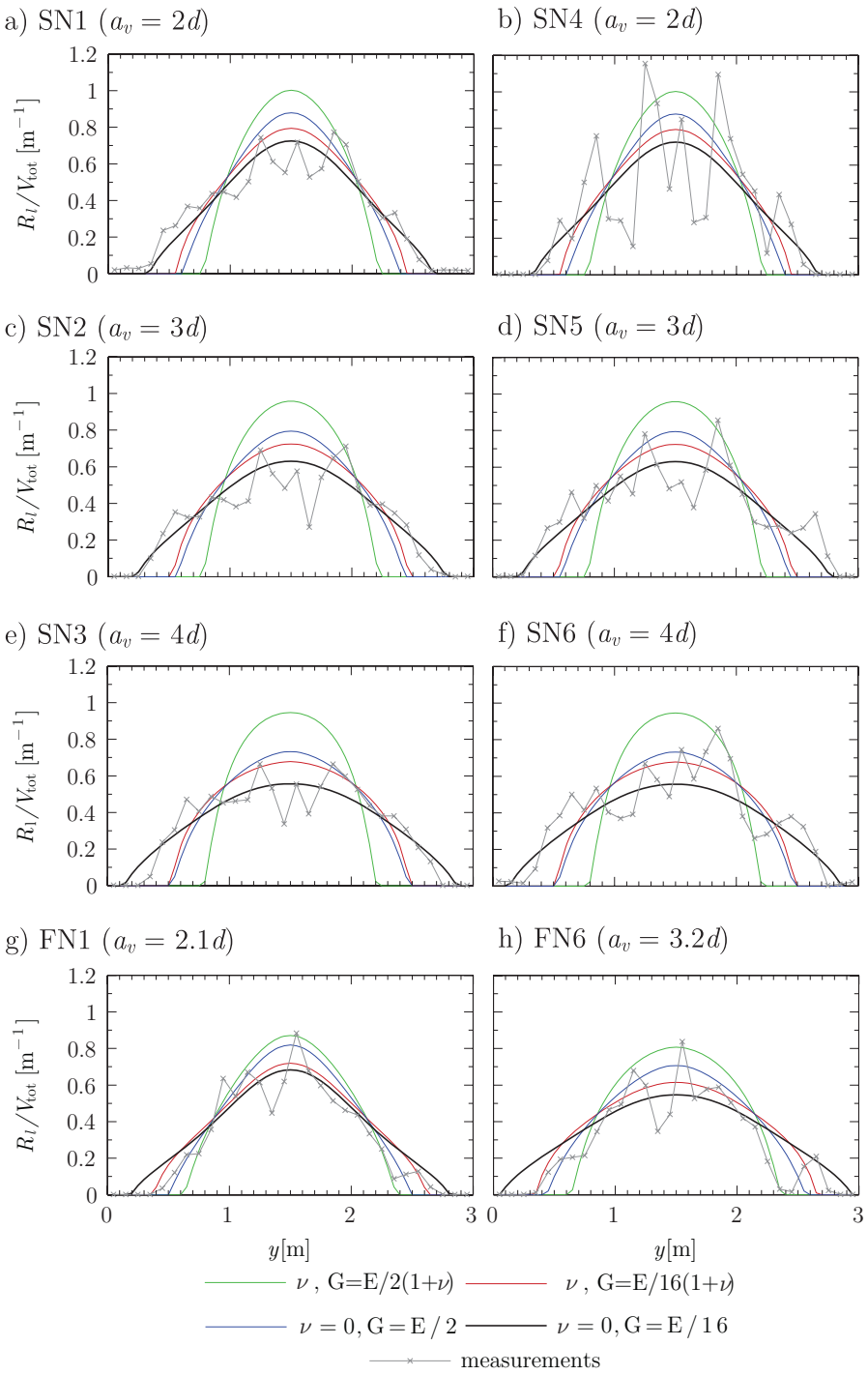

Figure 6.3: Comparison between measured line reactions at failure and the ones obtained with certain LEFE analyses

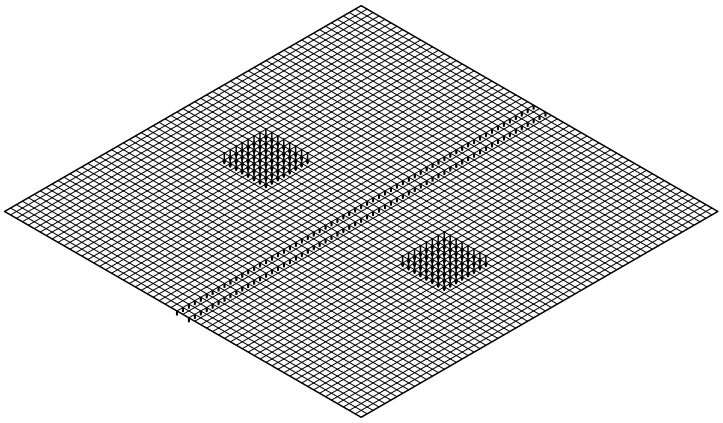

Figure 6.4: FE mesh used in SN and FN tests

$$\begin{bmatrix} \sigma_x \\ \sigma_y \\ \sigma_z \\ \sigma_{xy} \\ \sigma_{yz} \\ \sigma_{xz} \end{bmatrix} = \begin{bmatrix} E & 0 & 0 & 0 & 0 & 0 \\ 0 & E & 0 & 0 & 0 & 0 \\ 0 & 0 & 0 & 0 & 0 & 0 \\ 0 & 0 & 0 & G & 0 & 0 \\ 0 & 0 & 0 & 0 & \frac{G}{1.2} & 0 \\ 0 & 0 & 0 & 0 & 0 & \frac{G}{1.2} \end{bmatrix} \begin{bmatrix} \varepsilon_x \\ \varepsilon_y \\ \varepsilon_z \\ \varepsilon_{xy} \\ \varepsilon_{yz} \\ \varepsilon_{xz} \end{bmatrix} \tag{6.1}$$

The concentrated loads were modeled as surface pressures and line loads as nodal loads. Self-weight was neglected.

6.2.2 Control section and internal forces

For consistency with the CSCT principles (Section 3.2), the control section for checking one-way shear in clamped slabs subjected to concentrated loads is located near the support, as the highest bending moments developing in this region increase crack openings and reduce thus the shear strength, refer to Section 2.6 and Figure 2.17. In agreement with the proposed control section for beams under point loads [Mut08a] the control section is located at distance $d/2$ from the support (or the gusset edge in SN series). This distance has nevertheless to be limited to $a_v/2$.

LEFE calculations based on the uncracked behavior of reinforced concrete show a significant reaction force concentration along the transversal x symmetry axis, refer to Figure 6.3. Nevertheless, as previously shown in Section 4.3.5, the I-shaped profile measurements show that a significant redistribution of internal forces occurs at this region. This phenomenon must be related to bending and shear cracking, as in SN series reinforcement yielding has to be excluded.

In order to account for both bending and shear redistributions when using LEFE calculations based on the uncracked behavior of reinforced concrete, Natário el al. [Nat14a] proposed the adoption in a simplified manner of the average shear force in a distance $4d$

($v_{avg,4d}$, refer to Figure 6.5) centered at the location of maximum shear and combined with the bending moment at that location, which results in a simple approach for its use in practice. This approach was validated for the SN series.

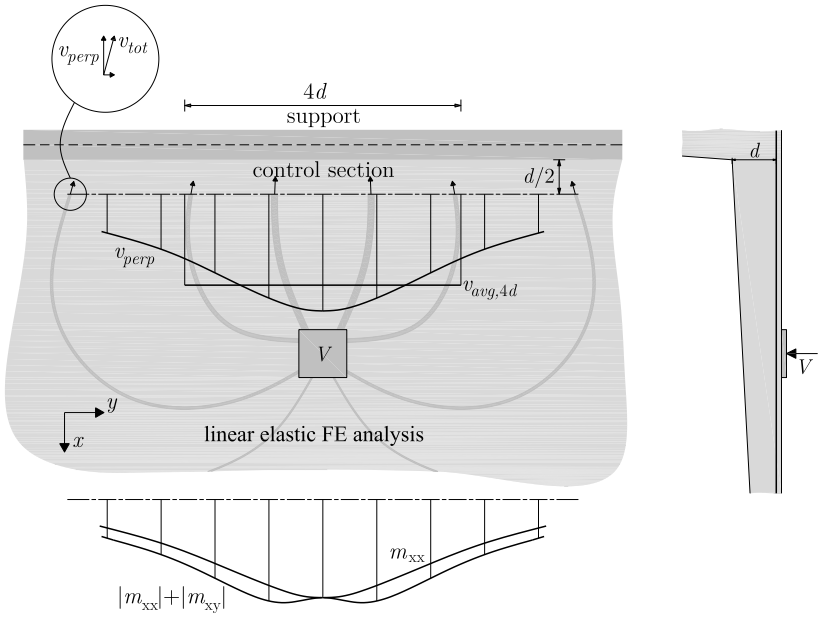

Figure 6.5: Definition of reduced shear force $v_{avg,4d}$

Figure 6.6 shows for SN series the comparison between maximum shear forces at the control section of a LEFE calculation based on the uncracked behavior of reinforced concrete $\left(\nu = 0.2; G = \frac{E}{2(1+\nu)}\right)$, a LEFE calculation with $\left(\nu = 0; G = \frac{E}{16}\right)$ and a nonlinear analysis (NLFE) considering the stiffness loss due to flexural cracking (given by a quadrilinear moment-curvature relation in each direction [Sag11]). For the NLFE analysis, several linear elastic calculations are performed in an iterative procedure, updating at each step the stiffness matrix of the elements. The shear modulus is taken as 1/8 of the calculated one, based on the updated stiffness of each direction, if the element is cracked [Sag11]. The values presented for the NLFE calculations correspond to the failure loads according to the approach presented in reference [Nat14a] combined with the CSCT, but without consideration of arching action.

Comparing the LEFE $\left(\nu = 0.2; G = \frac{E}{2(1+\nu)}\right)$ approach with the NLFE one, for free shear spans $a_v < 3.5d$, $v_{avg,4d}$ seems to account for both shear and bending related redistributions. However, for $a_v > 3.5d$, $v_{avg,4d}$ does not account for the total expected redistributions due to flexural cracks.

The LEFE $\left(\nu = 0; G = \frac{E}{16}\right)$ approach seems to account for both shear and bending related redistributions when $a_v > 1.5d$, in comparison with the NLFE calculations. The use of $v_{avg,4d}$ allows nevertheless to account for both shear and bending related redistributions when $a_v < 1.5d$ and to increase the importance of shear related redistributions when $1.5d < a_v < 4d$.

The redistributions due to the development of the inclined shear crack might be more

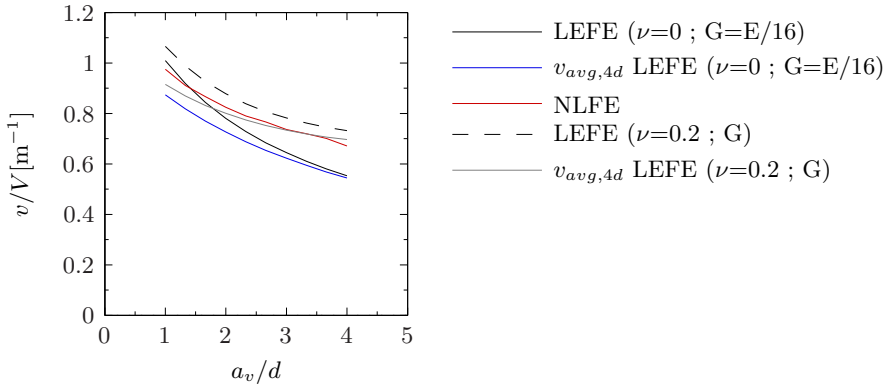

Figure 6.6: Comparison between maximum shear forces at control section for SN series ($d/2$ from the support)

intense than those due to bending cracks when the load is acting closer to the line support, associated with larger shear forces and lower bending moments. The use of $v_{avg,4d}$ seems to account for this aspect, as increasing values of free shear span a_v present less important differences between the peak and averaged acting shear forces.

6.2.3 Arching action

Arching action (refer to Section 2.2 and Section 2.6) is accounted assuming that the contribution of concentrated loads applied within a distance of $d < a_v \leq 2.75d$ from the face of the support to the design shear force v may be reduced by the factor:

$$\beta = a_v/2.75d \leq 1 \tag{6.2}$$

The proposed factor β is based on tests on beams [Kan66] (refer to Figure 2.22), tests on slab strips [Cul96], cantilevers subjected to distributed loads [Per12] and SN series.

6.2.4 Empty ducts

As it was discussed in Section 4.3.3, non-injected ducts reduce the shear strength when compared with regular slabs (with or without injected ducts). One approach to account for this strength reduction is to reduce the effective shear depth d_v (the one in the left part of Equation 3.5). The following expression:

$$d_v = d - \frac{\sqrt{2}}{2} d_0 \tag{6.3}$$

is proposed for round non-injected ducts horizontally spaced of d, where d_0 is the duct diameter. Of several expressions studied by the author, Equation 6.3 is the one in better agreement with the experimental data. The proposal might be extended to square inserts comprised in a d_0 diameter circle, refer to Figure 6.7.

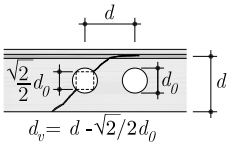

Figure 6.7: Effective shear depth reduction proposal

6.2.5 Validation with SN series

The use of the CSCT with the previously presented proposals is shown in Figure 6.8. The model is reasonably predicting the trend and measured shear strengths. The influence of arching action is quite significant and it is in agreement to the experimental results. Figure 6.8 also suggests that the decrease of the unitary shear force for an increasing a_v/d ratio (Figure 2.17) is compensated by the decrease of the unitary shear strength due to a diminishing arching action and the influence of the strain effect (increasing crack openings for larger bending moments leading to a lower capacity of the shear cracks to transfer shear). According to Figure 6.8 the model predicts that the minimum load leading to failure is found at the distance where the arching action starts to develop. However, in SN series, slabs with $a_v/d = 4$ ratios presented slightly lower failure loads than tests with $a_v/d = 3$, but the reduced number of tests and their differences might still be within normal laboratory scatter.

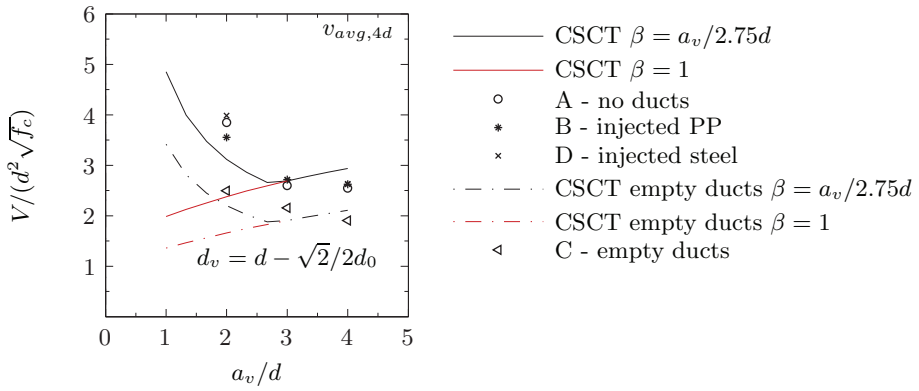

Figure 6.8: Comparison between tests of SN series and the CSCT combined with previously presented proposals

6.2.6 Comparison to tests from the literature

The combined use of the CSCT with the previously presented proposals is performed in this section for the tests presented in Section 2.7 and the static tests performed in this thesis (Chapters 4 and 5).

Figure 6.9 presents the FE mesh used to model the tests of Vaz Rodrigues et al. [Vaz08]. The linear support was modeled with linear elastic compression-only supports (axial stiffness of the supports) on the support block edges. The supports were not modeled at

the block center to better reproduce the acting bending moments in the cantilever, which are known to play a major role in the shear strength. The tensile support was modeled with fixed supports. The tests of Rombach and Latte [Rom09] and those of Reissen and Hegger [Rei13b] were modeled in the same way, except that the linear supports on the opposite side of the tested cantilever were modelled with linear elastic supports, refer to Figure 6.10.

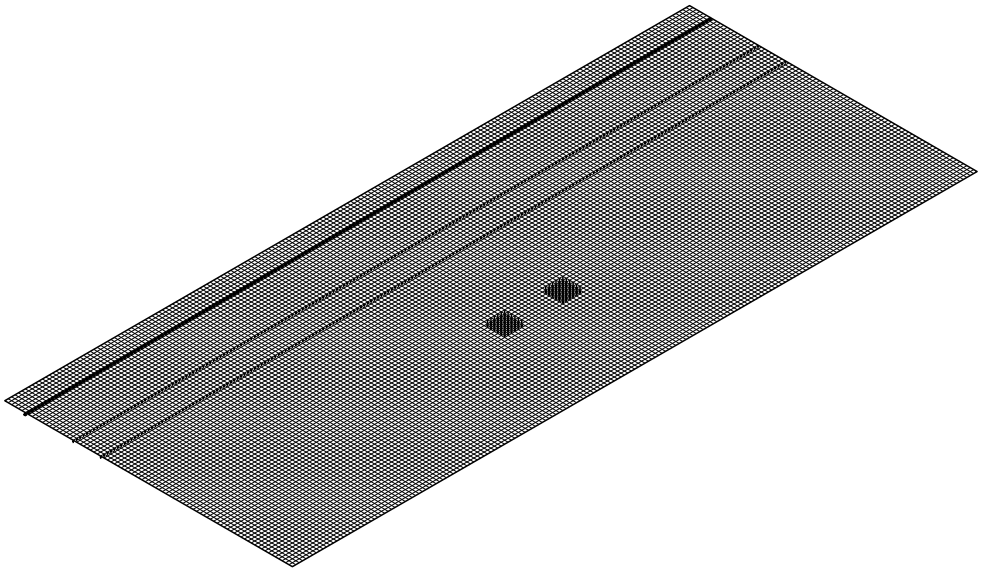

Figure 6.9: FE mesh for Vaz Rodrigues et al. [Vaz08]

Figure 6.11 and Table 6.1 show the comparison between the experimental tests and the proposed approach. In total 27 tests were considered, with 10 tests on haunched slabs and 5 subjected to a linear load at the cantilever tip.

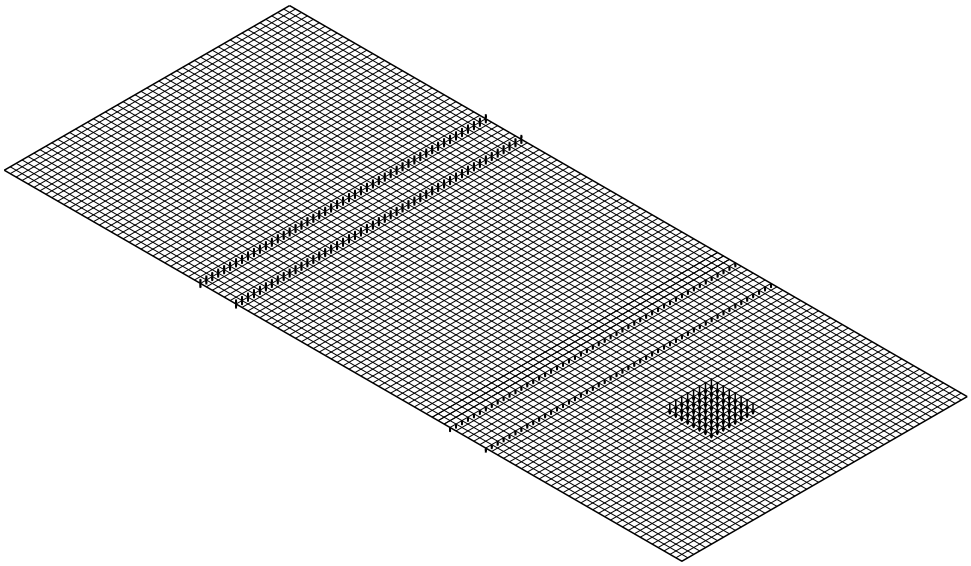

Figure 6.10: FE mesh for Rombach and Latte [Rom09] and Reissen and Hegger [Rei13b]

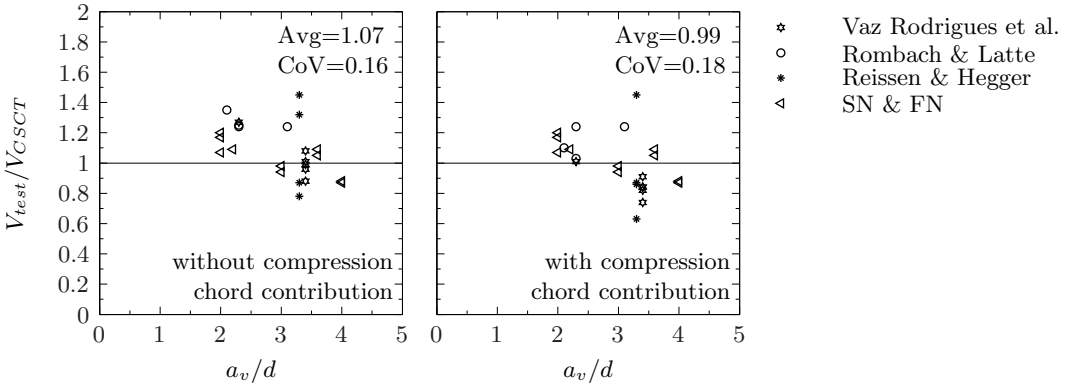

Figure 6.11: Comparison between tests on cantilever slabs under concentrated loads and the CSCT combined with previously presented proposals

Table 6.1: Comparison between experimental tests on cantilever slabs under concentrated loads and CSCT combined with proposals

Authors	test	d [m]	a_v/d	ρ [%]	f_y [MPa]	f_c [MPa]	d_g [mm]	$\tan\alpha$	q_l [kN/m]	V_{test} [kN]	no compression chord contribution V_{test}/V_{calc}	compression chord contribution V_{test}/V_{calc}
[Vaz08]	DR1-a	0.34	2.3	0.78	499	39.1	16	0.068		1397	1.27	1.01
[Vaz08]	DR1-b	0.34	3.4	0.78	499	39.9	16	0.068		1025	1.08	0.91
[Vaz08]	DR1-c	0.34	3.4	0.78	499	40.8	16	0.068		910	1.01	0.84
[Vaz08]	DR2-a	0.34	3.4	0.60	505	38.9	16	0.068		961	0.96	0.82
[Vaz08]	DR2-b	0.34	3.4	0.60	505	42.0	16	0.068		857	0.99	0.84
[Vaz08]	DR2-c	0.34	3.4	0.60	505	42.4	16	0.068		719	0.88	0.74
										Avg	0.98	0.83
										CoV	0.08	0.07
[Rom09]	VK1V1	0.25	2.1	0.81	554	35.0	16	0.067	32.1	690	1.35	1.10
[Rom09]	VK2V1	0.22	2.3	1.16	554	46.0	16		22.5	678	1.24	
[Rom09]	VK3V1	0.22	2.3	1.16	554	46.5	16	0.067	22.5	672	1.25	1.03
[Rom09]	VK4V1	0.17	3.1	1.20	554	42.5	16			487	1.24	
										Avg	1.27	1.15
										CoV	0.04	0.09
[Rei13b]	CS35B-1	0.24	3.3	0.98	920	37.0	16			569	0.87	
[Rei13b]	CS35B-2	0.24	3.3	0.98	920	38.4	16	0.067		475	0.78	0.63
[Rei13b]	CP35B-1	0.24	3.3	0.98	920	34.3	16		86.4	538	1.45	
[Rei13b]	CP35B-2	0.24	3.3	0.98	920	34.8	16	0.067	86.4	451	1.32	0.86
										Avg	1.10	0.95
										CoV	0.30	0.36
[Nat14a] Chapter 4	SN1A	0.15	2.0	1.32	547	30.3	32			489	1.17	
[Nat14a] Chapter 4	SN1B	0.15	2.0	1.32	547	28.3	32			437	1.07	
[Nat14a] Chapter 4	SN4D	0.15	2.0	1.32	547	28.8	32			494	1.20	
[Nat14a] Chapter 4	SN2A	0.15	3.0	1.32	547	30.1	32			330	0.94	
[Nat14a] Chapter 4	SN2B	0.15	3.0	1.32	547	29.5	32			341	0.98	
[Nat14a] Chapter 4	SN5D	0.15	3.0	1.32	547	28.7	32			335	0.98	
[Nat14a] Chapter 4	SN3A	0.15	4.0	1.32	547	30.4	32			328	0.87	

Continued on next page

Table 6.1 – *Continued from previous page*

Authors	test	d [m]	a_v/d	ρ [%]	f_y [MPa]	f_c [MPa]	d_g [mm]	$\tan\alpha$	q_l [kN/m]	V_{test} [kN]	no compression chord contribution V_{test}/V_{calc}	compression chord contribution V_{test}/V_{calc}
[Nat14a] Chapter 4	SN3B	0.15	4.0	1.32	547	29.7	32			330	0.88	
[Nat14a] Chapter 4	SN6D	0.15	4.0	1.32	547	28.9	32			327	0.88	
										Avg	1.00	
										CoV	0.12	
[Nat15a] Chapter 5	FN1W	0.20	2.2	1.03	579	45.2	16			591	1.09	
[Nat15a] Chapter 5	FN1E	0.20	2.2	1.03	579	46.6	16			597	1.09	
[Nat15a] Chapter 5	FN6W	0.19	3.6	1.10	579	45.7	16			474	1.05	
[Nat15a] Chapter 5	FN6E	0.19	3.6	1.10	579	46.5	16			499	1.09	
										Avg	1.08	
										CoV	0.02	
All										Avg	1.07	0.99
All										CoV	0.16	0.18

The analysis of the results indicates that accounting for an hypothetical compression chord contribution leads to some too large unsafe predictions (refer to tests DR2-c and CS35B-2). Even though the compression chord contribution yields an overall average closer to 1.00, its scatter is significantly larger than the one without this contribution. The use of the CSCT with the previously presented proposals without a compression chord contribution results in a more consistent approach, with a 1.07 Average and a 0.16 Coefficient of Variation. This fact is consistent with the available experimental evidence on beams (Section 2.3), which does not show unequivocally that there is a positive influence of a compression chord contribution to shear transferring in reinforced concrete members without shear reinforcement.

With respect to the arching action, it might develop even for slightly larger free shear spans a_v than $2.75d$, refer to the strengths underestimations for a_v/d around 2.0 and the estimations close to 1.0 for $a_v/d \geq 3$ (Figure 6.11).

The role of significant line loads at the cantilever tip cannot be understood with the used approach. The tests of Reissen and Hegger [Rei13b] show almost identical concentrated loads at failure, whether or not an important line load of $q_l = 86.4$ kN/m is acting. Assuming that the used control section is correct, this fact is in contradiction with the CSCT principles, because larger bending moments should imply lower shear strengths. However, for the tests of Rombach and Latte [Rom09] the strength predictions (without compression chord contribution) present a reduced dispersion. Based on these 8 tests it is difficult to extract valid conclusions. More experimental evidence on this subject is desirable.

The test DR1-a of Vaz Rodrigues et al. [Vaz08] was somewhat different from all other tests, as it failed in the region between the closest and farthest loads to the support. This fact is most probably due to a reduced reinforcement area in this region than at the clamped support. Considering a control section located at 3 cm from the edge of the farthest loading plates and not averaging the acting unitary shear force results in a V_{test}/V_{calc} ratio of 1.18, not considering a compression chord contribution. The same ratio at $d/2$ from the clamped support was slightly larger 1.27. The used approach predicts that failure occurs between the support and the closest loading plates. Even though this was not observed, failure at this region was imminent (refer to Figure 6.2) and it might be within normal laboratory scatter.

6.3 Simply supported slabs

In this section the shear and punching shear assessment of simply supported slabs presented in Section 2.8 subjected to concentrated loads near linear supports is investigated, based on the CSCT, and considering only the bending behavior of the slab (no membrane action [Ein15]).

6.3.1 Finite element modeling

The investigated slabs were modeled with the same proposals discussed in Section 6.2.1, *i.e.*, with shell finite elements (SHELL43 elements of ANSYS ®Academic Research [ANSYS] software, with shear deformation and $\nu = 0, G = \frac{E}{16}$). Figure 6.12 shows the typical FE mesh used to model these tests. The supports were linear elastic compression-only supports (axial stiffness of the supports) and the concentrated loads were modeled as surface pressures. The load introduction zone was considered as a rigid body in the tests performed by Damasceno [Dam07], to model the monolithic connection between the slab and the column. Self-weight was neglected.

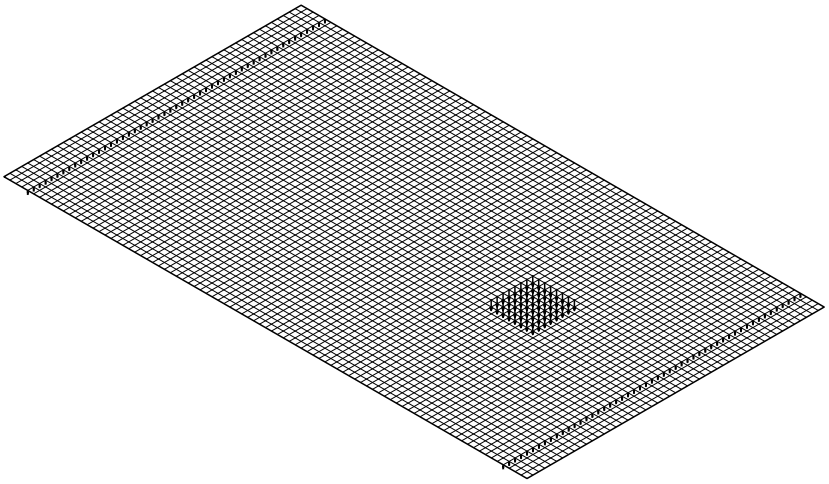

Figure 6.12: Typical FE mesh for simply supported slabs

6.3.2 Control section and internal forces for shear assessment

The proposals discussed in Section 6.2.2 for cantilever slabs are adapted to simply supported slabs. The first difference regards the control section location. As it was discussed in Section 2.6 and to be consistent with the CSCT principles (Section 3.2) the governing control section has to be located close to the concentrated load. The control section is thus located at $d/2$ from the edge of the load, refer to Figure 6.13. To take into account redistributions of internal forces, it is proposed to consider an average of the acting unitary shear force $v_{avg,4d+c_y}$ in a distance $4d + c_y$, centered at the location of maximum applied unitary shear force, combined with the acting bending moment at that location, refer to Figure 6.13. Arching action is taken into account according to what has been discussed in Section 6.2.3.

6.3.3 Control section, internal forces and rotation calculation for punching shear assessment

The punching shear assessment is performed with the CSCT($\psi_x - \psi_y$) method [Sag11], refer to Section 3.5. The control perimeter is located at $d_v/2$ from the concentrated

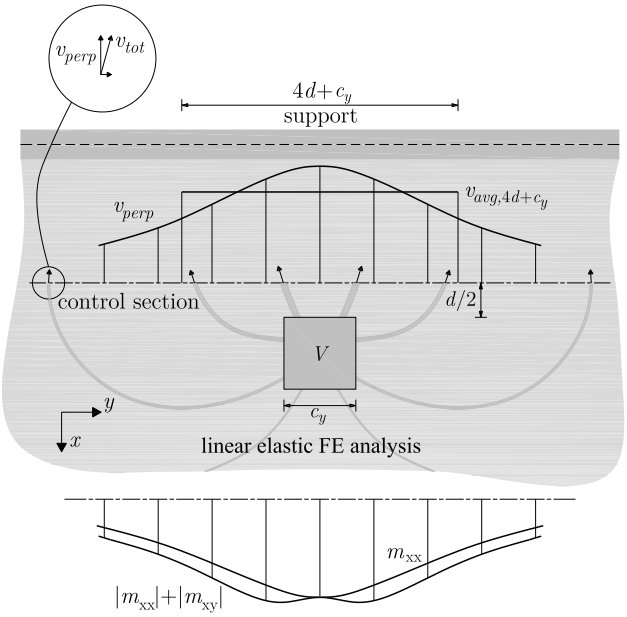

Figure 6.13: Control section location and reduced shear force $v_{avg,4d+c_y}$ definition for simply supported slabs

load, where d_v is the effective depth of the interface plane defined by points of contact between the reinforcement layers on both directions.

The rotation calculations are performed according to an approach based on the *fib*-Model Code [MC2010] method presented in reference [Tas11]. In each reinforcement direction and control perimeter face i, a rotation can be calculated as:

$$\psi_i = 1.2 \frac{r_{si}}{d_i} \frac{f_{yi}}{E_s} \left(\frac{m_{si}}{m_{Ri}} \right)^{\frac{3}{2}} \tag{6.4}$$

$$m_{si} = \frac{1}{b_s} \int_{-b_s/2}^{b_s/2} (|m_i| + |m_{ij}|) \, \mathrm{d}j \quad i \perp j \tag{6.5}$$

where r_{si} is the distance between the center of the concentrated load and the point where the applied bending moment in the the direction of the relevant reinforcement is zero, d_i is the effective flexural depth in the relevant direction, f_{yi} is the steel yielding stress, E_s is the Young's modulus of steel, m_{si} is the averaged applied bending moment at the loading plate edge i within the width b_s and m_{Ri} is the yielding moment (Equation 3.17), refer to Figures 6.14(a,d). The support strip width b_s is the minimum calculated value of:

$$b_s = 1.5\sqrt{r_{si} r_{sj}} \quad i \perp j \tag{6.6}$$

Equation 6.4 is of the same type as Equation 3.20 presented by Muttoni [Mut08b] which considers that the rotation depends on $(V/V_{flex})^{3/2}$. However, this last method is more adequate to axis-symmetric punching. For non-axis-symmetric punching, it is desirable

to calculate different rotations in each direction, related to the different flexural stiffness and r_s values.
For each of the control perimeter sides, it is proposed to calculate a reduced control perimeter given by the ratio between the maximum applied unitary shear force perpendicular to the control perimeter and the total shear force going through that perimeter, refer to Figure 6.14(b). For simplicity reasons, a control perimeter without rounded edges is proposed. When the applied loads are elongated, the recommendation of the *fib*-Model Code 2010 [MC2010] has been adopted, which considers that the punching shear control perimeter has to be limited (maximum of $3d_v$ per side), refer to Figure 6.14(c), and that shear has to be checked in the remaining control perimeter.
Adopting a similar formulation to *fib*-Model Code 2010 [MC2010] for punching shear, Muttoni's criteria [Mut08b] (Equation 3.19) allows the calculation of the unitary punching shear strength v_R as:

$$v_R = k_\psi f_c d_v \quad [\text{MPa, mm}] \tag{6.7}$$

$$k_\psi = \frac{1}{\frac{4}{3} + 0.625 k_{dg} \psi d_v} \leq 0.6 \quad d_v[\text{mm}] \tag{6.8}$$

$$k_{dg} = \frac{32}{16 + d_g} \geq 0.75 \quad d_g[\text{mm}] \tag{6.9}$$

where d_g is the maximum aggregate size and f_c the concrete compressive strength.

6.3.4 Comparison to tests from the literature

Table 6.2 summarizes the main geometric and material properties of the simply supported slabs presented in Section 2.8. The comparison of these tests with the proposed approaches based on the CSCT is given in Table 6.3 and shown in Figure 6.17. An additional flexural assessment was performed assuming the yield line pattern of Figure 6.15, which allows the calculation of the bending strength F_{flex} and corresponding shear force V_{flex}. For some tests, a punching shear assessment is not shown because a full control perimeter around the load can not geometrically develop. For some other tests of Damasceno [Dam07], a shear assessment is not given, because of the high unitary shear force concentration in the corners of the elongated monolithic columns. The given failures modes in Tables 6.2 et 6.3 were the ones reported by the authors, except for those of Reissen and Hegger [Rei13a], whose modes were attributed by the author of this thesis and in good agreement with the proposals of the database of Lantsoght et al. [Lan14a]. Failures were interpreted as punching shear if there was a visible punching cone on the bottom face of the slabs, but not visible on both side views, refer to Figure 6.16(b). Otherwise the failures were classified as shear (Figure 6.16(a)).
Considering all the tests where the concentrated load was not introduced with a monolithic column (Figure 6.17), punching shear failures occurred for ratios $c_y/b \leq 0.30$. The available data suggests that punching shear is the governing failure mode when $c_y/b \to 0$.

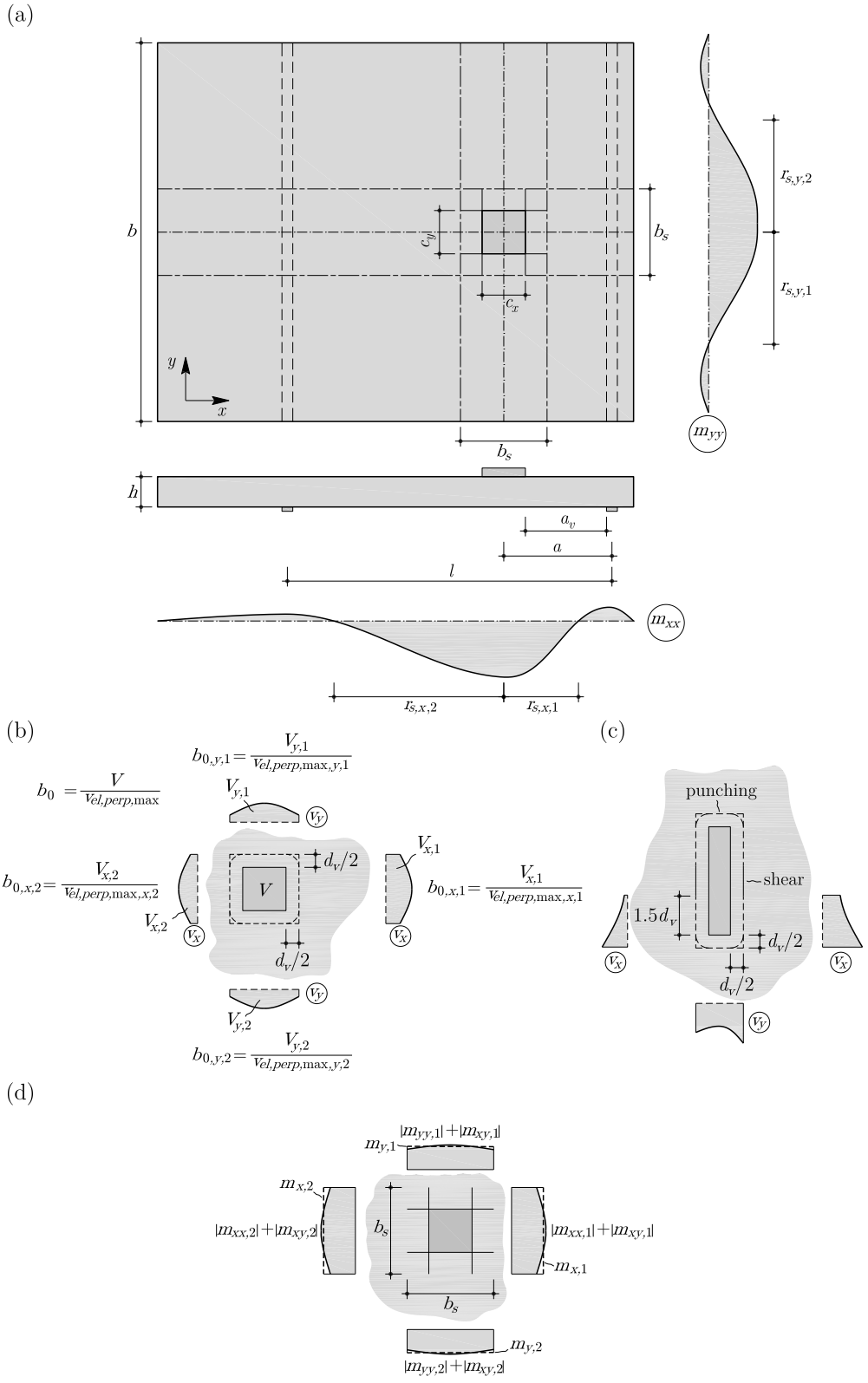

Figure 6.14: Definition of support strip widths, reduced control perimeters and averaged bending moments for the punching shear assessment of simply supported slabs: **(a)** definition of r_{si} distances; **(b)** definition of reduced control perimeters; **(c)** definition of punching control perimeter for elongated loads; and **(d)** definition of averaged acting bending moments at the edges of the concentrated load

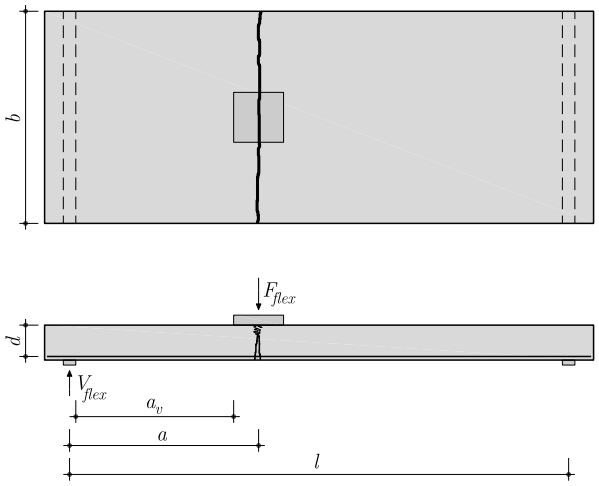

Figure 6.15: Assumed yield line to calculate the bending strength F_{flex} and corresponding shear force V_{flex}

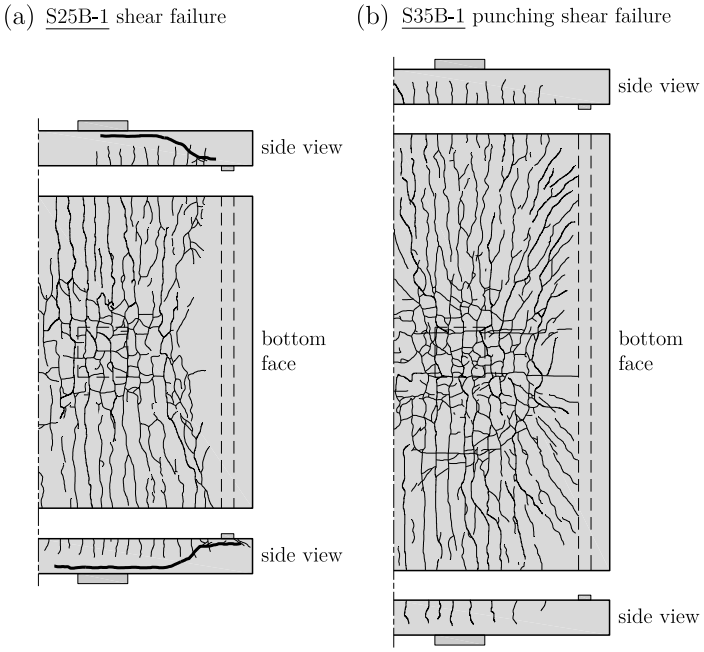

Figure 6.16: Shear and punching shear failures of Reissen and Hegger [Rei13a,Heg13]: **(a)** shear failure; and **(b)** punching shear failure

The proposed approaches combined with the CSCT are able to predict the correct failure mode of 74% the 62 tests used for this analysis. Knowing *a priori* the correct failure mode, the proposed approach has an Average ratio V_{test}/V_{calc} of 1.12, with a Coefficient of Variation of 0.11. Not knowing *a priori* the correct failure mode, the used approach has a 1.15 Average with a Coefficient of Variation of 0.12 (Figure 6.18).
The tests of Regan and Rezai-Jorabi [Reg88] and of Reissen and Hegger [Rei13a] are almost all predicted to fail in shear (refer to Figure 6.19). However, some tests of Ferreira [Ferr06] and Damasceno [Dam07] are predicted to fail in punching. It is interesting to note that the tests for which there is no correct prediction of the failure mode are relatively close to the border separating shear and punching shear failures (refer to Figure 6.19), which justifies the relatively similar Averages and Coefficients of Variation obtained, knowing or not *a priori* the correct failure mode. These tests might also be within normal laboratory scatter.
From the comparisons performed in this section, the use of the CSCT for both shear and punching shear combined with the proposals of this thesis leads to a safe design/assessment. Simply supported slab bridges are expected to fail in punching shear close to simply supported edges if the acting load (not monolithic) has a ratio $c_y/b \approx 0$. Concentrated loads with $c_y/b \approx 0$ applied close to a inner linear support (with a certain degree of clamping) may exhibit shear failures like the ones analysed in Section 6.2, if negative moments occur at the edges of the loads.

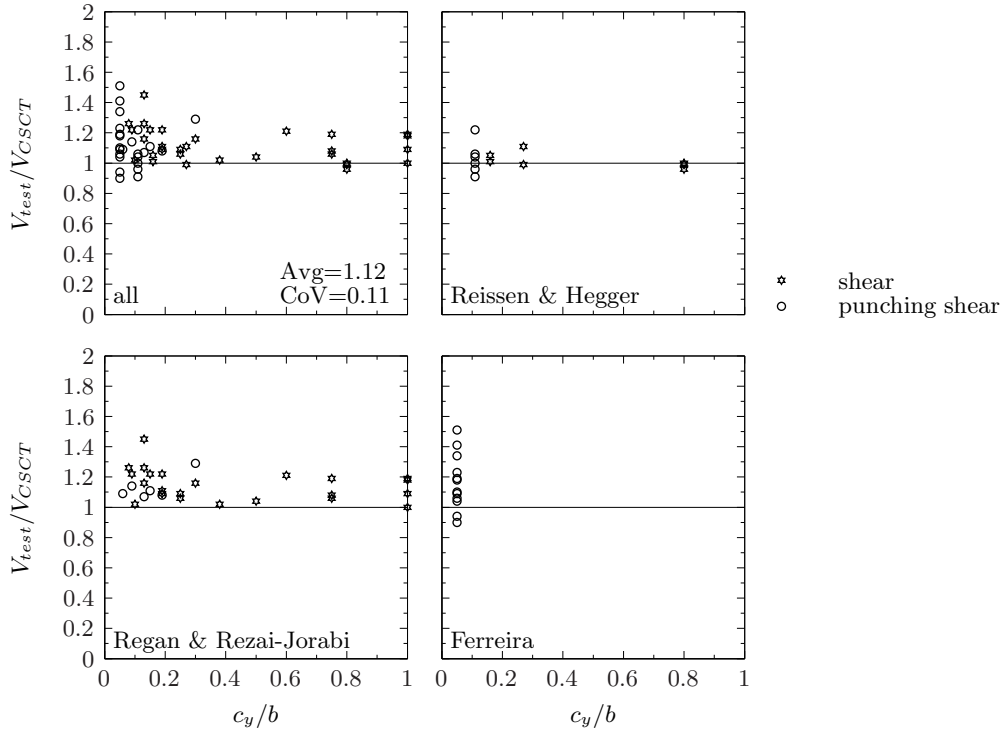

Figure 6.17: Comparison between experimental tests on simply supported slabs under concentrated loads and the CSCT combined with proposals, knowing *a priori* the correct failure mode

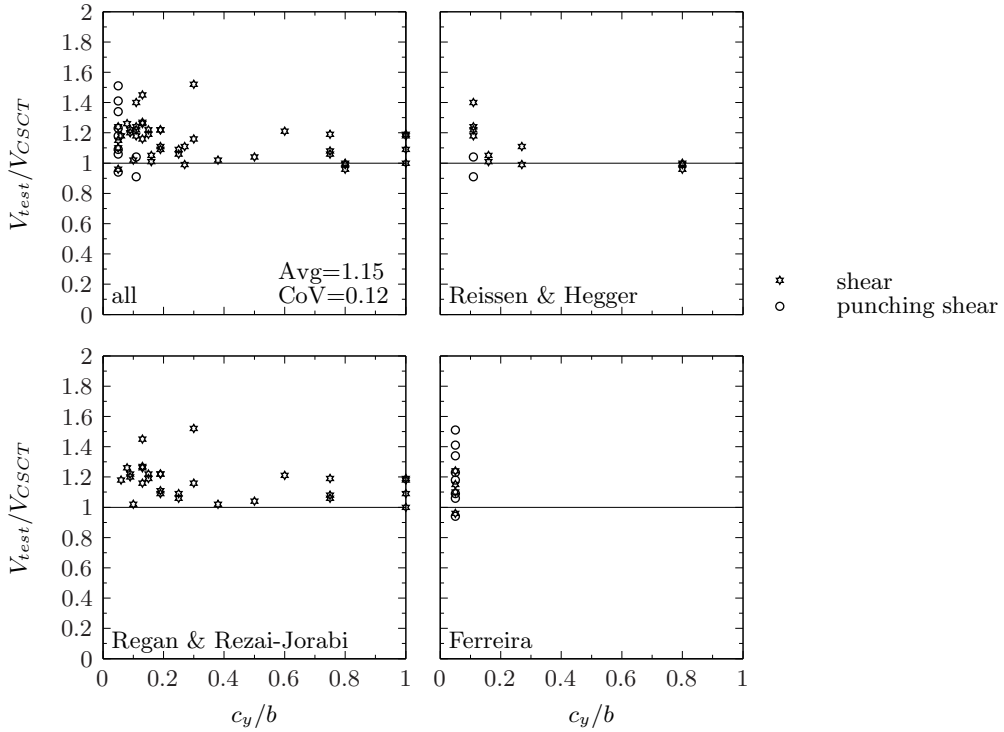

Figure 6.18: Comparison between experimental tests on simply supported slabs under concentrated loads and the CSCT combined with proposals, not knowing *a priori* the correct failure mode

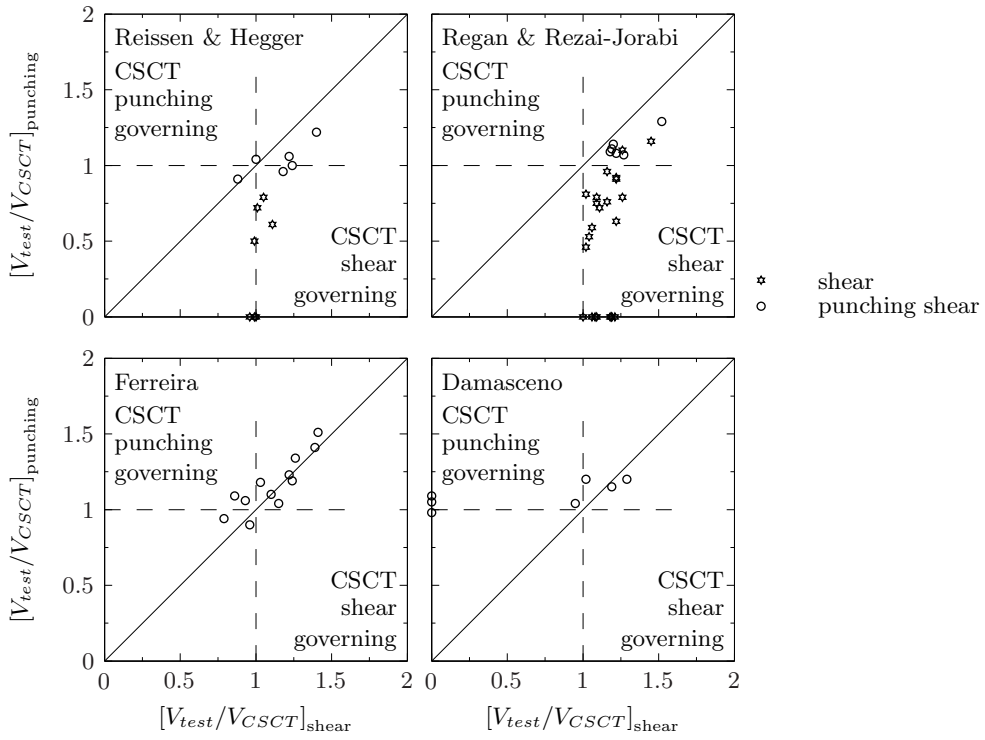

Figure 6.19: Comparison between experimental tests on simply supported slabs under concentrated loads and the CSCT combined with proposals, for both shear and punching shear

Table 6.2: Properties of simply supported slabs

Authors	test	Mode	b [m]	d_x [m]	d_y [m]	c_x [m]	c_y [m]	c_y/b	a [m]	a/d_x	a_v/d_x	l [m]	ρ_x [%]	ρ_y [%]	f_{yx} [MPa]	f_{yy} [MPa]	dg [mm]	f_c [MPa]	E_c [GPa]
[Reg88]	1	WB	0.40	0.08	0.08	0.08	0.08	0.19	0.45	5.42	4.37	1.35	1.66	0.63	670	743	10	37.8	37.0(1)
[Reg88]	2	WB	0.60	0.08	0.08	0.08	0.08	0.13	0.45	5.42	4.37	1.35	1.58	0.63	670	743	10	37.8	37.0(1)
[Reg88]	3	WB	0.80	0.08	0.08	0.08	0.08	0.09	0.45	5.42	4.37	1.35	1.54	0.63	670	743	10	37.8	37.0(1)
[Reg88]	4	WB	0.40	0.08	0.08	0.10	0.40	1.00	0.45	5.42	4.22	1.35	1.66	0.63	670	743	10	28.1	33.5(1)
[Reg88]	5	WB	0.60	0.08	0.08	0.10	0.60	1.00	0.45	5.42	4.22	1.35	1.58	0.63	670	743	10	28.1	33.5(1)
[Reg88]	6	WB	0.80	0.08	0.08	0.10	0.60	0.75	0.45	5.42	4.22	1.35	1.54	0.63	670	743	10	28.1	33.5(1)
[Reg88]	10	WB	0.40	0.08	0.08	0.10	0.15	0.38	0.45	5.42	4.22	1.35	1.66	0.63	670	743	20	33.4	35.5(1)
[Reg88]	11	WB	0.40	0.08	0.08	0.10	0.30	0.75	0.45	5.42	4.22	1.35	1.66	0.63	670	743	20	33.4	35.5(1)
[Reg88]	12	WB	0.60	0.08	0.08	0.10	0.15	0.25	0.45	5.42	4.22	1.35	1.58	0.63	670	743	20	33.4	35.5(1)
[Reg88]	13	WB	0.60	0.08	0.08	0.10	0.30	0.50	0.45	5.42	4.22	1.35	1.58	0.63	670	743	20	33.4	35.5(1)
[Reg88]	14	WB	0.80	0.08	0.08	0.10	0.15	0.19	0.45	5.42	4.22	1.35	1.54	0.63	670	743	20	31.0	34.6(1)
[Reg88]	15	WB	0.80	0.08	0.08	0.10	0.15	0.19	0.55	6.63	5.42	1.35	1.54	0.63	670	743	20	30.8	34.5(1)
[Reg88]	16	WB	0.80	0.08	0.08	0.10	0.80	1.00	0.45	5.42	4.22	1.35	1.54	0.63	670	743	20	31.2	34.7(1)
[Reg88]	17	WB	1.00	0.08	0.08	0.08	0.10	0.10	0.45	5.42	4.37	1.35	1.51	0.63	670	743	20	31.0	34.6(1)
[Reg88]	18	WB	1.00	0.08	0.08	0.10	0.30	0.30	0.45	5.42	4.22	1.35	1.51	0.63	670	743	20	31.2	34.7(1)
[Reg88]	19	WB	1.00	0.08	0.08	0.10	0.15	0.15	0.45	5.42	4.22	1.35	1.51	0.63	670	743	20	29.0	33.8(1)
[Reg88]	20	WB	1.00	0.08	0.08	0.10	1.00	1.00	0.45	5.42	4.22	1.35	1.51	0.63	670	743	20	30.8	34.5(1)
[Reg88]	21	P	1.20	0.08	0.07	0.10	0.07	0.06	0.45	5.63	4.38	1.35	1.64	0.65	670	743	20	38.2	37.1(1)
[Reg88]	22	P/WB	1.20	0.08	0.07	0.10	0.15	0.13	0.45	5.63	4.38	1.35	1.64	0.65	670	743	20	37.0	36.7(1)
[Reg88]	23	WB	1.20	0.08	0.07	0.10	0.30	0.25	0.45	5.63	4.38	1.35	1.64	0.65	670	743	20	35.4	36.2(1)
[Reg88]	24	WB	1.20	0.08	0.07	0.30	0.10	0.08	0.45	5.63	3.13	1.35	1.64	0.65	670	743	10	38.6	37.2(1)
[Reg88]	25	P*	1.20	0.08	0.07	0.10	0.15	0.13	0.55	6.88	5.63	1.35	1.64	0.65	670	743	10	30.3	34.3(1)
[Reg88]	26	WB	1.20	0.08	0.07	0.10	0.15	0.13	0.35	4.38	3.13	1.35	1.64	0.65	670	743	10	29.7	34.1(1)
[Reg88]	14R	P	0.80	0.08	0.08	0.10	0.08	0.09	0.45	5.42	4.22	0.90	1.54	0.63	670	743	20	31.0	34.6(1)
[Reg88]	15R	P	0.80	0.08	0.08	0.10	0.15	0.19	0.45	5.42	4.22	0.90	1.54	0.63	670	743	20	30.8	34.5(1)
[Reg88]	16R	WB	0.80	0.08	0.08	0.10	0.60	0.75	0.45	5.42	4.22	0.90	1.54	0.63	670	743	20	31.2	34.7(1)
[Reg88]	17R	WB	1.00	0.08	0.08	0.10	0.60	0.60	0.45	5.42	4.22	0.90	1.51	0.63	670	743	20	31.0	34.6(1)
[Reg88]	19R	P	1.00	0.08	0.08	0.10	0.15	0.15	0.45	5.42	4.22	0.90	1.51	0.63	670	743	20	29.0	33.8(1)
[Reg88]	20R	P	1.00	0.08	0.08	0.10	0.30	0.30	0.45	5.42	4.22	0.90	1.51	0.63	670	743	20	30.8	34.5(1)
[Ferr06]	L1a	P	1.80	0.10	0.09	0.09	0.09	0.05	0.80	8.23	7.17	1.60	1.33	0.61	488	639	12	42.4	30.0
[Ferr06]	L1b	FP	1.80	0.10	0.09	0.09	0.09	0.05	0.80	7.98	6.96	1.60	1.29	0.93	488	496	12	51.4	34.4
[Ferr06]	L1c	P	1.80	0.10	0.09	0.09	0.09	0.05	0.80	8.04	7.01	1.60	1.30	1.49	488	488	12	43.5	33.3
[Ferr06]	L2a	P	1.80	0.10	0.09	0.09	0.09	0.05	0.53	5.42	4.38	1.60	1.32	0.60	488	639	12	42.1	29.4
[Ferr06]	L2b	P	1.80	0.10	0.09	0.09	0.09	0.05	0.53	5.37	4.34	1.60	1.31	0.94	488	496	12	49.7	33.6
[Ferr06]	L2c	P	1.80	0.10	0.09	0.09	0.09	0.05	0.53	5.36	4.33	1.60	1.30	1.49	488	488	12	44.8	31.6
[Ferr06]	L3a	P	1.80	0.10	0.09	0.09	0.09	0.05	0.40	4.07	3.03	1.60	1.32	0.60	488	639	12	42.1	28.8
[Ferr06]	L3b	P	1.80	0.10	0.09	0.09	0.09	0.05	0.40	4.03	3.00	1.60	1.31	0.94	488	496	12	49.3	32.2
[Ferr06]	L3c	P	1.80	0.10	0.09	0.09	0.09	0.05	0.40	4.02	2.99	1.60	1.30	1.49	488	488	12	36.1	27.1
[Ferr06]	L4a	P	1.80	0.10	0.09	0.09	0.09	0.05	0.32	3.22	2.19	1.60	1.31	0.60	488	639	12	48.8	33.8
[Ferr06]	L4b	P	1.80	0.10	0.09	0.09	0.09	0.05	0.32	3.19	2.17	1.60	1.29	0.93	488	496	12	58.0	33.1
[Ferr06]	L4c	P	1.80	0.10	0.09	0.09	0.09	0.05	0.32	3.22	2.19	1.60	1.30	1.49	488	488	12	44.8	28.2
[Dam07]	L1A	P	1.80	0.10	0.08	0.09	0.09	0.05	0.80	8.37	7.30	1.60	1.14	1.31	600	600	12 (2)	41.3	26.5
[Dam07]	L2A	FP	1.80	0.10	0.08	0.09	0.26	0.14	0.80	8.38	7.30	1.60	1.14	1.31	600	600	12 (2)	40.0	27.3
[Dam07]	L3A	FP	1.80	0.11	0.09	0.09	0.43	0.24	0.80	7.55	6.58	1.60	1.03	1.17	600	600	12 (2)	39.7	27.8
[Dam07]	L4A	FP	1.80	0.10	0.09	0.09	0.60	0.33	0.80	7.63	6.65	1.60	1.04	1.18	600	600	12 (2)	40.4	22.5
[Dam07]	L1B	P	1.80	0.10	0.09	0.09	0.09	0.05	0.80	7.67	6.68	1.60	1.05	0.29	600	505	12 (2)	41.4	24.9
[Dam07]	L2B	P	1.80	0.10	0.09	0.09	0.26	0.14	0.80	8.27	7.21	1.60	1.13	0.32	600	505	12 (2)	42.0	25.3
[Dam07]	L3B	FP	1.80	0.10	0.09	0.09	0.43	0.24	0.80	8.08	7.05	1.60	1.10	0.31	600	505	12 (2)	41.6	21.6

Continued on next page

Table 6.2 – *Continued from previous page*

Authors	test	Mode	b [m]	d_x [m]	d_y [m]	c_x [m]	c_y [m]	c_y/b	a [m]	a/d_x	a_v/d_x	l [m]	ρ_x [%]	ρ_y [%]	f_{yx} [MPa]	f_{yy} [MPa]	dg [mm]	f_c [MPa]	E_c [GPa]
[Dam07]	L4B	FP	1.80	0.10	0.09	0.09	0.60	0.33	0.80	7.67	6.68	1.60	1.05	0.29	600	505	12 (2)	40.5	23.3
[Rei13a]	S5B-1	WB	0.50	0.24	0.25	0.40	0.40	0.80	1.00	4.16	3.13	4.00	0.98	0.45	885	573	16	39.2	26.2
[Rei13a]	S5B-2	WB	0.50	0.24	0.25	0.40	0.40	0.80	1.00	4.16	3.13	3.00	0.98	0.45	885	573	16	40.5	28.1
[Rei13a]	S5B-3	WB	0.50	0.24	0.25	0.40	0.40	0.80	1.00	4.16	3.13	3.00	0.98	0.45	920	573	16	33.7	26.2
[Rei13a]	S15B-1	WB	1.50	0.24	0.25	0.40	0.40	0.27	1.00	4.16	3.13	4.00	0.98	0.45	885	573	16	37.7	27.3
[Rei13a]	S15B-2	WB	1.50	0.24	0.25	0.40	0.40	0.27	1.00	4.16	3.13	3.00	0.98	0.45	885	573	16	38.2	27.6
[Rei13a]	S25B-1	WB	2.50	0.24	0.25	0.40	0.40	0.16	1.00	4.16	3.13	4.00	0.98	0.45	885	573	16	27.9	22.4
[Rei13a]	S25B-2	WB	2.50	0.24	0.25	0.40	0.40	0.16	1.00	4.16	3.13	3.00	0.98	0.45	885	573	16	29.5	21.0
[Rei13a]	S35B-1	P	3.50	0.24	0.25	0.40	0.40	0.11	1.00	4.16	3.13	4.00	0.98	0.45	885	573	16	35.9	28.2
[Rei13a]	S35B-2	P	3.50	0.24	0.25	0.40	0.40	0.11	1.00	4.16	3.13	3.00	0.98	0.45	885	573	16	38.2	28.2
[Rei13a]	S35C-1	P	3.50	0.24	0.25	0.40	0.40	0.11	1.30	5.41	4.38	4.00	0.98	0.45	920	573	16	39.6	27.2
[Rei13a]	S35A-1	P	3.50	0.24	0.25	0.40	0.40	0.11	0.70	2.91	1.88	3.00	0.98	0.45	920	573	16	41.3	29.9
[Rei13a]	S35C-2	P	3.50	0.24	0.25	0.40	0.40	0.11	1.30	5.41	4.38	4.00	0.98	0.45	905	556	16	29.5	22.7
[Rei13a]	S35A-2	P	3.50	0.24	0.25	0.40	0.40	0.11	0.70	2.91	1.88	3.00	0.98	0.45	905	556	16	29.0	23.3

Reported failure modes: WB - wide beam shear; P - punching shear; P* - punching shear around two loads; FP - flexural punching shear
(1) assumed values
(2) assumed values

Table 6.3: Comparison between experimental tests on simply supported slabs under concentrated loads and CSCT combined with proposals

Authors	test	Mode	c_y/b	a_v/d_x	F_{test} [kN]	V_{test} [kN]	F_{test}/F_y V_{test}/V_y	Shear F_{test}/F_{calc} V_{test}/V_{calc}	Punching F_{test}/F_{calc} V_{test}/V_{calc}	correct prediction of failure mode?	knowing the failure mode F_{test}/F_{calc} V_{test}/V_{calc}	knowing the failure mode F_{calc}/F_{flex} V_{calc}/V_{flex}
[Reg88]	1	WB	0.19	4.37		63	1.08	1.22	0.63	OK	1.22	0.88
[Reg88]	2	WB	0.13	4.37		85	1.02	1.26	0.79	OK	1.26	0.81
[Reg88]	3	WB	0.09	4.37		98	0.89	1.22	0.92	OK	1.22	0.73
[Reg88]	4	WB	1.00	4.22		55	1.00	1.19		OK	1.19	0.84
[Reg88]	5	WB	1.00	4.22		80	1.01	1.18		OK	1.18	0.86
[Reg88]	6	WB	0.75	4.22		97	0.94	1.08		OK	1.08	0.87
[Reg88]	10	WB	0.38	4.22		53	0.92	1.02	0.46	OK	1.02	0.91
[Reg88]	11	WB	0.75	4.22		55	0.97	1.06		OK	1.06	0.91
[Reg88]	12	WB	0.25	4.22		76	0.93	1.06	0.59	OK	1.06	0.88
[Reg88]	13	WB	0.50	4.22		80	0.97	1.04	0.53	OK	1.04	0.93
[Reg88]	14	WB	0.19	4.22		93	0.88	1.11	0.72	OK	1.11	0.79
[Reg88]	15	WB	0.19	5.42		85	0.99	1.09	0.75	OK	1.09	0.91
[Reg88]	16	WB	1.00	4.22		108	1.02	1.09		OK	1.09	0.94
[Reg88]	17	WB	0.10	4.37		90	0.69	1.02	0.81	OK	1.02	0.68
[Reg88]	18	WB	0.30	4.22		120	0.92	1.16	0.76	OK	1.16	0.80
[Reg88]	19	WB	0.15	4.22		111	0.87	1.22	0.91	OK	1.22	0.71
[Reg88]	20	WB	1.00	4.22		123	0.95	1.00		OK	1.00	0.95
[Reg88]	21	P	0.06	4.38		118	0.73	1.18	1.09	KO	1.09	0.67
[Reg88]	22	P/WB	0.13	4.38		122	0.76	1.16	0.96	OK	1.16	0.66
[Reg88]	23	WB	0.25	4.38		125	0.79	1.09	0.79	OK	1.09	0.73
[Reg88]	24	WB	0.08	3.13		150	0.93	1.26	1.10	OK	1.26	0.74
[Reg88]	25	P*	0.13	5.63		106	0.84	1.27	1.07	KO	1.07	0.79
[Reg88]	26	WB	0.13	3.13		138	0.70	1.45	1.16	OK	1.45	0.48
[Reg88]	14R	P	0.09	4.22	154	77	0.37	1.20	1.14	KO	1.14	0.64
[Reg88]	15R	P	0.19	4.22	172	86	0.41	1.22	1.08	KO	1.08	0.76
[Reg88]	16R	WB	0.75	4.22	233	117	0.55	1.19		OK	1.19	0.93
[Reg88]	17R	WB	0.60	4.22	275	138	0.53	1.21		OK	1.21	0.88
[Reg88]	19R	P	0.15	4.22	170	85	0.33	1.19	1.11	KO	1.11	0.60
[Reg88]	20R	P	0.30	4.22	265	133	0.51	1.52	1.29	KO	1.29	0.80
										Avg	1.14	
										CoV	0.09	
[Ferr06]	L1a	P	0.05	7.17	174		0.68	1.03	1.18	OK	1.18	0.58
[Ferr06]	L1b	FP	0.05	6.96	232		0.86	1.26	1.34	OK	1.34	0.65
[Ferr06]	L1c	P	0.05	7.01	190		0.72	1.10	1.10	KO	1.10	0.66
[Ferr06]	L2a	P	0.05	4.38	228		0.78	1.41	1.51	OK	1.51	0.52
[Ferr06]	L2b	P	0.05	4.34	211		0.71	1.22	1.23	OK	1.23	0.58
[Ferr06]	L2c	P	0.05	4.33	160		0.54	0.96	0.90	KO	0.90	0.60
[Ferr06]	L3a	P	0.05	3.03	225		0.65	1.39	1.41	OK	1.41	0.46
[Ferr06]	L3b	P	0.05	3.00	215		0.61	1.24	1.19	KO	1.19	0.51
[Ferr06]	L3c	P	0.05	2.99	179		0.52	1.15	1.04	KO	1.04	0.50
[Ferr06]	L4a	P	0.05	2.19	194		0.47	0.86	1.09	OK	1.09	0.43
[Ferr06]	L4b	P	0.05	2.17	191		0.45	0.79	0.94	OK	0.94	0.48
[Ferr06]	L4c	P	0.05	2.19	206		0.50	0.93	1.06	OK	1.06	0.47
										Avg	1.16	
										CoV	0.16	

Continued on next page

Table 6.3 – *Continued from previous page*

Authors	test	Mode	c_y/b	a_v/d_x	F_{test} [kN]	V_{test} [kN]	F_{test}/F_y V_{test}/V_y	Shear F_{test}/F_{calc} V_{test}/V_{calc}	Punching F_{test}/F_{calc} V_{test}/V_{calc}	correct prediction of failure mode?	knowing the failure mode F_{test}/F_{calc} V_{test}/V_{calc}	knowing the failure mode F_{calc}/F_{flex} V_{calc}/V_{flex}
[Dam07]	L1A	P	0.05	7.30	189		0.73	1.19	1.15	KO	1.15	0.64
[Dam07]	L2A	FP	0.14	7.30	254		0.99	1.29	1.20	KO	1.20	0.82
[Dam07]	L3A	FP	0.24	6.58	297		1.03		1.09	OK	1.09	0.95
[Dam07]	L4A	FP	0.33	6.65	325		1.14		1.09	OK	1.09	1.05
[Dam07]	L1B	P	0.05	6.68	172		0.61	1.02	1.20	OK	1.20	0.50
[Dam07]	L2B	P	0.14	7.21	195		0.74	0.95	1.04	OK	1.04	0.71
[Dam07]	L3B	FP	0.24	7.05	232		0.86		1.05	OK	1.05	0.83
[Dam07]	L4B	FP	0.33	6.68	255		0.90		0.98	OK	0.98	0.91
										Avg	1.10	
										CoV	0.07	
[Rei13a]	S5B-1	WB	0.80	3.13	183	137	0.62	0.96		OK	0.96	0.65
[Rei13a]	S5B-2	WB	0.80	3.13	215	143	0.64	0.99		OK	0.99	0.65
[Rei13a]	S5B-3	WB	0.80	3.13	204	136	0.60	1.00		OK	1.00	0.61
[Rei13a]	S15B-1	WB	0.27	3.13	543	407	0.61	0.99	0.50	OK	0.99	0.62
[Rei13a]	S15B-2	WB	0.27	3.13	683	425	0.69	1.11	0.61	OK	1.11	0.62
[Rei13a]	S25B-1	WB	0.16	3.13	664	498	0.47	1.01	0.72	OK	1.01	0.47
[Rei13a]	S25B-2	WB	0.16	3.13	780	520	0.49	1.05	0.79	OK	1.05	0.46
[Rei13a]	S35B-1	P	0.11	3.13	985	739	0.48	1.24	1.00	KO	1.00	0.48
[Rei13a]	S35B-2	P	0.11	3.13	1024	683	0.44	1.18	0.96	KO	0.96	0.46
[Rei13a]	S35C-1	P	0.11	4.38	1166	787	0.64	1.40	1.22	KO	1.22	0.52
[Rei13a]	S35A-1	P	0.11	1.88	1143	876	0.38	1.00	1.04	OK	1.04	0.36
[Rei13a]	S35C-2	P	0.11	4.38	924	624	0.53	1.22	1.06	KO	1.06	0.50
[Rei13a]	S35A-2	P	0.11	1.88	892	684	0.32	0.88	0.91	OK	0.91	0.35
										Avg	1.02	
										CoV	0.08	
									OK?	74%	1.12	Avg
											0.11	CoV

Reported failure modes: WB - wide beam shear; P - punching shear; P* - punching shear around two loads; FP - flexural punching shear

Chapter 7

Shear-fatigue

7.1 Introduction

In this chapter a simpler and more practical model to analyse shear-fatigue failures than the one presented by Gallego et al. [Gal14a] (Section 3.8) is proposed, grounded on the same principles. This model is developed in combination with the Critical Shear Crack Theory (CSCT) [Mut08a] (Section 3.2). The combined use of both approaches leads to simple design expressions, whose comparison to available test results on beams shows sound agreement for the various mechanical and geometrical parameters. Also, both the *S-N* curves and Goodman diagrams for fatigue loading can be derived using an analytical manner, showing consistent agreement to test data, improving current empirical design formulas proposed by codes of practice [EC2-1, MC2010, SIA262:2013]. The model is also compared with the fatigue tests performed in the framework of this thesis, refer to Chapter 5.
The majority of this chapter's content can also be found in reference [Fer15].

7.2 Existing design approaches for shear-fatigue design

First attempts of developing design approaches for shear-fatigue failures were early developed by Chang and Kesler [Cha58a, Cha58b], who proposed a curve statistically obtained from their experimental tests in a semi-logarithmically *S-N* diagram ($V_{\max}/V_{static}$ *vs* $\log N$, where $V_{\max}$ is the maximum applied load, V_{static} is the static strength load and N is the fatigue life). The proposal presented a threshold for a maximum applied load of about 60% of the static failure load. In a discussion of the works of Chang and Kesler, Taylor [Tay59] pointed out that the fatigue strength was not only influenced by the maximum applied load, but also by the ratio between minimum and maximum applied loads and the size of the members. These investigations were later followed by the works of Higai [Hig78] and Farghaly [Far79] who proposed linear relationships in a semi-logarithmically *S-N* diagram without fatigue limits. One of the best known approaches was later established by Ueda [Ued82]. Ueda proposed a logarithmic *S-N*

formulation acknowledging the influence of the quasi-static (monotonic) shear strength and the levels of shear loading:

$$\log\frac{V_{\max}}{V_{cu}} = -0.036\left(1 - \frac{V_{\min}}{V_{\max}}\left|\frac{V_{\min}}{V_{\max}}\right|\right)\log N \tag{7.1}$$

where $V_{\min}$ refers to the minimum applied shear force, $V_{\max}$ to the maximum level of shear force and V_{cu} to the quasi-static shear strength. This expression showed a reasonable fitting to test results and is even applicable to reverse shear loading, although comparisons to tests were not provided by the author in reference [Ued82]. The formula was proposed without a consistent demonstration based on rational models, but a physical discussion on the influencing parameters is available and its shape was derived following logical considerations (its constants being fitted on the basis of tests).

Codes of practice like Eurocode 2 [EC2-1], the Swiss code [SIA262:2013] or *fib*-Model Code 2010 [MC2010] present shear-fatigue provisions for reinforced concrete members without shear reinforcement that are based on empirical Goodman diagrams or *S-N* formulations.

Eurocode 2 [EC2-1] distinguishes two different loading regimes. If the minimum ($V_{E,\min}$) and maximum ($V_{E,\max}$) applied shear forces have the same sign (no reverse loading), the code proposes for normal strength concrete (up to C50/60) the following Goodman diagram:

$$\frac{|V_{E,\max}|}{|V_{R,c}|} \leq 0.5 + 0.45\frac{|V_{E,\min}|}{|V_{R,c}|} \leq 0.9 \tag{7.2}$$

where $V_{R,c}$ is the static strength (Equation 3.10). If the maximum and minimum shear forces do not have the same sign (reverse loading cases), Equation 7.2 is modified as follows:

$$\frac{|V_{E,\max}|}{|V_{R,c}|} \leq 0.5 - \frac{|V_{E,\min}|}{|V_{R,c}|} \tag{7.3}$$

The Swiss code [SIA262:2013] proposes the same approach as Eurocode 2 [EC2-1]. However the static strength is calculated with a different formulation (Equation 3.12).

fib-Model Code 2010 [MC2010] presents the following *S-N* formulation:

$$\log N \leq 10\left(1 - \frac{V_{\max}}{V_{Ref}}\right) \tag{7.4}$$

where $V_{\max}$ is the maximum applied shear force, V_{Ref} the static shear strength (Equation 3.6) and N the fatigue life. It can be noted that this formulation does not include any consideration on the level of minimum applied shear force (which has nevertheless been observed as a potentially significant parameter [Ued82] and is explicitly incorporated by Eurocode 2 [EC2-1] and the Swiss code [SIA262:2013]). Equation 7.4 was already included in the previous version of the Model Code, but with a different formulation for the estimate of the static strength.

Recently, a rational approach for shear-fatigue has been proposed by Gallego et al. [Gal14a] (Section 3.8). The fatigue strength is obtained as a result of the breakdown of resisting mechanisms due to the propagation of a shear crack. The model includes a two-parameter Fracture Mechanics-based propagation law, in which the stress intensity factor is evaluated at the tip of the effective shear crack. The model allows to understand the mechanics of the shear-fatigue process, even though its application for practical purposes is not straightforward.

7.3 Consistent design for shear-fatigue

In this section, a new formulation for the shear strength of members without shear reinforcement subjected to fatigue loading is presented. This model is grounded on the principles of Fracture Mechanics (FM) applied to quasi-brittle materials (Section 3.7) together with the Paris-Erdogan law for crack propagation (Section 3.7.5). The analyses will be performed assuming also long-length cracks (as those characterizing shear failures). The validity of this assumption for concrete members failing in shear was previously investigated by Gallego et al. [Gal14a].
As it was discussed in Section 3.6.4, according to Linear Elastic Fracture Mechanics (LEFM) the propagation of a crack with the load cycles ($\mathrm{d}a/\mathrm{d}N$) depends on the amplitude of the stress intensity factor at the crack tip (ΔK), refer to Equation 3.58.
For application to concrete, the Paris-Erdogan law has shown to provide suitable results provided that it incorporates the size effect factor (refer to [Baz91], Section 3.7.5), which can be consistently described by Equation 3.89, which can be rewritten as:

$$\frac{\mathrm{d}a}{\mathrm{d}N} = \overline{C}\left(\Delta\sigma\sqrt{1+\beta}\right)^m \tag{7.5}$$

Assuming, as a first approximation, that factors β (related to size effect) and $\overline{C}$ (depending on material and geometrical properties) are roughly constant (other assumptions could be adopted but will not be investigated hereafter), it is obtained by integration:

$$a - a_0 = \overline{C}\,(1+\beta)^{m/2}\,\Delta\sigma^m N \tag{7.6}$$

where failure occurs for a crack $a = a_c$ at a number of cycles N_R, progressing from an initial crack length a_0. The expression thus turns into:

$$N_R^{1/m} = \frac{\left(\frac{a_c - a_0}{\overline{C}(1+\beta)^{m/2}}\right)^{1/m}}{\Delta\sigma} \tag{7.7}$$

This equation provides the number of cycles required to lead to failure. Its direct evaluation is possible [Gal14a], yet time-consuming and might be unpractical for simple design. Instead, the different terms can be correlated to physical values in the following manner:

— the stress amplitude can be assumed to be linearly dependent on the amplitude of the shear action, thus $\Delta\sigma \propto V_{c,N} - V_{\min}$, where $V_{c,N}$ refers to the shear force

leading to failure at a number N_R of cycles and $V_{\min}$ to the minimum acting shear force during the load cycles;

— the term $\left((a_c - a_0) / \left(\overline{C}\,(1+\beta)^{m/2}\right)\right)^{1/m} = \left(N_R^{1/m}\,(V_{c,N} - V_{\min})\right)$ is assumed to be linearly dependent on the shear strength under monotonic loading minus the minimum acting shear force, thus $\left((a_c - a_0) / \left(\overline{C}\,(1+\beta)^{m/2}\right)\right)^{1/m} \propto V_{c,1} - V_{\min}$.

It can be noted that the first hypothesis is reasonable and physically consistent, as the stresses acting in the member are proportional to the acting actions (provided that yielding of the reinforcement or crushing of concrete are not governing). Thus the acting range of stresses ($\Delta\sigma$) has to depend on the difference between maximum and minimum actions during load cycles ($V_{c,N} - V_{\min}$).

With respect to the second hypothesis, it is grounded on the fact that the crack length progresses from an initial length (a_0) to a critical one (a_c). This progression ($a_c - a_0$) takes place during a number of cycles N, when the applied shear force is increased (and thereafter decreased) in each cycle from a minimum acting shear force ($V_{\min}$) to a higher level. The critical length (a_c) can be assumed to be comparable to that developed by an identical member but loaded to failure in a monotonic manner (corresponding then to a shear force $V_{c,1}$). Thus, the increase of length of the crack from the minimum value during the load cycles to the critical one ($a_c - a_0$) could be related to the difference in the actions between the monotonic strength of the member and the minimum acting shear force during the load cycles ($V_{c,1} - V_{\min}$). The validity of this assumption can be easily verified for $N \to 1$, when $V_{\min} \to V_{c,1}$ leading to $a_0 \to a_c$. For other cases, its accuracy will be checked against available test results. It can be noted that future theoretical work is nevertheless required to assess or to correct the generality of this hypothesis.

With these assumptions Equation 7.7 turns to be:

$$N_R^{1/m} = \frac{V_{c,1} - V_{\min}}{V_{c,N} - V_{\min}}\kappa \tag{7.8}$$

The term κ is a coefficient that accounts for the proportionality of the two terms $V_{c,N} - V_{\min}$ and $V_{c,1} - V_{\min}$. Its value can be obtained by means of comparison to test results. As it will be shown later, $\kappa = 1$ yields good predictions of the actual behavior and will be adopted in the following.

For the use of Equation 7.8, it may also be noted that it is convenient to include in the notation the term $R = V_{\min}/V_{c,N} \geq 0$, leading thus to:

$$\frac{V_{c,N}}{V_{c,1}} = \frac{1}{R + N_R^{1/m}\,(1-R)} \tag{7.9}$$

It can be noted that evaluation of Equation 7.9 requires assessing the shear strength under monotonic loading (term $V_{c,1}$). This term depends on the material and geometrical parameters of the member and is influenced by some effects, as size effect (refer to term β). For evaluation of this term, the CSCT [Mut08a] (Section 3.2) can be used in a consistent manner. This formulation has in-built the influence of size effect (referring to the effective depth on which the crack width relies) and considers the geometrical and

mechanical parameters of the member in a consistent manner [Mut08a].
It should be noted that the CSCT is accepted valid for slender members ($a/d \geq 3$) and in cases without reverse loading. These restrictions will thus be applied for the use of Equation 7.9, and further studies should be performed to analyze its validity and potential modifications for these cases as well as other phenomena (like the damage accumulation (Palgrem-Miner effect)).
It can also be noted that the estimate of the monotonic shear strength $V_{c,1}$ incorporates already a number of influences (size and strain effects, concrete and aggregate properties). In addition, the loading rate can also be considered to estimate the shear strength. The loading rate increases or decreases the concrete strength [Rus60, Fer07] and this holds true also for shear-related failures under impact loading [Mic14] (with increasing nominal shear strength) or sustained loading [Sar13] (with decreasing nominal shear strength).

7.4 Comparison to test results on beams without shear reinforcement and existing design models

The previous design expression is compared in this section to the available experimental evidence. To that aim, the database presented by Gallego et al. [Gal14a] will be used, considering only slender members ($a/d \geq 3$) to avoid any arching action. The results are presented in terms of both of S-N and Goodman diagrams.
It is to be noted that the loading rate is accounted for in the comparisons. This is justified as the quasi-static reference strength provided by the shear design formula of the CSCT (or other design models) is aimed at quasi-static failures, in cases when loading duration is about one hour time (typical testing time). However, tests failing in fatigue loading are typically performed at much higher loading rates, typically 1 Hz. This implies that for $N_R \to 1$, the observed strength at higher loading rates should be higher than the corresponding one for a reference (quasi-static) specimen [Sar13, Mic14]. This phenomenon is accounted for in a simplified manner by using *fib*-Model Code 2010 [MC2010] expressions for modifying the concrete strength as a function of the loading rate. According to *fib*-Model Code 2010, the increase of the concrete strength for tests performed at a loading rate of 1 Hz with respect to quasi-static specimens (1 hour-time for failure) is approximately 10% ($\eta = 1.10 \approx 3600^{0.014}$). This value will be accepted as affecting the monotonic shear strength $V_{c,1}$, although a more refined investigation of this parameter will require future work.
In addition, the threshold value for propagation of crack lengths (refer to previous section) will be assumed as $V_{c,N}/V_{c,1} = 0.50$ (same as the one suggested by Eurocode [EC2-1] and the Swiss code [SIA262:2013]):

$$\frac{V_{c,N}}{V_{c,1}} = \frac{\eta}{R + N_R^{1/m}\,(1-R)} \geq 0.50 \tag{7.10}$$

Figure 7.1 shows the results obtained with the proposed approach (Equation 7.10) com-

pared to the available test dataset [Gal14a]. To that purpose, it has been proposed a value $m = 17$ and $\eta = 1.10$. In addition, only tests with values of $R \leq 10\%$ have been selected. The influence of this parameter is investigated with the Goodman diagrams. These values (m, η and threshold) refer to the average response of the test results, and could be adapted, if necessary, to respect a target safety level (5% fractile or other). A very good agreement is obtained for this sub-set of tests, with an average ratio between $V_{\max}/V_{c,1}$ ($V_{c,1}$ calculated according to Equation 3.5) and $V_{c,N}/V_{c,1}$ (substituting the experimental N in Equation 7.10) equal to 1.06 with a CoV of 13%, refer to Table 7.1. It should be noted that the predictions show a very low scatter, with a value similar to that obtained by the CSCT for evaluation of monotonic shear failures [Mut08a], thus the model for cyclic behavior adding no further scatter to the estimate of the shear strength. In addition, the threshold for shear crack propagation is attained for a number of cycles close to 10^6.

The comparison of the test results in terms of Goodman diagrams allows observing the influence of the load levels ($V_{c,N}$ and $V_{\min}$) on the shear-fatigue strength. Such diagrams are shown in Figure 7.2 for the complete range of R. The predictions are again consistent, suitably incorporating the influence of R. The results show a good agreement between the predicted and measured strengths (average ratio between $V_{\max}/V_{c,1}$ and $V_{c,N}/V_{c,1}$ equal to 1.00) with a low value of the CoV (15%), refer to Table 7.1. It can be noted that the value selected for the threshold is considered independent of the ratio R in good agreement to test results. This aspect could however be developed in future research (for high values of parameter R, the specimen is permanently subjected to a high level of shear stresses, which may lead to the phenomenon of concrete fatigue under sustained loading [Fer07]).

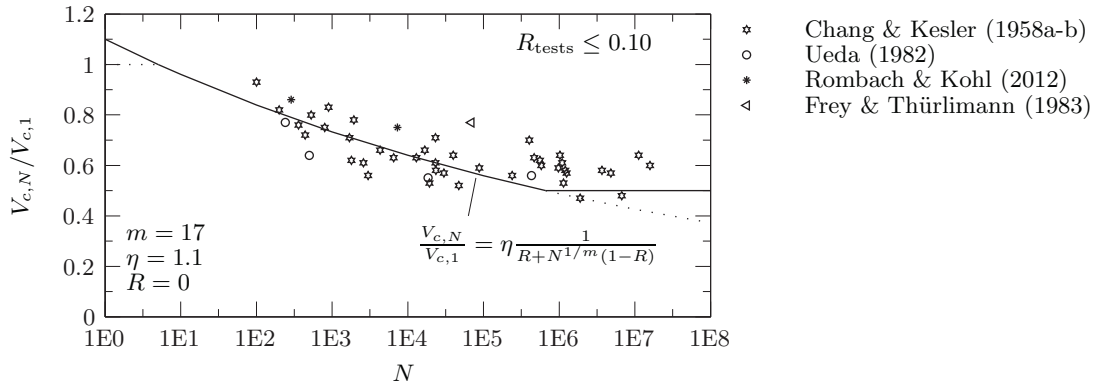

Figure 7.1: Comparison of the proposed approach and available test data ($R \leq 10\%$) as a S-N diagram showing shear-fatigue failure

With respect to codes of practice, it can be noted that the formulas of Eurocode 2 [EC2-1] and the Swiss code [SIA262:2013] are not an estimator of the number of cycles to failure, but they provide a suitable threshold to avoid premature shear failures. Its application to the database provides thus quite safe estimates of the shear-fatigue failures (Average

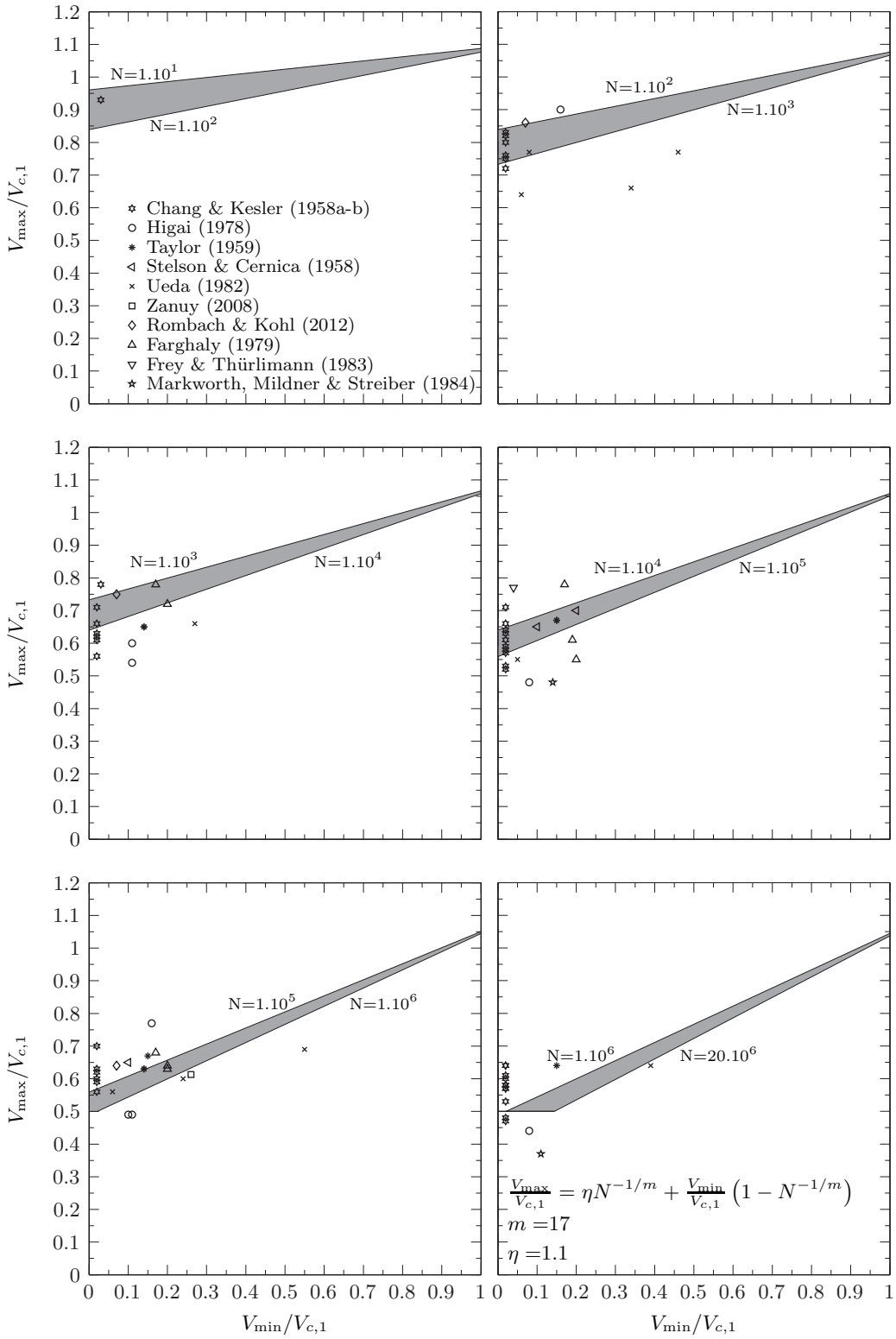

Figure 7.2: Comparison of the proposed approach and available test data in Goodman diagrams

= 1.29, CoV = 0.20 for Eurocode 2, Average = 1.33, CoV = 0.19 for SIA262:2013), refer to Table 7.1 and to Figures 7.3 and 7.4. With respect to *fib*-Model Code 2010 [MC2010], the formula yields safe estimates of the strength (Average = 1.52, CoV = 0.22, as it should be expected for a design code), particularly for members failing under a large number of cycles, as it does not present any threshold, refer to Table 7.1 and to Figure 7.5. It can be noted that both design codes lead in fact to quite safe estimates on average, but with significant scatter in the predictions. The test results are on the contrary well estimated with the proposed LEFM (for quasi-brittle materials) and the CSCT approach, with consistent and low scatter for both low and high number of cycles.

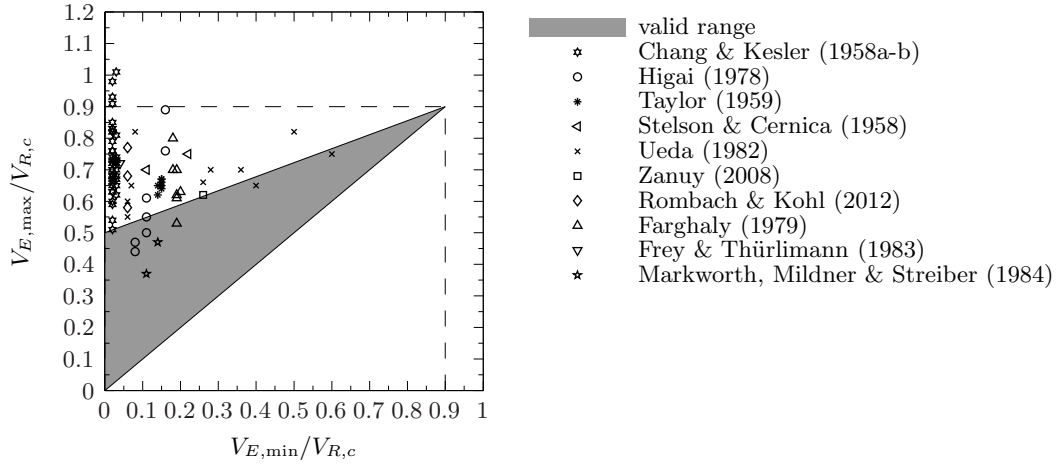

Figure 7.3: Comparison of Eurocode 2 and available test data

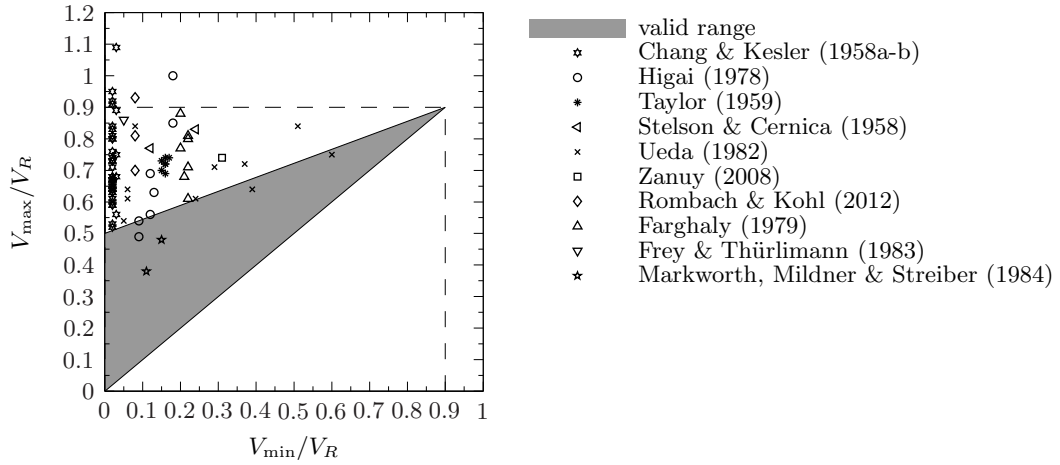

Figure 7.4: Comparison of SIA262:2013 and available test data

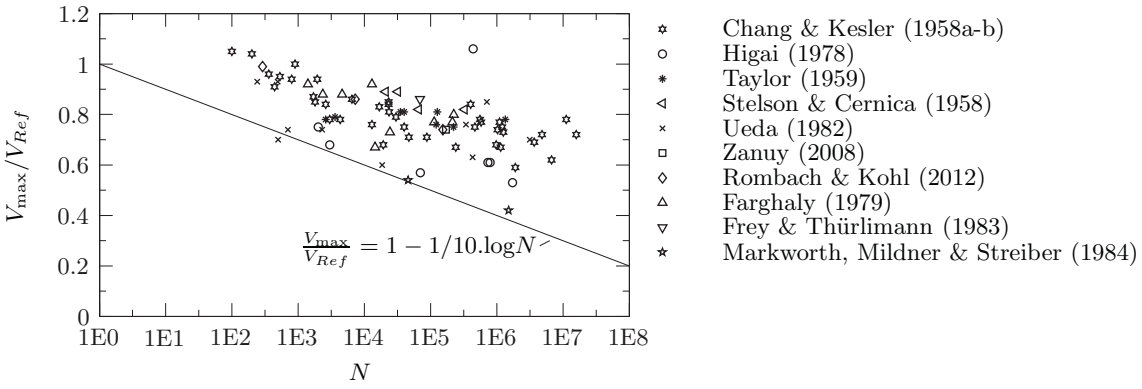

Figure 7.5: Comparison of *fib*-Model Code 2010 and available test data

Table 7.1: Comparison between experimental tests and investigated models

Authors	Test ID	b [m]	d [m]	ρ_l [%]	f_c [MPa]	a/d	d_g [mm]	R	$V_{\max}$ [kN]	N experimental	CSCT $R=0$	CSCT R	MC2010	EC2	SIA262:2013
[Cha58a, Cha58b]	2	0.10	0.14	1.02	42.7	3.7	25	0.04	12	23500	0.96	0.94	1.44	1.37	1.21
[Cha58a, Cha58b]	3	0.10	0.14	1.02	41.2	3.7	25	0.04	12	3000	0.82	0.81	1.19	1.32	1.16
[Cha58a, Cha58b]	4	0.10	0.14	1.02	34.1	3.7	25	0.04	12	6500	0.96	0.95	1.40	1.47	1.31
[Cha58a, Cha58b]	5	0.10	0.14	1.02	36.2	3.7	25	0.04	12	1800	0.87	0.86	1.26	1.44	1.28
[Cha58a, Cha58b]	9	0.10	0.14	1.02	36.9	3.7	25	0.04	12	2600	0.88	0.87	1.28	1.43	1.27
[Cha58a, Cha58b]	10	0.10	0.14	1.02	30.5	3.7	25	0.05	10	47100	0.90	0.88	1.34	1.21	1.09
[Cha58a, Cha58b]	12	0.10	0.14	1.02	38.3	3.7	25	0.04	12	23200	1.00	0.99	1.49	1.42	1.26
[Cha58a, Cha58b]	22	0.10	0.14	1.02	44.1	3.7	25	0.04	12	30000	0.95	0.93	1.44	1.34	1.18
[Cha58a, Cha58b]	4-6	0.10	0.14	1.86	29.3	3.7	25	0.03	16	800	1.00	1.00	1.33	1.62	1.64
[Cha58a, Cha58b]	4-7	0.10	0.14	1.86	32.1	3.7	25	0.02	18	200	1.02	1.01	1.36	1.80	1.80
[Cha58a, Cha58b]	4-8	0.10	0.14	1.86	32.0	3.7	25	0.03	13	557000	1.22	1.20	1.84	1.35	1.35
[Cha58a, Cha58b]	4-9	0.10	0.14	1.86	27.0	3.7	25	0.03	13	16800	1.07	1.05	1.44	1.43	1.46
[Cha58a, Cha58b]	4-11	0.10	0.14	1.86	27.2	3.7	25	0.05	10	1900200	0.94	0.94	1.58	1.01	1.02
[Cha58a, Cha58b]	4-12	0.10	0.14	1.86	29.6	3.7	25	0.04	11	1142100	1.06	1.06	1.70	1.15	1.16
[Cha58a, Cha58b]	4-14	0.10	0.14	1.86	37.3	3.7	25	0.04	12	19300	0.86	0.85	1.19	1.17	1.15
[Cha58a, Cha58b]	4-15	0.10	0.14	1.86	14.8	3.7	25	0.04	12	1940	1.11	1.09	1.39	1.59	1.75
[Cha58a, Cha58b]	4-16	0.10	0.14	1.86	29.2	3.7	25	0.03	15	440	0.94	0.93	1.24	1.57	1.58
[Cha58a, Cha58b]	4-17	0.10	0.14	1.86	29.6	3.7	25	0.03	16	360	0.97	0.96	1.28	1.65	1.66
[Cha58a, Cha58b]	4-19	0.10	0.14	1.86	35.9	3.7	25	0.04	11	6690200	0.97	0.97	1.95	1.06	1.05
[Cha58a, Cha58b]	4-24	0.10	0.14	1.86	31.7	3.7	25	0.04	12	4822400	1.14	1.14	2.17	1.24	1.24
[Cha58a, Cha58b]	4-25	0.10	0.14	1.86	29.5	3.7	25	0.04	13	1097300	1.21	1.21	1.93	1.31	1.33
[Cha58a, Cha58b]	4-27	0.10	0.14	1.86	35.3	3.7	25	0.03	13	1250400	1.14	1.14	1.86	1.25	1.24
[Cha58a, Cha58b]	4-28	0.10	0.14	1.86	37.4	3.7	25	0.03	14	578800	1.20	1.18	1.83	1.33	1.31
[Cha58a, Cha58b]	4-29	0.10	0.14	1.86	37.0	3.7	25	0.03	13	1207600	1.16	1.16	1.91	1.28	1.27
[Cha58a, Cha58b]	1-5	0.10	0.14	2.89	19.9	3.7	25	0.04	12	1027200	1.28	1.28	1.86	1.41	1.47
[Cha58a, Cha58b]	2-5	0.10	0.14	2.89	19.7	3.7	25	0.04	11	976100	1.17	1.17	1.69	1.28	1.34
[Cha58a, Cha58b]	3-5	0.10	0.14	2.89	25.0	3.7	25	0.03	13	467200	1.24	1.22	1.72	1.43	1.44
[Cha58a, Cha58b]	5-3	0.10	0.14	2.89	32.6	3.7	25	0.03	17	23200	1.16	1.14	1.51	1.64	1.59
[Cha58a, Cha58b]	5-4	0.10	0.14	2.89	37.0	3.7	25	0.02	18	1700	1.00	1.00	1.28	1.68	1.61
[Cha58a, Cha58b]	5-5	0.10	0.14	2.89	32.2	3.7	25	0.03	16	402900	1.36	1.34	1.91	1.62	1.58
[Cha58a, Cha58b]	5-6	0.10	0.14	2.89	34.7	3.7	25	0.03	14	15871700	1.19	1.19	2.57	1.39	1.34
[Cha58a, Cha58b]	5-3	0.10	0.14	2.89	34.5	3.7	25	0.03	16	11217700	1.29	1.29	2.63	1.50	1.45
[Cha58a, Cha58b]	5-10	0.10	0.14	2.89	14.9	3.7	25	0.03	16	100	1.11	1.10	1.31	1.99	2.16
[Cha58a, Cha58b]	5-11	0.10	0.14	2.89	24.8	3.7	25	0.03	13	39800	1.08	1.06	1.39	1.43	1.45
[Cha58a, Cha58b]	5-12	0.10	0.14	2.89	28.0	3.7	25	0.02	18	530	1.06	1.05	1.31	1.84	1.83
[Cha58a, Cha58b]	5-13	0.10	0.14	2.89	30.6	3.7	25	0.03	13	3666500	1.16	1.16	2.02	1.34	1.31
[Cha58a, Cha58b]	5-14	0.10	0.14	2.89	36.8	3.7	25	0.03	16	13000	0.99	0.98	1.29	1.47	1.41
[Cha58a, Cha58b]	5-15	0.10	0.14	2.89	33.2	3.7	25	0.03	13	239000	1.06	1.04	1.46	1.30	1.26
[Cha58a, Cha58b]	5-16	0.10	0.14	2.89	27.6	3.7	25	0.03	14	4300	0.98	0.97	1.23	1.50	1.49
[Cha58a, Cha58b]	5-17	0.10	0.14	2.89	35.8	3.7	25	0.03	14	87800	1.04	1.03	1.41	1.38	1.32
[Cha58a, Cha58b]	5-20	0.10	0.14	2.89	32.7	3.7	25	0.02	20	900	1.13	1.12	1.42	1.94	1.89
[Ste58]	1	0.13	0.11	2.90	26.6	5.6	13	0.15	13	66000	-	1.05	1.59	1.30	1.44
[Ste58]	2	0.13	0.11	2.90	26.6	5.6	13	0.15	13	323000	-	1.14	1.83	1.30	1.44
[Ste58]	7	0.13	0.11	2.90	26.6	5.6	13	0.29	14	32000	-	1.01	1.61	1.31	1.45
[Ste58]	8	0.13	0.11	2.90	26.6	5.6	13	0.29	14	20800	-	0.99	1.56	1.31	1.45
[Tay59]	2	0.19	0.22	1.21	29.5	4.1	19	0.23	31	1340000	-	1.16	2.02	1.14	1.24
[Tay59]	3	0.19	0.22	1.21	29.5	4.1	19	0.22	33	40000	-	1.02	1.50	1.20	1.29
[Tay59]	5	0.19	0.22	1.49	29.5	4.1	19	0.22	35	126000	-	1.09	1.66	1.20	1.33
[Tay59]	6	0.19	0.22	1.49	29.5	4.1	19	0.22	35	35000	-	1.02	1.49	1.20	1.33

Continued on next page

Table 7.1 – *Continued from previous page*

Authors	Test ID	b [m]	d [m]	ρ_l [%]	f_c [MPa]	a/d	d_g [mm]	R	$V_{\max}$ [kN]	N experimental	CSCT $R=0$	CSCT R	MC2010	EC2	SIA262:2013
[Tay59]	9	0.19	0.22	1.83	29.5	4.1	19	0.22	35	121000	-	1.02	1.54	1.12	1.26
[Tay59]	10	0.19	0.22	1.83	29.5	4.1	19	0.21	36	3600	-	0.88	1.22	1.17	1.31
[Tay59]	13	0.19	0.22	2.33	29.5	4.1	19	0.23	38	222000	-	1.04	1.62	1.16	1.29
[Tay59]	14	0.19	0.22	2.33	29.5	4.1	19	0.22	39	2600	-	0.86	1.18	1.21	1.34
[Hig78]	FT 3	0.20	0.20	2.15	39.8	4.0	15 (*)	0.19	27	1740000	-	0.83	1.40	0.80	0.90
[Hig78]	FT 4	0.20	0.20	2.15	39.8	4.0	15 (*)	0.17	29	70000	-	0.77	1.11	0.88	0.99
[Hig78]	FT 13	0.20	0.16	2.40	31.1	5.0	15 (*)	0.18	28	2000	-	0.80	1.12	1.12	1.27
[Hig78]	FT 14	0.20	0.16	2.40	29.1	5.0	15 (*)	0.20	25	3000	-	0.73	1.04	1.00	1.14
[Hig78]	FT 16	0.20	0.16	2.40	32.8	5.0	15 (*)	0.22	23	790000	-	0.87	1.49	0.90	1.02
[Hig78]	FT 19	0.20	0.16	2.40	35.1	5.0	15 (*)	0.21	24	730000	-	0.87	1.47	0.90	1.01
[Hig78]	FT 6	0.20	0.11	1.80	34.4	6.4	15 (*)	0.18	28	500	-	1.12	1.71	1.64	1.84
[Hig78]	FT 7	0.20	0.11	1.80	35.5	6.4	15 (*)	0.21	24	440000	-	1.33	2.44	1.38	1.54
[Far79]	3.5-F-70-1	0.30	0.22	1.74	30.1	3.5	20 (*)	0.31	55	24300	-	0.87	1.30	1.09	1.17
[Far79]	3.5-F-70-2	0.30	0.22	1.74	22.5	3.5	20 (*)	0.25	55	223500	-	1.11	1.73	1.24	1.36
[Far79]	3.5-F-80-1	0.30	0.22	1.74	22.5	3.5	20 (*)	0.22	63	1400	-	1.01	1.34	1.44	1.58
[Far79]	3.5-F-80-2	0.30	0.22	1.74	22.5	3.5	20 (*)	0.22	63	13000	-	1.12	1.57	1.44	1.58
[Far79]	4.5-F-60-1	0.30	0.22	1.74	26.0	4.5	20 (*)	0.36	44	14500	-	0.74	1.14	0.89	1.02
[Far79]	4.5-F-70-1	0.30	0.22	1.74	26.0	4.5	20 (*)	0.31	51	214000	-	1.00	1.65	1.06	1.22
[Far79]	4.5-F-70-2	0.30	0.22	1.74	26.3	4.5	20 (*)	0.31	51	113700	-	0.97	1.56	1.06	1.21
[Far79]	4.5-F-80-1	0.30	0.22	1.74	26.0	4.5	20 (*)	0.28	58	2350	-	0.93	1.33	1.23	1.41
[Far79]	4.5-F-80-2	0.30	0.22	1.74	26.3	4.5	20 (*)	0.28	58	4600	-	0.96	1.38	1.22	1.41
[Ued82]	1A	0.20	0.44	0.68	33.4	3.5	25	0.10	49	500	0.84	0.81	0.96	1.25	1.23
[Ued82]	1B	0.20	0.44	0.68	33.4	3.5	25	0.61	49	3140000	-	0.90	2.01	0.95	0.93
[Ued82]	2A	0.20	0.44	0.68	45.5	3.5	25	0.10	46	18600	0.89	0.85	1.05	1.06	1.04
[Ued82]	3B	0.20	0.44	1.67	33.4	3.5	25	0.51	71	700	-	0.74	1.04	1.08	1.12
[Ued82]	4A	0.20	0.44	1.67	45.5	3.5	25	0.10	67	430000	1.10	1.04	1.45	1.14	1.16
[Ued82]	4B	0.20	0.44	1.67	45.5	3.5	25	0.41	79	2300	-	0.81	1.12	1.15	1.17
[Ued82]	5B	0.40	0.22	0.68	34.2	3.5	25	0.40	58	341000	-	0.91	1.71	1.08	1.00
[Ued82]	7A	0.40	0.22	1.67	34.2	3.5	25	0.60	98	490	-	0.82	1.28	1.20	1.23
[Ued82]	7B	0.40	0.22	1.67	34.2	3.5	25	0.10	98	240	0.96	0.94	1.23	1.57	1.61
[Ued82]	8A	0.40	0.22	1.67	46.0	3.5	25	0.80	99	706000	-	0.79	2.06	0.96	0.96
[Fre83]	BII-7	0.30	0.37	1.72	32.3	4.3	16	0.05	95	69000	1.35	1.31	1.67	1.41	1.68
[Mar84]	H2-4	0.30	0.30	0.84	40.0	3.5	16	0.30	45	46000	-	0.70	1.01	0.82	0.84
[Mar84]	H2-5	0.30	0.30	0.84	40.0	3.5	16	0.30	35	1512000	-	0.65	1.10	0.64	0.65
[Zan08]	VA1	0.30	0.26	2.51	25.0	5.2	20	0.42	60	170718	-	0.89	1.55	1.00	1.20
[Rom12]	V-3	0.20	0.30	1.56	39.0	5.0	16	0.08	60	289	1.09	1.06	1.31	1.49	1.79
[Rom12]	V-4	0.20	0.30	1.56	39.0	5.0	16	0.10	53	7290	1.15	1.11	1.40	1.30	1.56
[Rom12]	V-5	0.20	0.30	1.56	39.0	5.0	16	0.11	45	153000	-	1.11	1.53	1.10	1.32
										Avg	1.06	1.00	1.52	1.29	1.33
(*) assumed values										CoV	0.13	0.15	0.22	0.20	0.19

7.5 Comparison to test results on cantilever slabs under concentrated loads

Figure 7.6 shows the comparison between the proposed model and the tests performed in this thesis and presented in Chapter 5. The monotonic shear strength was calculated according to Section 6.2. The shear-fatigue strength is underestimated and the $V_{c,N}/V_{c,1}$ ratios of the tests compared with the model have an Average of 1.27 (CoV= 0.14) for $a_v/d = 2.1$ and 1.10 (CoV= 0.10) for $a_v/d = 3.2$, just considering the tests that experienced shear failures (with or without rebar fracture) and excluding the reference tests.

As the number of cycles increases, the safety margin seems to remain approximately constant, indicating the pertinence of the shear-fatigue prediction and the presence of internal forces redistributions also for fatigue specimens (refer to the internal forces redistributions accounted for in the calculation of $V_{c,1}$). It has to be noted that the values of maximum applied load were relatively high (60% or more of the static shear strength) and thus no fatigue threshold was observed.

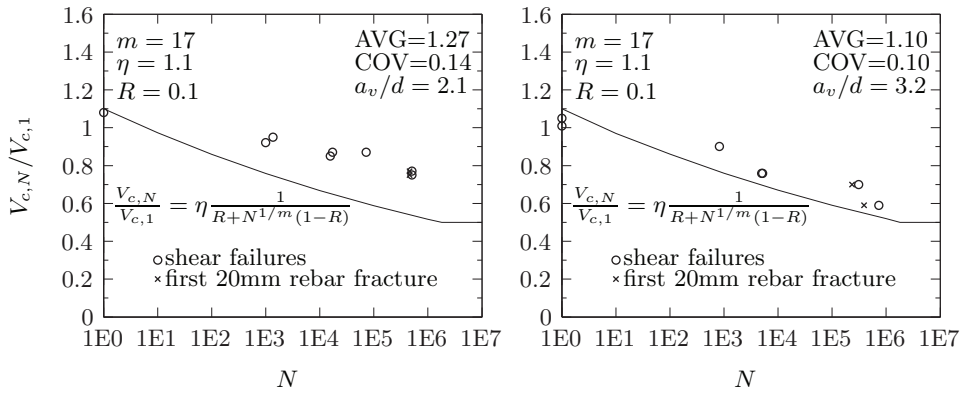

Figure 7.6: Comparison to test results on cantilever slabs under concentrated loads

Chapter 8

Conclusions

8.1 Introduction

The present chapter presents a summary of the main findings and contributions of this thesis, and identifies open questions that might be interesting to investigate in future work.

In this thesis the static and fatigue shear behavior of reinforced concrete slabs without shear reinforcement under concentrated loads near linear supports has been investigated. These structures differ from beams (or one-way slabs loaded over the full width) and flat slabs supported on columns, because shear forces do not develop perfectly in a parallel or radial manner, and shear and bending moments in the shear critical regions may vary due to redistributions on shear and moment fields, after flexural and/or shear cracking. Despite these differences, most available experimental results have only concentrated on beams (or one-way slabs loaded over the full width) and two-way slabs with axis-symmetric punching conditions. In the framework of this thesis, two experimental campaigns on full-scale cantilever slabs under a concentrated load have been performed, both under monotonic and fatigue loading. The specimens were meant to reproduce typical cantilever deck slabs of European bridges.

The first experimental campaign (static campaign) performed on square slabs (3.00 m x 3.00 m x 0.18 m) linearly supported in the center (aluminium profile that allows tracing the linear reaction evolution) aimed at studying the influence of the location of the concentrated load and the presence or not of injected and non-injected ducts (typical of prestressed concrete balanced cantilever bridges). Twelve tests were performed on six slabs.

The second experimental campaign (fatigue campaign), also performed on square slabs (3.00 m x 3.00 m x 0.25 m) linearly supported in the center, aimed at studying the influence of the location of the concentrated load and of the level of applied fatigue loads. Four monotonic tests were performed on two slabs, and eleven fatigue tests were performed on eight slabs.

In the framework of the Critical Shear Crack Theory (CSCT), studies have been performed on how to apply it for the shear/punchig shear assessment/design of reinforced

concrete slabs under concentrated loads near linear supports. With the aim of keeping a complexity level comparable to Level III of *fib*-Model Code 2010 [MC2010], proposals were made on how to model these structures with Linear Elastic Finite Elements (LEFE), and on how to account for shear redistributions due to both flexural and shear cracking. The combined use of the CSCT with the proposals herein was compared with tests (both from this thesis and from the literature) on cantilevers slabs and on simply supported slabs.
Also in the framework of the CSCT, a consistent design approach for shear-fatigue was presented, applying the principles of fracture mechanics (FM) of quasi-brittle materials combined with the CSCT. The approach leads to a simple, yet sound and rational design equation incorporating the different influences of fatigue loading (minimum and maximum load levels) and shear strength (size and strain effects, material and geometrical properties). The accuracy of the assessment/design expression was checked against available test data on beams and on cantilever slabs under concentrated loads near linear supports.

8.2 Contributions and conclusions

The present section identifies the main contributions and conclusions of this thesis.

8.2.1 Static tests

The static tests performed in the framework of this thesis, both from the static experimental campaign (twelve tests on six square slabs (3.00 m x 3.00 m x 0.18 m) linearly supported in the center) and the experimental fatigue campaign (four tests on two square slabs (3.00 m x 3.00 m x 0.25 m) linearly supported in the center), contribute with an important number of tests to the existing testing available in the literature. The main conclusions of these tests on cantilever slabs are:

- The tests showed shear failures to be governing for all investigated specimens, with different locations of the load and duct types. This is consistent with the observed crack patterns of the center saw-cuts;
- Prior to failure, redistributions of shear forces were measured as a consequence of the opening of shear cracks in the region between the load and the line support;
- The two-way behavior of slabs indicates that tests on beams are not necessarily representative of bridge deck slabs;
- Low free shear span-to-effective flexural depth ratios ($a_v/d \approx 2$) present high shear strengths when compared with larger values (3 or 4), indicating a dependence on the arching action. For larger values of a_v/d (3 or 4), even though the acting shear force close to the support decreases for larger a_v/d ratios, the unitary bending moment increases (leading to larger crack openings, thus limiting shear transfer through cracks, *i.e.*, reducing the unitary shear strength), resulting in a fairly constant shear strength for the static experimental campaign;

— No significant shear strength differences were observed between regular reinforced concrete slabs and those with injected ducts. In the case of empty ducts, the shear strength was noticeably reduced.

8.2.2 Fatigue tests

The fatigue tests performed in the framework of this thesis (eleven tests on eight square slabs (3.00 m x 3.00 m x 0.25 m) linearly supported in the center) contribute with an important number of tests to the literature. To the author's knowledge these tests are among the first to be performed on cantilever slabs under concentrated loads. The main conclusions of these tests are:

— Fatigue loading of cantilever slabs with two-way action exhibits a similar influence on the shear strength as in beams (or one-way slabs loaded over the full width) without transverse reinforcement, decreasing the shear strength with increasing number of cycles;
— Redistribution of shear forces were measured for slabs failing under fatigue loading;
— The redistribution of internal forces enhances the shear strength of cantilever slabs with respect to equivalent beams failing in shear;
— Shear-fatigue failures without rebar fractures only occur for very high levels of maximum applied load;
— Slabs failing in shear after rebar fractures occured show a considerable remaining fatigue life after the first rebar fracture;
— Slabs presenting rebar fractures eventually fail in shear.

8.2.3 Assessment based on the CSCT

With respect to the shear/punching shear assessment of slabs under concentrated loads near linear supports, the following conclusions could be drawn:

— Cantilever slabs are unlikely to fail in punching shear. Shear is most likely the governing failure mode of typical European cantilever deck slabs;
— The governing failure mode of simply supported slabs without significant in-plane confinement seems to be related to the ratio between the load dimension parallel to the support and the slab width (c_y/b). Tests from the literature suggest that punching shear is the governing failure mode when $c_y/b \to 0$;
— The consideration of shear transferring by a compression chord is not grounded on unequivocal experimental evidence. Accounting for this effect is not recommended;
— Arching action seems to develop for free shear spans up to approximately 3 times the effective flexural depth.

In this thesis several proposals were presented to perform the shear/punching shear assessment of slabs under concentrated loads near linear supports with the CSCT. The following contributions were developed for shear assessment:

— LEFE analyses with shell elements with shear deformation and $\left(\nu = 0; G = \frac{E}{16}\right)$ are a useful simple tool to determine the internal forces in reinforced concrete slabs under concentrated loads. Comparisons between calculated linear reactions and measurements at failure ground this modeling choice, provided that the finite element local axis and the reinforcement directions coincide;
— Cantilever slabs should be assessed in shear at a control section located at $d/2$ from the support, provided that no reinforcement changes or abrupt thickness variations occur. Otherwise one has to search for a control section where the applied shear force and concomitant bending moment yields the minimum shear strength;
— Shear redistributions in cantilever slabs might be considered in a simplified manner by considering an averaged shear force over a distance $4d$ combined with the bending moment at the location of maximum shear;
— Simply supported slabs should be assessed in shear at a control section located at $d/2$ from the load;
— Simply supported slabs might be assessed with an average shear force calculated over a distance $4d + c_y$ combined with the bending moment at the location of maximum shear;
— Arching action might be accounted assuming that the contribution of concentrated loads applied within a distance $d < a_v < 2.75d$ from the face of the support to the design shear force may be reduced by the factor $\beta = a_v/2.75d \leq 1$;
— Round non-injected ducts or inserts of diameter d_0 (or square ones comprised in a d_0 diameter) spaced d from each other might be considered reducing the effective shear depth ($d_v = d - \sqrt{2}/2d_0$).

With the aim of keeping a complexity level comparable to Level III of *fib*-Model Code 2010 [MC2010], the following methodology was adopted to perform punching shear assessments of simply supported slabs (keeping the same FE modeling as for shear):

— Punching shear redistributions can be accounted according to the CSCT for non-axis-symmetric punching [Sag11];
— Rotations in each reinforcement direction and load face can be calculated according to an approach based on the *fib*-Model Code 2010 [MC2010];
— A reduced control perimeter in each reinforcement direction and load face might be considered. It is proposed to take the elastic control perimeter at each control perimeter segment.

The combined used of the CSCT with the proposals of this thesis has been shown to be reasonably adequate for cantilever slabs. For simply supported slabs, the failure mode could not always be predicted. However, the proposals yield a safe design approach when compared with the available experimental evidence.

Inner slabs with negligible in-plane confinement, where concentrated loads act close to a linear support and are subjected to negative bending moments in the region between the support and the load can be treated in the same way as cantilever slabs.

8.2.4 Shear-fatigue

A consistent design approach for shear-fatigue of slender reinforced concrete members ($a/d \geq 3$) without transverse reinforcement was presented in this thesis, applying the principles of FM for quasi-brittle materials in combination with the CSCT.
The following conclusions could be drawn:

- Shear-fatigue failures are due to development and growth of shear cracks. Consistent design can thus be performed on the basis of FM for quasi-brittle materials combined with the CSCT. This approach leads to a simple, yet sound and rational design equation incorporating the different influences of fatigue actions and shear strength: minimum and maximum load levels, size and strain effects, material and geometrical properties;
- Shear-fatigue on beams seems not to occur for values of maximum applied load below approximately 50% of the static shear strength, and this value can be satisfactorily used as a threshold for shear crack propagation when compared to test results (the number of tests with fatigue failure occurring at a number of cycles larger than 10^6 cycles is yet limited);
- Consistent agreement is obtained with the proposed approach in terms of Wöhler and Goodman diagrams, being the estimate of the number of cycles until failure significantly more accurate and with lower scatter than current empirical shear-fatigue formulation of *fib*-Model Code 2010 [MC2010]. The scatter obtained with the proposed approach is in addition similar to that of the CSCT for members failing in shear under monotonic loading and thus the proposed formulation adds no significant further scatter to the phenomenon;
- With respect to cantilever slabs under concentrated loads, as the number of cycles increases the safety margin of the proposed approach seems to remain approximately constant, indicating the pertinence of the shear-fatigue predictions and the presence of internal forces redistributions also for fatigue tested specimens. As the values of maximum applied load in this thesis were relatively high (60% or more of the static shear strength), no fatigue threshold was observed.

8.3 Future work

In this section, some propositions of research to be considered in future works are presented.
At the experimental level:

- More static tests on cantilever slabs under concentrated loads subjected to important line loads at the cantilever tip, in order to clarify their influence. The existing test database is insufficient to extract valid conclusions;
- More static tests on cantilever slabs under concentrated loads, varying the longitudinal bottom reinforcement, in order to verify if there is an influence of this parameter on the shear strength and redistribution capacity;

— Fatigue tests on cantilever slabs under moving concentrated loads, in order to study the influence of this parameter.

At the simplified assessment level, in order to keep the used approaches simple for their use in practice:

— Improvements have to be made in order to make possible the prediction of the correct failure mode of simply supported slabs under concentrated loads;
— The study of other control sections, other ways to calculate rotations and ways to consider shear redistributions might be performed.

At the assessment level, increasing the complexity level:

— The use of the CSCT failure criteria combined with nonlinear finite element (NLFE) analyses seems to be promising, refer to the work of Belletti et al. [Bel14];
— A method with a mechanical basis to consider internal forces redistributions due to shear cracking is desirable;
— The correct determination of internal bending moments and shear forces is extremely important for both monotonic and fatigue assessment. Even though it is out of the scope of this thesis, with respect to the assessment of rebar failures due to fatigue loading, this importance is even greater to correctly assess the fatigue life. Reliable NLFE models with input variables that can be easily determined by engineers are though desirable. In this same particular point, concerning the rebar stress amplitude determination, another relevant aspect that can be investigated is the determination of the residual strains in the reinforcement due to imperfect crack closure and negative adherence (refer to Figure 5.13). The commonly stress amplitude calculation based on the applied bending moment and an elastic strain distribution with cracked section might be too conservative.

At the theoretical level:

— Shear and punching shear are closely related phenomena. A unified model for shear and punching shear should be possible to be developed.

Bibliography

[ANSYS] **ANSYS®Academic Research**, *Release 11.0 documentation for ANSYS*

[Ars12] **Arshi H.S., Günzel F.K., Stone K.J.L.**, *Shear resistance of reinforced concrete beams with pre-cast circular web openings*, The Structural Engineer, pp. 51-56, 2012

[Bat78] **Batchelor B.d.V., Hewitt B.E., Csagoly P.**, *An investigation of the fatigue strength of deck slabs of composite steel/concrete bridges*, Transportation Research Record, No. 664, pp. 153-161, 1978

[Baz83] **Bažant Z.P., Oh B.H.**, *Crack band theory for fracture of concrete*, Materials and Structres, Vol. 16, pp. 155-177, 1983

[Baz84] **Bažant Z.P.**, *Size effect in blunt fracture: concrete, rock, metal*, Journal of Engineering Mechanics, Vol. 110, No. 4, pp. 518-535, 1984

[Baz90] **Bažant Z.P., Kazemi M.T.**, *Determination of fracture energy, process zone length and brittleness number from size effect, with application to rock and concrete*, International Journal of Fracture, Vol. 44, pp. 111-131, 1990

[Baz91] **Bažant Z.P., Xu K.**, *Size effect in fatigue fracture of concrete*, ACI Materials Journal, Vol. 88, No. 4, pp. 390-399, 1991

[Baz02] **Bažant Z.P., Becq-Giraudon E.**, *Statistical prediction of fracture parameters of concrete and implications for choice of testing standard*, Cement and Concrete Research, Vol. 32, pp. 529-556, 2002

[Bel14] **Belletti B., Damoni C., Hendriks, M.A.N., de Boer A.**, *Analytical and numerical evaluation of the design shear resistance of reinforced concrete slabs*, Structural Concrete, Vol. 15, No. 3, pp. 317-330, 2014

[Ben06] **Bentz E.C., Vecchio F.J., Collins M.P.**, *Simplified modified compression field theory for calculating shear strength of reinforced concrete elements*, ACI Structural Journal, Vol. 103, No. 4, pp. 614-624, 2006

[Bru89] **Brühwiler E., Roelftra P.E.**, *Tensile softening properties and structural response of a concrete member*, Recent Developments in the Fracture of Concrete and Rock, pp. 682-692, 1989

[Cam13a] **Campana S., Fernández Ruiz M., Anastasi A., Muttoni A.**, *Analysis of shear-transfer actions on one-way RC members based on measured cracking pattern and failure kinematics*, Magazine of Concrete Research, UK, Vol. 56, No. 6, pp. 386-404, 2013

[Cam13b] **Campana S.**, *Reinforced concrete elements subjected to a combinadion of flexure, shear and deviation forces* (in French: *Éléments en béton armé soumis à une combinaison de flexion, effort tranchant et forces de déviation*), PhD Thesis, EPFL, 162p., 2013

[Car11] **Carpinteri A., Carmona J.R., Ventura G.**, *Failure mode transitions in reinforced concrete beams - part I: theoretical model*, ACI Structural Journal, Vol. 108, No. 3, pp. 277-285, 2011

[CEB88] **CEB**, *Fatigue of concrete structures - state of the art report*, Bulletin d'information 188, 1988

[Cha58a] **Chang T.S., Kesler C.E.**, *Static and fatigue strength in shear of beams with tensile reinforcement*, ACI Journal, Vol. 54, No. 6, pp. 1033-1057, 1958

[Cha58b] **Chang T.S., Kesler C.E.**, *Fatigue behavior of reinforced concrete beams*, ACI Journal Proceedings, Vol. 55, No. 8, pp. 245-254, 1958

[Cif13] **Cifuentes H., Alcalde M., Medina F.**, *Measuring the size-independent fracture energy of concrete*, Strain, Vol. 49, pp. 54-59, 2013

[Coi07] **Coin A., Thonier H.**, *Shear tests on reinforced concrete slabs* (in French: Essais sur le cisaillement des dalles en béton armé), Annales du Bâtiment et des Travaux Publics, pp. 7-16, 2007

[Cul96] **Cullington D.W., Daly A.F., Hill M.E.**, *Assessment of reinforced concrete bridges: collapse tests on Thurloxton underpass*, Bridge Management, Vol. 3, pp. 667-674, 1996

[Dam07] **Damasceno L.**, *Experimental analysis of one-way reinforced concrete flat slabs in punching shear with rectangular columns* (in Portuguese: *Análise experimental de lajes lisas unidirecionais de concreto armado com pilares retangulares ao puncionamento*), Universidade Federal do Pará, 2007

[Deb82] **Debaiky, S.Y., Elniema E.I.**, *Behavior and strength of reinforced concrete haunched beams in shear*, ACI Journal, Vol. 79, pp. 184-194, 1982

[Dru61] **Drucker D.C.**, *On structural concrete and the theorems of limit analysis*, Publications, International Association for Bridge and Structural Engineering, Vol. 21, pp. 49-59, 1961

[Dua02] **Duan K., Hu, X.-Z., Wittmann F.H.**, *Explanation of size effect in concrete fracture using non-uniform energy distribution*, Materials and Structures, Vol. 35, pp. 326-331, 2002

[Dug60] **Dugdale D.S.**, *Yielding of steel sheets containig slits*, Journal of the Mechanics and Physics of Solids, Vol. 8, pp. 100-104, 1960

[Ein15] **Einpaul J., Fernández Ruiz M., Muttoni A.**, *Influence of moment redistribution and compressive membrane action on punching strength of flat slabs*, Engineering Structures, Vol. 86, pp. 43-57, 2015

[EC1-2] **CEN**, *Eurocode 1: Actions on structures - Part 2: Traffic loads on bridges*, 164p., 2003

[EC2-1] **CEN**, *Eurocode 2: Design of concrete structures - Part 1-1: General rules and rules for buildings*, 198p., 2005

[EN196-1] **CEN**, *EN 196-1: Methods of testing cement - Part 1: Determination of strength*, 33p., 2005

[Far79] **Farghaly S.A.**, *Shear design of reinforced concrete beams for static and repeated loads* (in Japanese). PhD thesis. University of Tokyo, 1979

[Fer07] **Fernández Ruiz M., Muttoni A., Gambarova, P.G.**, *Relationship between nonlinear creep and cracking of concrete under uniaxial compression*, Journal of Advanced Concrete Technology, Japan, Vol. 5, No. 3, pp. 383-393, 2007

[Fer08] **Fernández Ruiz M., Muttoni A.**, *Shear strength of thin-webbed post-tensioned beams*, ACI Structural Journal, Vol. 105, No. 3, pp. 308-317, 2008

[Fer15] **Fernández Ruiz M., Zanuy C., Natário F., Gallego J.M., Albajar L., Muttoni A.**, *Influence of fatigue loading in shear failures of reinforced concrete members without transverse reinforcement*, Journal of Advanced Concrete Technology, Vol. 13, pp. 263-274, 2015

[Ferr06] **Ferreira M.**, *Experimental analysis of one-way reinforced concrete flat slabs in axis or non-axis-symmetric punching shear* (in Portuguese: *Análise experimental de lajes lisas unidirecionais de concreto armado ao puncionamento simétrico ou assimétrico*), Universidade Federal do Pará, 2006

[Fre83] **Frey R., Thürlimann B.**, *Fatigue tests of RC beams with and without web reinforcement* (in German: *Ermüdungsversuche an Stahlbetonbalken mit und ohne Schubbewehrung*), Report No. 7801-01, Institut für Baustatik und Konstruktion ETH Zürich, 1983

[Gal14a] **Gallego J.M., Zanuy C., Albajar L.**, *Shear fatigue behaviour of reinforced concrete elements without shear reinforcement*, Engineering Structures, Vol. 79, pp. 45-57, 2014

[Gal14b] **Gallego J.M.**, *Shear-fatigue behavior of linear reinforced concrete members without shear reinforcement* (in Spanish: *Comportamiento a fatiga por cortante de elementos lineales de hormigón armado sin cercos*), PhD Thesis, UPMadrid, 190p., 2014

[Gra02] **Graddy J.C., Kim J., Whitt J.H., Burns N.H., Klingner R.E.**, *Punching-shear behavior of bridge decks under fatigue loading*, ACI Structural Journal, Vol. 99, No. 3, pp. 257-266, 2002

[Gri21] **Griffith A.A.**, *The phenomena of rupture and flow in solids*, Philosophical Transactions of The Royal Society of London, Vol. 221, pp. 163-198, 1921

[Gua09] **Guandalini S., Burdet O., Muttoni A.**, *Punching tests of slabs with low reinforcement ratios*, ACI Structural Journal, Vol. 106, No. 1, pp. 87-95, 2009

[Han69] **Hanson J.M.**, *Square openings in webs of continuous joists*, Research and Development Bulletin PCA, pp. 1-14, 1969

[Haw76] **Hawkins N.M.**, *Fatigue design considerations for reinforcement in concrete bridge decks*, ACI Journal Vol. 73, No. 9, pp. 104-115, 1976

[Heg13] **Hegger J., Reissen K.**, *Shear strength of deck slabs - Adaptation of the DIN technical report "Concrete Bridges" to final Eurocodes and national Annexes, including comparative calculations* (in German: *Querkrafttragfähigkeit von Fahrbahnplatten - Anpassung des DIN-Fachberichtes "Betonbrücken" an endgültige Eurocodes und nationale Anhänge einschliesslich Vergleichsrechnungen*), BAST Brücken- und Ingenieurbau, Vol. B93, 2013

[Hig78] **Higai T.**, *Fundamental study on shear failure of reinforced concrete beams*, Proceedings of the Japanese Society of Civil Engineers, Vol. 1, No. 279, pp. 113-126, 1978

[Hil76] **Hillerborg A., Modéer M., Petersson P.-E.**, *Analysis of crack formation and crack growth in concrete by means of fracture mechanics and finite elements*, Cement and Concrete Research, Vol. 6, pp. 773-782, 1976

[Hil83] **Hillerborg A.**, *Analysis of single crack*, Fracture Mechanics of Concrete, Wittmann F.H. (ed.), Elsevier,pp. 223-249, 1983

[Hsu81] **Hsu T.T.C.**, *Fatigue of plain concrete*, ACI Journal, Vol. 78, pp. 292-304, 1981

[Hu92] **Hu, X.-Z., Wittmann F.H.**, *Fracture energy and fracture process zone*, Materials and Structures, Vol. 25, pp. 319-326, 1992

[Hu00] **Hu, X.-Z., Wittmann F.H.**, *Size effect on toughness induced by crack close to free surface*, Engineering Fracture Mechanics, Vol. 65, pp. 209-221, 2000

[Hu04] **Hu, X.-Z., Duan K.**, *Influence of fracture process zone height on fracture energy of concrete*, Cement and Concrete Research, Vol. 34, pp. 1321-1330, 2004

[Hu07] **Hu, X.-Z., Duan K.**, *Size effect: influence of proximity of fracture process zone to specimen boundary*, Engineering Fracture Mechanics, Vol. 74, pp. 1093-1100, 2007

[Hwa10] **Hwang H., Yoon H., Joh C., Kim B.-S.**, *Punching and fatigue behavior of long-span prestressed concrete deck slabs*, Engineering Structures, Vol. 32, pp. 2861-2872, 2010

[Ing13] **Inglis C.E.**, *Stresses in a plate due to the presence of cracks and sharp corners*, Spring Meetings of the Fifty-fourth Session of the Institution of Naval Architects, 1913

[Irw68] **Irwin G.R.**, *Linear fracture mechanics, fracture transition, and fracture control*, Engineering Fracture Mechanics, Vol. I, pp. 241-257, 1968

[Jen85] **Jenq Y., Shah S.P.**, *Two parameter fracture model for concrete*, Journal of Engineering Mechanics, Vol. 111, pp. 1227-1241, 1985

[Joh04] **Johansson U.**, *Fatigue tests and analysis of reinforced concrete bridge deck models*, Licentiate thesis, Royal Institute of Technology, Stockholm, Sweden, 2004

[Kan64] **Kani G.N.J.**, *The riddle of shear failure and its solution*, ACI Journal, Vol. 61, No. 4, pp. 441-467, 1964

[Kan66] **Kani G.N.J.**, *Basic facts concerning shear failure*, ACI Journal, Vol. 63, No. 6, pp. 675-692, 1966

[Kin60] **Kinnunen S., Nylander H.**, *Punching of concrete slabs without shear reinforcement*, Transactions of the Royal Institute of Technology, No. 158, 112 pp., 1960

[Kup69] **Kupfer H., Hilsdorf H.K., Rüsch, H.**, *Behavior of concrete under biaxial stresses*, ACI Journal - Proceedings, Vol. 66, pp. 656-666, 1969

[Kwa01] **Kwak K.H., Park J.G.**, *Shear-fatigue behaviour of high-strength reinforced concrete beams under repeated loading*, Structural Engineering and Mechanics, Vol. 11, No. 3, pp. 301-314, 2001

[Lan13a] **Lantsoght E., van der Veen C., Walraven J.**, *Shear in one-way slabs under concentrated load close to support*, ACI Structural Journal, Vol. 110, No. 2, pp. 275-284, 2013

[Lan13b] **Lantsoght E.**, *Shear in reinforced concrete slabs under concentrated loads close to supports*, PhD Thesis, TU Delft, 306p., 2013

[Lan14a] **Lantsoght E., van der Veen C., Walraven J., de Boer A.**, *Database of wide concrete members failing in shear*, Magazine of Concrete Research, Vol. 67, No. 1, pp. 33-52, 2014

[Lan14b] **Lantsoght E., van der Veen C., de Boer A., Walraven J.**, *Influence of width on shear capacity of reinforced concrete members*, ACI Structural Journal, Vol. 111, No. 6, pp. 1441-1450, 2014

[Lat10] **Latte S.**, *Strength of reinforced concrete deck slabs without shear reinforcement* (in German: *Zur Tragfähigkeit von Stahlbeton-Fahrbahnplatten ohne Querkraftbewehrung*), PhD thesis, Technische Universität Hamburg-Harburg, 2010

[Leo62] **Leonhardt F., Walther R.**, *Contributions to the treatment of shear problems in reinforced concrete* (in German: *Beiträge zur Behandlung der Schubprobleme im Stahlbetonbau*), Beton- und Stahlbetonbau, No. 3, pp. 54-65, 1962

[Lu02] **Lu H.-Y.**, *Behaviour of reinforced concrete cantilevers under concentrated loads*, PhD Thesis, University of Cambridge, 244p., 2003

[Lub06] **Lubel A.**, *Shear in wide reinforced concrete members*, PhD Thesis, University of Toronto, 2006

[Mac94] **MacLeod I.A., Houmsi A.**, *Shear strength of haunched beams without shear reinforcement*, ACI Structural Journal, Vol. 91, No. 1, pp. 79-89, 1994

[Mar84] **Markworth E., Mildner K., Streiber A.**, *Shear bearing capacity of RC beams under cyclic loads* (in German: *Versuche zur Querkrafttragfähigkeit von Stahlbetonbalken unter dynamischer Belastung*), Die Strasse, Vol. 6, pp. 175-180, 1984

[Mar90] **Marti P.**, *Design of concrete slabs for transverse shear*, ACI Structural Journal, Vol. 87, No. 2, pp. 180-190, 1990

[Mic14] **Micallef K., Sagaseta J., Fernández Ruiz M., Muttoni A.**, *Assessing punching shear failure in reinforced concrete flat slabs subjected to localised impact loading*, International Journal of Impact Engineering, Vol. 71, pp. 17-33, 2014

[Min45] **Miner M.A.**, *Cumulative damage in fatigue*, Journal of Applied Mechanics, Vol. 12, No. 3, pp. A159-A164, 1945

[MC2010] **fib**, *Model Code 2010 - Final draft, Volume 1 and 2*, *fib* Bulletin 65, 350p., *fib* Bulletin 66, 370p., 2012

[Mor29] **Mörsch**, *Reinforced concrete - theory and application* (in German: *Der Eisenbetonbau, seine Theorie und Anwendung*), Verlag von Konrad Wittwer, 541p., 1929

[Moo54] **Moody K.G., Viest M., Elstner R.C., Hognestad E.**, *Shear strength of reinforced concrete beams - Part 1: tests of simple beams*, ACI Journal, Proceedings Vol. 51, No. 4, pp. 317-332, 1954

[Mut90] **Muttoni A.**, *The aplicability of the plasticity theory in reinforced concrete design* (in German: *Die Anwendbarkeit der Plastizitätstheorie in der Bemessung von Stahlbeton*), PhD thesis, Institut für Baustatik und Konstruktion ETH Zürich, 1990

[Mut91] **Muttoni A., Schwartz J.**, *Behavior of beams and punching in slabs without shear reinforcement*, IABSE Colloquium, Vol. 62, pp. 703-708, 1991

[Mut06] **Muttoni A., Burdet O., Hars E.**, *Effect of duct type on shear strength of thin webs*, ACI Structural Journal, Vol. 103, No. 5, pp. 729-735, 2006

[Mut08a] **Muttoni A., Fernández Ruiz M.**, *Shear strength of members without transverse reinforcement as function of critical shear crack width*, ACI Structural Journal, Vol. 105, No. 2, pp. 163-172, 2008

[Mut08b] **Muttoni A.**, *Punching strength of reinforced concrete slabs without transverse reinforcement*, ACI Structural Journal, Vol. 105, No. 4, pp. 440-450, 2008

[Mut10] **Muttoni A., Fernández Ruiz M.**, *Shear in slabs and beams: should they be treated in the same way?*, *fib* Bulletin 57, pp. 105-128, 2010

[Mut12] **Muttoni A., Fernández Ruiz M.**, *Levels-of-approximation approach in codes of practice*, Structural Engineering International, Vol. 2, pp. 190-194, 2012

[Nat14a] **Natário F., Fernández Ruiz M., Muttoni A.**, *Shear strength of RC slabs under concentrated loads near clamped linear supports*, Engineering Structures, Vol. 76, pp. 10-23, 2014

[Nat14b] **Natário F., Muttoni A.**, *Static and fatigue strength of RC slabs under concentrated loads near linear supports*, Proc. of the 10th fib International PhD Symposium in Civil Engineering, Quebec, Canada, pp. 449-454, 2014

[Nat15a] **Natário F., Fernández Ruiz M., Muttoni A.**, *Experimental investigation on fatigue of concrete cantilever bridge deck slabs subjected to concentrated loads*, Engineering Structures, Vol. 89, pp. 191-203, 2015

[Nat15b] **Natário F., Fernández Ruiz M., Muttoni A.**, *Shear-fatigue behaviour of RC cantilever bridge deck slabs under concentrated loads*, Proc. of the fib Symposium, Concrete-Innovation and Design, Copenhagen, Denmark, 2015

[Oka78] **Okada K., Okamura H., Sonoda K.**, *Fatigue failure mechanism of reinforced concrete bridge deck slabs*, Transportation Research Record, No. 664, pp. 136-144, 1978

[Par63] **Paris P.C., Erdogan F.**, *A critical analysis of crack propagation laws*, Tans. ASME, J. Basic Eng., Vol. 85, pp. 528-533, 1963

[Per88] **Perdikaris P.C., Beim S.**, *RC bridge decks under pulsating and moving load*, Journal of Structural Engineering, Vol. 114, No. 3, pp. 591-607, 1988

[Per89] **Perdikaris P.C., Beim S.R., Bousias S.N.**, *Slab continuity effect on ultimate and fatigue strength of reinforced concrete bridge deck models*, ACI Structural Journal, Vol. 86, No. 4, pp. 483-491, 1989

[Per12] **Pérez Caldentey A., Padilla P., Muttoni A., Fernández Ruiz M.**, *Effect of load distribution and variable depth on shear resistance of slender beams without stirrups*, ACI Structural Journal, Vol. 109, No. 5, pp. 595-603, 2012.

[Pig71] **Bureau Technique PIGUET S.A.**, *The viaducts of Chillon (Switzerland)* (in French), La Technique des Travaux, pp. 47-60, No. 327, 1971

[Reg82] **Regan P.E.**, *Shear resistance of concrete slabs at concentrated loads close to supports*, Polytechnic of Central London, 1982

[Reg88] **Regan P.E., Rezai-Jorabi H.**, *Shear resistance of one-way slabs under concentrated loads*, ACI Structural Journal, pp. 150-157, 1988

[Rei13a] **Reissen K., Hegger J.**, *Experimental investigations on the effective width for shear of single span bridge deck slabs* (in German), Beton- und Stahlbetonbau, Vol. 108, No. 2, pp. 96-103, 2013

[Rei13b] **Reissen K., Hegger J.**, *Experimental investigations on the shear-bearing behaviour of bridge deck cantilever slabs under wheel loads* (in German), Beton- und Stahlbetonbau, Vol. 108, No. 5, pp. 315-324, 2013

[Rom04] **Rombach G.**, *Finite element design of concrete structures - practical problems and their solution*, Thomas Telford, 285p., 2004

[Rom05] **Rombach G., Velasco R.**, *Greatest bending moments and shear forces in deck slabs of concrete bridges due to wheel loads* (in German), Beton- und Stahlbetonbau, Vol. 100, No. 5, pp. 376-389, 2005

[Rom09] **Rombach G., Latte S.**, *Shear resistance of bridge decks without transverse reinforcement* (in German), Beton- und Stahlbetonbau, Vol. 104, No. 10, pp. 642-656, 2009

[Rom11] **Rombach G., Nghiep V.H**, *Shear strength of haunched concrete beams without transverse reinforcement* (in German), Beton- und Stahlbetonbau, Vol. 106, No. 1, pp. 11-20, 2011

[Rom12] **Rombach G., Kohl M.**, *Resistance of concrete members without shear reinforcement to fatigue loads*, Proceedings of the IABSE conference Innovative Infrastructures - Towards Human Urbanism, 2012

[Rom13] **Rombach G., Kohl M.**, *Shear design of RC bridge deck slabs according to Eurocode 2*, Journal of Bridge Engineering, Vol. 18, Special Section: Eurocodes and their implications for bridge design: background, implementation, and comparison to North American practise, pp. 1261-1269, 2013

[Rus60] **Rüsch, H.**, *Research towards a general flexural theory for structural concrete*, ACI Journal, Vol. 57, No 1, pp. 1-28, 1960

[Sag10] **Sagaseta J., Vollum R.L.**, *Shear design of short-span beams*, Magazine of Concrete Research, Vol. 62, No. 4, pp. 267-282, 2010

[Sag11] **Sagaseta J., Muttoni A., Fernández Ruiz M., Tassinari L.**, *Non-axis symmetrical punching shear around internal columns of RC slabs without transverse reinforcement*, Magazine of Concrete Research, Paper 1000098, No. 3, 17p., 2011

[Sag14] **Sagaseta J., Tassinari L., Fernández Ruiz M., Muttoni A.**, *Punching of flat slabs supported on rectangular columns*, Engineering Structures, Vol. 77, pp. 17-33, 2014

[Sal77] **Salam S.A.**, *Beams with openings under different stress conditions*, Our World in Concrete & Structures - Conference Papers, Vol. 1, pp. 259-267, 1977

[Sar13] **Sarkhosh R., Walraven J.C., Den Uijl J.A., Braam C.R.**, *Shear Capacity of Concrete Beams under Sustained Loading*, Assessment, Upgrading and Refurbishment of Infrastructures IABSE Conference, Rotterdam, the Netherlands, 2013

[Saw71] **Sawko F., Saha G.P.**, *Effect of fatigue on ultimate load behavior of concrete bridge decks*, ACI Journal Proceedings SP 26-36, pp. 942-961, 1971

[Sch98] **Schläfli M., Brühwiler E.**, *Fatigue of existing reinforced concrete bridge deck slabs*, Engineering Structures, Vol. 20, No. 11, pp. 991-998, 1998

[Ser02] **Serna-Ros P., Fernandez-Prada M.A., Miguel-Sosa P., Debb O.A.R.**, *Influence of stirrup distribution and support width on the shear strength of reinforced concrete wide beams*, Magazine of Concrete Research, Vol. 54, No. 3, pp. 181-191, 2002

[SIA262:2013] **SIA**, *Concrete structures*, 102p., 2013

[Sig13] **Sigrist V., Bentz E., Fernández Ruiz M., Foster S., Muttoni A.**, *Background to the fib Model Code 2010 shear provisions - part I: beams and slabs*, Structural Concrete, Vol. 14, No. 3, pp. 204-214, 2013

[Som74] **Somes N.F., Corley W.G.**, *Circular openings in webs of continuous beams*, Special Publication SP-42 ACI, pp. 359-398, 1974

[Son82] **Sonoda K., Horikawa T.**, *Fatigue strength of reinforced concrete slabs under moving loads*, Fatigue of steel and concrete structures, pp. 455-462, 1982

[Ste58] **Stelson T.E., Cernica J.N.**, *Fatigue properties of concrete beams*, ACI Special Publication, Vol. 55, No. 8, pp. 255-259, 1958

[Tas11] **Tassinari L.**, *Non-axis-symmetric punching of reinforced concrete slabs* (in French: *Poinçonnement non symétrique des dalles en béton armé*), PhD thesis, EPFL, No. 3739, 163p., 2011

[Tay59] **Taylor R.**, *Discussion of a paper by Chang T.S., Kesler C.E. Fatigue behaviour of reinforced concrete beams*, ACI Journal; Vol. 55, No. 14, pp. 1011-1015, 1959

[Ten84] **Teng S., Ma W., Tan K.H., Kong F.K.**, *Fatigue tests of reinforced concrete deep beams*, The Structural Engineer, Vol. 76, No. 18, pp. 347-352, 1984.

[Tou01] **Toutlemonde F., Ranc G.**, *Fatigue tests of cracked reinforced concrete slabs for estimating the service life of composite bridge decks*, Revue Française de Génie Civil, Vol. 5, No. 4, pp. 483-494, 2001

[Tou98] **Toumi A., Bascoul A. Turatsinze A.**, *Crack propagation in concrete subjected to flexural-cyclic load*, Material and Structures, Vol. 31, pp. 451-458, 1998

[Ued82] **Ueda T.**, *Behaviour in shear of reinforced concrete beams under fatigue loading*, PhD thesis, University of Tokyo, 1982

[Wal81] **Walraven J.C.**, *Fundamental analysis of aggregate interlock*, ASCE Journal of Structural Engineering, Vol. 107, No. 11, pp. 2245-2270, 1981

[Wan96] **Wang C.H.**, *Introduction to Fracture Mechanics*, DSTO Aeronautical and Maritime Research Laboratory, Australia, 1996

[Wei51] **Weibull W.**, *A statistical distribution function of wide applicability*, ASME Journal of Applied Mechanics, Transactions of the American Society of Mechanical Engineers, pp. 293-297, 1951

[Wes39] **Westergaard H.M.**, *Bearing pressures and cracks*, Journal of Applied Mechanics, Vol. 61, pp. A49-A53, 1939

[Vaz02] **Vaz Rodrigues R.**, *Experimental test of a cantilever slab under concentrated load* (in French: *Essai d'un porte-à-faux de pont sous charge concentrée*), EPFL, 88p., 2002

[Vaz07] **Vaz Rodrigues R.**, *Shear strength of reinforced concrete bridge deck slabs*, PhD thesis, EPFL, No. 3739, 114p., 2007

[Vaz08] **Vaz Rodrigues R., Fernández Ruiz M., Muttoni A.**, *Shear strength of R/C bridge cantilever slabs*, Engineering Structures, Vol. 30, pp. 3024-3033, 2008

[Vaz10] **Vaz Rodrigues R., Muttoni A., Fernández Ruiz M.**, *Influence of shear on rotation capacity of reinforced concrete members without shear reinforcement*, ACI Structural Journal, Vol. 107, No. 5, pp. 516-525, 2010

[Ver62] **Verna J.R., Stelson T.E.**, *Failure of small reinforced concrete beams under repeated loads*, ACI Journal Proceedings, Vol. 59, No. 10, pp. 1489-1504, 1962

[Vec86] **Vecchio F.J., Collins M.P.**, *The modified compression-field theory for reinforced concrete elements subjected to shear*, ACI Journal, Vol. 83, No. 2, pp. 219-231, 1986

[You98] **Youn S.-G., Chang S.-P.**, *Behavior of composite bridge deck slabs subjected to static and fatigue loading*, ACI Structural Journal, Vol. 95, No.3, pp. 249-258, 1998

[Zan08] **Zanuy C.**, *Sectional analysis of reinforced concrete elements subjected to fatigue, including sections between cracks* (in Spanish: *Analisis seccional de elementos de hormigón armado sometidos a fatiga, incluyendo secciones entre fisuras*), PhD thesis, UPMadrid, 2008

[Zha07] **Zhang N., Tan K.-H.**, *Size effect in RC deep beams: Experimental investigation and STM verification*, Engineering Structures, Vol. 29, No. 12, pp. 3241-3254, 2007

FRANCISCO NATÁRIO
CIVIL ENGINEER

Rue de Crissier 3
1020 Renens (VD)
Suisse

fmmnatario@gmail.com
Mobile : +41774908219

29 years old
married
born in Viseu
Portugal

LANGUAGES

PORTUGUESE : mother tongue
ENGLISH : advanced user (C1)
FRENCH : advanced user (C1)
SPANISH : mutual intelligibility with Portuguese

EDUCATION

PhD — Mar. 2011 - Jul. 2015
Structural Concrete Laboratory (IBETON)
École Polytechnique Fédérale de Lausanne (EPFL)

MEng in Civil Engineering - Structures - 17/20 Very Good — Sep. 2006 - Sep. 2008
Technical University of Lisbon (Instituto Superior Técnico)

BEng in Civil Engineering - 17/20 Very Good — Sep. 2003 - Jul. 2006
Technical University of Lisbon (Instituto Superior Técnico)

WORK EXPERIENCE

PhD Research Assistant — Mar. 2011 - Jul. 2015
Structural Concrete Laboratory (IBETON) http://ibeton.epfl.ch
École Polytechnique Fédérale de Lausanne (EPFL)
Experimental research on the static and fatigue behavior of reinforced concrete bridge deck slabs

Geotechnical and Structural Engineer — Nov. 2008 - Jan. 2011
Teixeira Duarte, S.A. http://www.tduarte.pt
Design of deep foundations, retaining walls, reinforced and prestressed concrete structures, steel structures, development of construction methods

JOURNAL PUBLICATIONS

Journal of Advanced Concrete Technology — 2015
Fernández Ruiz M., Zanuy C., Natário F., Gallego, J.M., Albajar L., Muttoni A., *Influence of fatigue loading in shear failures of reinforced concrete members without transverse reinforcement*, Journal of Advanced Concrete Technology, Vol. 13, 2015, pp. 263-274

Engineering Structures — 2015
Natário F., Fernández Ruiz M., Muttoni A., *Experimental investigation on fatigue of concrete cantilever bridge deck slabs subjected to concentrated loads*, Engineering Structures, Vol. 89, 2015, pp. 191-203

Engineering Structures — 2014
Natário F., Fernández Ruiz M., Muttoni A., *Shear strength of RC slabs under concentrated loads near clamped linear supports*, Engineering Structures, Vol. 76, 2014, pp. 10-23

PRIZES AND AWARDS

First prize of the 10th *fib* International PhD Symposium in Civil Engineering — 2014

Winner of the **Mário Silva Physics Prize** (prize awarded by the main Portuguese newspaper Público) – General and Restrict Relativity and the Global Positioning System - GPS — 2004

Winner of the **National Qualifier for the International Physics Olympiads** in Taiwan — 2003

2nd place in the **National Physics Olympiads - Level B** (11th grade) — 2002

Winner of the **National Physics Olympiads - Level A** (9th grade, teams of 3 members) — 2000